Copyright is owned by the Author of the thesis. Permission is given for a copy to be downloaded by an individual for the purpose of research and private study only. The thesis may not be reproduced elsewhere without the permission of the Author.

Synthesis of Nanoscale Metal-Organic Frameworks in Non-Ionic Microemulsions

A thesis presented in partial fulfilment of the requirements of the degree of

Masters of Science

in

Nanoscience

at Massey University, Manawatu, New Zealand

Timothy Martin Craig

2020

Abstract

MOFs are a versatile class of porous materials made from metal ions and organic ligands. The structural and functional diversity of these materials allows them to be used in wide variety of applications. However, the mechanisms behind crystal growth are far from fully understood. As a result, control of the MOF particle size has remained largely inconsistent. Several methods have been used to control MOF particle size including microwave assisted synthesis and adjusting the metal: ligand ratio. Recently, researchers have begun to explore the use of microemulsions as an environment to synthesize precise size-controlled nanoscale MOFs. However, this field has been largely unexplored. Herein it is proposed that a non-ionic water/hexanol/Triton X-100/cyclohexane microemulsion can be used as a generic environment for the synthesis of MOF nanoparticles.

In chapter 2, microemulsion synthesis was applied to synthesize ZIFs; the most common MOF subclass. ZIF-8 **sod** was synthesized with a tuneable particle length ranging from 27.3 to 87.3 nm. This was achieved primarily by adjusting the time taken to add the ligand solution to the metal solution. This technique was then applied to synthesize ZIF-67 and Zn-IM MOFs. A relatively rare $Zn(IM)_2$ **neb** topology was observed during synthesis.

In chapter 3, it was demonstrated that microemulsion synthesis could be utilized to synthesize the protein complexes BSA@ZIF-8 & BHG@ZIF-8. The resulting materials had high loading efficiency values up to ~17%. Furthermore, the particle size could be finely tuned from 69.7 to 87.6 nm and 55.9 to 75.3 nm respectively by adjusting the addition time.

In chapter 4, microemulsion synthesis was extended to UiO-66. The newly developed synthesis is both room temperature and does not require the environmentally harmful use of DMF. By altering the addition time or ω_0 value the UiO-66 particles size could be altered from 4.09 to 31.0 nm. Hence, the synthesis of the smallest sample on record was achieved.

Finally, in chapter 5, the results of the previous chapters were summarised. It was acknowledged that significant room for reaction parameter optimization exists in all chapters discussed thus far. However, testing all these parameters would be tedious and may not necessarily lead to significant insights. Hence, it was instead proposed that cyro-TEM, SAXS and *in situ* PXRD are used to monitor the growth of a MOF using either, $Zn(IM)_2$ **neb**, ZIF-8 or UiO-66. Such a study on the mechanistic behaviour of MOFs synthesized using microemulsion synthesis would be invaluable to expanding work in this field.

Acknowledgements

I wish to take this opportunity to acknowledge the people who have contributed towards this MSc. research and thesis. First and foremost, I wish to thank my supervisor, Prof. Shane Telfer. The guidance he has provided in the holistic and technical aspects of this project has been invaluable. He has also provided me with incredible support and encouragement. As part of his group, I have had the opportunity to present at the 2018 MOF Conference and 1st Catalyst Grant Workshop. These opportunities have allowed me to grow and develop as a researcher.

Furthermore, I would like to thank my research group for the support, patience and advice they have shown throughout this project. I wish to thank Dr. John Clements and Dr. Lauren Mcreadie. Discussions and ideas from John have been invaluable in the early conception of this project. Lauren has provided significant insight into the properties and analysis of the UiO-66 framework. Both Lauren and John, have provided significant assistance in the editing of this thesis.

I would also like to thank the School of Fundamental Sciences' (SFS) staff for their support. Prof. Gill Norris has provided materials and research advice for the work done in chapter 3. I would also like to thank SFS for allowing the use of instruments required for data collection such as the scattering lab and NMR. Further acknowledgement should be given to the Manawatu Microscopy and Imaging Centre (MMIC) for allowing me to collect images using their transmission electron microscope.

Lastly, I would like to thank my friends and family. Their support over the years has been incredible. These contributions have been invaluable, and I could not have done it without everyone's support.

Abbreviations

AOT	Sodium bisethyl hexyl sulphosuccinate
BDC	Benzene-1,4-dioic acid
BET	Brunauer Emmett Teller
BHG	Bovine haemoglobin
BSA	Bovine serum albumin
BTC	Benzene-1,3,5-trioic acid
CCDC	Cambridge Crystallographic Data Centre
CDF	Cumulative distribution function
CTAB	Centrimonium bromide
DFT	Density functional theory
DLS	Dynamic light scattering
DMF	Dimethyl formamide
ECDF	Empirical CDF
FTIR	Fourier transform infrared spectroscopy
HIM	Imidazole
HmIM	2-methylimidazole
LE	Loading Efficiency
MOF	Metal-organic framework
MW	Microwave
o/w	Oil in water
PDF	Probability distribution function
PSD	Particle size distribution
PXRD	Powder x-ray diffraction
RD	rhombic dodecahedron
RSD	Relative standard deviation
SBU	Secondary building unit
SD	Standard deviation

SDS	Sodium dodecyl sulphate
TEM	Transmission electron microscopy
TGA	Thermal gravimetric analysis
TRD	Truncated rhombic dodecahedron
TX-100	Triton X-100
UiO	University of Oslo
US	Ultrasound
w/o	Water in oil
ZIF	Zeolitic imidazole framework
Zn-IM	Zinc imidazole MOF
μEL	Ligand containing microemulsion
μEM	Metal containing microemulsion
ω_o	Molar ratio of water to surfactant

Table of Contents

Chapter 1 - Introduction

1.1. Metal-Organic Frameworks

Metal-organic framework (MOFs) are a subclass of coordination polymers consisting of metallic nodes and ligands, arranged to form an extended crystalline lattice (Figure 1.1). In MOFs, the metallic nodes are either metal ions or metal ion containing clusters, with multiple sites available for ligand binding. The ligands are divergent multi-dentate organic molecules, which can have a range of geometries, properties and binding modes.[1] MOFs are typically porous and possess some of the highest surface areas of any known materials, with several structures possessing surface areas of ~7000 m^2 g^{-1}. This is approximately the area of an American football field packed into a single gram of material.[2-4] In addition to their enormous surface area, MOFs possess enormous structural diversity with approximately 70,000 structures identified in the Cambridge Crystallographic Data Centre (CCDC).[5] Furthermore, MOFs are often highly chemically/thermally stabile due to the combination of strong metal ligand bonds and high connectivity.[1, 6] The combination of these three properties has allowed MOFs to be used in a diverse range of applications (1.1.4 Applications).

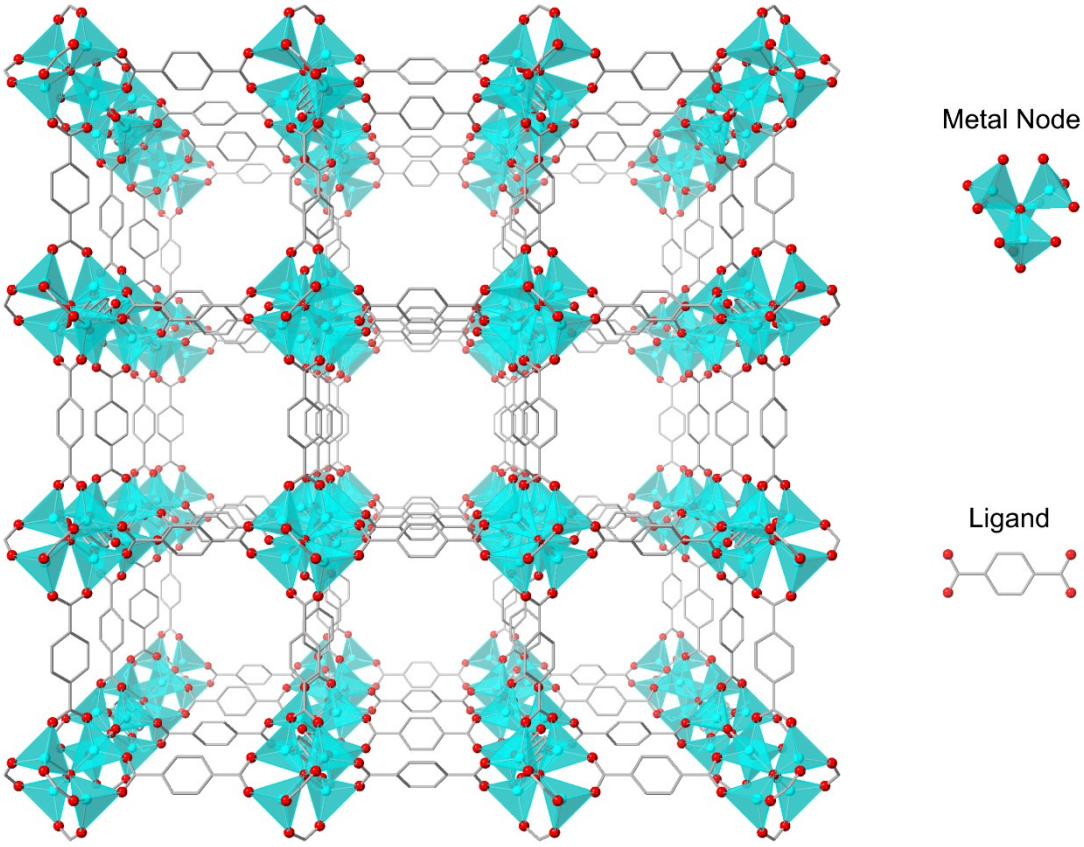

Figure 1.1 Typical Metal-Organic Framework[7, 8]

1.1.1. Nomenclature

MOFs are typically named with an abbreviated name and number code (e.g. HKUST-1[9], NU-1000[10] etc.) given by their discoverer. There is no consistent naming scheme used by all MOFs. In many cases, this name is a reference to the institution that housed the group that discovered them e.g. MUF-77 (Massey University Framework).[11] Alternatively, the name can refer to their structure e.g. ZIF-8 (Zeolitic Imidazole Framework).[12] As the naming is left to the researchers, ambiguities and inconsistencies are common. For instance, tetramethyl substituted MOF-5 is given a new name (IRMOF-18) whereas amine substituted UiO-66 (UiO-66-NH_2) is not.[13, 14] Alternately, a MOF can be identified using an abbreviated chemical formula e.g. $Zn_4(IM)_{10}$ (IM= imidazole).[15, 16] However, the use of MOF names is preferred because of the existence of structurally different MOFs with the same chemical formula. This is discussed further in 1.1.5.1 Topology. In addition to MOF nomenclature, ligands are often provided with abbreviated names e.g. H_2BDC (1,4-benzene dicarboxylic acid). Unless specifically described in this introduction, ligands are referred to by their abbreviation and their full names and structures are found in the appendices (Figure C.2).

1.1.2. History

One of the earliest coordination polymers was Prussian Blue, which dates to 1706. This material consists of CN^- ligands and Fe(II/III) ions arranged in a cubic lattice and was an inspiration for the development of later coordination polymers. In 1990, Hoskins and Robson took inspiration from these materials and proposed that a new class of materials (MOFs) could be produced using metal nodes and rod-like ligands. They proposed that these materials would have several properties, including:

1. Significant mechanical and thermal stability due to strength and connectivity of metal ligand bonds.
2. Large cavities which could be evacuated to provide empty pores allowing for a large surface area and low density.
3. A crystalline structure which allows easy resolution using X-ray crystallographic techniques.
4. A highly tuneable pore environment that can be designed through ligand modification and which may allow guest uptake, exchange and catalysis.
5. The ability to be chemically modified after synthesis in order to provide new functionality.[17]

Despite earlier syntheses, these predictions were only truly realised in 1999 with the independent synthesis of two ground-breaking MOFs: MOF-5 and HKUST-1 (Figure 1.2). MOF-5, produced by Yaghi and colleagues, consists of cubically arranged BDC and Zn_4O tetrads. It was revolutionary, as it displayed stability at temperatures up to 300 ºC. Furthermore, it retained its structure despite the removal of guest molecules from its pores, a process now referred to as activation. It possessed an enormous BET (Brunauer Emmett Teller) surface area of 2320 m^2 g^{-1} - the largest surface area of any material known at the time. A later breakthrough with MOF-5 was achieved by Yaghi in 2002. They substituted the BDC ligand in MOF-5 with a series of ligands with identical coordination sites but different lengths or functional groups. This resulted in a series of MOFs with different functional groups on the ligand but the same overall topology (1.1.5.1 Topology); known as IRMOFs (**i**so**r**eticular MOFs). This process of substituting the metallic or organic components with analogues that maintain the same geometry is known as isoreticular chemistry.[13]

HKUST-1 was produced by Williams and colleagues. This MOF consists of $Cu_2(CO_2)_4$ paddle-wheel clusters bound to BTC and axial water. Like, MOF-5 it displayed an enormous surface area of 1850 m^2 g^{-1}. However, they also displayed that water molecules bound to the paddle-wheel cluster could be removed through heat treatment. The replacement of axial water with pyridine was one of the earliest examples of what later became known as the 'post synthetic modification' of MOFs. Furthermore, it was found that the removal of axial water creates free Cu coordination sites which could be utilised as Lewis acid catalysts highlighting the potential of these materials for catalytic applications.[9]

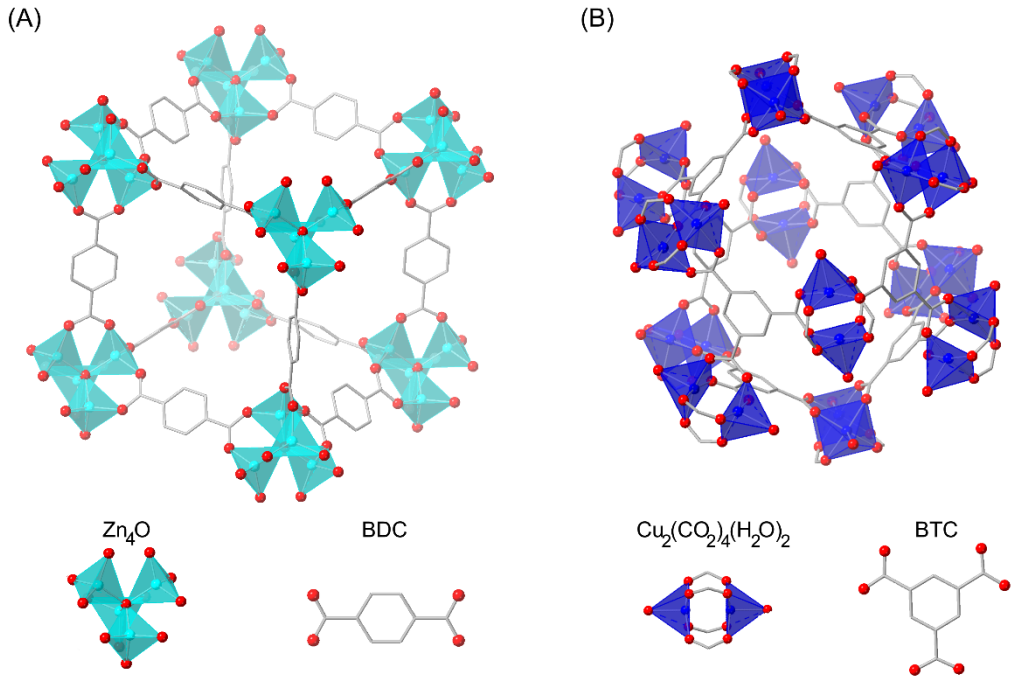

Figure 1.2 (A) MOF-5 and (B) HKUST-1

Since the achievement of these milestones research conducted in MOF chemistry has exploded. To date, a Web of Science search for the term "MOF" will yield 20,978 results and will continue to rise as researchers discover new structures and applications.[18]

1.1.3. Synthesis Methods

Typically, MOFs are synthesized using a solvothermal approach where the metal salts and protonated ligands (e.g. H_2BDC) are mixed with a solvent and heated in an oven. This often requires high temperatures (100-200 °C) and long growth periods (several hours to days). The solvent is typically *N*,*N*′-dimethylformamide (DMF) or *N*,*N*′-diethyformamide (DEF), as these promote deprotonation of the ligand (e.g. H_2BDC to BDC) at elevated temperatures over time. As deprotonated ligands sequester metal binding sites, the MOF slowly grows. Solvothermal synthesis has aptly been dubbed "shake and bake" chemistry due to the discovery of multiple MOF structures by testing various ligand metal combinations and environmental conditions with solvothermal methods.

Unsurprisingly, with the volume of publications in the MOF field, there is enormous diversity in the synthetic methods used for synthesis. This is often for the purposes of improving yields, scalability, or obtaining specific properties in the resulting products. These include electrochemical, room-temperature, microwave, ultrasound and microemulsion

syntheses, amongst others. A select few of these are discussed more thoroughly in 1.1.5.2.3 Morphology Control .

1.1.4. Applications

The variety in MOF structures and the ability to tune their pore environments (1.1.5 Crystal Design) has resulted in the synthesis of MOFs containing a vast array of different properties, including: catalysis[19, 20], florescence[21], and magnetism.[22, 23] Furthermore, the porous nature of MOFs allows molecules to defuse into these cavities and interact with the MOF surface. Unsurprisingly, the combination of these two properties has allowed MOFs to be utilized in a vast array of applications. These include sensors, MRI contrasting agents, membranes, photovoltaics, drug delivery, gas storage and catalysis. A select few of the more prominent ones are discussed below.

1.1.4.1. Gas Storage and Separation

In gas storage applications, surface interactions such as Van der Waals attractions, or electrostatic interactions between open metal sites of the MOF host and guest molecules, can allow for a higher uptake of gas molecules than the same volume of gas stored in bulk at ambient pressures. With climate change becoming an increasing concern, this technique has found usage in the high-density storage of sustainable energy sources such as methane and hydrogen gas as well as the separation of carbon dioxide.[24] In recent years, MOFs that absorb water have found applications. These materials are highly sought out for: low energy dehumidifiers and providing drinking water from atmospheric condensation for humanitarian purposes. For such applications, the MOF must have a high water uptake capacity in arid conditions and must be amenable to repeated cycles of water adsorption and desorption. Recently, Yaghi's group tested a MOF-808 ($Zr_6O_4(OH)_4$(fumarate)$_6$) system outdoors in Arizona.* They found that the MOF-808 system had a 25% by weight uptake and could be entirely solar driven with adsorption and desorption occurring during night day cycles.† Thus, both criteria were fulfilled with a commercially applicable system.[25] The commercial viability of water absorbent MOFs is further highlighted by a recent start-up company Molecule Ltd., which is proposing 2020-21 pilots for desiccation systems based on a proprietary MOF.[26, 27]

Along with gas storage, MOFs are also utilized for molecular separations. These include noble gas purification[28] and separation of CO_2 from flue gasses from the post-combustion of fossil fuels.[29] One approach to molecular separations is size exclusion, which prevents one

* Relative humidity ~30%
† Night time temperature ~15 ºC. Day time temperature ~30 ºC

material entering the MOF cavity whilst letting the other through. Another approach is *via* selective adsorption, where one material has a higher affinity towards the MOF surface then the other.[30] A recent example of this approach was for a system separating ethylene and ethane mixtures. Ethylene is critical to the synthesis of various polymers and organic molecules. However, it is typically produced by thermal cracking of hydrocarbons - a process which produces impurities such as ethane. Ethylene is industrially purified using cryogenic distillation, an energy inefficient and costly process. In fact, purification of ethylene and propylene alone accounts for an estimated 0.3% of the global energy consumption. This is approximately the same the energy consumption of Singapore.[31] and Last year, our research group published an effective MOF that is well able to separate these gas mixtures, MUF-15, which consists of Co^{2+} and benzene 1,3-dicarboxylate (isophthalate). MUF-15 has small pore dimensions that maximise Van der Waals interactions between benzene and ethane while allowing ethylene through. Hence, MUF-15 is highly efficient at separating these two gasses and is capable of purifying 14 L kg^{-1}* ethylene from an equimolar mixture of ethane and ethylene.[32]

1.1.4.2. Drug Delivery

Targeted drug delivery is a significant objective of medical research since bioactive compounds are often insoluble, or toxic, to otherwise healthy tissue. For instance, the chemotherapy drug cisplatin, $[Pt(NH_3)_2Cl_2]$, is highly toxic to proliferating tissues as it interferes with DNA synthesis. Hence, patients exhibit side effects including nausea, vomiting, anemia, diarrhoea and immunodeficiency. The predominant requirements three predominant requirements when designing carriers for drug delivery are listed below.

1. The carrier should have a high loading efficiency (LE).† However, this must be paired with reasonable drug retention to prevent drug leaching on distribution.
2. The carrier must be transportable to the delivery target and be able to release the drug on delivery.
3. The carrier must have a low toxicity. [33, 34]

For the first criteria, as already noted, the porous cavities of MOFs are excellent environments for molecular storage. Indeed, researchers have designed MOF drug complexes with incredibly high LE values by entrapping the drug within the MOF pores. At the high end, Teplensky and colleagues encapsulated the anticancer drug α-cyano-4-hydroxycinnamic acid

* Litres ethylene per kg MUF-77 per adsorption cycle.
† Drug mass as a percentage of the total mass.

inside NU-1000 with a 68.5 % LE.[35] However, the reported LE has substantial variability depending on the affinity of the MOF drug pair. This is highlighted by literature indicating LE values as low as 1.5%.[36] Hence, significant optimization is often required to maximising host-guest interactions and LE values. Fortunately, the structural tunability and diversity of MOFs allows researchers to develop alternate strategies to trap drugs with high LE values. One such strategy is to incorporate the drug as part of the MOF through synthesis or PSM. Lin and colleagues used this method to obtain 72% for a MOF composed of DCSP (cisplatin(succinate)$_2$) ligands and Tb^{3+} ions developed using this strategy.[37] However, the ability to perform this strategy is highly dependent on the drug chemistry.

For the second criteria, drug release is typically achieved through dissolution of the MOF or desorption of the drug in response to stimuli[38]. To improve retention time and prevent drug leaching before delivery, the MOF is often coated in a layer of lipids, silica, or polyvinyl propylene (PVP) which improves the MOF stability, drug retention, and biodistribution[33, 34]. Since the coating is typically hydrophilic, it also improves the dispersity of the MOF carrier allowing for improved transport. Furthermore, the surface coating can be functionalized to improve its affinity for the target. This was demonstrated by Lin's group who loaded cisplatin into the MOF NCP-1 coated with silica. The silica surface coating was then functionalized with a peptide chain that had a high affinity for receptor proteins common in cancer cells. Receptor binding triggers uptake of the MOF carrier. NCP-1@silica releases cisplatin after 5-9 hours due to degradation in physiological conditions (pH 7.4, 37 ^{o}C). The authors postulated that this time delay is sufficient to allow deposition in tumour cells, due to its targeted delivery[37]. This is considered active delivery because the target is selected through chemical recognition. Alternatively, passive delivery can occur and is where distribution is nonspecific. In such cases, environmentally induced drug release is typically the targeting mechanism. One such mechanism was proposed by Sun and colleagues in 2012. They proposed using ZIF-8 to deliver the anticancer drug 5-fluorouracil on the basis that cancer cells possess an acidic environment (pH 5.5 – 6). ZIF-8 degrades in acidic conditions (pH >6), thus releasing the drug[39]. Since this study ZIF-8 has regularly been used as a passive pH sensitive carrier[40-42]. Whilst these approaches are promising distribution of nanocarriers within a living organism is complex. The shape and size of a carrier can critically affect its overall distribution. For instance, carriers less than 150 nm in diameter are more likely to be delivered to the cellular interior by endocytosis[43, 44]. Though, larger carriers have been demonstrated to enter by this mechanism depending on the shape. This can impact their likelihood of reaching the target site. For instance, NPs less than 200 nm in length tend to accumulate at tumour cells by travelling through the leaky

endothelium. Furthermore, even the path by which NPs are filtered out of the body is size-dependent as 200 nm particles have been demonstrated to be filtered through the spleen, but NPs less than 10 nm traverse the kidney. Our current inability to precisely control the shape and size of MOF crystals and our lack of understanding of the overall impact of these factors on their biodistribution are severe limitation on the real-world usage of these materials[33, 34, 45].

Studies on MOF carrier toxicity are equally promising. Common drug delivery MOFs, include low cytotoxicity ligands (BDC, BTC imidazole) and metals (e.g. Cu^{2+}, Zn^{2+}, Fe^{2+}, Fe^{3+})[33] and have displayed limited cytotoxicity *in vitro*. One such study by Hoop and colleagues concluded ZIF-8 had limited cytotoxic effects on kidney, skin, breast, blood, bones, and connective tissues[46]. *In vivo*, multiple studies have demonstrated the use of these materials is biocompatible in mice[47-49]. Unfortunately, limited information is available about the safety of these materials *in vivo* in humans. Currently only the University of Chicago and RiMO Therapeutics Inc. are conducting any human trials. Furthermore, this is only in phase I and is expected to last until March 2021 before phase II and III trials can even begin[50, 51].

1.1.4.3. Catalysis

MOFs have many properties that endear them towards catalytic applications. They are a solid material and can be easily extracted and recycled as heterogenous catalysts. Their diverse and tuneable pore environments allow the introduction of catalytic sites in the form of open metal sites[19] or as part of the ligand.[52, 53] Therefore, these can be used in a wide array of catalytic applications, including CO_2 reduction[54] and nerve gas degradation.[55, 56] By introducing multiple catalytic sites, MOFs can perform tandem catalytic processes.[57] Furthermore, the catalytic viability of MOFs is further enhanced by its large surface area and porous nature, which allows a high density of catalytic sites to be exposed to reactants migrating through their pores. Hence, they are often highly effective catalysts.[52, 53]

In addition to high catalytic efficiency and a diverse range of catalytic functionality, by tuning the shape of the pore environment or the size of the pore aperture, MOF catalysts can be imparted with size or shape selectivity towards products or reactants.[58, 59] This is highlighted by a 2018 study by Farha's group., in which they used UiO-66-Ir(II) to catalyse the borylation of methane to monoborylated methane, instead of its thermodynamically preferred diborylated methane. The monoborylated variant has a length of 0.88 nm whereas the diborylated variant has a length of 1.39 nm. As the pore width of UiO-66-Ir(II) is 1.1 nm, the smaller monoborylated product is selectively synthesized.[20]

1.1.5. Crystal Design

This diversity in MOF structure function and applications arises largely from their tuneable nature. Instead of selecting an application based on the properties of a material, MOFs have the potential to have the material properties selected to suit the specific application. For this reason, some researchers have referred to them as potential designer materials. Whilst significant progress has been made to this affect, the development of new methods to tune MOF properties is still a significant area of ongoing research.

1.1.5.1.Topology

Whilst isoreticular synthesis and PSM focus predominantly on maintaining the underlying connectivity while altering the functionality of the MOF, in many instances it is desirable to alter the underlying connectivity and pore structure. This can influence selectivity, stability and guest adsorption behaviour. The underlying arrangement of the atoms within the crystal is known as the topology.[60]

MOF topologies are described using nets. A net is a graph of vertices connected by uni-directed edges where all vertices/edges are connected.[61] To represent a MOF as a net, a repeated substructure within the MOF, known as a secondary building unit (SBU), is represented as either an edge or vertex and abstracted to a net of the MOF's overall structure (Figure 1.3). Known nets are recorded in databases such as the Reticular Chemistry Structure Resource (RCSR) database. The RCSR database identifies nets using lower-case bold three letter codes e.g. **dia**.[62*] By selecting SBUs with specific geometries, the topology can often be rationally designed. For instance, the combination of an octahedral cluster and linear ligand will most likely form a **pcu** net.[63]

[*] It should be noted that suffixed codes such as **dia-c** exist. However, these do not appear within the scope of this thesis. Such codes occur where the unit cell symmetry may differ but the tiling remains the same. E.g an interpenetrate **dia** net (**dia**-c) or a **dia** net with two differing vertices or linkers (**dia-b**).[62]

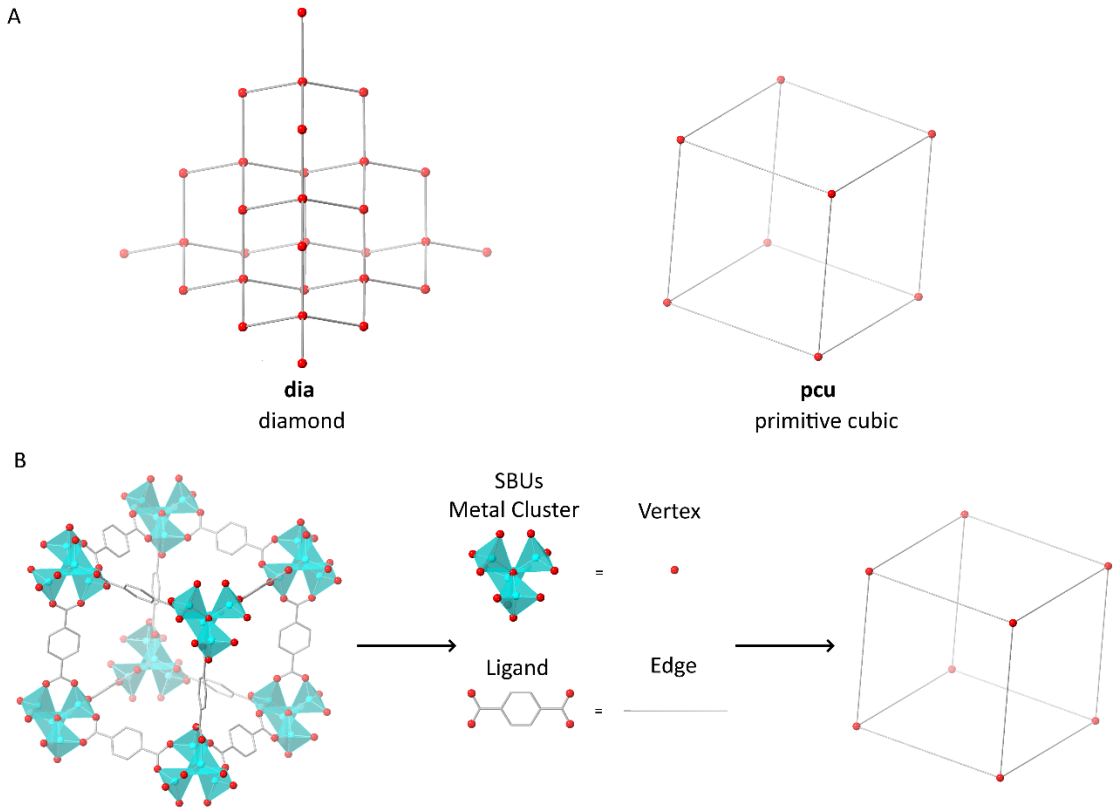

Figure 1.3 (A) Example RCSR nets. (B) Abstraction of MOF-5 to a **pcu** net.

Unfortunately, the resulting topology cannot always be rationally inferred from the structure of the starting materials. The formation and growth of MOFs is a nuanced process often involving several intermediates. As a result, the product's topology is often highly sensitive to specific reaction conditions. Studies have demonstrated that topological changes will occur because of changes to the temperature, metal salt selection, solvent, and multiple other conditions. This was highlighted by Nakamura and colleagues. when they demonstrated that $Zn(NO_3)_2.6H_2O$ and H_2BDC could alternatively form MOF-2 (2D sheets) or MOF-5 (**pcu**) solely due to a 25 °C temperature difference during solvothermal synthesis. In Nakamura's case, this was attributed to the formation of a $Zn_2(CO_2)_4(H_2O)_2$ paddle wheel cluster during the lower temperature synthesis. Thus, 2D sheets of MOF-2 were formed in place of MOF-5 due to the differing SBU geometry.[64]

This topological dependence on the reaction environment is further complicated by the existence of topoisomers. A topoisomer is where two structures consist of components with the same geometry but have different overall topologies. This is highlighted by NU-1000 (**csq**) and NU-901 (**scu**), which both possess the same zirconium cluster and 1,3,6,8-tetrakis(p-benzoic acid)pyrene ligand, but different topologies (Figure 1.4). The task of elucidating the influence of different synthetic conditions on such structures is non-trivial, with slight synthetic changes

resulting in significant topological changes. For instance, the substitution of benzoic acid with 4-aminobenzoic acid will result in NU-901 being synthesized instead of NU-1000. For this reason, topological control of MOF formation is still a major field of ongoing of research.[65]

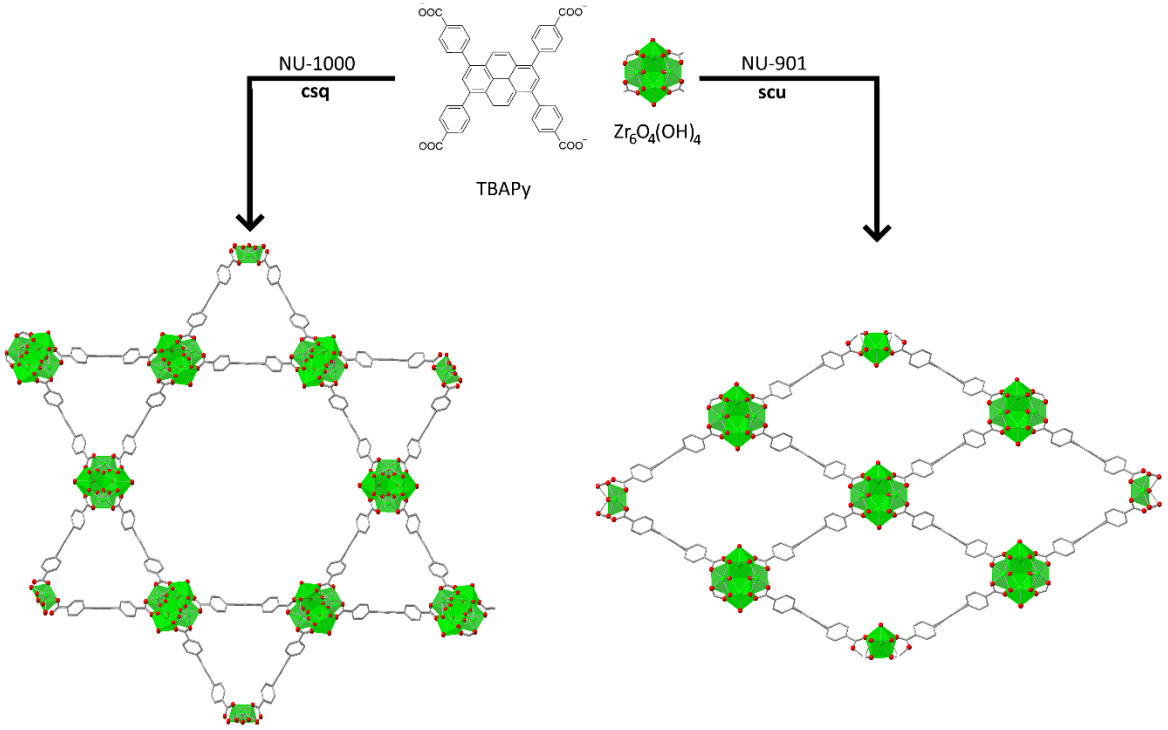

Figure 1.4 NU-1000 **csq** and NU-901 **scu** synthesis derived from the same hexanuclear Zr(IV) SBUs.

1.1.5.2. Morphology

Morphology refers to the overall form of the crystal i.e. its size, shape and dispersity (size range) (Figure 1.5). Whilst it is predominantly influenced by the topology, MOF morphology is highly sensitive to the reaction conditions, can change during the MOF synthesis and is difficult to precisely control (1.1.5.2.3 Morphology Control). Furthermore, the morphology can have a drastic impact on the properties and usage of a MOF. For instance, the MOF morphology influences the packing of the MOF with itself or other materials. This influences the adsorption profile by changing the volume of interstitial voids between crystals.[66] It can even impact the integration of MOFs into membranes or the properties of composite complexes.[67-69] An example of this was highlighted by Avci and colleagues. They synthesized arrays of ZIF-8 particles which reflected light of specific wavelengths. By changing the particle of ZIF-8 NPs by 49 nm the wavelength reflected could be shifted from blue to red.[70]

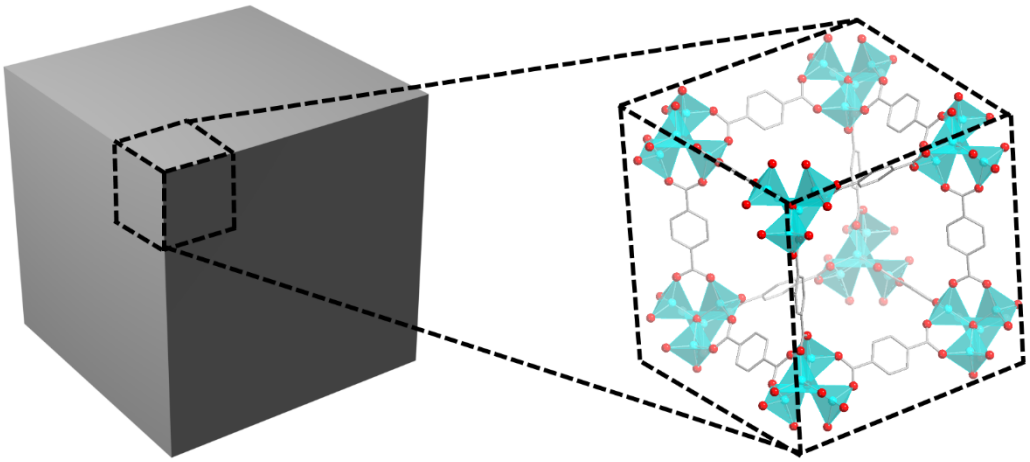

Figure 1.5 Cubic morphology of MOF-5

1.1.5.2.1. Nanoscaling

A significant objective in morphological control studies is to synthesize sub-100 nm MOF nanoparticles (NPs). These materials are highly valued because they can exhibit properties not typically seen in the bulk material. For instance, they can be dispersed in solvents as colloids, allowing them to be more readily used in solution phase applications. Furthermore, their reduced dimensions influence their accelerated adsorption and diffusion kinetics. This is advantageous in catalytic applications, as it allows faster introduction of reactants to catalytic sites. This was highlighted by Wang and colleagues. in 2017. They synthesized 40 nm, 850 nm and 1.5 μm ZIF-8 particles containing platinum NPs (Pt@ZIF-8) and utilized them for the hydrogenation of hexene. They found that the amount of hexene converted to hexane over a 2 hour period decreased substantially from 95.3% (40 nm) to 7.6% (1.5 μm) as the size increased.[68]. In addition, precise morphology control of NPs is essential for controlled *in vitro* distribution (1.1.4.2 Drug Delivery). It is important to note, when evaluating NP synthesis techniques, that the dispersity is often as critical in its application as the average size. There is no consistent standard used in the MOF literature for reporting the NP size and dispersity. A review by Marshall and colleagues recommended that future studies report the average NP size (ϕ), standard deviation (SD) and the sample size. This was used as the reporting standard for this thesis.[71] In the literature the dispersity* is also often reported as the polydispersity index (PDI) (eq. 1.1) or relative standard deviation (RSD) (eq. 1.2). A PDI of 0.05 (RSD 22.4%) is generally considered useable for calibration standards. Whereas, a PDI of 0.2 is generally deemed acceptable for drug delivery (RSD 44.7%).[72] Given the majority of MOF NPs where

* Particle size range within a single sample

dispersity data is published fall into this later bracket,[71] an RSD of less than 45% was taken as reasonably monodispersed in the context of this thesis.

$$\mathbf{PDI} = \left(\frac{\mathbf{SD}}{\boldsymbol{\phi}}\right)^{\mathbf{2}} \quad \textbf{1.1}$$

$$\mathbf{RSD} = \frac{\mathbf{SD}}{\boldsymbol{\phi}} * \mathbf{100} \quad \textbf{1.2}$$

1.1.5.2.2. MOF Formation

The topic of this thesis is an evaluation of a specific MOF morphology control technique (1.2.1 Microemulsion Synthesis). For this purpose, knowledge of crystal formation mechanisms is required to understand the rationale behind this and similar techniques. Unfortunately, the current understanding of MOF formation is far from complete and is beyond the scope of this study. For this reason, a brief overview of crystal formation as it pertains to MOF formation is provided in this section.

In the 1950s, LaMer proposed the model of burst nucleation to describe crystal formation, which is considered the basis for scientific understanding of crystal formation. It proposes that in a supersaturated (C_S) solution of precursors crystal formation occurs in two separate steps that deplete precursors from the solvent; nucleation and crystal growth (Figure 1.6). During the nucleation phase, initial solid seed crystals are developed from a supersaturated solution of precursors. The Gibb's free energy of nucleation (ΔG) is the sum of two opposing contributions (eq. 1.3). The favourable contribution is the Gibb's energy lost due to increasing the non-interfacial bulk volume. It is dependent on the energy difference between the solid crystal phase and the solvent phase (Δg). The unfavourable contribution is the energy gain due to increasing the interfacial free energy. It is dependent on the interfacial surface energy (γ) which in turn is a function of the external surface area of the developing crystal.

$$\boldsymbol{\Delta G} = \mathbf{4}\boldsymbol{\pi r^2}\boldsymbol{\gamma} - \frac{\mathbf{4}\boldsymbol{\pi}}{\mathbf{3}}\boldsymbol{r^3}\boldsymbol{\Delta g} \quad \textbf{1.3}$$

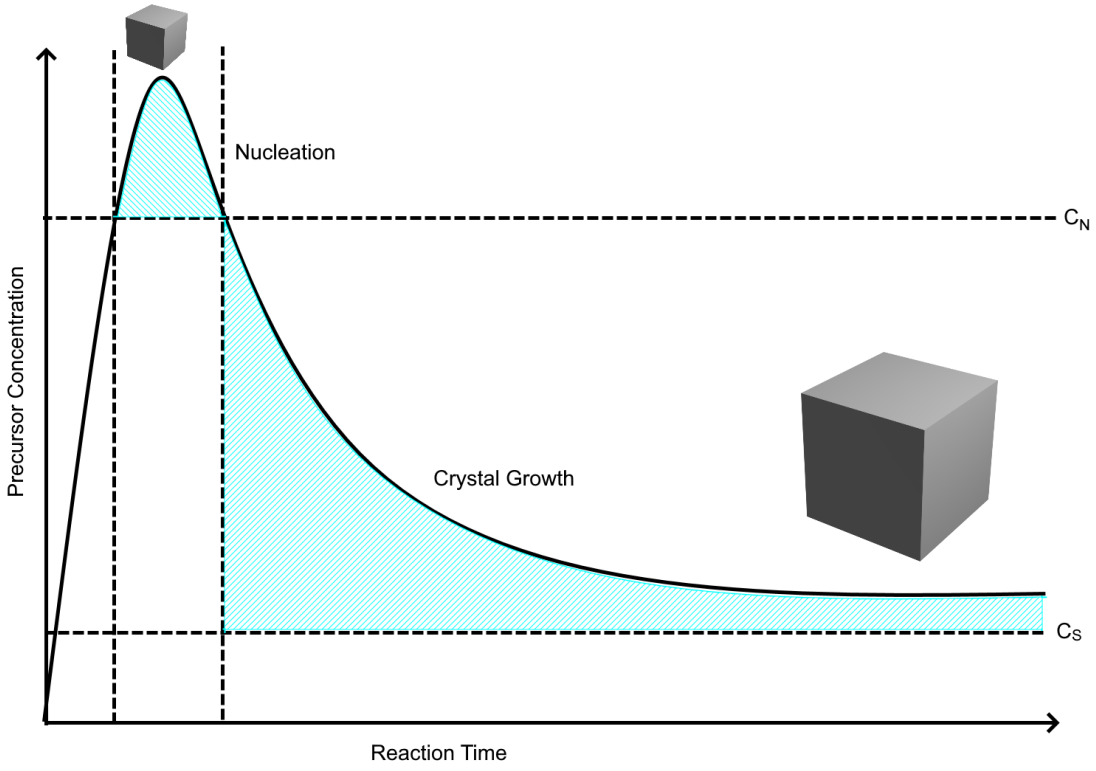

Figure 1.6 MOF Precursors nucleate forming seed crystals which agglomerate and sequester MOF precursors for further crystal growth.

Both contributions are a product of the nuclei radius (r) to differing powers. Hence, until a critical nucleus radius (r_c) (eq. 1.4) is obtained, crystal dissolution to regenerate the precursors is favoured. Hence there is an energy barrier (ΔG_A) (eq. 1.5) that must be overcome for nucleation to occur.

1.4 $$r_c = \frac{2\gamma}{\Delta g}$$

1.5 $$\Delta G_A = r_c^2(4\pi\gamma - \frac{4\pi}{3} r_c \Delta g)$$

However, this model of nucleation assumes homogenous nucleation. In actuality, nucleation predominantly occurs on pre-existing surfaces, such as the container walls or adventitious debris (heterogenous nucleation). This reduces the interfacial free energy of the growing crystal, thus reducing the activation barrier. Hence, the nucleation rate is significantly influenced by the availability and composition of heterogenous nucleation sites and it employed to good effect in laboratory processes such as scratching the interior of a crystallisation vessel with a glass rod.[73] The importance of this process in nucleation has extensively been studied with water. Whilst the melting point is 0 °C the freezing point and nucleation rate can vary significant depending on the available nucleation sites.[74] In a 2008

study by Zobrist and colleagues, a 20 ºC difference in freezing temperature was observed using 4 different nucleating materials (nonadecanol, silica, silver iodide and Arizona test dust).[75]

During the crystal growth phase, crystal growth occurs as a result of several processes driven by the favoured increase in bulk crystal size. These include sequestration of precursors onto the nuclei surface, aggregation of pre-existing seed crystals, and Ostwald ripening. Ostwald ripening is the process where unstable or meta-stable prenucleation crystals are dissolved back into the solution for their precursors to be redeposited onto larger crystals.[76]

Generally, the crystal size is modifiable by altering the nucleation and growth rates. As the nucleation rate is increased more seed-crystals are produced and a shorter growth period is required before growth is terminated. Hence, smaller crystals are obtained. Early termination of the growth period will also result in smaller crystals. Whilst the LaMer model is the primary model used to describe crystal growth and develop morphological control techniques, it is often insufficient to fully describe the complex growth behaviour of MOFs.[71, 76] An example of this can be seen with ZIF-8 which increases in NP size as the reactant concentration increases. This is counterintuitive using the LaMer model which predicts faster nucleation due to increased concentration. This result was attributed to the formation of intermediates during the nucleation process. Amorphous intermediates are re-dissolved as part of its nucleation process, slowing nucleation.[77]

The crystal shape is primarily dependent on the topology. The crystal topology determines which crystal facets are exposed to the outer surface. Hence, growth along different crystal facets occurs at different rates dependent on the topology. However, the growth rate along a facet is also dependent on the concentration of reactants/intermediates present in the solution. Due to the variability of this over time, the shape evolves as crystal growth proceeds. The thermodynamic equilibrium shape is defined by the slowest growing facet (Wulff's rule).[78] For instance, HKUST-1 has competitive growth along two faces [100] and [111]. Hence, HKUST-1 typically possess an octahedral, cuboctahedral or cubic morphology (Figure 1.7). Faster growth along the [111] facet will favour a cubic morphology whereas octahedral crystals are obtained when growth is faster along the [100] facet.[79]

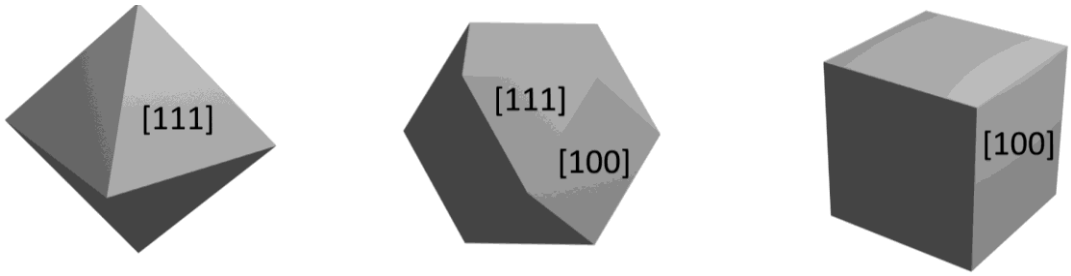

Figure 1.7 From left to right: common HKUST-1 morphologies octahedral, cuboctahedral, and cubic morphologies.

1.1.5.2.3. Morphology Control

Controlling crystal morphology is an ongoing challenge in MOF chemistry. This particularly applies to the production of NMOFs. Whilst significant progress has been made in their production, less than 100 structures have been prepared at the nanoscale. Furthermore, structures with crystals less than 20 nm in size are particularly rare. Researchers have developed several strategies for morphology control including interfacial synthesis, modulation, etching and templating. However, many of these focus on the production of 2D layers and macrostructures, which is not the focus of this thesis. Only a few techniques have found significant usage for MOF NP synthesis: reaction optimization, microwave (MW) & ultrasound (US) synthesis, modulation and microemulsion synthesis.

During MOF synthesis, many different reaction parameters can be tuned to modify the morphology. These include, the reactant concentration, temperature, metal to ligand ratio, and the choice of metal salts etc. For instance, Schejn and colleagues. found that the size of ZIF-8 crystals could be varied from 50 nm to 600 nm simply by substituting the Zn^{2+} salt. More reactive salts such as $Zn(NO_2)_2$ tended to produce smaller crystals than less reactive salts such as $ZnCl_2$.[80] Unfortunately, this approach is far from generically applicable. For instance, ZIF-8 and UiO-66 have both been demonstrated to reduce in NP size as the ligand metal ratio increased.[81, 82] This is because the excess ligands occupy all available metal binding sites faster, increasing the nucleation rate. However, even this cannot be universally applied. HKUST-1 produced with excess BTC has been demonstrated to increase the NP size.[83] Because of these often-contradictory results, rigorous optimization of synthetic protocols is often required to obtain a desired morphology. Hence, high throughput screening or repetitive trial synthesize are used to compile comprehensive literature on their morphological behaviour.[81, 82, 84] However, such an approach is time consuming, costly, and inefficient.

A more generically applicable method to modify the MOF morphology is to alter the heating conditions using microwave (MW) or ultrasound (US) synthesis. These methods produce local hot spots throughout the solution promoting fast energy transfer and homogenous nucleation.[85] Therefore, these methods typically possess faster nucleation and crystal growth rates. This was highlighted by Haque and colleagues, who compared the nucleation and growth rate of conventional heating with US/MW methods for MIL-53. They found that both the nucleation and growth rate followed the same general trend; US proceeded faster than MW, which in turn was significantly faster than conventional heating.[86] Unsurprisingly, the increased nucleation and growth rates allows the production of smaller crystals and shortens the synthetic time. This reduction in synthetic time was observed in the first MW MOF synthesis of Cr-MIL-100 by Jhung, Lee, and Chang in 2005. The synthetic time was reduced from 4 days with conventional heating to 4 hours by MW synthesis.[87] Later reports demonstrate synthetic times of an hour or less. As to the impact on particle size, comparative syntheses of the same MOFs using MW/US and conventional heating highlights that the size decreases as the nucleation and growth rates increase. This is demonstrated with MIL-53, which was synthesized using conventional heating (5-25 μm), MW (1-2 μm) and US (400-800 nm).[86] Furthermore, the particle size is often adjustable by altering the reaction time or power output.[88, 89] Whilst this provides a promising route toward tuneable NMOF synthesis, in practice, MW/US syntheses often have reproducibility issues because of different reaction apparatus/setups that are difficult to control for. In addition, increased power output can result in increased dispersity (reduced uniformity) and amorphization of the product.

Further limitations of MW/UW synthesis are seen in its size range, scalability and power output. Whilst particle size is often reduced by using these techniques, the production of NMOFs below 100 nm in diameter is rare. Where NMOFs have been synthesized, MW/US synthesis is often used in combination with reaction optimization or modulation to achieve the desired morphology. In addition, scale-up of MW synthesis is generally regarded as a significant challenge due to limited penetrated depth of energy supply in a bulk solution. Finally, it should be noted that in some cases, delicate molecules are incorporated into the MOF, such as proteins, drugs and thermally sensitive ligands. In such cases, MW/US synthesis is unsuitable (Chapter 3 - *In situ* Protein Encapsulation in Microemulsions).

In 2009, Kitagawa's group proposed that the size and morphology of MOF crystals could be tuned by adding a monodentate ligand (which is not incorporated into the MOF) into the reaction mixture.[59] This method, known as modulation, controls particle growth by two mechanisms. The first is pH modulation, where the modulator changes the rate of ligand

deprotonation. A basic modulator will deprotonate the ligand allowing for enhanced ligand metal coordination. For this reason, triethylamine is used in the synthesis of ZIF-8, and MOF-5 NMOFs. The other mechanism is coordination modulation, where modulators compete for metal sites with the ligands and temporarily substitute them by coordinating available sites. Hence, increased modulator concentration slows the growth and nucleation rates allowing for larger crystals to be formed.[71]

A variant of modulation, known as surfactant assisted synthesis, uses a surfactant in place of standard modulators. A surfactant is an amphiphilic molecule with a long hydrophobic tail and a polar head group. Different crystal facets have different binding energies. Therefore, surfactants added to the solution will preferentially bind specific facets, slowing the growth along that facet by competing with ligand binding. This was first demonstrated by Ma and colleagues in 2011 to synthesize IRMOF-1, 2 and 3 with Cetrimonium bromide (CTAB)[90]. Another early example of this technique for shape control was by Kitagawa's group. in 2011. They modified the morphology of HKUST-1 in a stepwise fashion from octahedral to cuboctahedral to cubic. This was achieved by adding increasing amounts of dodecanoic acid, which preferentially binds the <100> face.[79] In addition to shape control, surfactant assisted synthesis can be utilized to modify the particle size. This is demonstrated by Pan and colleagues, who increased the length of ZIF-8 particles from 100 nm to 4 μm by decreasing the concentration of CTAB.[91] Furthermore, surfactant assisted synthesis often produces colloidal MOFs with low dispersity (high uniformity). This was best demonstrated by Avci and colleagues in 2017, with the synthesis of ZIF-8, UiO-66 and MOF-5. These syntheses were remarkable because they displayed high uniformity in both shape and size* which allowed the crystals to be arranged into packed layers with long-ranged ordering. Furthermore, the length of ZIF-8 crystals could be tuned from 178 to 227 nm. However, this size tuning was due to optimizing the ligand and CTAB concentration and could not be generalized to other syntheses.[70] However, this approach highlights how surfactant assisted synthesis could be used in tandem with other approaches to produce highly uniform, tuneable MOF NPs.

Despite continuing research into various methods for MOF morphology control, to date, no existing method offers facile, tuneable, synthesis of uniform MOF NPs. For this reason, continued investigation into new morphology control techniques or more comprehensive investigations of the factors influencing MOF morphology are required before MOF with specific morphologies can be designed without extensive reaction optimization. Herein, a

* 5% standard error in particle length

relatively novel technique (microemulsion synthesis) is investigated to determine its effects on MOF morphology.

1.2. Microemulsions

Microemulsions are transparent, thermodynamically stable, colloidal mixtures of two immiscible liquids. The most common colloidal mixture is formed from hydrocarbons and water where small particles of one phase become suspended in the other. They were first documented in the scientific literature by Hoar and Schulman in 1943.[92] Because of this long history, microemulsions have been well documented in a series of books. These results are used to provide a general overview of microemulsion in this section.[93, 94]

Microemulsions are generally stabilized with a surfactant which is typically arranged at the interface between the two phases, though this is not always the case.[95] Surfactants are often referred to by their head group charge e.g. cationic, anionic, non-ionic or zwitterionic. Whilst similar to typical emulsions, microemulsions are distinguished by having an incredibly low interfacial surface tension. Typically, this is achieved by the addition of a cosurfactant; typically an alcohol with a short carbon chain. The cosurfactant is weakly amphiphilic and perforates the oil-water interface spacing surfactant molecules and reduces intermolecular repulsion between surfactant head groups. However, microemulsions have also been produced without a cosurfactant. This has been achieved by using surfactants with multiple tail groups such as dioctyl sodium sulfosuccinate (AOT)[96], where the second tail substitutes the cosurfactant's role. Alternatively, cosurfactant free microemulsions have also been made by using non-ionic surfactants, such as Tween-80.[97] This is presumably due to the reduction of intermolecular repulsion between that is expected for charged head groups.

As a result of the low interfacial tension, microemulsions are thermodynamically stable, optical transparent, and have a low viscosity. The thermodynamic stability of an emulsion is determined by the Gibb's free energy of formation (eq. 1.6). The dispersion of both phases causes a favourable increase in enthalpy (ΔS) but brings about an unfavourable increase in the interfacial surface area (ΔA). In a microemulsion, the surface tension (γ) is sufficiently low such that $\gamma\Delta A$ outweighs ΔS. Hence, microemulsion formation is thermodynamically favoured and spontaneous. For typical emulsions, the Gibb's free energy is positive. Hence, energy must be supplied to stabilize the emulsion through stirring otherwise agglomeration of the dispersed phase and phase separation occur.[98]

$$\Delta G = \gamma \Delta A - \Delta S \quad (1.6)$$

Microemulsions are broadly classified as oil in water (o/w), water in oil (w/o), or bicontinuous microemulsions (Figure 1.9); historically denoted Windsor I-III[*]. Oil in water (o/w) microemulsions consist of an excess of the hydrophilic phase with the hydrophobic phase dispersed in micelles. For bicontinuous microemulsions, both the oil and water exist as a continuous phase dispersed throughout the microemulsion, like a sponge. In w/o microemulsions, the structure is inversed from the w/o variant. The micelles entrap the aqueous phase with the polar head groups facing inwards. These are often called reverse micelles though this term has been inconsistently used in the literature. Some proponents instead opt for reverse micelles to only refer to these structures when they contain no free water. e.g. all water molecules in the micelle are bound to the surfactant water interface.

[*] Other microemulsion structures exist such as surfactant free microemulsions. Most notably, ionic liquid (IL) microemulsion substituting the hydrophobic/hydrophilic phases with an IL (IL/o or w/IL) have become increasingly prevalent.

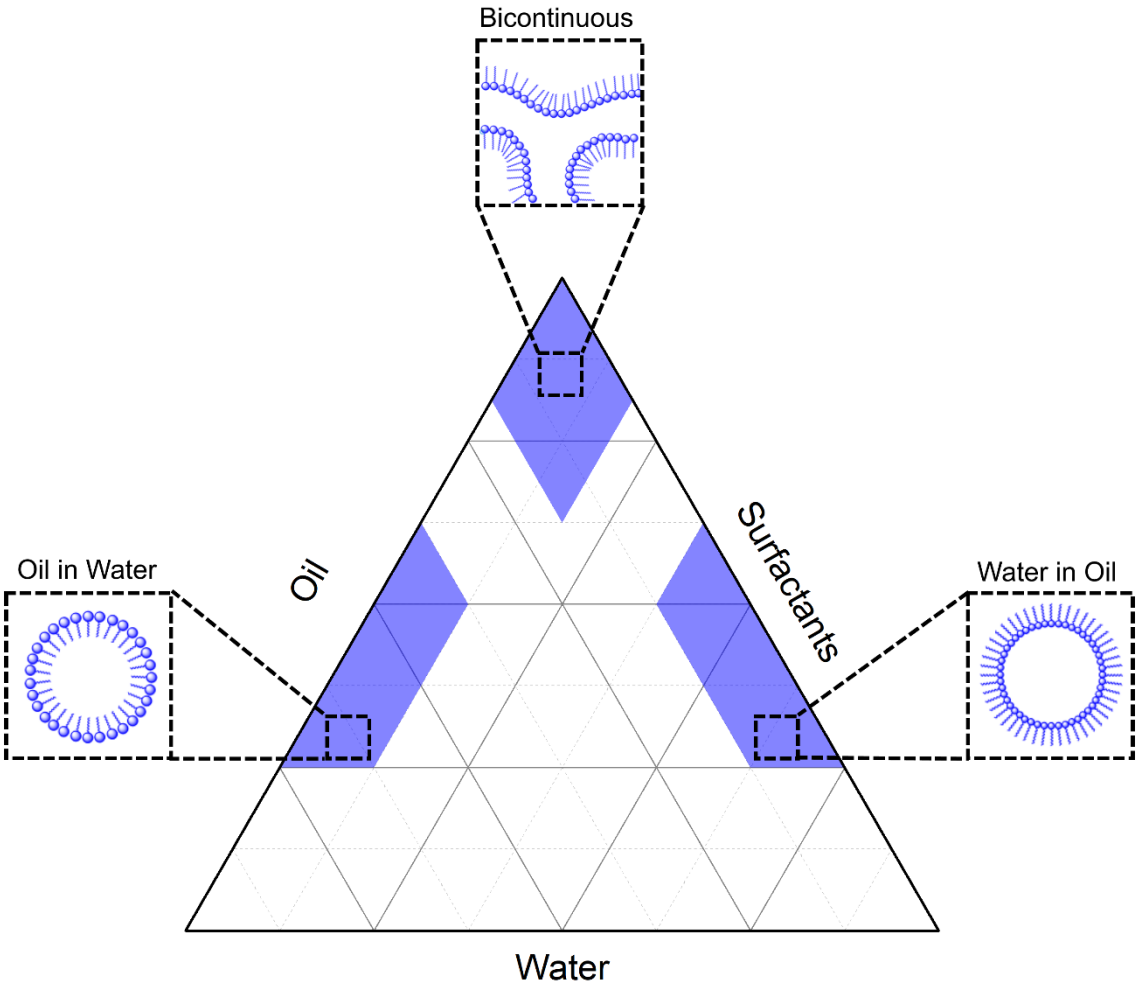

Figure 1.8 Generic volume ratio of emulsion components and the resulting microemulsion phases.

In addition to the ratio of different components, the microemulsion structure is also influenced by other factors such as the solvent, temperature, dispersant and the presence of salts. Two surfactant properties play a significant role in the formation of micellular structures: the hydrophobic lipophobic balance (HLB) and the critical packing parameter (cpp). The HLB is typically defined using eq. 1.7. In this definition each hydrophilic and lipophilic group is assigned a value (c_h & c_l). The HLB is a function of the sum of the contribution of each hydrophilic function group minus the contribution of each lipophilic group.

1.7 $$\mathbf{HLB} = 7 + \sum \boldsymbol{c_h} - \sum \boldsymbol{c_l}$$

The cpp is described by eq. 1.8 with the surfactant volume (v), the head group area (a_h) and the length of the tail group (l_t).

1.8 $$\mathbf{cpp} = \frac{\boldsymbol{v}}{\boldsymbol{a_h l_t}}$$

Generally, a smaller cpp parameter and larger HLB favour the formation of o/w microemulsions over water in oil microemulsions. These properties can also influence the shape of micellular structures. For instance, a cpp value of less than 0.33 would imply a spherical micelle whereas rod-like or hexagonal structures are more prevalent at cpp values between 0.33 and 0.5.[99]

The focus of this thesis is on w/o microemulsions because these are extensively used for morphology control of inorganic nanoparticles and to date are the only microemulsions utilized for MOF synthesis. For the sake of brevity, the term microemulsion or micelle will be referring specifically to w/o microemulsions and reverse micelles, unless otherwise stated.

1.2.1. Microemulsion Synthesis

One application of microemulsions is as a template for the synthesis of monodispersed nanoparticles. This was first achieved by Boutonnet and colleagues in 1982, with the synthesis of Pt, Pd, Rh, & Ir nanoparticles[100]. Since then microemulsion synthesis has been extensively utilized to synthesize metal nanoparticles, core-shell materials, semiconducting quantum dots and silica nanoparticles.

Microemulsion synthesis, is a templated precipitation technique where a precipitating agent is introduced to the material precursors within the micelles' confined aqueous phase. For metal nanoparticle synthesis, the precursors are a metal salt and a reducing agent e.g. ($NaBH_4$, NaOH) used to induce precipitation. The precipitating agent is introduced either as an aqueous solution (single microemulsion method) or as the aqueous phase of a separate microemulsion (two microemulsion method) (Figure 1.9). The nucleation and growth kinetics of nanoparticles within microemulsions is dependent on two factors, the reaction rate and the micellular kinetics. Micelles travel through the solvent and collide due to Brownian motion. On collision, temporary dimers are formed which last between 10 μs and 1 ms before splitting apart. The formation of dimers allows for exchange of the components inside the micelles, inducing growth and nucleation. This is typically the rate limiting step in nanoparticle growth.[101, 102]

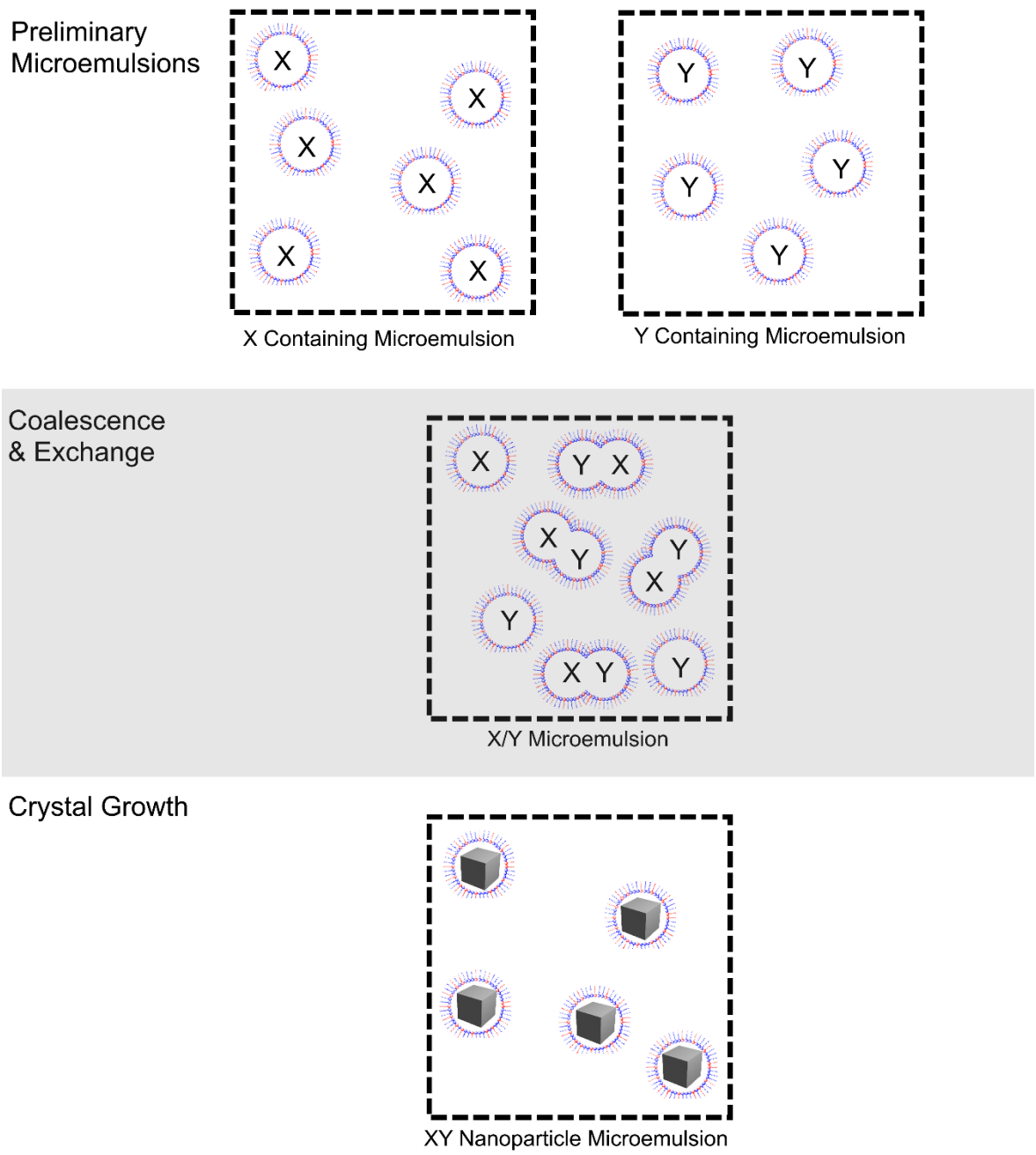

Figure 1.9 Generic microemulsion synthesis using the two-emulsion protocol.

Initially, it was thought that the primary influence on particle morphology was the morphology of the micellular template. Indeed, this templating effect does play a significant role. In 2005, Li and collegues. proposed a templating mechanism where nucleation occurs at the surfactant water interface and particles grow inwards mimicking the microemulsion shape and size. This was after they observed ZnSe hollow spheres evolving into 200-300 nm nanospheres using transmission electron microscopy (TEM)[103]. This result is consistent with several studies reporting the growth of hollow spheres using microemulsion synthesis. However, it is still unclear why this inward growth occurred. Eastoe proposed that since the

reaction rate was significantly faster than the coalescence rate, nucleation was induced at the micellular interface immediately on coalescence.[101] However, this is unconvincing given that heterogenous nucleation on the micellular interface also seems sufficient to explain this observation.

Considering that templation effects have long been considered the primary mechanism for size control, many researchers have attempted to control particle morphology by altering the template morphology. For this reason, extensive research has gone into tuning the particle size by adjusting the water/surfactant ratio, ω_0 (eq. 1.9). The ω_0 value is related to the micelle size by eq. 1.10, where d is the micelle diameter, SA is the surfactant surface area and V is the aqueous volume. By increasing the water volume, the micelle size increases. Thus, the particle size of the final nanomaterial also increases.

1.9 $$\boldsymbol{\omega_0 = \frac{[water]}{[surfactant]}}$$

1.10 $$\boldsymbol{d = \frac{6V}{SA}}$$

Whilst many studies have utilized this approach successfully to tune the particle size, it is not generically applicable, and several studies have observed no correlation between ω_0 and the resulting particle size.[101] This has led to the conclusion that the particle morphology is more nuanced then initially expected. For instance, microemulsion dimensions are not only influenced by ω_0. The presence of cosurfactants, the surfactant chemistry, temperature and the aqueous composition all play a considerable role. Calandra and colleagues highlighted this effect by synthesizing AOT microemulsions containing aqueous $AgNO_3$ and AgCl. Both microemulsions possessed a larger micellular diameter and greater polydispersity then the equivalent microemulsion containing pure water[104].

Furthermore, the particle morphology is not solely dictated by templating effects. Multiple studies report the synthesis of NPs significantly larger or smaller than the micellular template, in contradiction with a templating model. These observations are often rationalized with the concept of interfacial fluidity. Interfacial fluidity is the bending modulus of the interfacial surfactant layer and denotes the layer's rigidity. The interfacial fluidity is primarily dependent on the surfactant layer's packing parameter. Denser packing results in a less fluid interface. Hence, longer tail groups with stronger Van der Waals interactions will produce a more rigid interface, whereas the use of ionic head groups will increase interfacial fluidity due to repulsion. The more fluid the interface is the faster the rate of intermicellar exchange. However, membrane fluidity also increases the likelihood of micelle agglomeration as the particle grows.[101, 102]

The impact of interfacial fluidity and the complexity of growth mechanics in microemulsion systems was recently highlighted by a mechanistic study by Sunaina and collegues.[105] They studied the growth of copper oxalate within a water/iso-octane microemulsion using CTAB as the surfactant (Figure 1.10). They used 1-octanol and 1-butanol as cosurfactants. The longer chain of 1-octanol significantly reduced the interfacial fluidity. In both microemulsions growth occurred in a two-stage process. The first stage was growth within the microemulsion until the microemulsion was fully occupied. In both cases, the product collected after this stage was spherical. However, due to the reduced interfacial fluidity of the 1-octanol microemulsion this process took 7-hours instead of the 1-2 hours required for 1-butanol. This was attributed to the slowed exchange rate. In the second stage, the microemulsion and NPs expanded in tandem. For the 1-butanol microemulsion, the final product was elongated up to 74.5 nm in length. This was attributed to the denser packing of the 1-butanol surfactant distorting the initial microemulsion into an ellipsoid. The surfactant molecules along the NP were bound to the NP surface. Whereas an unbound domain existed at both ends of the NP, where micellular exchange was able to continue. No mechanism was provided for the synthesis of the cube-like NPs formed with 1-butanol.[105] This is indicative of the further work needed to fully elucidate the mechanisms of growth control during microemulsion synthesis.

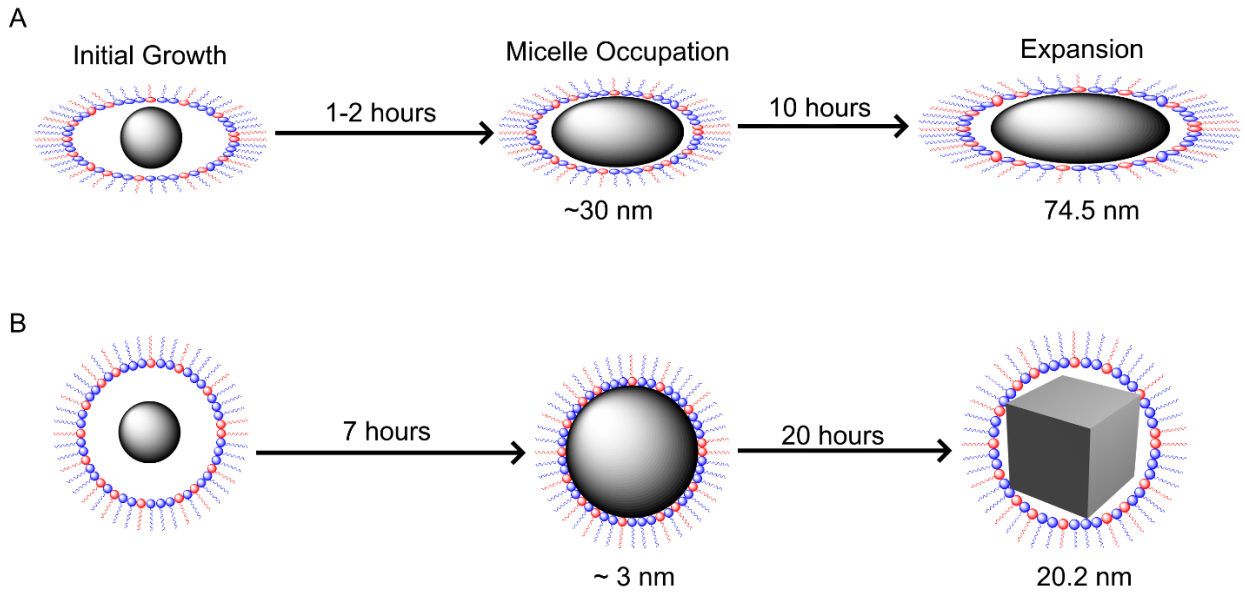

Figure 1.10 Copper oxalate growth schematic in CTAB/alcohol w/o microemulsion using (A) 1-butanol and (B) 1-octanol as the cosurfactant.

1.3. Microemulsion MOF Synthesis

To date, literature in the field of microemulsion synthesis of MOFs is a miniscule subset of the overall work in either the MOF or microemulsion fields (Table 1.1). The application of microemulsion synthesis to MOF chemistry was first achieved by Lin's group in 2006. They synthesized $Gd(BDC)_{1.5}$ rods (BDC = 1,4 benzene dicarboxylate) with a length of 100-125 nm and 1-2 μm within a CTAB w/o microemulsion for use as MRI contrasting agents.[106] Since this initial work, several studies have been conducted on microemulsion synthesis of MOFs. As a subset of the microemulsion field, these studies are at least representative of some of the more commonly used surfactant systems. Triton X-100, CTAB and AOT are highly prevalent non-ionic, cationic, and anionic surfactants, respectively. Furthermore, there is some coverage of different addition strategies. Most of these studies used a two microemulsion approach whereby the ligand and metal are initially confined to different microemulsions (denoted herein as μEL and μEM). In all cases, μEL was then added to the μEM. Alternatively, Xia and colleagues used a single emulsion approach to synthesize Eu_xTb_{x-1}(oxalate)(fumarate). Here, an aqueous solution containing the ligands was added to the metal containing microemulsion. Another unique approach was by Melindandri's group. They used a three microemulsion method to synthesize a series of zinc(II) and copper(II) carboxylate MOFs. μEL was first added to μEM. Precipitation was then induced by adding a third NaOH containing microemulsion.

Table 1.1 Microemulsion Synthesized MOFs*

Surfactants	MOF	Ligand	Metal	Length	Morph.†	Ref.‡
BRIJ-C10	ZIF-8§	mIM	Zn^{2+}	~30 nm	RD	69
TX-100	ZIF-8	mIM	Zn^{2+}	2.2 nm	Spherical	108
Hexanol	ZIF-67	mIM	Co^{2+}	2.3 nm	Spherical	108
	HKUST-1	BTC	Cu^{2+}	1.6 nm	Spherical	108
	La-BTC	BTC	La^{3+}	~0.1 - 5 μm	Mixed**	109
CTAB	Gd MOFs	BDC	Gd^{3+}	21 nm - 1.3 μm	Rods	102
Hexanol				100-125 nm		106
				~1-2 μm		
	Ln MOFs	BDC/BTC	$Gd/Eu/Tb^{3+}$	~100 – 400 nm	Rods	110
	Gd-BTC	BTC	Gd^{3+}	70-113 nm	Mixed	102
	Eu-BDC	BDC	Eu^{3+}	~100 nm	Rods	111
	ZIF-8	mIM	Zn^{2+}	2.3 nm	Spherical	112
	ZIF-67	mIM	Co^{2+}	2.7 nm	Spherical	112
	$Mn_3(BTC)_2(H_2O)_6$	BTC	Mn^{2+}	50 nm – 2 μm	Mixed	113
AOT	Eu_xTb_{x-1}-MOF	Oxa/Fum‡‡	Eu/Tb^{2+}	150-350 nm	Rods	114
	Zn^{II}-NCP††	C_nCOOH	Zn^{2+}	23-40 nm	Raspberry	115
	Cu^{II}-NCP	C_nCOOH	Cu^{2+}	13-17 nm	Raspberry	115

Unfortunately, these studies represent a very limited subset of the of the diverse MOF structures available. Despite the stunning structural diversity in the MOF literature, all but two microemulsion studies use one of three ligands: 2-methylimidazole (mIM), terephthalic acid (BDC) and trimesic acid (BTC). The two exceptions are the studies conducted by Xia and Melindandri. Xia and colleagues synthesized Eu_xTb_{x-1}(oxalate)(fumarate) by incorporating two ligands oxalate and fumurate. Melindandri's group incorporated a series of C_nCOOH ligands

* A study referring to ultrasound assisted reverse micelle synthesis were explicitly excluded. This is because the technique only involves one solvent phase despite using the misleading term reverse micelle.[107]
† Morphology
‡ References
§ZIF-8 and ZIF-8 complexed with horseradish peroxidase.
**Several samples were produced with differing morphologies.
†† Synthesized series of zinc and copper carboxylate MOFs
‡‡ Oxalate and fumurate

into MOFs denoted as Cu/Zn NCPs. Given the limited array of available MOFs, further screening of different MOFs that can be synthesized using this technique is highly valuable.

From the limited existing literature there is promise that microemulsion syntheses can produce MOF NPs. Except for Xia and colleagues, all studies managed to produce MOF NPs with a length less than 100 nm. However, the objective of MOF NP synthesis is not solely to produce incrementally smaller MOFs. The dispersity and tuneability of the product are critical parameters to consider when selecting a synthetic technique. Unfortunately, the MOF literature is inconsistent when reporting the dispersity. Of the microemulsion MOFs, this has only been reported in three cases. The most extensive analysis of NP dispersity was performed by Hatakeyama and colleagues on Gd MOFs. They found that across 28 samples the RSD in length varied from 19 to 50 %.[102] Sun and colleagues synthesis of ZIF-8 and ZIF-67 reported an improved RSD of 17 and 18 %.[112] Melindandri's group reported RSD values between 24 and 30 % across 4 samples.[115]

As to the tuneability, several studies do not report any attempt to tune the particle size or shape at all or test only sporadic conditions.[112, 108, 110, 113]. This is highlighted by Zheng and colleagues. They added ethanol into the reaction mix for the synthesis of HKUST-1 in a TX-100/hexanol microemulsion system. The resulting crystals were more uniform and smaller than their counterpart synthesized without ethanol. However, with only two samples it is difficult to gauge the actual effect ethanol had on the microemulsion or HKUST-1 growth. Of the studies that place focus on systematic synthesis, ω_o is generally the only factor investigated. Whilst a strong correlation is observed between ω_o and the NP size in all cases,[109, 106, 114] the small subset of structures makes it unlikely this would hold true in later studies. Hatakeyama's 2011 study is the most comprehensive on the record. It explores both ω_o and the addition of three different amphiphilic additives used to change the interfacial tension of the microemulsion. They attempted to synthesize Gd BTC and Gd BDC. Interestingly, in all cases, an increase of ω_o resulted in an increased NP size. However, the addition of sodium salicylate increased the NP size of Gd BDC but decreased the size of Gd BTC NPs.[102] Aditionally, Melindandri's 2016 study investigated the impact of changing the rate of addition of the precipitating agent (NaOH) to the μEL/μEM microemulsion mixture. For both Cu/Zn NCPs this resulted in a reduction in the NP size.[115] Nevertheless these studies only investigate a small fraction of available reaction space e.g. concentration of surfactants, type of surfactant, temperature, addition time etc. Given this, systematic investigation of different parameters on the NP size, morphology and dispersity appears to be a highly relevant area of study.

1.4. Research Outline

The purpose of this study is to investigate the application of microemulsion synthesis as a generic protocol for synthesizing morphology controlled NMOFs. Because of the large scope of synthetic variables in microemulsion systems, the study was limited to a w/o microemulsion system consisting of a variable ratio of cyclohexane, TX-100, 1-hexanol and water. As a generic protocol, two microemulsions were added together. These were identical, except for the composition of the aqueous phase. One microemulsion contains the metal salt (μEM) and the other contains the ligand (μEL). μEL was added to μEM at a controlled variable rate. The mixed microemulsion was then left stirring for a set growth time before rupturing with

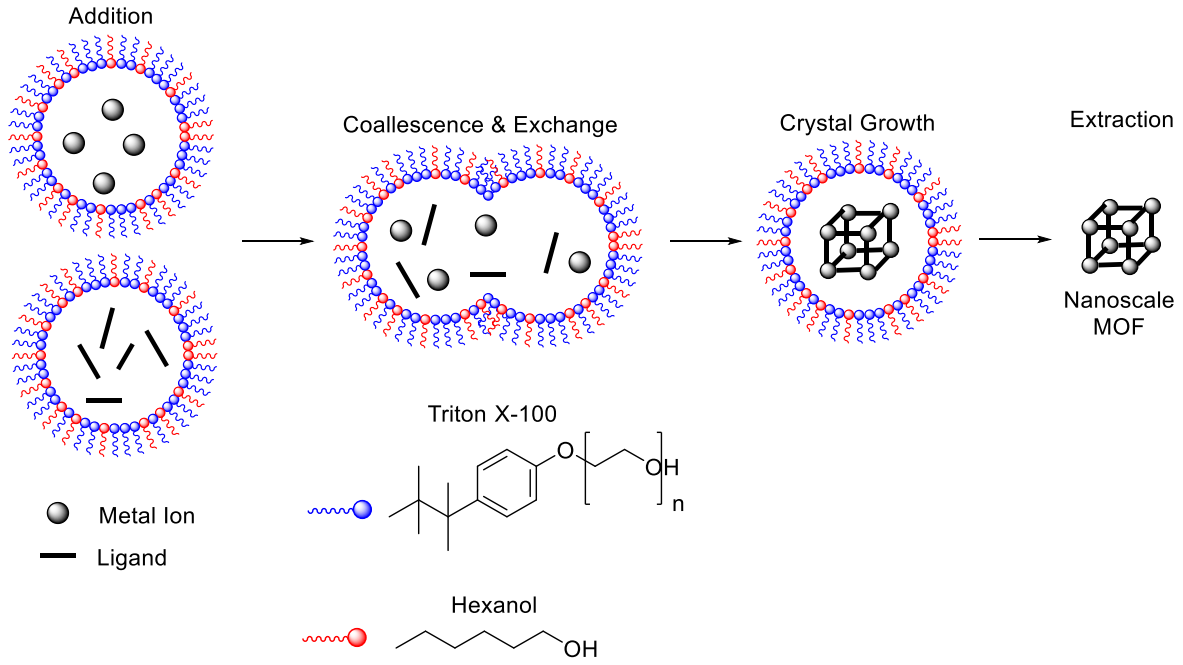

Figure 1.11 Microemulsion synthesis protocol.

methanol and acetone and extracting by centrifugation (Figure 1.11).

The microemulsion addition time was controlled by injecting μEL into μEM using a syringe pump with a set flow rate (Figure 1.12).

The objectives of this study were to:

1. Establish a protocol for NMOF synthesis. This was achieved by synthesizing a common MOF with well understood morphological behaviour (Chapter 2 - Zeolitic Imidazole Framework Synthesis in Microemulsions).
2. Screen different MOFs to investigate the utility of this system for NMOF synthesis more broadly.

3. Investigate the influence of selected reaction variables on the morphology and topology of resulting MOFs crystals. The primary interest was whether the addition rate or ω_o could be adjusted to tune the NP dimensions.
4. Investigate the use of this technique for synthesizing protein/NMOF complexes (Chapter 3 - *In situ* Protein Encapsulation in Microemulsions).

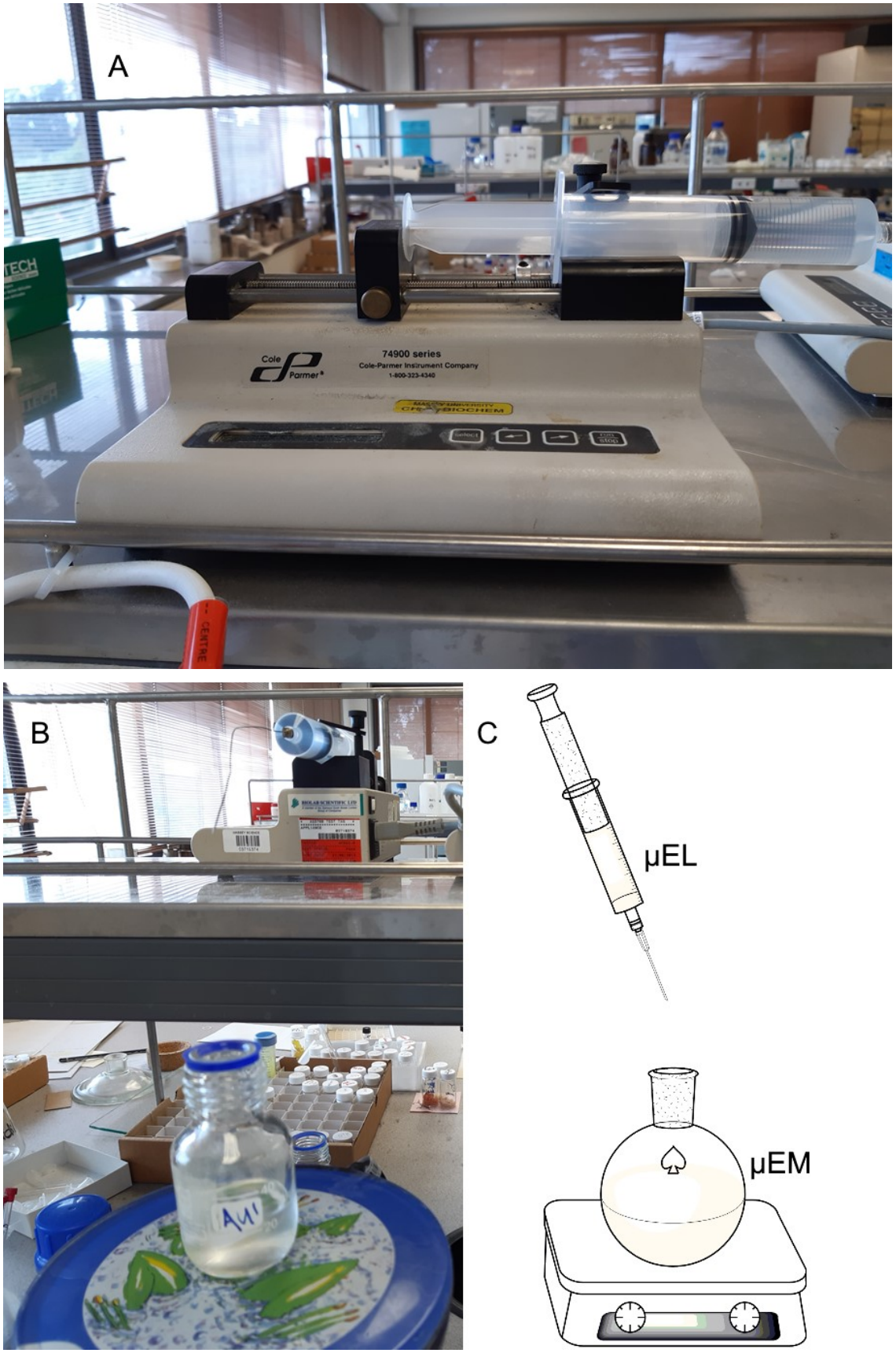

Figure 1.12 (A) µEL Syringe on a syringe pump. (B) µEL addition to µEM. (C) Schematic of the same process.

1.4.1. Characterization Techniques

To satisfy the research goals, three characterization techniques were extensively used in this study. Powder X-ray diffraction (PXRD) was utilized to determine the topology of the synthesized material. Transmission electron microscopy (TEM) was utilized to determine the MOF morphology. Some experimental techniques whilst helpful were unavailable or unachievable during the course of this study (5.1 Experimental Challenges).

1.4.1.1. Powder X-Ray Diffraction

X-ray diffraction involves shining monochromatic X-rays through a crystalline sample acting as a diffraction grating. A sample's long-range ordering (topology) is determined by the location of bright spots on the detector (shown as dark lines in Figure 1.13), defined by Bragg's law. In powders consisting of nanocrystallites, the orientation of crystals within the sample is assumed to be homogenized and random. Hence, X-ray diffraction is detected from every periodic plane within the sample. The rotational randomization of the crystallites results in the formation of Debye rings on the detector, each corresponding to a periodic plane. This is plotted as a 1D diffroctragram, or powder pattern. The y-axis is the diffraction intensity. The x-axis is the scattering angle (2θ); the angle between the ring and the sample that satisfies the Bragg law (Figure 1.13).

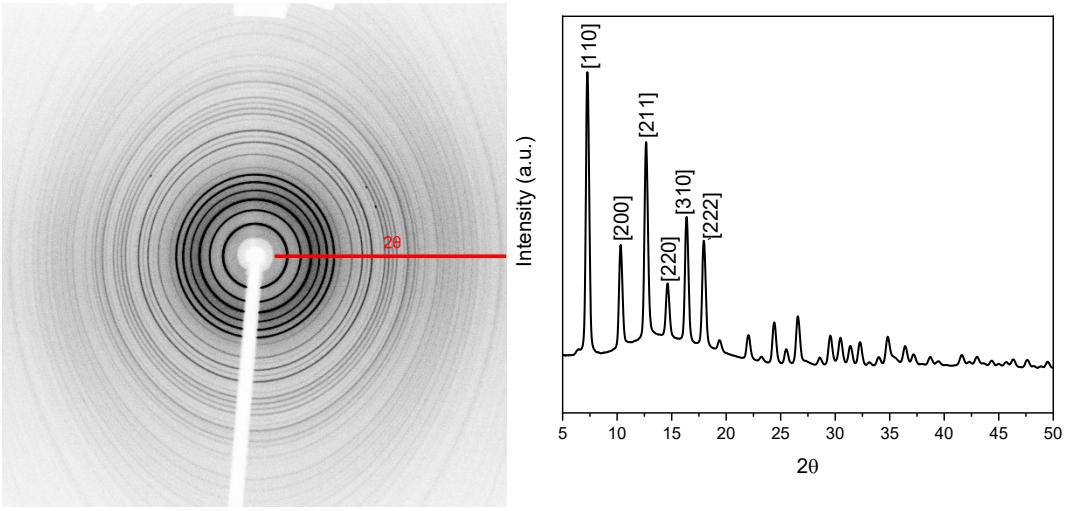

Figure 1.13 (Left) PXRD diffraction rings; red line represents 2θ. (Right) annotated 1D diffractogram.

A material's powder pattern can be simulated from its structure. By comparison of a sample's powder pattern with known samples from a database of crystalline materials (CCDC) a crystalline materials structure can be identified.

1.4.1.2. Electron Microscopy

Nanoparticle morphology was determined by imaging. The maximum resolution (R) of imaging techniques is dependent on the numerical aperture (NA) and the source wavelength (λ) (eq. 1.11).

1.11 $$R = \frac{\lambda}{2NA}$$

Unfortunately, nanoparticles are often smaller than the maximum resolution obtained by optical microscopy. In electron microscopy the source wavelength is reduced to that of an electron beam allowing for atomic resolution. In TEM, electrons are excited from a filament, often tungsten, by supplying a high voltage to the filament. The electron beam is focused onto the sample using magnetic "lenses". The detector detects electrons which are transmitted through the sample. Image contrast is obtained because fewer electrons are transmitted through

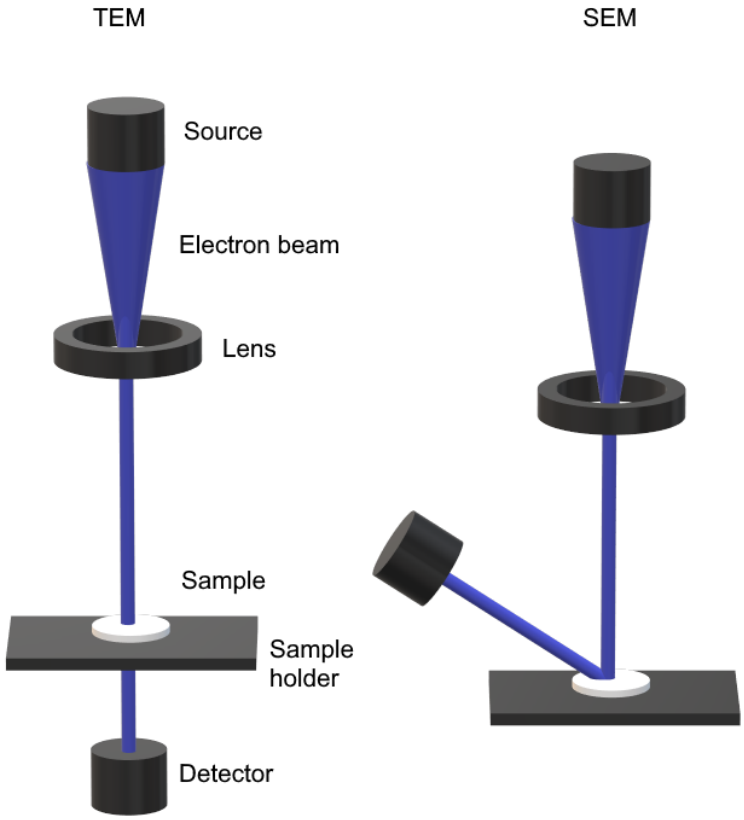

Figure 1.14 TEM and SEM schematic

electron dense regions of the sample due to diffraction.

An alternative microscopy technique is scanning electron microscopy. In SEM the detector measures secondary electrons that are emitted from the sample surface by the electron beam. In SEM nonconductive samples accumulate electrons on the sample surface reducing image contrast (Figure 1.14). These samples must be prepared with a conductive carbon coating to

transfer electrons away from the sample surface. Unfortunately, this coating is ~10 nm thick. This artificially inflates the particle size and masks the particle shape. Hence TEM was used for sample imaging. Whilst other techniques such as cryo-TEM or HAADF STEM would provide higher resolution or insight into the growth mechanism, the equipment for these techniques was not readily available.

1.4.1.3. Particle Size Analysis

In accordance to best practice, the particle size distribution (PSD) obtained by TEM imaging is reported with the mean NP size in length, the SD and the RSD from 100 or more NPs. The NP size was determined automatically using imaging software (A.1.2 Transmission Electron Microscopy). However, this alone is insufficient to provide an accurate description of the PSD. This is because the PSD is not necessarily gaussian. Two samples could have the same SD and average size but exhibit different physical properties due to differing distributions.[116] By modelling the PSD with a common distribution some information can be obtained as to the shape of the distribution. PSD data was modelled primarily with the Weibull curve. For modelling PSDs, the Weibull distribution was used, where x is the NP length, α is the shape parameter, and β is the scale parameter (eq. 1.12 & 1.13). The PDF is the probability distribution function or the probability that the NP length is equal to x. The CDF is the cumulative distribution function or the probability the NP length is less than or equal to x. This model was selected as it is used in PSD analysis and can model asymmetric distributions providing some information regarding the PSD shape unlike a gaussian distribution.[117] Throughout this work, the raw PSDs are provided in the appendixes where modelled PSDs of various sample are plotted together in the text as it is easie to visualize trends and ignores binning artefacts typical of plotting raw PSDs.

The Kolmogrov Smirnov test (A.1.4 Kolmogorov Smirnov Tests) was used to verify that the fitted model matches the experimental data. This test was also used to verify that differences in PSD of different samples was significant rather than a product of statistical variability.

$$\mathbf{1.12} \quad \boldsymbol{PDF(x)} = \frac{\boldsymbol{\beta}}{\boldsymbol{\alpha}}\left(\frac{\boldsymbol{x}}{\boldsymbol{\alpha}}\right)^{\boldsymbol{\beta-1}} \boldsymbol{e}^{-\left(\frac{\boldsymbol{x}}{\boldsymbol{\alpha}}\right)^{\boldsymbol{\beta}}}$$

$$\mathbf{1.13} \quad \boldsymbol{CDF(x)} = \mathbf{1} - \boldsymbol{e}^{-\left(\frac{\boldsymbol{x}}{\boldsymbol{\alpha}}\right)^{\boldsymbol{\beta}}}$$

Chapter 2 - Zeolitic Imidazole Framework Synthesis in Microemulsions

2.1. Introduction

Zeolitic imidazole frameworks (ZIFs) are a MOF subclass consisting of tetrahedrally arranged transition metal ions and imidazolate (IM) ligands with the overall formula ML_2*. They are formed due to the deprotonation of imidazole (HIM) to imidazolate (IM) ions which have two available metal binding sites.

Their name is derived from their structural similarity to zeolites, a class of porous material consisting of interconnected XO_4 (X=Al, Si) tetrads. ZIFs possess a ~145° bond angle across the M-Im-M bond; analogous to the X-O-X bond in zeolites (Figure 2.1)[12]. Like their zeolitic counterparts, ZIFs have immense structural diversity. A 2018 review by Noh and colleagues cites, 46 unique topologies and 239 experimentally discovered ZIF frameworks. Whilst this allows significant diversity in the applications of ZIFs, it makes topological control of these materials complex. The archetypical ZIF, ZIF-1 ($Zn(IM)_2$) has 23 known alternate topologies that can be synthesized using the same precursors and typically defaults to nonporous dense topologies.[16]

*ZIF nomenclature is loosely defined[16]. Structures can be named differently but still recognized as ZIFs providing this definition fits e.g. CDIF-4 ($Cd(eIM)_2$)[118, 119]. Furthermore, structures derived from ZIFs are recognized as ZIFs despite not fitting this definition e.g. ZIF-5, which contains octahedrally arranged Indium[12, 120].

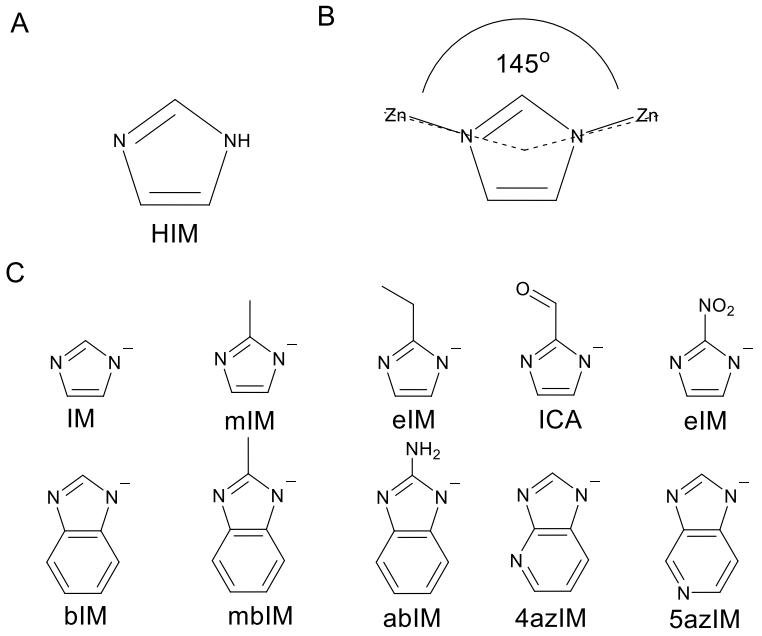

Figure 2.1 (A) imidazole. (B) Typical X-IM-X bond angle within ZIFs. (C) Selected imidazolate derivatives that have been used to make ZIFs.

A breakthrough in ZIF chemistry was achieved by Huang and colleagues in 2006. By substituting the hydrogen on the second carbon of the imidazolate ligands with a methyl (mIM) or ethyl group (eIM), denser topologies became sterically unfavourable. This resulted in the formation of three new MOFs: MAF-4 ($Zn(mIM)_2$), MAF-5 ($Zn(eIM)_2$) and MAF-6($Zn(mIM/eIM)_2$). MAF-4, more commonly known as ZIF-8, possesses a **sod** topology with 6 square faces and 8 hexagonal faces (Figure 2.2). The synthesis of ZIF-8 was significant as it was the first open framework ZIF produced and it had a reasonable BET surface area of 1030 $m^2\ g^{-1}$.[121] More recently, improved protocols for the evacuation of ZIF-8 pores has resulted in ZIF-8 samples with a BET surface area as high as 1810 m^2g^{-1}.[12]

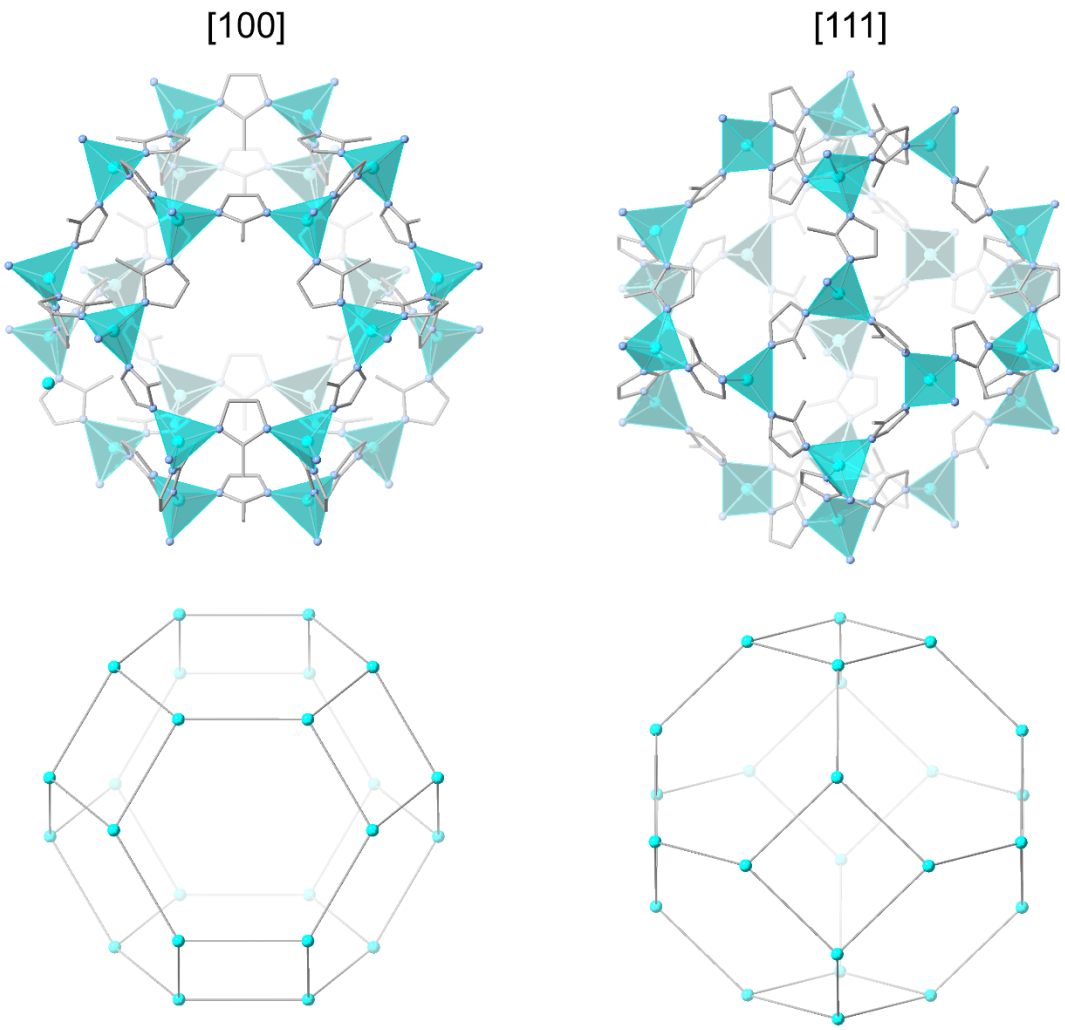

Figure 2.2 ZIF-8 and **sod** topology viewed along the [100] and [111] planes.

2.1.1. Synthesis and Application

ZIF-8 is one of the most common MOFs in the literature with applications in catalysis, gas storage and drug delivery etc.[16] It often used a model MOF for investigating new synthetic protocols or characterization techniques. This was highlighted in 2018 by Cleuvenbergen and colleagues. They demonstrated the use of a new nonlinear optical technique as a benchtop method to monitor the topology and morphology during *in situ* crystal growth. As a model for MOFs, this technique was tested using ZIF-8.[122]

A major advantage of ZIF-8 over other MOFs is that it is easily synthesized in a wide range of conditions and is stable to aqueous and alkaline solvents.[12] Hence, ZIF-8 has been prepared with protocols including flow synthesis,[123] mechanosynthesis[124] and microemulsion synthesis.[69, 108, 112] Furthermore, it has a wide variety of facile room temperature synthetic

protocols. The first of which was demonstrated by Cravillon and colleagues in 2009.[125] They synthesized ZIF-8 in methanol with an 8:1 ligand to metal ratio. This was expanded upon by Pan and colleagues in 2011. They made the first aqueous room temperature protocol by upping the ligand to metal ratio to 70:1.[126] This has extended its application into the encapsulation of thermally and solvent sensitive materials and drug delivery (Chapter 3 - *In situ* Protein Encapsulation in Microemulsions).

2.1.2. Morphology

Throughout the literature, the morphology of ZIF-8 crystals has been extensively studied particularly for the purposes of producing colloidal NPs for drug delivery. As such, a wide range of different morphologies have been produced. The three most prevalent ZIF-8 morphologies are: rhombic dodecahedron (RD), cubic and truncated rhombic dodecahedron (TRD)(Figure 2.3). In 2012, Cravillon demonstrated that these morphologies occur due to competitive growth along the [100] and [111] crystal facets by imaging samples at different growth stages. Whilst initial particles exhibit a cubic morphology due to [100] growth, increased growth times allowed evolution of the [111] facet. Thus, cubic crystals morph into truncated rhombic dodecahedrons and eventually rhombic dodecahedral crystals over time. By isolating the samples after different reaction times cubic and TRD morphologies could be obtained.[127] A milestone in ZIF-8 shape control was achieved by Pan and colleagues in 2011, who managed to synthesize ZIF-8 using surfactant assisted synthesis with CTAB. The addition of CTAB slowed growth along the [100] facet allowing cubic and TRD crystals to be isolated. This approach has been utilized to discover a range of different ZIF-8 morphologies.[91] For instance, tris(hydroxymethyl)aminomethane (TRIS), which slows growth along the [111] facet, was added to ZIF-8 during solvothermal synthesis. By changing the concentration of TRIS from 50 to 100 mM, the NPs changed shape from octahedral to nanoflowers. They further experimented on using a combination of CTAB and TRIS to produce novel burr box and hexapod morphologies.[128]

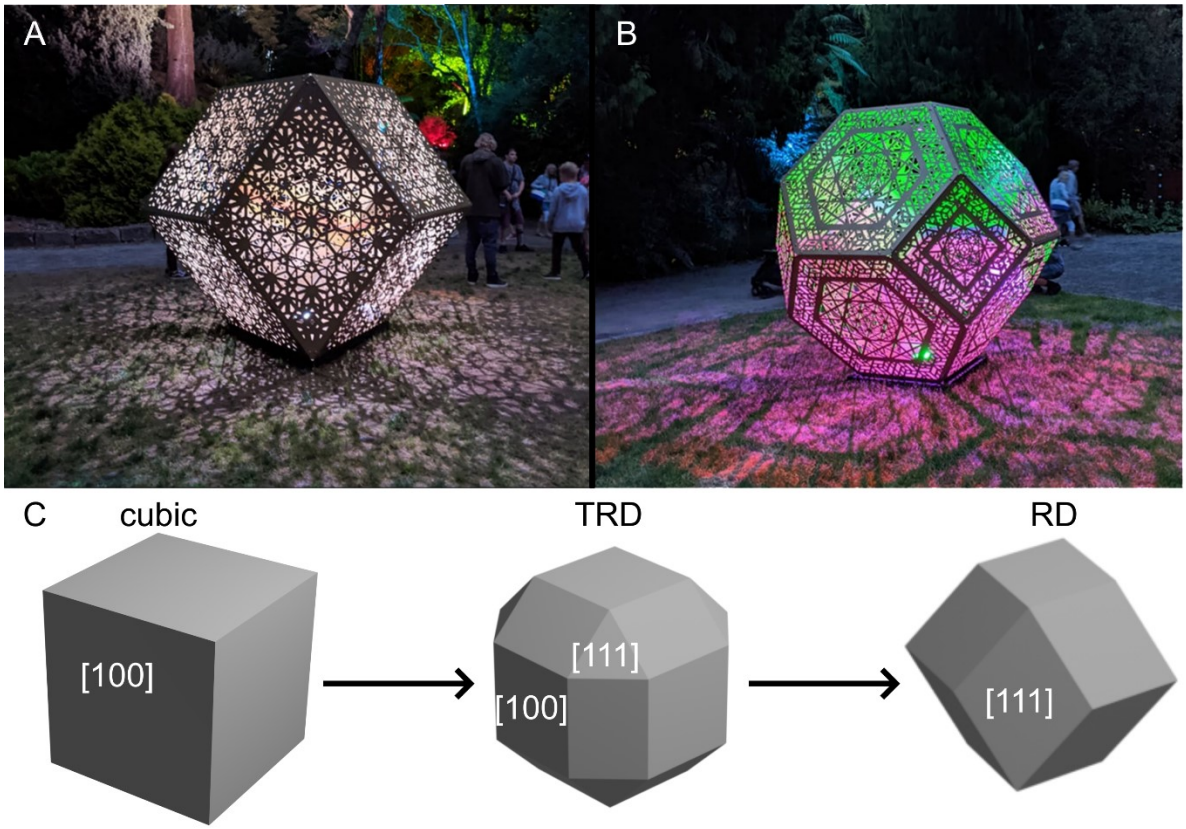

Figure 2.3 (A) RD and (B) TRD geometries. Photograph obtained from the HYBYCOZO exhibit at the TSB Festival of Lights in Taranaki New Zealand. (C) Formation of ZIF-8 crystals by [111] directed growth.

Except for microemulsion synthesis, ZIF-8 particle size in literature reports ranges from 9 nm to several µm. Typically, reports of tuneable particle size originate from reaction parameter optimization. For instance, it is widely acknowledged that increasing the ligand to metal ratio reduces the particle size by increasing the nucleation rate. The most comprehensive study on this condition was by Kida and colleagues in 2013. They demonstrated that by changing the ligand to metal ratio from 40:1 to 100:1 in an aqueous solution the particle size decreased from 2 µm to 250 nm.[82] It is also acknowledged that by adding amines to the synthesis the particle size will decrease. This is because the addition of amines deprotonates HmIM allowing faster sequestration of Zn^{2+} by the deprotonated sites. This method was utilized by Cravillon and colleagues in 2011 to produce 9 nm ZIF-8 NPs by adding n-butylamine to the synthesis.[129] The size control methods discussed thus far can be rationalized by LaMer theory, however this is not always the case. ZIF-8 particle size increases with increased concentration of Zn^{2+} and HmIM. This is counterintuitive according to LaMer theory. This result was justified by Yeung and colleagues using a model whereby ZIF-8 growth is dictated by two processes (Figure 2.4).

Firstly, Zn^{2+} coordinates to mIM/HmIM nitrogen atoms. Secondly, HmIM is deprotonated to mIM creating an additional binding site. It should be noted that the solvent competes with mIM/HmIM for Zn^{2+} binding sites to alter the nucleation rate. Increased concentration results in faster sequestration of HmIM by Zn^{2+}. This slows later growth because the resulting product is $Zn(HmIM)_4^{2+}$ which has no available binding sites. Slower initial growth produces molecules such as $Zn(mIM)_2$ which has two available mIM and zinc binding sites.[77] This model can also be used to explain prior results. For instance, whilst the increased ratio of HmIM to Zn^{2+} increases the initial nucleation rate, it also increases the availability of mIM because HmIM is basic and can deprotonate other HmIM molecules.

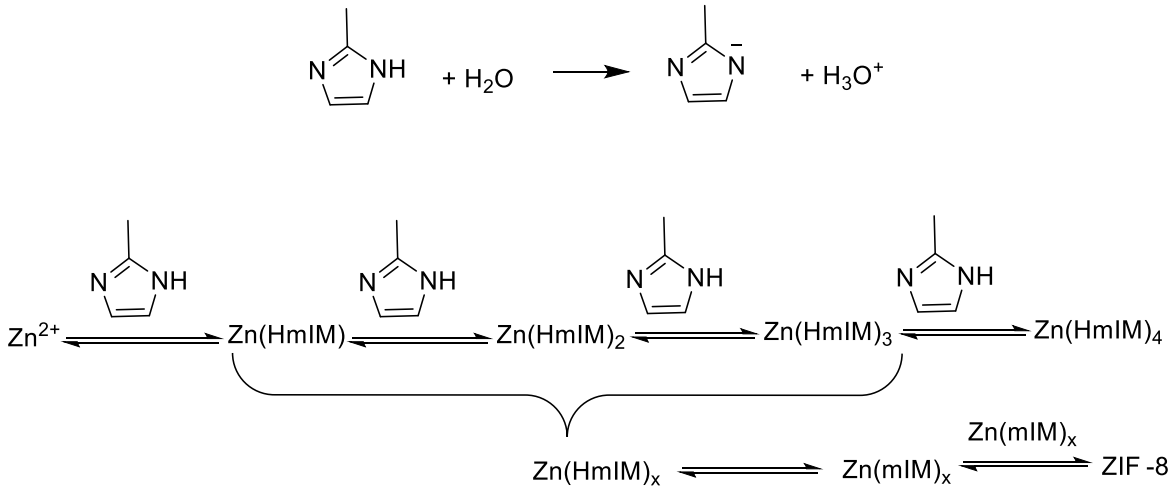

Figure 2.4 ZIF-8 growth schematic. x is equal to 1,2 or 3.

2.1.3. Microemulsion Synthesis

Given the extensive literature available on the morphology of ZIF-8, the availability of aqueous synthetic protocols for comparison, and its common use as a testbed MOF, ZIF-8 is an ideal candidate for investigating microemulsion synthesis. Unsurprisingly, three studies have already been conducted on the use of microemulsion synthesis to synthesize ZIF-8. The Sun group synthesized ZIF-8 in a water/TX-100/hexanol/ionic liquid microemulsion and a water/CTAB/hexanol/cyclohexane microemulsion.[108, 112] In both cases, they produced 2.2-2.3 nm spherical NPs; the smallest samples on record. Chulkaivalshucharit reported the synthesis of 30 nm RD ZIF-8 crystals containing the protein horseradish peroxidase.[69] However, between all three studies the only parameter investigated was the concentration of Zn^{2+} and mIM. No correlation was found with the NP size. Thus, significant work is still required to investigate the impact of synthetic parameters on ZIF-8 morphology

2.1.4. Research Outline

In this chapter, a TX-100 based w/o microemulsion was used to synthesize ZIF-8, its cobalt analogue, ZIF-67, and ZIF-1 ($Zn(IM)_2$). The objectives of this chapter were as follows:

1. Establish a microemulsion method to synthesize MOF NPs using ZIF-8 as an exemplar.
2. Evaluate the effect of changing various conditions on the overall morphology of the ZIF-8 product.
3. Screen different ZIFs to investigate the use of this technique as a generic morphology control method.

The ligand and metal combinations selected for screening were Co^{2+}/HmIM and Zn^{2+}/HIM. The combination of Co^{2+} and HmIM usually forms ZIF-67, $Co(mIM)_2$, the **sod** cobalt analogue of ZIF-8. It displays very similar morphological behaviour and is often synthesized by simple substitution of the precursor zinc(II) salt by its cobalt(II) analogue. Furthermore, ZIF-67 is a highly regarded catalytic MOF. In addition to being used as a template for the synthesis of other catalytic materials, ZIF-67 is used in applications such as photocatalysis and electrocatalysis. This was highlighted by Qin and colleagues who demonstrated that ZIF-67 could be utilized as co-catalyst for the photoreduction of CO_2 to CO. In addition, ZIF-67 demonstrated an improved performance over other commonly utilized MOFs including ZIF-8, MIL-100-NH_2 and UiO-66-NH_2. A quantity of just 0.1 mg of ZIF-67 produced 29.6 μmols of CO over a 30 minute period compared to the next highest value of 4.7 μmols (MIL-100-NH_2)[130].

As mentioned earlier, the combination of Zn^{2+} and HIM can produce multiple different topologies. The simplest ZIF, ZIF-1, is $Zn(IM)_2$ and it adopts the **crb** topology. However, ZIF-1 is of little research interest due to its low porosity.[12] However, the **cag** topology of ZIF-4, which also has the $Zn(IM)_2$ formula, is often studied. This is often because it can be melted to form a porous glass at 300 °C.[131] MOF glasses are highly valued for producing membranes for gas filtration. Typically, MOF membranes are made by mixing a polymer and MOF together. These membranes can have gaps and defects at the boundary between the two materials: compromising their gas selectivity. These are not apparent with MOF glasses.[132] Morphological tuning of ZIF-4 would be valuable as it would potentially allow further study to be conducted on the impact of MOF morphology on the formation of MOF glasses.

2.2.Results & Discussion

The initial microemulsion ZIF-8 synthesis methodology was provided by Otago University through correspondence (ZIF-8a-1x)(2.4.2 Microemulsion ZIF-8 Synthesis).The PXRD of this ZIF-8a material possesses peaks at 7.3º, 10.3º, 12.7º, 14.6º, 16.4º, 17.9º (Figure 2.5A). These are characteristic of the [011], [002], [112], [022], [013], and [222] lattice planes. This is consistent with the **sod** topology of ZIF-8. However, this synthetic method had several issues. Primarily, it produced a low absolute yield of ~1 mg which made it difficult to perform multiple characterization analyses on the same sample batch. Additionally, whilst most crystals had a RD morphology this was far from consistent (Figure 2.5C-D & B.1). Furthermore, the particle size achieved was 68.7 ± 31.3 nm (N = 101) (Figure 2.4B). Whilst this in the desired nanoparticle size range, the SD is 45.5 % of the mean; hence, the sample has a broad PSD. This PSD could not be modelled with a continuous distribution (Figure B.2) possibly indicating polydispersity within the sample.

The strategy adopted to improve the yield was to increase the amount of TX-100, hexanol, and the aqueous phase increased four-fold by mass (ZIF-8d-120). This significantly increased the yield to 41.5 mg; an increase that could not solely be attributed to the increased concentration of reactants. This was likely the result of extraction from the solution being considerably easier with a more concentrated solution. By making this change the morphology also became much more uniformly rhombic dodecahedral (though some cubic particles can still be seen by TEM). The NP size increased to 87.3 ± 22.4 nm (N = 131). Whilst, the overall size increased, the percentage SD decreased to 25.6%. This is generally considered monodisperse. Because of the increased yield and improved dispersity, this sample was used as a basis for further study.

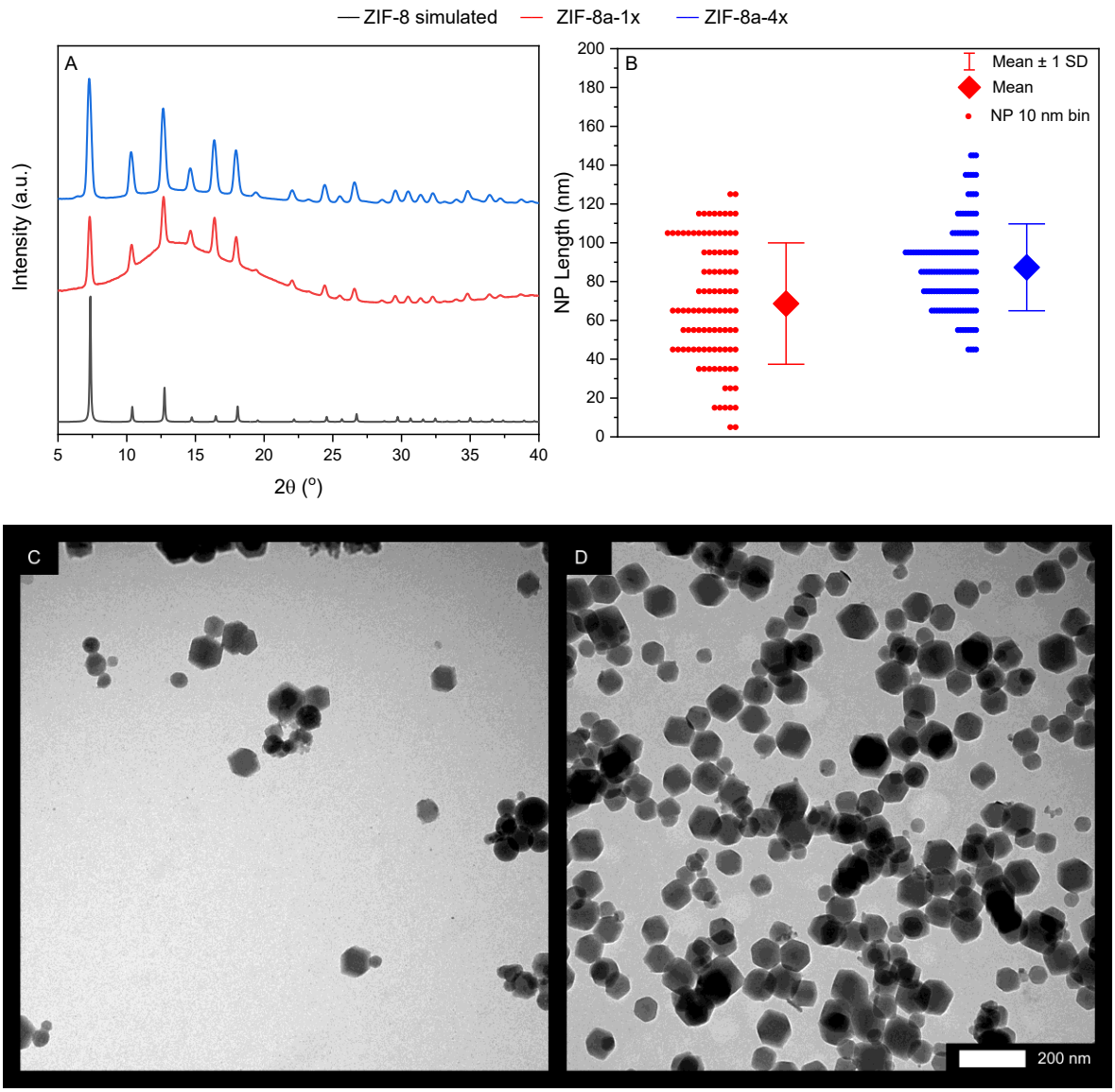

Figure 2.5 (A) PXRD patterns and (B) plot of the particle size distributions (PSD). TEM images of (C) ZIF8a-1x and (D) ZIF-8b-4x. The scale bar is 200 nm.

2.2.1. Addition Rate

Samples were then synthesized using a variable addition time. The ligand microemulsion (μEL) was added to the metal microemulsion (μEM) dropwise using a syringe pump over a 0, 15, 30, 60, 90 and a 120 min period. For the 0 min synthesis, μEL was directly pipetted into μEM. Samples were denoted ZIF-8b-time except the 30 min and 120 min samples which were denoted ZIF-8d-2 and ZIF-8d-1 respectively. Samples denoted ZIF-8d appear in multiple subsections of this chapter. The PXRD profile of all samples is consistent with ZIF-8 (Figure 2.6A). No additional peaks were identified indicating that topologically pure **sod** ZIF-8 was formed.

The sample morphology varied with the addition time (Figure 2.6C-H). When μEL was added directly to μEM, the crystals exhibited a uniformly pseudospherical morphology. This was consistent with the 15 min synthesis. It is unclear as to why spherical crystals would form in these conditions. It is possible that the small size of the crystals limited visibility of the crystal edges and factes giving them the *appearance* of spherical particles. As the addition time increased to 30 min RD particles became predominant. Whilst this remained the case for longer addition times, cubic and TRD crystals were also noticeable in the 90 and 120 min samples. Shorter addition times generally result in a faster initial nucleation rate and more time spent in the crystal growth phase. This is consistent with the observed morphologies as the samples with shorter addition times did not display cubic and TRD particles which are generally apparent in early stages of crystal growth.

As the addition rate decreased the particle size increased (Figure 2.6B, B.3 & Table B.2). However, the increase in particle size became less apparent at longer addition times. For example, the average size of ZIF-8b-0 was 27.3 ± 9.1 nm (N = 103). ZIF-8b-30 was an average of 74.6 ± 18.0 nm (N = 107). Hence, a change of 30 min resulted in a 50.9 nm change in NP size. ZIF-8b-90 had a particle size of 78.2 ± 25.7 nm (N = 118). Hence, the same 30 min change in addition time induced only a 9.1 nm change in NP size. This increased to 87.3 ± 22.4 nm (N = 131). As a general trend, the SD in particle size tended to increase with addition time. However, the RSD remained relatively consistent between 33.4% and 24.1%. Interestingly, sample ZIF-8b-0 possessed the lowest SD and the highest RSD (9.1 nm, 33.4%). The small NP size of this sample causes small SD values to result in relatively large RSD values.

Given the success of size tuning ZIF-8 nanoparticles using the addition rate, future work could focus on the physical properties of these samples e.g. gas adsorption and

thermogravimetric analysis should be used to investigate whether the NP size influences the surface area or decomposition temperature of these samples.

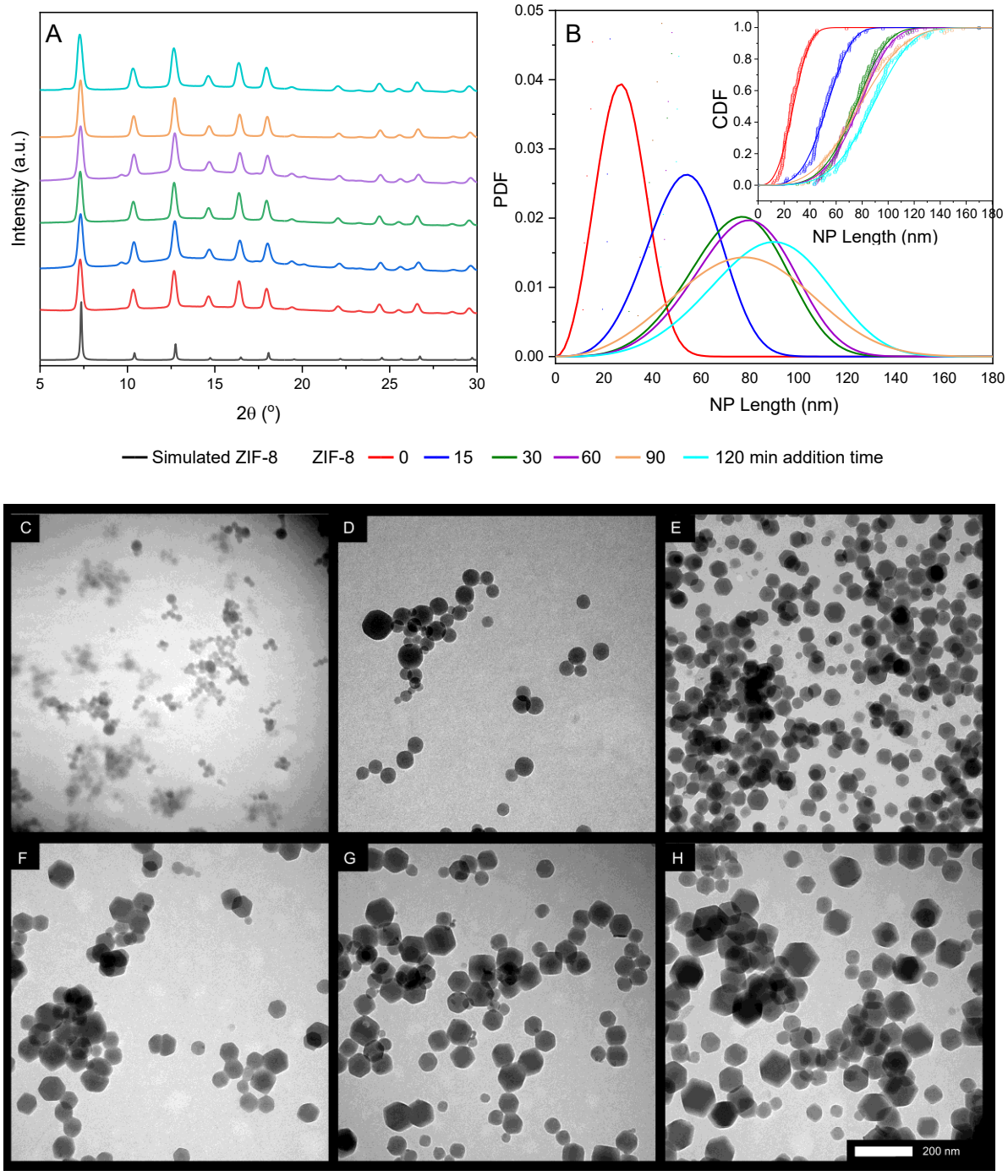

Figure 2.6 (A) PXRD patterns and (B) Weibull modelled PSD displaying the (Outset) PDF and (Inset) CDF for ZIF-8 samples synthesized with a variable addition time. Individual data points show the empirical CDF (ECDF). TEM images of ZIF-8 synthesized with a (C) 0, (D) 15, (E) 30, (F) 60, (G) 90 and (H) 120 min addition time. The scale bar is 200 nm.

It should be noted that the PSD of almost every sample in this chapter was adequately described with both the Weibull and Gaussian distributions. However, this was not the case for ZIF-8b-0; the smallest sample ZIF-8 in this chapter. ZIF-8b-0 was adequately described with a Weibull but not Gaussian distribution. Comparison of the CDF and PDF of both models shows (Figure 2.7& Table B.1) a broader Weibull distribution. However, a rapid drop-off occurs in the lower tail of the Weibull distribution suggesting an asymmetric distribution. With the Gaussian model 9% of NPs are less than 10 nm in size. This reduces to 4% for NPs less than 5 nm in diameter. For the Weibull distribution, the equivalent values are 3% and 0.3%. This is consistent with the raw data, where the smallest observed NP was 11.9 nm. The average length and standard deviation corrected for the Weibull model is 27.2 ± 9.7 (N = 103) RSD 35.7 %. Lower tail asymmetry also occurs for the two smallest samples from 2.2.2 ω_o. In classical nucleation theory, NPs are considered metastable below a critical radius because of their tendency to aggregate or dissolve. This could explain why sub-10 nm NPs are not present in the sample despite a uniform distribution predicting that they would be.

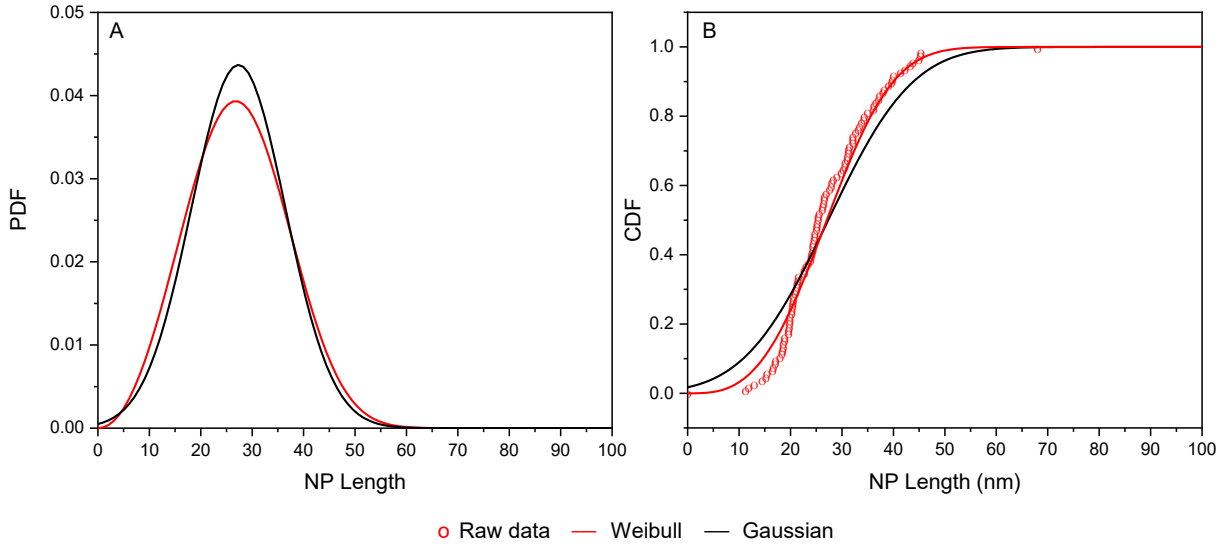

Figure 2.7 (A) PDF and (B) CDF of ZIF-8b-0 PSD

In comparison to the literature ZIF-8b-0 is one of the smallest samples on record. Four studies have managed to produce smaller NPs.[108, 112, 129, 133] Whilst Cravillon and colleagues managed to produce several samples smaller than ZIF-8b-0, measurements were performed using SAXS and *in situ* PXRD and no PSD information was provided.[129] In 2018, Lan and colleagues synthesized 27 nm ZIF-8 by adjusting the ligand metal ratio to 55:1. In their case, the NP size was obtained through TEM and the experimental PSD was provided. However, this came in the form of a histogram without the raw data. The dispersity was not calculated;

hence it is difficult to compare the PSD of this sample with ZIF-8b-0. However, from the experimental PSD no NPs less than 15 nm were present.[133]

However, the idea that ultra-small ZIF-8 NPs are unstable is contradicted by the two microemulsion studies by Sun's group, which reportedly synthesized ~2 nm NPs.[39, 108] However, this is not the only unusual feature of these studies. Firstly, PXRD can be used to determine the crystallite size using the Debye-Scherrer equation. (Side-note: This was not performed in this chapter because the technique is only accurate for small NPs and our PXRD instrument has significant instrumental broadening. This would have created inaccuracies in the larger ZIF-8 samples). In the case of the putative 2.2 nm ZIF-8 NPs, significant broadening of the PXRD peaks would have been expected because of the reduction in the number of periodic units along each plane (Figure B.4). This broadening was not observed in Sun's studies. Secondly, CTAB and TX-100 w/o microemulsions behave very differently. The same NP synthesized using both systems can have drastically different sizes and morphologies.[134] Hence, it is unusual that these systems would have produced ZIF-8 NPs with remarkably similar morphologies, as reported. Thirdly, sub-10 nm MOF NPs are incredibly rare. Whilst, Cravillon demonstrated that this was possible for ZIF-8, the number of repeating units in a (connectivity) 9 nm and 2.2 nm ZIF-8 NPs are incomparable. In one case, the average NP contains 78 unit cells, whereas the other would possess just over 1 unit cell (unit cell length = 1.7012 nm).[129] Two cases of MOF NPs with comparable dimensions are noted: HKUST-1 (2.6 nm)[135] and UiO-66 (~4 nm)(Chapter 4 - Microemulsion Synthesis of UiO-66). In both cases, significant PXRD peak broadening was observed. Furthermore, both MOFs have greater connectivity than ZIF-8; this would improve the stability of ultra-small NPs. HKUST-1 has 4 BTC molecules per copper paddle-wheel cluster and three paddlewheels per BTC ligand. UiO-66 has 12 BDC molecules per zirconium cluster and two clusters per BDC molecule. Given these points, further work to reproduce these results would be warranted.

2.2.2. ω_o

ZIF-8 was synthesized with ω_o values of 22.3, 16.7, 11.1, 10 and 5.6. These correspond to 4.0, 3.0, 2.0, 1.8, and 1.0 mL of the aqueous phase used during synthesis. The samples were denoted ZIF-8c-volume e.g. ZIF-8c-4. The 1.8 mL sample was ZIF-8d-30. All samples displayed PXRD peaks expected for ZIF-8 and appeared to be phase pure (Figure 2.8A).

When imaged by TEM (Figure 2.8C-E), all samples displayed mostly rhombic dodecahedral crystals. On closer inspection, ZIF-8c-4 possesses a significant portion of irregularly shaped NPs. Interestingly, there appeared to be no apparent correlation between NP size and the water volume (Figure 2.8B, B.5 & Table B.3), despite significant variability in NP size between samples. At the upper end of sizes, the 1.8 mL sample produced a NP length of 74.7 ± 24.0 (N = 107). At the lower end, the 3 mL sample led to a NP length of 39.9 ± 15.9 (N = 218). Furthermore, significant range exists in the samples' dispersity with RSD values ranging from 24.0% for the 1.8 mL sample to 39.3% for the 3 mL sample. The lack of correlation between ω_0 and the NP size is in contradiction with a templating model of microemulsion synthesis. The templating model would suggest the NP size would decrease as the amount of water (and ω_0) decreased. Interestingly, this same trend was investigated for UiO-66 (Chapter 4 - Microemulsion Synthesis of UiO-66) and a strong correlation was found between the ω_0 and the NP size. This suggest that the effect of this parameter is likely due to some degree of interplay between the MOF components, the nucleation process, and the microemulsion.

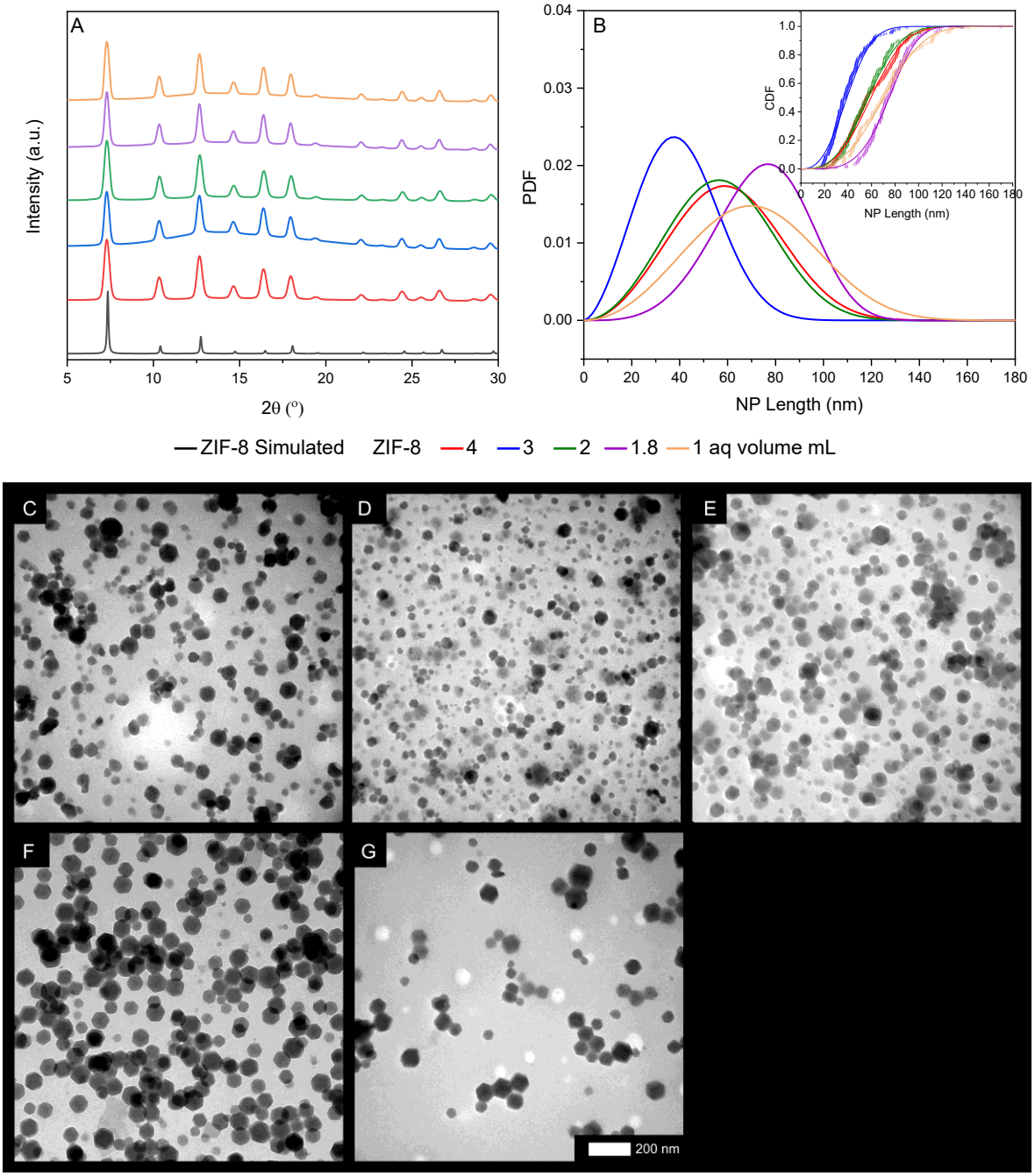

Figure 2.8 (A) PXRD and (B) Weibull modelled PSD displaying the (Outset) PDF and (Inset) CDF. Individual data points show the ECDF. TEM images of ZIF-8 synthesized with (C) 4, (D) 3, (E) 2, (F) 1.8 and (G) 1 mL of aqueous phase. The scale bar is 200 nm.

Like ZIF-8b-0, two samples could not be adequately described with a Gaussian model: ZIF-8c-3 and ZIF-8c-4 (Figure 2.9). The Weibull modelled NP size for these two samples results in NP dimensions of 39.9 ± 16.1 (N = 218, RSD 40.3%) and 60.1 ± 22.0 (N = 168, RSD

36.6 %). Both samples show significantly less NPs at the lower tail end of the distribution than would be expected by a Gaussian distribution.

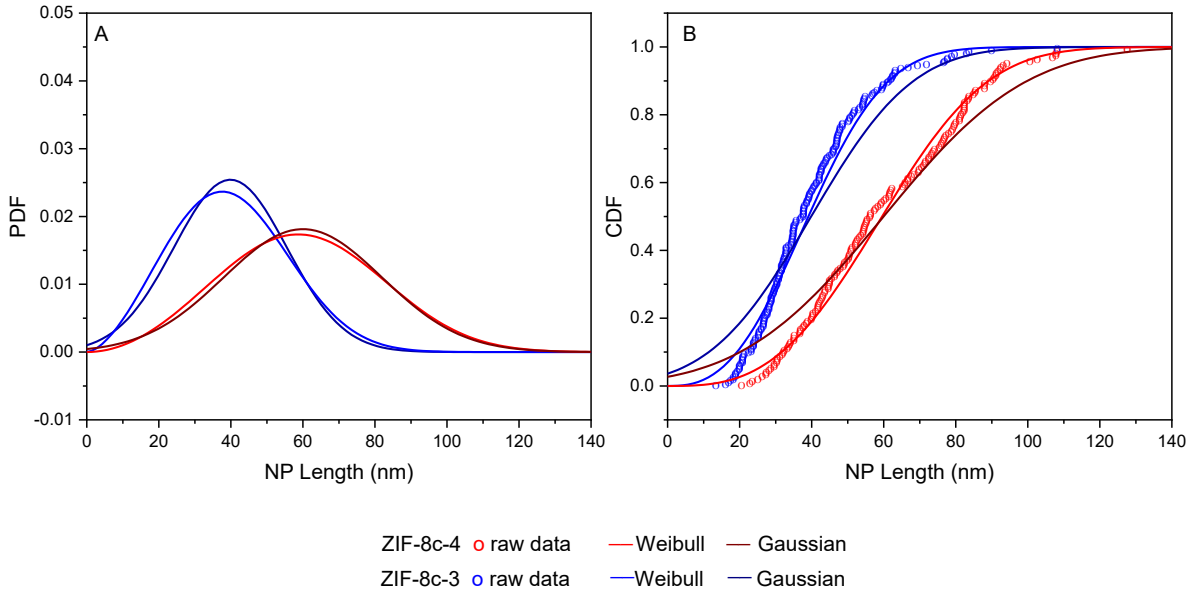

Figure 2.9 (A) PDF and (B) CDF of ZIF-8c-4 and ZIF-8c-3 PSD

2.2.3. Metal Ligand Ratio

ZIF-8 was then synthesized using a variable mIM to Zn^{2+} ratio while maintain a 30 min addition time. The Zn^{2+} concentration was maintained at 0.19 M. The ratios used were 40:1, 20:1, 10:1, 5:1 and 8.42:1 (denoted ZIF-8e-equivalents e.g. ZIF-8e-40). The 8.42:1 sample was ZIF-8d-30. The only sample that delivered a phase pure product was the 8.42:1 ratio (Figure 2.10A). As the ratio increases to 10, 20 and 40 additional peaks appear at 8.6 and 9.6°. Reduction of the ligand metal ratio to 5:1 results in additional peaks at 9.6 and 11.1° alongside standard ZIF-8 peaks. This is unusual behaviour since conventional aqueous synthetic protocols typically utilize ligand metal ratios of 40:1 or greater unless an amine is added. The contrasting behaviours of microemulsion and aqueous synthesis supports the notion that further processes are in play during microemulsion synthesis rather than simple templation of aqueous synthesis. Either, the template is interacting with ZIF-8 during growth or the growth kinetics are substantially altered by confinement within the microemulsion. To contrast microemulsion synthesis with aqueous synthesis, ZIF-8 was synthesized in an aqueous solution using a ligand equivalence of 8.42 and 40. An equivalence of 8.42 produced ZIF-L (Figure 2.10B); a topology of 2D sheets often formed as an intermediate in the synthesis of ZIF-8. The presence of peaks at 7.3, 7.8, 8.9, 10.3, 10.9 and 11.6° corresponded to the [400], [222], [004], [040], [224] and [404] planes of ZIF-L. This result is consistent with the prior literature.[82, 136] An equivalence of 40 produced a typical ZIF-8 powder pattern.

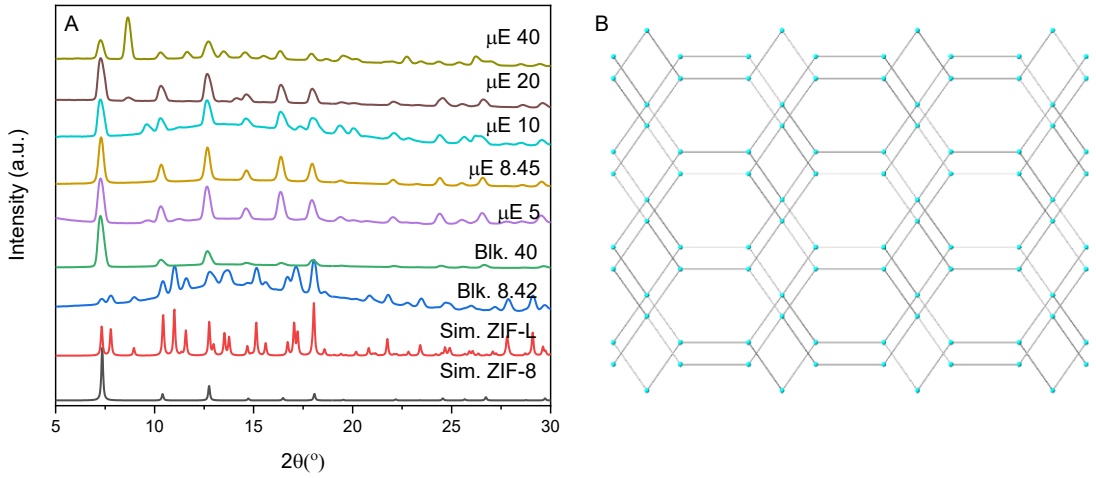

Figure 2.10 (A) PXRD of bulk and microemulsion ZIF-8 synthesized with variable ligand equivalents. (B) ZIF-L structure

2.2.4. ZIF Screening

ZIF-67 and ZIF-1 were synthesized using the microemulsion method. ZIF-67 is the cobalt analogue of ZIF-8 with the same **sod** topology. Because of its structural and chemical similarity, it was a useful reference point to investigate other materials. ZIF-67 was synthesized by substituting zinc nitrate with cobalt nitrate during standard ZIF-8 synthesis all other reaction conditions used for ZIF-8-d-30 were maintained. Hence, the ligand equivalence was 8.42, the addition time was 30 min and 1.8 mL of aqueous phase was used during synthesis. Unsurprisingly, the PXRD of the ZIF-67 sample was consistent with the simulated **sod** ZIF-67 structure (Figure 2.11A). However, due to the structural similarity of ZIF-8 and ZIF-67 this is indistinguishable from ZIF-8. ZIF-67 NPs were 120.7 ± 22.0 nm (N = 105) in length. This is considerably larger than their ZIF-8 equivalent which was 74.6 ± 18.0 nm (N = 107) (Figure 2.11B). This is consistent with the literature where equivalent methods generally produce larger ZIF-67 particles.[137] In addition, the morphology of ZIF-67 is RD but considerably less well defined than the equivalent ZIF-8 NPs. This is likely due to the higher lability of Zn mIM bonds compared to the cobalt equivalent. Interestingly, except for Sun's group which synthesized 2.3 nm ZIF-67 NPs, the next smallest sample is 80 nm synthesized by Wang and colleagues in 2018.[138] The disparity between the size of ZIF-8 and ZIF-67 samples in the literature could be due to the considerably smaller subset of the literature dedicated to ZIF-67 or imply that synthesis of ZIF-67 NPs is considerably more difficult.

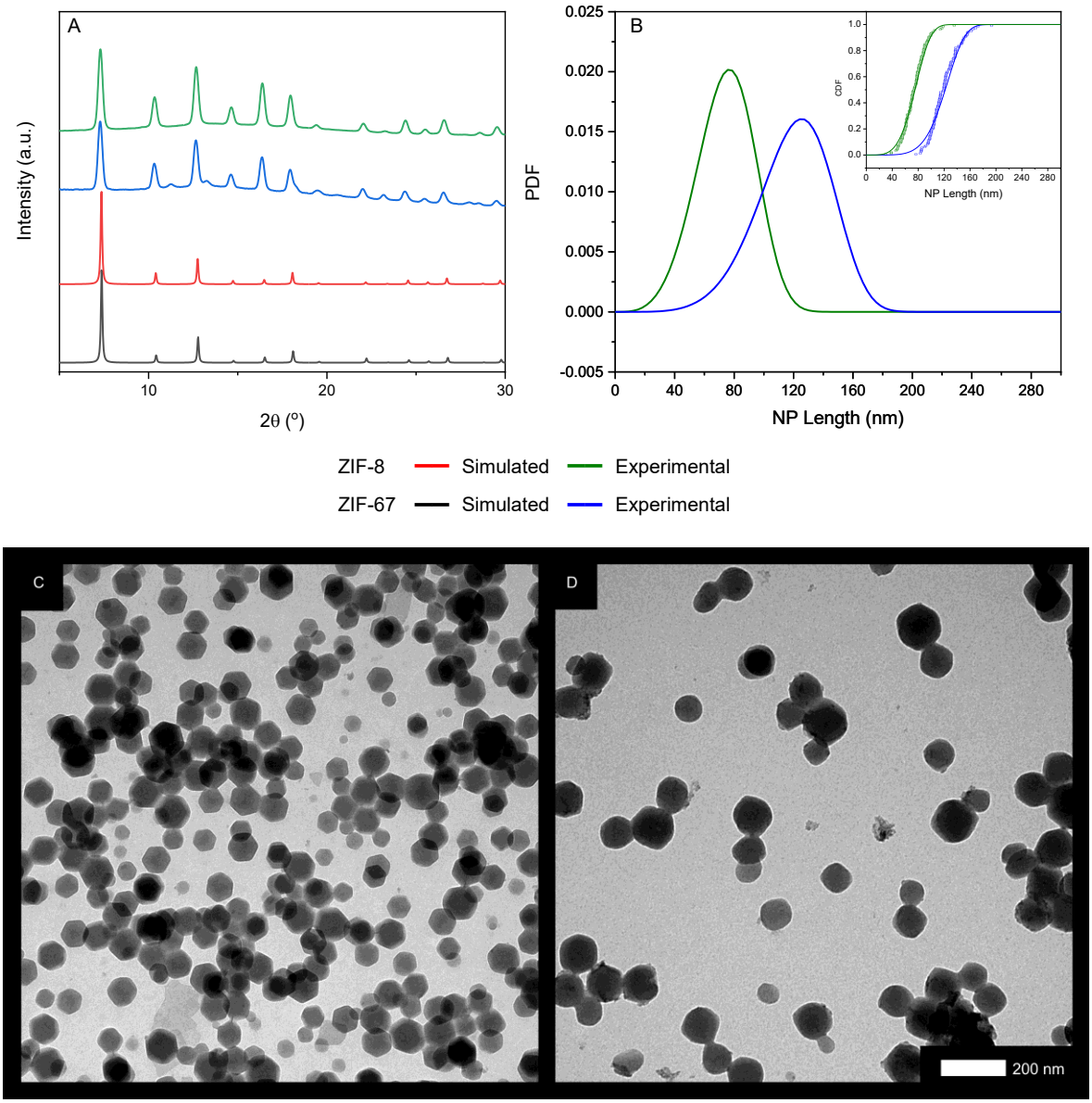

Figure 2.11 (A) PXRD and (B) Weibull modelled PSD displaying the (Outset) PDF and (Inset) CDF. Individual data points show ECDF. TEM images of ZIF-8 (C) and ZIF-67 synthesized using the microemulsion method

Microemulsion synthesis was used to synthesize MOFs from the combination of Zn^{2+} and HIM. These samples were denoted Zn-IM-1 and Zn-IM-2 and varied in the ω_0 value (16.7, 10.0). Interestingly, by varying the ω_0 value the MOF topology and morphology varied substantially. Zn-IM-1 possessed PXRD peaks (Figure 2.12A) at 11.3, 11.9, 14.9 and 20.0°. These corresponded to the [111], [220], [131] and [151 planes of the $Zn(IM)_2$ **neb** phase (Figure 2.12B). ZIFs with the **neb** phase are relatively rare and has only been synthesized using solvothermal synthesis at 140 °C in two studies.[139, 140] Hence, a new ambient protocol for the

synthesis of $Zn(IM)_2$ **neb** is at least interesting. Unfortunately, $Zn(IM)_2$ **neb** is not a particularly desirable product as it has low stability and porosity. However, the low porosity of this material is generally the result of adding a templating agent which occupies the MOF pores e.g pyridine.[139] This is a procedure that is not performed during microemulsion synthesis. Hence, determining the porosity of this material using gas adsorption would be worthwhile for future study. As to Zn-IM-2, despite comparison to all known Zn^{2+}/IM topologies, this material could not be identified. To identify this material, Rietveld refinement of the crystal structure from PXRD data is required. However, it would be preferable if this were performed on synchrotron data to reduce background noise and instrumental broadening in the PXRD. As to the morphology (Figure 2.12C & D), Zn-IM-1 tended to form large aggregates. Surprisingly, Zn-IM-2 formed relatively uniform pseudospherical NPs ~ 70 nm in length.

It is interesting to note that the topology of ZIF materials was altered by adjusting the ω_0 value. This is the first instance of topological changes being observed due to the adjustment of microemulsion parameters. Given this, it would be interesting to do a comprehensive investigation on different microemulsion parameters and their resulting Zn-IM topology. However, there was insufficient time in this study for further investigation into these materials.

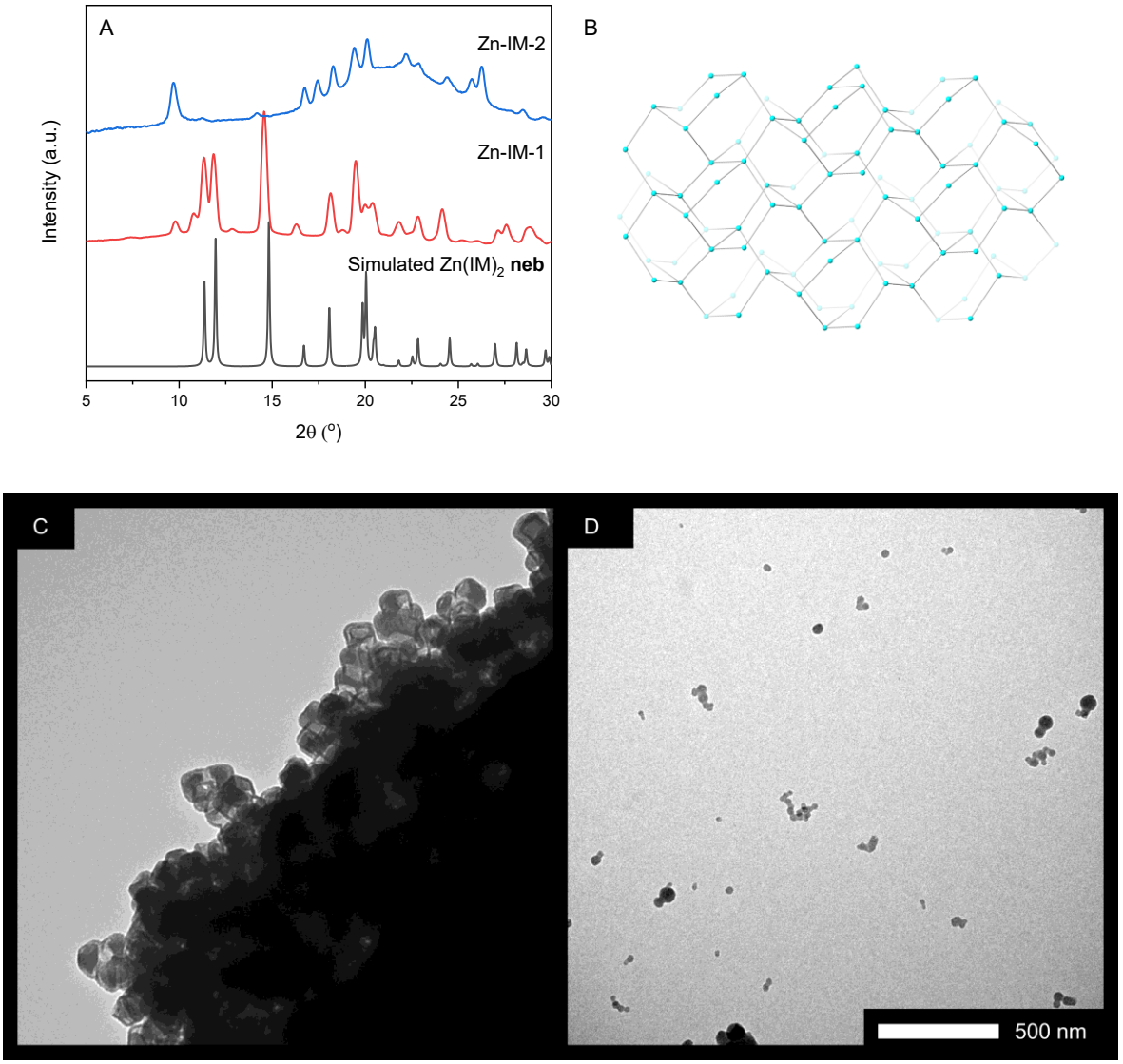

Figure 2.12 (A) PXRD of Zn-IM samples. (B) $Zn(IM)_2$ **neb** structure. TEM images of (C) Zn-IM-1 and (D) Zn-IM-2.

2.3. Conclusion

In conclusion ZIF-8 was successfully synthesized with nanoscale dimension using the TX-100/hexanol w/o microemulsion system. Interestingly, no correlation could be observed between ω_o and the NP size. Furthermore, microemulsion synthesized ZIF-8 lost phase purity when synthesized with greater ligand/metal ratios. Both behaviours would not be expected if templation of an aquous synthesis was the primary mechanism for MOF growth in this system. This suggests templated aqueous growth is not the primary mechanism for size control. This is further supported by the success of synthesis with an 8.42 ligand equivalence which is atypical of standard aqueous synthesis. Despite this nonstandard behaviour NP size control was achieved through changing the addition time. NP length was adjusted from 27.3 ± 9.1 to 87.3 ± 22.4 by changing the addition time from 0 to 120 min. Microemulsion synthesis was then applied to synthesize ZIF-67 and $Zn(IM)_2$ **neb**. When measuring the NP size and distribution, the reporting standard adopted by Marshall and colleagues was used. However, this does not account for changes in the PSD. Three ZIF-8 samples were synthesized which did not conform to a standard Gaussian distribution. It is recommended that future studies provide the ECDF to allow comparison of the PSD shape.

2.4. Experimental Methods

2.4.1. Materials

All chemicals and reagents were sourced from commercial suppliers at a purity of 99.8% or greater and used without further purification.

2.4.2. Microemulsion ZIF-8 Synthesis

For all ZIF-8 samples prepared using microemulsion synthesis, two solutions were prepared by mixing various quantities of TX-100, 1-hexanol and cyclohexane. To each mixture an aqueous solution containing either $Zn(NO_3)_2.4H_2O$ (0.19 M) or HmIM was added. The volume of aqueous phase in µEM and µEL was always the same. Both microemulsions were left stirring for 24 hours to homogenize. µEL (20 mL) was added to µEM (20 mL) dropwise over a set addition time. The solution was then left stirring for an hour. The resulting mixture was ruptured with methanol/acetone (50% v/v, 20 mL). MOF crystals were extracted by centrifugation at 6000 rpm for 20 min. The extracted solid was washed with acetone, cyclohexane, and methanol (10 mL) before lyophilization overnight. The composition and addition time for each sample is shown in Table 2.1.

Table 2.1 Synthesized ZIF-8 samples

Sample	Add Time	Microemulsion Composition*									
		Cyclohexane		TX-100		1-hexanol		Aq.	$[Zn^{2+}]$	[HmIM]	$\frac{\dagger[HmIM]}{[Zn^{2+}]}$
	min	mL	mmol	g	mmol	mL	mmol	ml	M	M	
ZIF-8a-1x	120	20	185	1.56	2.41	0.6	4.82	0.45	0.19	1.6	8.42
ZIF-8b-0	0	20	185	6.24	9.64	2.4	19.3	1.8	0.19	1.6	8.42
ZIF-8b-15	15	20	185	6.24	9.64	2.4	19.3	1.8	0.19	1.6	8.42
ZIF-8b-60	60	20	185	6.24	9.64	2.4	19.3	1.8	0.19	1.6	8.42
ZIF-8b-90	90	20	185	6.24	9.64	2.4	19.3	1.8	0.19	1.6	8.42
ZIF-8c-4	30	20	185	6.24	9.64	2.4	19.3	4	0.19	1.6	8.42
ZIF-8c-3	30	20	185	6.24	9.64	2.4	19.3	3	0.19	1.6	8.42
ZIF-8c-2	30	20	185	6.24	9.64	2.4	19.3	2	0.19	1.6	8.42
ZIF-8c-1	30	20	185	6.24	9.64	2.4	19.3	1	0.19	1.6	8.42
ZIF-8d-120	120	20	185	6.24	9.64	2.4	19.3	1.8	0.19	1.6	8.42
ZIF-8d-30	30	20	185	6.24	9.64	2.4	19.3	1.8	0.19	1.6	8.42
ZIF-8e-40	30	20	185	6.24	9.64	2.4	19.3	1.8	0.19	7.6	40
ZIF-8e-20	30	20	185	6.24	9.64	2.4	19.3	1.8	0.19	3.8	20
ZIF-8e-10	30	20	185	6.24	9.64	2.4	19.3	1.8	0.19	1.9	10
ZIF-8e-5	30	20	185	6.24	9.64	2.4	19.3	1.8	0.19	0.95	5

2.4.3. Microemulsion ZIF-67 & Zn-IM synthesis

ZIF-67 was synthesized in a microemulsion using the procedure outlined in 2.4.2 Microemulsion ZIF-8 Synthesis for sample ZIF-8d-30. $Zn(NO_3)_2.4H_2O$ was substituted the same concentration of $Co(NO_3)_2.4H_2O$ (0.19 M).

Zn-IM-1 & Zn-IM-2 samples were prepared using the procedure outlined in 2.4.2 Microemulsion ZIF-8 Synthesis for sample ZIF-8d-30. The aqueous phase of μEL was substituted with an aqueous HIM solution (1.9 M). μEL & μEM were prepared with a variable aqueous phase volume (Zn-IM-1, Zn-IM-2: 3 mL, 1.8 mL).

* Composition of constituent microemulsions used to make the sample. E.g. sample ZIF-8a-1x is made from two microemulsions both are composed of 20 mL cyclohexane, 1.56 g TX-100, 0.6 mL hexanol and 0.45 mL aqueous phase. The aqueous phase is either 0.19 M Zn^{2+} or 1.6 M HmIM.

† Ligand to metal equivalence of final composition after addition of μEL to μEM.

2.4.4. Aqueous ZIF-8 Synthesis

ZIF-8 was synthesized by mixing aqueous $Zn(NO_3)_2.4H_2O$ (0.19 M, 20 mL) with 20 mL of an aqueous HmIM solution of variable concentration (1.6 M, 7.6 M). The sample was left at room temperature without stirring for 24 hours. Crystals were extracted from the solution by centrifugation at 6,000 rpm for 20 min. The sample was washed 3x with water (10 mL) before lyophilization.

2.4.5. Transmission Electron Microscopy

Samples were prepared for TEM imaging by dispersing ~1 mg in 1 mL ethanol and sonicating for 20 seconds. A drop of this solution was added to a negative staining grid and left for 5 minutes before drying and imaging using a FEI Tecnai G2 Biotwin transmission electron microscope. NP size information was determined using ImageJ 1.52a. Threshold masking was determined manually, and the particle size was determined with holes excluded. The Feret's diameter was used as the NP length (A.1.2 Transmission Electron Microscopy). NP size was determined across ~100 samples.

2.4.6. Powder X-Ray Diffraction

X-ray diffraction data was collected using a Rigaku Spider diffractometer equipped with a Micromax MM007 rotating anode generator with Cuα radiation (λ = 1.54180 Å), high flux osmic multilayer mirror optics, and a curved image plate detector, and finally processed into 1D diffractograms using 2DP.

Chapter 3 - *In situ* Protein Encapsulation in Microemulsions

3.1. Introduction

A recent application of MOFs is to use them as substrates for the immobilization of proteins and protein catalysts (enzymes). Proteins are highly sought after as industrial catalysts, biosensors, and drugs due to their high selectivity, reactivity and perceived environmental friendliness.[141] However, their applicability is often limited by their low-stability and recyclability. Protein recyclability can be improved by immobilization onto solid substrates such as hydrogels[142-144], carbon nanomaterials[145], zeolites and MOFs. Such composites can often be more readily extracted from reaction media then reused. Furthermore, protein stability can be enhanced if immobilized internally within the pores of a substrate. This process is known as encapsulation.[146] In this thesis protein encapsulating MOF complexes are denoted protein@MOF.

Protein stability is enhanced by encapsulation by preventing denaturation, which can otherwise occur through unfolding/agglomeration due to slight changes in the local environment.[147, 148] For instance, high temperatures,[147, 149, 150] chemical agents,[151] and proteases[149] have all been observed to cause denaturation. By encapsulating a protein within a MOF the protein is stabilized by two mechanisms. The first is that it prevents access to the protein by denaturing agent. For instance, horseradish peroxidase (HRP)@ZIF-8 is protected from trypsin (a common protease) induced denaturation because trypsin is too large to enter the MOF pores.[149] The second mechanism is that confinement within the MOF reduces the structural mobility of the protein to prevent unfolding. For instance, Liao and colleagues made catalyse@ZIF-90 and introduced urea at 80 ºC. Free catalyse showed no activity when exposed to urea, whereas the activity of catalyse@ZIF-90 was preserved. They then encapsulated urease in ZIF-90. Urease degrades urea and increases the solution pH. Urease maintained its activity despite internal its encapsulation in ZIF-90, implying that urea can be accommodated in the MOF pores.[151]

3.1.1. Enzyme Encapsulation in MOFs

MOFs are particularly sought out encapsulation substrates. Their enormous internal surface area provides a significant area for intermolecular interactions with the protein surface. Hence, MOFs typically have a high loading efficiency* (LE) and low leaching rate compared to other encapsulating substrates.[152] In addition, by modifying the ligands MOFs have been designed to further enhance LE through protein-MOF interactions such as π-π stacking or covalent

* Mass of encapsulated protein as a percentage of the total protein-substrate complex mass.

linkages.[153] Furthermore, because of their extensive structural diversity, MOFs can be functionalized to have roles beyond simply being a protein carrier. For instance, by selecting the pore dimensions MOFs can allow specific substrates selective access to enzymatic active sites; enhancing catalytic specificity. This was highlighted by Knedel and colleagues by encapsulating laccase within ZIF-8. The resulting laccase@ZIF-8 could catalyse the substrate 2,6-dimethoxyphenol but not the bulkier dye 2,2'-azino-bis(3-ethylbenzothiazoline-6-sulfonic acid (ABTS). This indicates ABTS could not enter the ZIF-8 pores to reach the laccase active sites.[154] Another example of the functional role of MOFs in protein@MOF complexes was demonstrated by Li and colleagues. They synthesized cytochrome C@HKUST-1. Cytochrome C catalyses the decomposition of hydrogen peroxide. They postulated encapsulation in HKUST-1, a Cu^{2+} containing MOF, would result in a protein@MOF complex with greater activity than the protein. This was because Cu^{2+} promotes increased cytochrome C activity and HKUST-1 also catalyses the degradation of hydrogen peroxide. This postulation proved true and a 12-fold increase in catalytic activity was observed in cytochrome C@HKUST-1 compared to cytochrome C.[155]

To date, there are four categories of techniques to immobilise proteins to MOFs: surface adsorption, covalent attachment, post synthetic loading and *in situ* synthesis.[146] The first two are solely immobilization techniques and will not be covered. However, they have been extensively reviewed in prior literature.[146, 156, 157] The latter two will be briefly covered below (Figure 3.1).

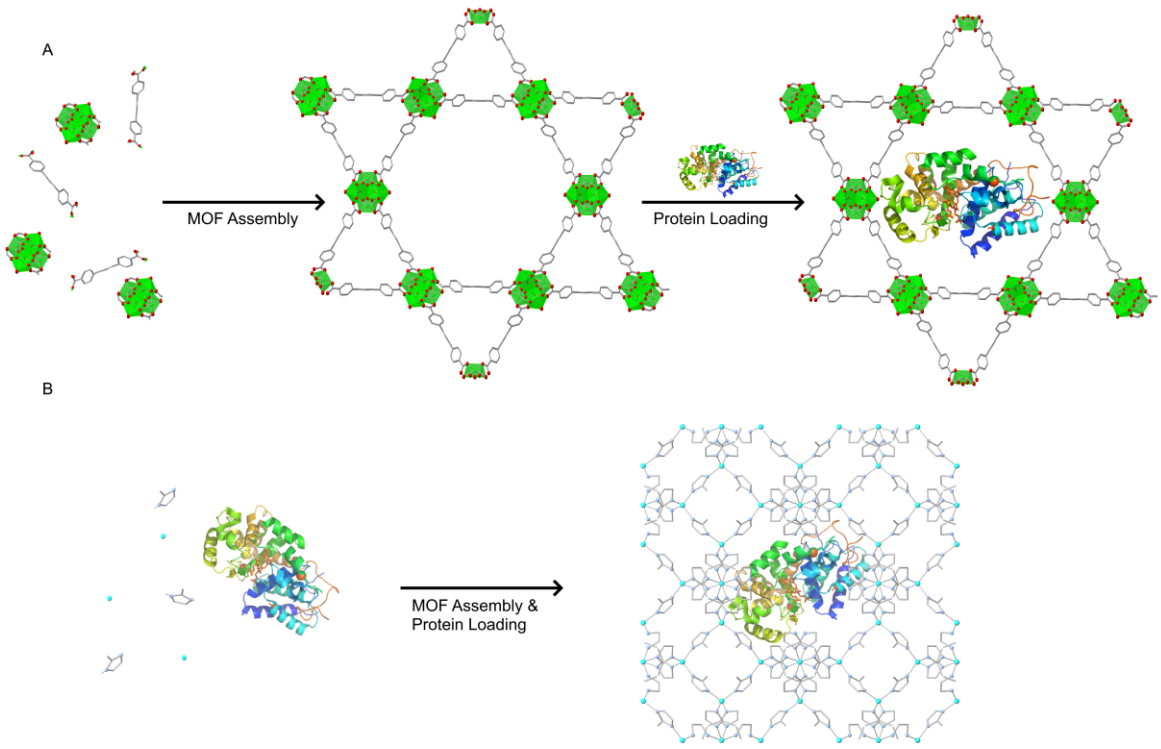

Figure 3.1 Protein encapsulation within (A) NU-1000 using post synthetic loading and (B) ZIF-8 using *in situ* synthesis.

3.1.1.1.Post Synthetic Loading

Post synthetic loading, was pioneered by Lykourinou and colleagues in 2011 to encapsulate the protein MP-11 in TB-mesoMOF.[152] The technique involves pre-synthesizing the MOF and then loading the enzyme into the MOF pores. The protein is stabilized within the pores by intermolecular interactions with the MOF surface.[153] Two design rules have been proposed to optimize the catalytic efficiency of these materials. The first states the MOF should contain pores of similar dimensions to the encapsulated protein. If the protein is significantly larger than the pore dimensions, it will not be incorporated into the pore*. If the other way around, the MOF-protein surface interactions will be reduced, and the protein will not be retained in the MOF. The second design rule states the MOF should be hierarchically porous i.e. it should have multiple pores of different dimensions. One set of cavities can be utilized to encapsulate proteins while the other can be kept free. Free pores act as channels for reactants to diffuse to protein active sites increasing catalytic rates within the crystal.[159] These two design rules were utilized by Lian and colleagues to encapsulate glucose oxidase (GOx) and HRP within PCN-888. PCN-888 has 3 pores of different diameters (6.2, 5.0 and 2.0 nm). The 6.2

* Proteins can be encapsulated within MOFs where the pore aperature is smaller than the protein. This is achieved by a conformational shift in the protein to squeeze into the MOF pores.[158]

pore was used to encapsulate HRP. GOx was encapsulated in the 5.0 nm pore and the third pore was left free. The resulting GO/HRP@PCN-888 was used to catalyse the conversion of the ABTS dye to its blue form (Figure 3.2). This was attributed to the paired location of HRP and GOx. This allowed fast transport of hydrogen peroxide from GOx to HRP.[160]

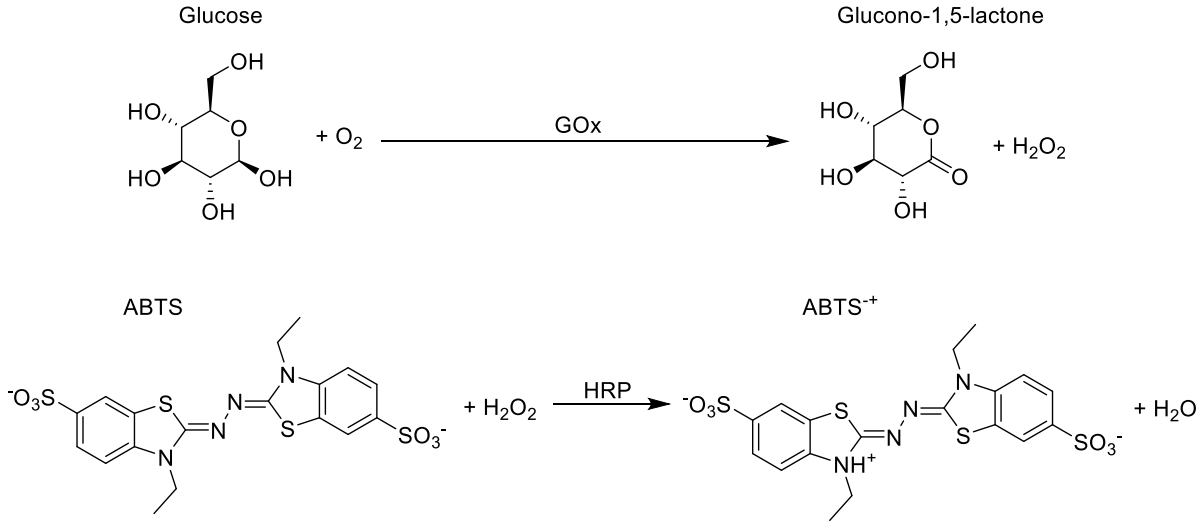

Figure 3.2 GOx/HRP catalysed tandem reaction

Whilst pore/protein size pairing allows for precise control over loading and catalytic properties, it severely limits the enzyme/MOF combinations that can be made. The requirement for size pairing limits the applicable MOFs to those with several nm pores e.g. NU-1000 (3.1 nm pore).[161] In theory, pore expansion could be achieved by isoreticular synthesis using larger ligands e.g. NU-1007 (6.7 nm pore). However, the synthesis of the required ligands becomes both tedious and difficult limiting the practicality of this approach.[162, 163]

3.1.1.2. *In Situ* Synthesis

In situ synthesis refer to methods where the protein is encapsulated within the MOF as part of the MOF synthesis procedure. In these approaches, the MOF forms around the protein creating a large cavity or defect where the protein resides. The earliest *in situ* procedure, coprecipitation, involves adding a capping agent to the protein before introducing the MOF precursors.[164, 165] This was pioneered by Lyu and colleagues in 2014, to encapsulate polyvinyl propylene (PVP) capped cytochrome C within ZIF-8 via room temperature synthesis in methanol.[164] An alternative approach, known as biomineralization, was later developed by the Doonan group in 2015.[149] In this approach, the protein surface acts as a nucleation site to sequester charged precursor ions to induce MOF nucleation.[166] Whereas Lyu and colleagues used PVP to stabilize the protein from denaturation within methanol, Doonan's group

conducted the synthesis in an aqueous environment where the addition of the coprecipitating agent was unnecessary. [149, 164, 165]

Like post synthetic loading, only a limited range of MOFs can be used for *in situ* synthesis. This is because the MOF must be synthesized in ambient conditions where the protein will not denature. As such, ZIFs have been commonly used for this approach; particularly ZIF-8.[146] Other MOFs such as HKUST-1[155, 167] and UiO-66-NH_2[124] have also been used to some extent. However, this approach provides significantly more diversity in the range of biological materials that can be encapsulated as there is no limitation on their size. This was dramatically highlighted by Doonan's group who coated an entire yeast cell (~4 μm) with ZIF-8 (1.16 nm pores).[168] Due to the flexibility and relative ease of *in situ* methods, their use has expanded to other biological materials such as RNA complexes[169] and viruses.[170]

One of the defining advantages of *in situ* encapsulation is the improvement of protein@MOF stability. Because the encapsulated material is often larger than the pores of the surrounding MOF, the biological material is entrapped and prevented from leaching out of the MOF.[146, 149, 171] However, this is not always the case. Gascon and colleagues observed between ~5 and 10% protein leaching within a 30-hour period for *in situ* synthesized β-glucosidase@NH_2-MIL-53. However, this composite is unusual in the *in situ* literature because it could be produced using both *in situ* and post synthetic means.[150] Therefore, β-glucosidase is small enough to enter and exit the MOF pores. Hence, β-glucosidase is not confined within NH_2-MIL-53 in the same manner that is typical for *in situ* protein@MOF complexes. Despite this, the 5 to 10% observed leaching of *in situ* synthesized β-glucosidase@NH_2-MIL-53 is still reasonably low. The comparative post synthetic complex displayed ~20% protein leaching over the same time period.[150] Why this is the case is not entirely known.[150]

Furthermore, since the MOF is grown around the protein, the formed cavity size is comparable to the encapsulated protein. Thus, the protein's mobility and denaturation is highly restricted. For this reason *in situ* complexes often have high stability to denaturing conditions. For instance, HRP@ZIF-8 could retain 88% of its activity despite boiling in DMF at 153°C.[149]

3.1.1.2.1. Crystal Growth and Design

The major drawback of *in situ* synthesis is the lack of synthetic control. The target when synthesizing protein@MOF complexes is often to maximise their catalytic activity. This is predominantly a product of the LE and the retained protein catalytic activity upon encapsulation. Unfortunately, these properties are very sensitive to the reaction environment e.g. concentration of precursors,[69, 172] or presence of salts.[173] Substituting the MOF or protein

can lead to dramatic variations. For instance, MAF-7 encapsulates catalase with an LE of 0.9%, whereas the LE of catalase@ZIF-8 is 3.3%.[174] Furthermore, when encapsulated in FeBTC, alcohol dehydrogenase retains just 3.7% of its activity. GOx@FeBTC synthesized using approximately the same amount of protein had an activity of ~240% of its native state.[172] However, the effectiveness of these materials is not solely a contribution of their reaction environment or MOF protein selection. The spacial arrangement of proteins within the MOF can dramatically influence their overall properties.[155, 175] An example of this was by Hu and colleagues. They synthesized GOx@ZIF-8 and HRP@ZIF-8 under a microfluidic flow. The activity was enhanced drastically when the protein was added after pre-synthesis of ZIF-8 seed crystals. This was attributed to the formation of a protein@ZIF-8 layer close to the outer surface of the MOF allowing for faster diffusion of reactants to the enzymatic active sites.[175] Furthermore, the MOF shape and pore structure can impact the materials overall activity. For instance, Cui and colleagues synthesized catalase@ZIF-8 with a crucifix-like morphology. This material had a higher loading efficiency (LE) and activity when compared to a rhombic dodecahedral (RD) equivalent.[176] Recently, Wu and colleagues managed to synthesize a GOx@ZIF-8 complex that was amorphized. The complex retained a LE of ~10%, similar to standard RD GOx@ZIF-8. However, this complex had a 20-fold improvement on the activity when compared to RD GOx@ZIF-8.[177]

Unfortunately, morphological control of MOFs is difficult. Furthermore, the addition of protein during synthesis further complicates this challenge. In the Doonan group's initial biomineralization study using ZIF-8, they observed a range of different morphologies when they encapsulated different proteins. These include: RD, truncated rhombic dodecahedron (TRD), nanoleaf, nanoflower, and cubic crystals. Furthermore, these samples ranged from 400 nm to several μm in size. This led to the conclusion that the protein structure plays a substantial role in the sequestration of MOF precursors and the overall MOF morphology.[149] To further investigate this effect, they encapsulated the 20 natural amino acids. They found that the crystal size and shape varied substantially depending on the charge of the amino acid. ZIF-8 was not formed at all when lysine, arginine, or histidine were added. This was attributed to the basic side groups of these amino acids being unable to sequester zinc(II) ions.[166] This is in strong agreement with their 2018 study on the impact of the protein isoelectric points (pI) on the formation of protein@MOF complexes. They found that proteins with lower pI values were more likely to be successfully encapsulated within ZIF-8. Furthermore, by applying a negative surface charge to a protein, biomineralization could be induced. For instance, haemoglobin (pI = 7.0 – 8.1) does not induce ZIF-8 biomineralization. However, haemoglobin succinylation

allowed a heamoglobin@ZIF-8 complex to form.[178] However, given potential risks of denaturing delicate products by surface modification, which were not investigated, it is unlikely this strategy is generally feasible or facile.

Whilst the protein selection impacts the MOF morphology this is not the only influence. In fact, in 2017, Cui and colleagues found they could not identify a correlation between protein structure and MOF morphology during ZIF-8 synthesis. They synthesized ZIF-8 with a high HmIM concentration (0.7 – 1.0 M). This resulted in the formation of a crucifix morphology. This same morphology was achieved when synthesized with no protein, lipase, HRP, trypsin and GOx. They concluded this result was in contradiction with the conclusions drawn by the Doonan group.[176] However, a further study by the Doonan group concluded that the growth trends of ZIF-8 remain the same regardless of protein selection. However, different proteins tended to form different morphologies and topologies using lower Zn/HmIM concentrations.[179] Therefore, it could be the differing effect of proteins in these studies is not contradictory. Rather, it may just be the impact of investigating the biomineralization effect while using substantially different Zn/HmIM concentrations. Nevertheless, significant work is still required before rational morphology control of protein@ZIF-8 samples can be achieved.

3.1.1.2.2. Protein@MOF Nanoparticles

The formation of protein@MOF NPs is particularly valued for two predominant reasons. Firstly, these complexes are often used for drug delivery.[44, 180, 181] For instance, Duan and colleague synthesized ZIF-8 encapsulating insulin and GOx (insulin/GOx@ZIF-8). This material has significant promise for reducing the risk of insulin overdose in diabetic patients. During standard treatment, the patient's blood glucose must be continuously monitored, and insulin must be injected during spikes. However, with insulin/GOx@ZIF-8, the GOx catalyses the production of hydrogen peroxide in the presence of glucose. This causes the degradation of ZIF-8 and the release of insulin. Therefore, insulin is only released during a glucose spike.[180] Unfortunately, as discussed before (1.1.4.2 Drug Delivery), the distribution of MOFs i*n vivo* during drug delivery is highly dependent on their morphology.

The second advantage of producing protein@MOF NPs is that by reducing the NP dimensions the time taken for substrates to diffuse through the MOF to enzymatic active sites decreases. Generally this increases the activity of the overall complex.[69, 159] This has been known to increase the activity of these complexes. There are two notable existing strategies to tune the size of protein@ZIF-8 complexes *in situ*. Both strategies synthesized bovine serum albumin (BSA)@ZIF-8. In the first case, Chen and colleagues increased the ligand to metal

ratio to 70:1. They managed to synthesize BSA@ZIF-8 NPs ranging in size from 60 to 138 nm depending on the BSA concentration.[44] In the latter case, the Doonan group synthesized BSA@ZIF-8 ranging from 40 to 100 nm by varying the flow rate in a specialized continuous flow apparatus.[182] Unfortunately, whilst BSA is a cheap protein useful for modelling protein@MOF behaviour it does not possess enzymatic activity. Therefore, the impact of MOF size on activity could not be determined in either study.

3.1.1.3. Microemulsion Synthesis

Microemulsions can be highly biocompatible environments for synthesis since they prevent protein aggregation and improve their stability. In fact, microemulsions have already seen usage for the delivery of proteins.[183, 184] Thus, suggesting proteins can be retained in microemulsions without denaturation. This was highlighted by Perinelli and colleagues. They demonstrated that BSA could maintain its native-state without denaturing in a Tween-80 w/o microemulsion for 6 months.[185] Given their biocompatibility and usage for size-controlled MOF synthesis, microemulsions appears to be an ideal candidate environment for protein@MOF synthesis. However, microemulsion synthesis has only been used for protein@MOF synthesis on one occasion. This was by Chulkaivalsucharit and colleagues in 2018.[69] They encapsulated HRP in ZIF-8 using a BRIJ-C10 w/o microemulsion. Three different samples were produced using zinc nitrate concentrations of 0.25, 0.5 and 1.0 M and a M:mIM ratio of 1:4. The resulting samples had a uniform spherical morphology with a 30 nm radius and an activity enhancement when compared to the free enzyme in solution.[69] Whilst this work is promising, much of the potential benefits of this technique have yet to be explored. This includes the potential to tune the composite size, control its morphology and encapsulate different proteins.

3.1.2. Research Outline

In this chapter, the applicability of microemulsion synthesis was explored using the techniques developed in Chapter 2 - Zeolitic Imidazole Framework Synthesis in Microemulsions. Specifically, the focus was placed on ZIF-8d-30 and various proteins added to the aqueous phase of μEL before synthesis. The main objectives of this study were to:

1. Evaluate whether microemulsion synthesis could be used to encapsulate proteins in ZIF-8.
2. Evaluate whether the inclusion of proteins impacts the MOF morphology.
3. Evaluate whether the morphology of these protein@ZIF-8 complexes is tuneable.

To achieve these goals BSA and bovine haemoglobin (BHG)(Figure 3.3) were encapsulated in ZIF-8. For characterization, we used a combination of a UV-Vis Bradford assay and Fourier transform infrared (FTIR) spectroscopy in addition to the standard protocols outlined in Chapter 2 - Zeolitic Imidazole Framework Synthesis in Microemulsions. BSA was selected for encapsulation because it is a common, cheap and readily available protein that has previously been used as a model protein for testing encapsulation methods. BHG was used to test microemulsion synthesis of protein@ZIF-8 because its high pI (~8.2) makes it difficult to encapsulate *in situ*. Additional information on the structure of these proteins can be found in the supporting information (Table C.1)

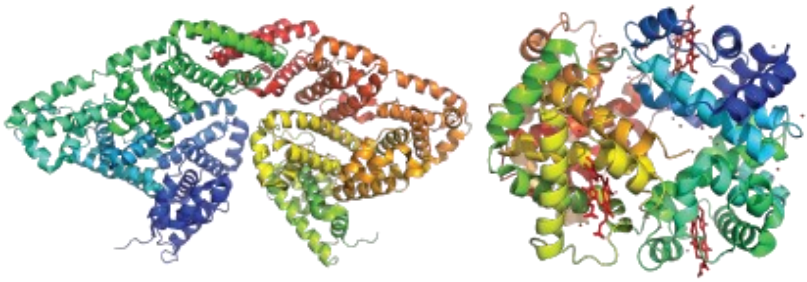

Figure 3.3 BSA (left) and BHG (right)

3.2. Results & Discussion

3.2.1. Protein Quantity

BSA@ZIF-8 was synthesized using the standardized protocol from Chapter 2 - Zeolitic Imidazole Framework Synthesis in Microemulsions (ZIF-8d-30) where 2.5 mg, 5 mg and 10 mg of BSA was added per mL of μEL aqueous phase during synthesis (denoted BSA@ZIF-8-BSA quantity e.g. BSA@ZIF-8-10). These samples were then treated with sodium dodecyl sulphate (SDS), a denaturing surfactant used to remove proteins from a composite's surface.[44, 165]

The synthesis of ZIF-8 was confirmed using PXRD and FTIR (Figure 3.3A&B). The sample PXRD patterns were consistent with **sod** ZIF-8, indicating that protein addition did not alter the MOF morphology. Furthermore, all samples possessed peaks corresponding to C=N stretching modes (1580 cm^{-1}), and out of plane (757 cm^{-1}) and in plane (995 and 1309 cm^{-1}) bending of an imidazolate ring. This is consistent with ZIF-8 or its mIM ligand. In addition to this, BSA possesses two peaks at ~1540 and ~1660 cm^{-1} from the amide I and II bands.[186] The amide I and II bands result from the combination of multiple vibrations of the amide bonds of a protein's backbone. For amide I, this is predominantly C=O and C-N stretching vibrations with minor contributions from N-H out of plane bending. For amide II, this results predominantly from in-plane N-H bending and C-O stretching with minor contributions from C-O, N-C and C-C stretching vibrations. The amide II band is clearly present in all BSA@ZIF-8 samples indicating the successful inclusion of BSA.[187] Because the samples were SDS treated these peaks are due to encapsulated BSA rather than BSA coating the surface of the ZIF-8 crystals. This was confirmed by independently surface coating ZIF-8 crystals with BSA and performing the same treatment on the surface coated BSA#ZIF-8 crystals. Before SDS treatment was performed BSA#ZIF-8 crystals possessed both amide I and II peaks which were removed post treatment (Figure B.7).

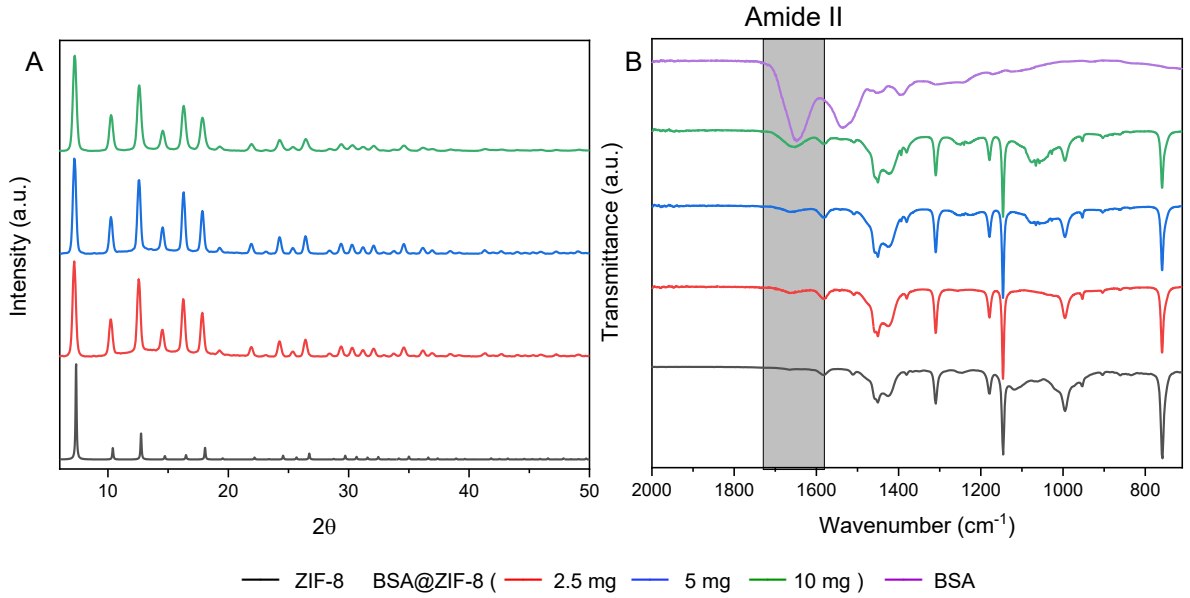

Figure 3.4 (A) PXRD and (B) FTIR BSA@ZIF-8 synthesized with different quantities of BSA.

To determine the protein LE (A.4.2 Loading Efficiency), a Bradford assay was used. In this assay, Bradford reagent was added to the digested protein@MOF composite. Bradford reagent contains Coomassie Blue G-250 which binds to the amino and aromatic groups of proteins in acidic conditions (pH > 5). This causes a shift in the dye's UV-vis absorption peak from 465 to 595 nm.[188] Measuring the absorptivity allows the amount encapsulated protein to be quantified by comparison to a standard curve (Figure B.8). The LE was 0.91, 4.77, and 17.1% for the 2.5, 5 and 10 mg samples, respectively. This result arrives at the unremarkable conclusion that if more protein is introduced more protein is encapsulated. Interestingly, in the scope of *in situ* literature, these values are unremarkable since protein@MOF complexes have been formed with LE values as high as 21.2%.[69] However, this is atypical and multiple studies consider LE values less than 10% as acceptable.[150, 151, 164, 172] In one such study by Gascon and colleagues, LE values ranged from 10.0% at maximum for alcohol dehydrogenase@FeBTC to 0.1% for GOx@ZIF-8.[172] In the context of BSA@ZIF-8, the LE value of 17.1% is remarkably high. Typical BSA@ZIF-8 LE is ~5%.[44, 182] The encapsulation efficiency* (A.4.3. Encapsulation Efficiency) of the 2.5, 5 and 10 mg samples were 4.3%, 7.26%, and 18.1%. In all three cases the encapsulation efficiency is relatively low. However, it should be noted that these calculations were based on the final yield of product after SDS washing which was 19.0, 13.7, and 21.3 mg respectively. It should be noted substantially higher yields are observed before this procedure. For instance, the synthesis of pure ZIF-8 using the microemulsion

* The mass protein encapsulated as a percentage of protein added during synthesis

method, from which these synthesizes are derived (ZIF-8d-30), yields 43 mg of product. Synthesis of the 10 mg BSA@ZIF-8 sample yields 55 mg before SDS washing. As the mass loss during SDS washing is greater than the amount of protein added during synthesis it is reasonable to conclude a substantial portion of the crystals were also resuspended in the solution and not recollected during this step. It is worth noting, that when SDS washing is employed in the literature the idea this may cause resuspension of the crystals is generally not considered, though the crystals this technique have been applied to are far larger and less likely to get resuspended.[149] Accounting for this procedural fault, the encapsulation efficiency could be as high as 52.3%. This is not high but is with in a reasonable nominal range. [150, 151, 164, 172] It is worth noting that the encapsulation efficiency appeared to have increased as the amount of protein added increased. It is not obvious why this would be the case.

The morphology of BSA@ZIF-8 samples was assessed using TEM (Figure 3.4). In all cases, distinct RD crystals were observed. Surprisingly, no correlation was observed between the NP size and the amount of protein added. The 0 mg sample (ZIF-8d-30) possessed an average NP size of 74.5 ± 17.9 nm (N = 108). This decreased to 58.0 ± 15.7 nm (N = 132) for the 2.5 mg sample. The RSD was consistently with all samples between 21.6 and 27.1%. For the 5 mg sample, the average NP size was 82.3 ± 21.7 nm (N = 113). For the 10 mg sample, the average NP size was 69.7 ± 15.1 nm (N = 103). It should be noted that unlike other chapters all sample PSDs in this chapter could be modelled with a standard Gaussian distribution (Table B.4). Surprisingly, this is consistent with the results from chapters 2 & 4, where all samples possessed a Gaussian distribution except for the smallest samples studied. The purpose of this chapter was not to develop a synthetic protocol for the smallest protein@ZIF-8 NPs. Rather, the objective was to investigate whether the size and shape trends observed in Chapter 2 - Zeolitic Imidazole Frameworks hold true when protein is added during synthesis. The modified conditions which produced the smallest ZIF-8 sample (an addition time of 0 min, ZIF-8b-0) was not tested on protein@ZIF-8 samples in this thesis. This could be tested in future work.

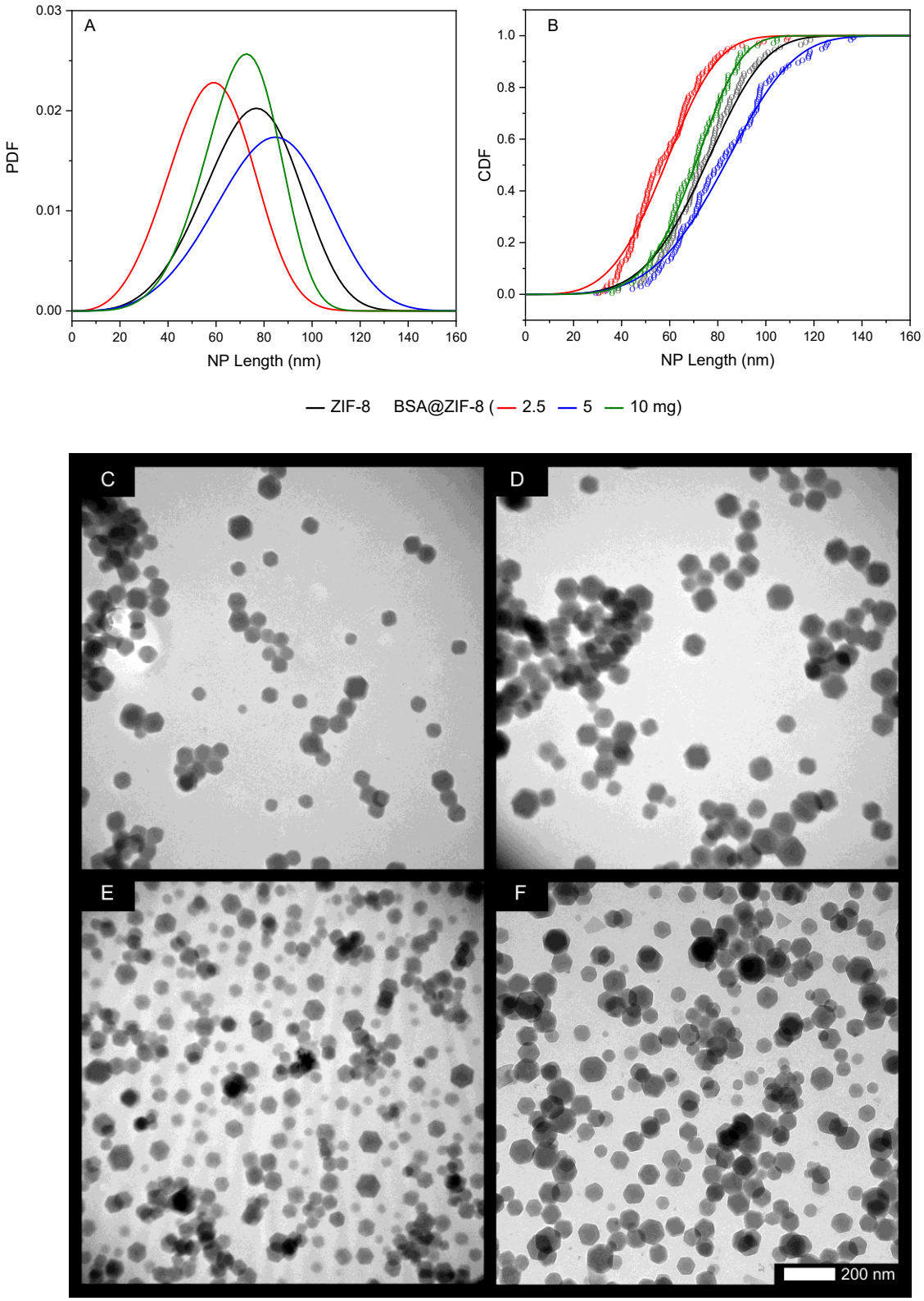

Figure 3.5 Weibull modelled PSD displaying the (A) PDF and (B) CDF of ZIF-8 synthesized with variable BSA quantities. Individual data points show the ECDF. TEM images of BSA@ZIF-8 synthesized with (C) 0, (D) 2.5, (E) 5, and (F) 10 mg BSA. The scale bar is 200 nm.

3.2.2. Addition Rate

From previous research, it was found that altering the addition rate alters the size of ZIF-8 crystals (2.2.3 Addition Rate). Therefore, the question of whether addition rate could be used to tune particle morphology was investigated with BSA@ZIF-8. Hence, BSA@ZIF-8 was synthesized using three different addition times (15, 30 and 120 min) (samples BSA@ZIF-8b-time). Sample BSA@ZIF-8c was used as the 30 min sample. PXRD and FTIR of all three samples was consistent with the formation of **sod** ZIF-8 encapsulating BSA (Figure 3.6).

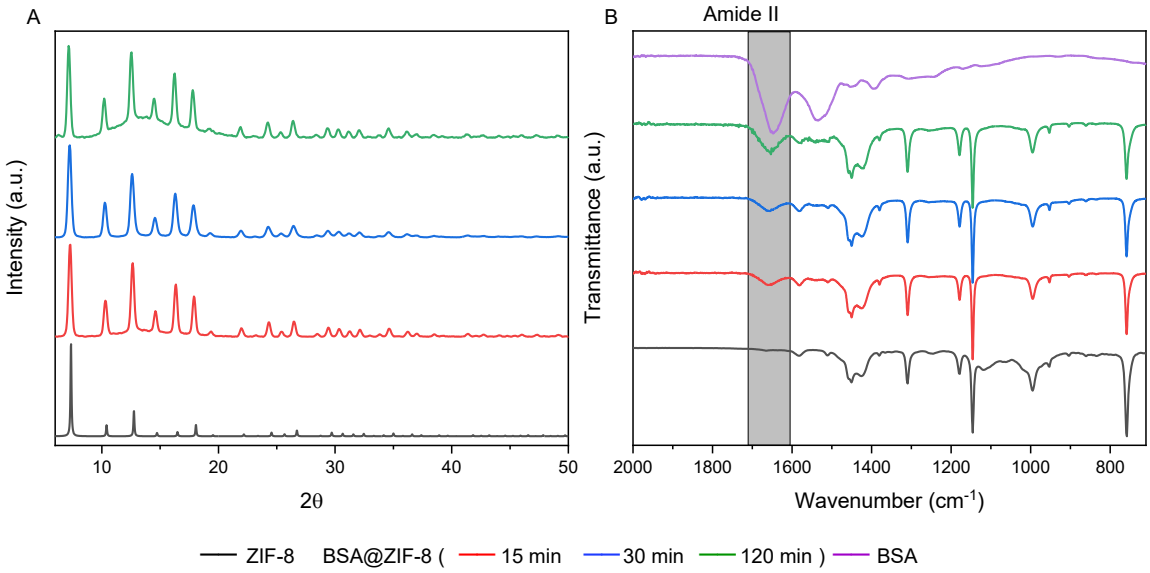

Figure 3.6 (A) PXRD and (B) FTIR of BSA@ZIF-8 synthesized with variable addition times.

The Bradford assay determined LE for each sample was relatively consistent regardless of addition time. At 15 minutes, the LE was 12.5%. This increased to 17.1 and 17.7% for the 30 min and 120 min addition times. Interestingly, this suggests that slow addition leads to sequestration of more protein. The encapsulation efficiency of the 15, 30, and 120 min samples were 10.8%, 18.1% and 13.9%. Though it should be noted this is subject to the same experimental error observed in 3.2.1. Protein Quantity.

The sample morphology of all BSA@ZIF-8 samples was generally RD (Figure 3.4C-E). The 120 min BSA@ZIF-8 appears to also possess some cubic crystals. In comparison, pure ZIF-8 had RD morphology for only the 120 and 30 min samples and the 15 min ZIF-8 sample had a psuedospherical morphology (Figure 3.6F-H). As the addition time increased, the BSA@ZIF-8 composite size increased. For the 15 min samples, the NP size increased from

52.7 ± 14.4 nm (N = 102) to 69.7 ± 15.1 nm (N = 103). For the 30 min samples, little difference was observed in either the average particle size or SD. Pure ZIF-8 was 74.6 ± 18.0 nm (N = 107) whereas BSA@ZIF-8 was 72.2 ± 17.0 nm (N = 119). For the 120 min samples, ZIF-8 was 87.3 ± 22.4 nm (N = 131) and BSA@ZIF-8 was 87.6 ± 24.5 nm (N = 108). Notably the trend in BSA@ZIF-8 NP size is the same as that of pure ZIF-8 suggesting the addition rate can be utilized to tune the NP size of BSA@ZIF-8.

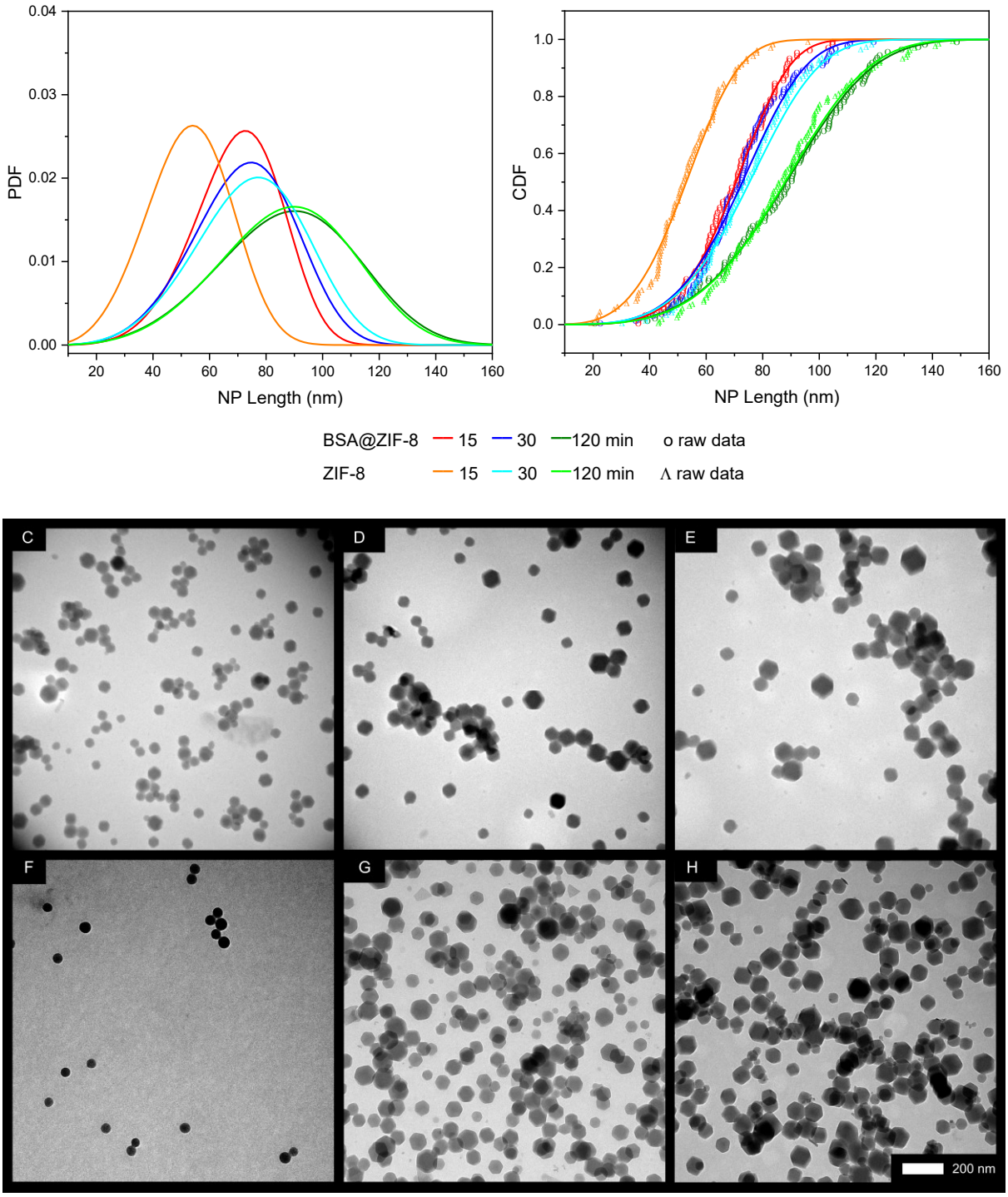

Figure 3.7 Weibull modelled PSD displaying the (A) PDF and (B) CDF of BSA@ZIF-8 samples synthesized with a variable addition time. Individual data points show the ECDF. TEM images of BSA@ZIF-8 synthesized with a (C) 15, (D) 30, and (E) 120 minute addition time. TEM images of ZIF-8 with a (F) 15, (G) 30, and (H) 120minute addition time. The scale bar is 200 nm.

3.2.3. Bovine Haemoglobin

In this section, the encapsulation of bovine haemoglobin (BHG) was attempted. BHG encapsulation was attempted for two reasons. The first was that different proteins can behave differently when encapsulated. Hence, BHG was used as a model protein to investigate how the addition rate influences the morphology of a complex other than BSA@ZIF-8. Secondly, haemoglobin@ZIF-8 is notoriously difficult to produce. This is attributed to it possessing a net positive surface charge. Hence, it struggles to sufficiently sequester Zn^{2+} ions for biomineralization.[178] Only two studies have synthesized it: both by the Doonan group.[149, 178] In the first study, BHG@ZIF-8 was synthesized using a standard biomimetic mineralization protocol.[149] However, through correspondence with Natasha Maddigan (a current Doonan group member), it was found that replication issues occurred during this synthesis and very few crystals were obtained with poor crystallinity. This suggests the present ZIF-8 crystals grew around some form of contaminant or trace quantities of haemoglobin in the original study. In the later study, haemoglobin@ZIF-8 was synthesized. However, surface modification of haemoglobin was required to achieve this result.[178]

In the previous sections (3.2.1 Protein Quantity & 3.2.2Addition Rate), BSA@ZIF-8 was synthesized with a high LE of ~17%. This was attributed to the localized confinement of BSA and the ZIF-8 precursors within the microemulsion. If that is the case, an aqueously soluble protein with a low binding affinity for ZIF-8 precursors could be encapsulated by confinement within the same micelle as the growing crystal. Hence, BHG encapsulated within ZIF-8 was attempted using three different addition times (15, 30, and 120 min) during synthesis. These were denoted BHG@ZIF-8-addtime e.g. BHG@ZIF-8-15.

PXRD patterns and FTIR spectra of all samples was consistent with **sod** ZIF-8. Furthermore, the amide II band is present in all samples even following SDS washing (Figure 3.7A& B). Pure ZIF-8 was surface coated with BHG. No amide II peaks were present in the surface coated sample after SDS washing (Figure B.7). Therefore, the presence of the amide II band in BHG@ZIF-8 samples indicates the successful encapsulation of BHG in all samples.

From the TEM images all BHG@ZIF-8 samples were determined to have a RD morphology (Figure 3.7C-G &). This is consistent with the behaviour of BSA@ZIF-8 using the same addition times. Interestingly, the TEM images show an increased tendency for BHG@ZIF-8 crystals to aggregate as the addition time decreased. This is understandable since smaller crystals tend to aggregate due to having a large outer surface area to volume ratio. At 15 min, BHG@ZIF-8 was produced with an average size of 55.9 ± 22.4 nm (N = 105). This is

larger than the equivalent ZIF-8 sample but smaller than the equivalent BSA@ZIF-8 sample. For the 30 min and 120 min samples, BHG@ZIF-8 syntheses consistently produced smaller crystals than their ZIF-8 and BSA@ZIF-8 counterparts (Table B.5). At 30 min, the BHG@ZIF-8 size was 62.6 ± 21.7 nm (N = 107). At 120 min, the size was 75.3 ± 29.9 nm (N = 103). The BHG@ZIF-8 size follows the general trends observed with ZIF-8 and BSA@ZIF-8. As the addition time increases the NP size increases. Therefore, it is likely that addition time control can be used generically to tune the size of protein@ZIF-8 complexes within this microemulsion system. However, it should be noted, that adding BHG during synthesis substantially increased the dispersity of the resulting crystals. The BHG@ZIF-8 RSD ranged from 34.7 to 40.0. In Chapter 1 - Introduction, samples were considered to have a reasonably low dispersity if the RSD was below 45%. These samples fulfil this requirement. However, these samples possess the three largest RSD values of any sample in this thesis, except ZIF-8a-1x (RSD = 45.5%) (Chapter 2 - Zeolitic Imidazole Framework Synthesis in Microemulsions). ZIF-8a-1x was specifically noted for having a broad PSD because it was an early stage unsuccessful ZIF-8 synthesis attempt.

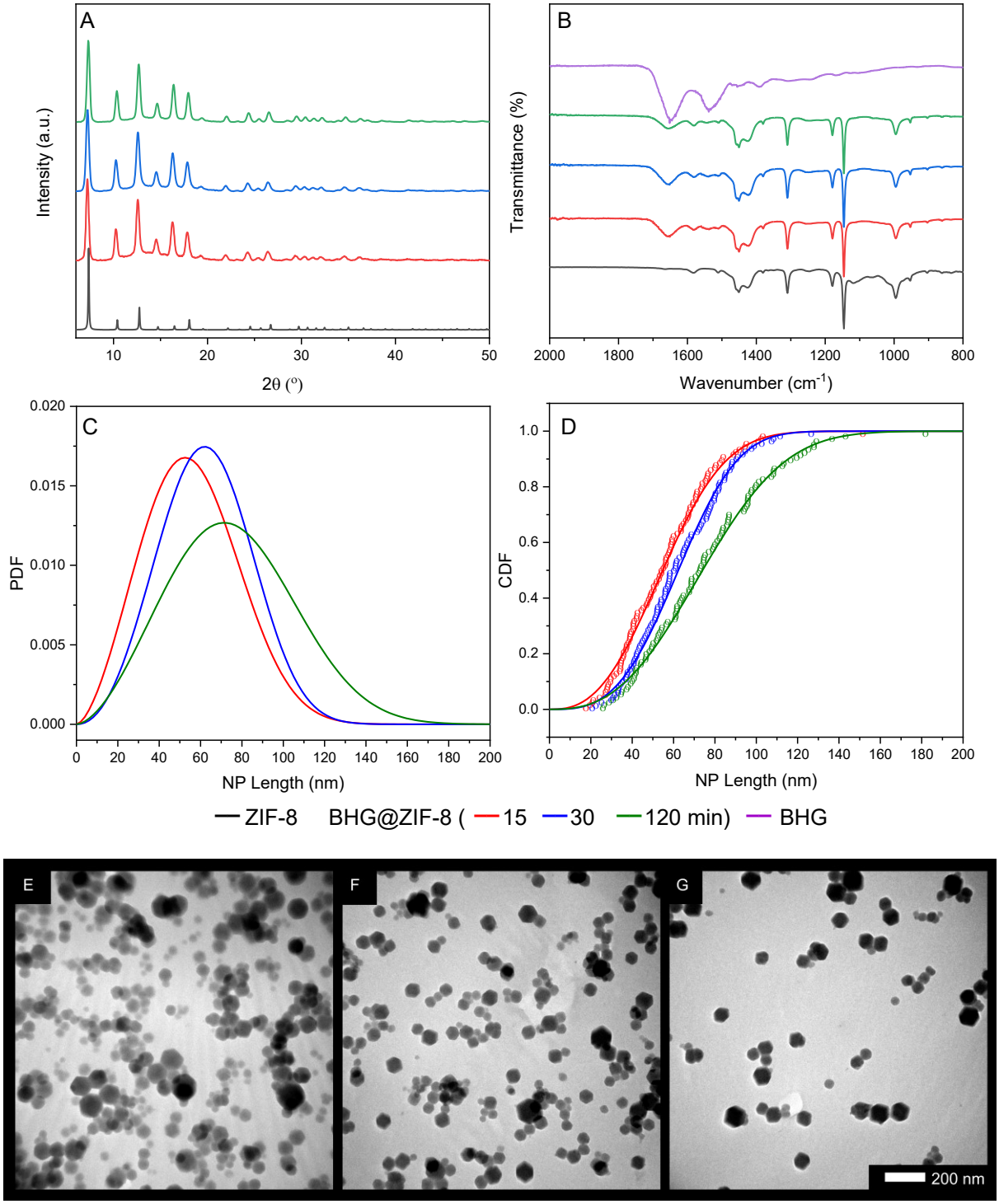

Figure 3.8 (A) PXRD and (B) FTIR of BHG@ZIF-8 samples. (C) Weibull modelled PDF of sample PSD. (D) Weibull CDF of BHG@ZIF-8 PSD. Open dots represent the ECDF. TEM images of (E) BHG@ZIF-8-15, (F) BHG@ZIF-8-30, and (G) BHG@ZIF-8-120.

3.3. Future Work

Obtaining the LE of BHG@ZIF-8 complexes is an important area of future work required to complete this study. However, due to time constraints this was not finished. Another useful area of future work is investigating the activity of protein@ZIF-8 complexes. The two proteins investigated thus far (BHG and BSA) have no enzymatic activity. The role of this study was to investigate the morphological properties of the protein@MOF complexes formed. However, this does not consider the conformational changes a protein may undergo during encapsulation. A complex with a high LE would be functionally useless if the protein was denatured during the encapsulation process. To investigate the enzymatic activity of these complexes an enzyme should be encapsulated (e.g. HRP, or GOx) and characterized.

3.4.Conclusion

In this chapter, it was demonstrated that microemulsion synthesis could be utilized to synthesize BSA@ZIF-8 NPs. The resulting materials had high LE values up to ~17%. Furthermore, the particle size could be finely tuned from 69.7 ± 15.1 to 87.6 ± 24.5 nm by adjusting the addition time. All samples had a relatively consistent RSD between 21.6 and 27.9%. Microemulsion synthesis was then applied to synthesize BHG@ZIF-8 crystals. BHG was successfully encapsulated despite its significant difficult in the literature. This marks the first facile and reproducible approach to synthesize this protein@MOF complex. Furthermore, like BSA@ZIF-8 and ZIF-8 the NP size could be tuned by modifying the addition time. Thus, marking this approach as a potentially generic method to produce tuneable sized protein@ZIF-8 NPs. Further work should be done to obtain the LE of BHG@ZIF-8 and to encapsulate an active enzyme e.g. β-glucosidase or HRP.

3.5. Experimental Methods

3.5.1. Materials

As per section 2.4.1. Materials, all chemicals and reagents were sourced from commercial suppliers at a purity of 99.8% or greater and used without further purification. Protein samples were acquired as lyophilized powders.

3.5.2. Synthesis Procedure

Protein@MOF complexes were synthesized using the method outline in 2.4.2 Microemulsion ZIF-8 for sample ZIF-8d-30 with minor variation. The aqueous phase of μEL was prepared with a variable concentration of either BSA or BHG. The addition time where

μEL was added to μEM was also varied. The composition and addition time for individual samples is provided in Table 3.1.

Table 3.1 Microemulsion Synthesis of Protein@ZIF-8 samples

Sample	Protein		Addition Time (min)
	Type	Quantity (mg mL^{-1})*	
BSA@ZIF-8a-2.5	BSA	2.5	30
BSA@ZIF-8a-5	BSA	5	30
BSA@ZIF-8c	BSA	10	30
BSA@ZIF-8b-15	BSA	10	15
BSA@ZIF-8b-30	BSA	10	120
BHG@ZIF-8-15	BHG	10	15
BHG@ZIF-8-30	BHG	10	30
BHG@ZIF-8-120	BHG	10	120

3.5.3. Surface Protein Wash

To wash the protein off the outer surface of the MOF, samples were dispersed in aqueous SDS (0.1 mL per 1 mg sample, 2 mM SDS). The samples were then heated to 70 °C for 10 min before centrifugation (5000 rpm, 10 min) and washing with water (3 x 0.1 mL per 1 mg)[44]. Samples were sonicated for ~5-10 s to resuspend them during SDS and water washing cycles. The samples were then lyophilized.

3.5.4. Characterization Methods.

Protein@MOF samples were characterized by the methodology below in addition to the characterization methods performed on ZIF-8 in 2.4 Experimental Methods.

3.5.4.1. Bradford Assay

Bradford reagent was prepared by dissolving Coomassie Blue G-250 in 95% ethanol (50 mL, 2.34 mM). Phosphoric acid was then added (100 mL, 85% w/v). The mixture was then diluted to one litre in water, before filtering through Whatman paper to remove the precipitate. The solution was then stored at 4 °C until further use. Bradford reagent was warmed to room temperature before use.

* This is the amount of protein per mL of aqueous 2-methylimidazole.

For Coomassie Blue G-250 to bind BSA, ZIF-8 must be degraded to release BSA. This was achieved by dissolving the ZIF-8 sample (1 mg) in aqueous HCL (0.1 M, 1 mL). Sample standards were prepared by digesting pure ZIF-8 in HCL as per previous digestion instructions. BSA was added to the digestion mixture at various concentrations (0 – 10 μg mL^{-1}, 1 μg mL^{-1} increments).

Bradford reagent (3 mL) was added to digested protein@ZIF-8 samples (0.1 mL). Sample absorption was measured at 595 nm using a Shimadzu UV-1800 spectrophotometer running UVProbe version 2.62 software. The protein concentration was calculated by comparison to a linear fitted standard curve. The LE was calculated as specified in the appendix (A.4.2 Loading Efficiency).

3.5.4.2. FTIR

IR data was collected using a Thermo Scientific Nicolet iS5 infrared spectrometer with an iD7 diamond crystal ATR attachment. Transmittance FTIR spectra were collected using OMNIC 9.9.535 for 32 scan across the wavenumber range 750 – 2000 cm^{-1}

Chapter 4 - Microemulsion Synthesis of UiO-66

4.1. Introduction

Synthesized in 2008 by the Lillerud group,[189] UiO-66 (Universitetet i Oslo*) is widely considered the archetype of the zirconium carboxylate MOFs; a MOF subclass regarded highly for their high stability and crystal defects (4.1.1 Crystal Defects). This has allowed them to become one of the most studied MOF subcategories in the literature.[190] UiO-66 consists of $Zr_6O_4(OH)_4^{12+}$ octahedral clusters bound to 12 BDC ligands with an overall formula of $Zr_6O_4(OH)_4(BDC)_6$. This is arranged as a face centred cubic **fcu** net with $Fm\bar{3}m$ symmetry (Figure 4.1). The high connectivity of this structure results in UiO-66 being one of the most stable MOFs in the literature. It can withstand temperatures up to 500 °C and significant mechanical stress.[190] Furthermore, it can retain its structure in a wide range of solvents including water, DMF, and benzene.[189]

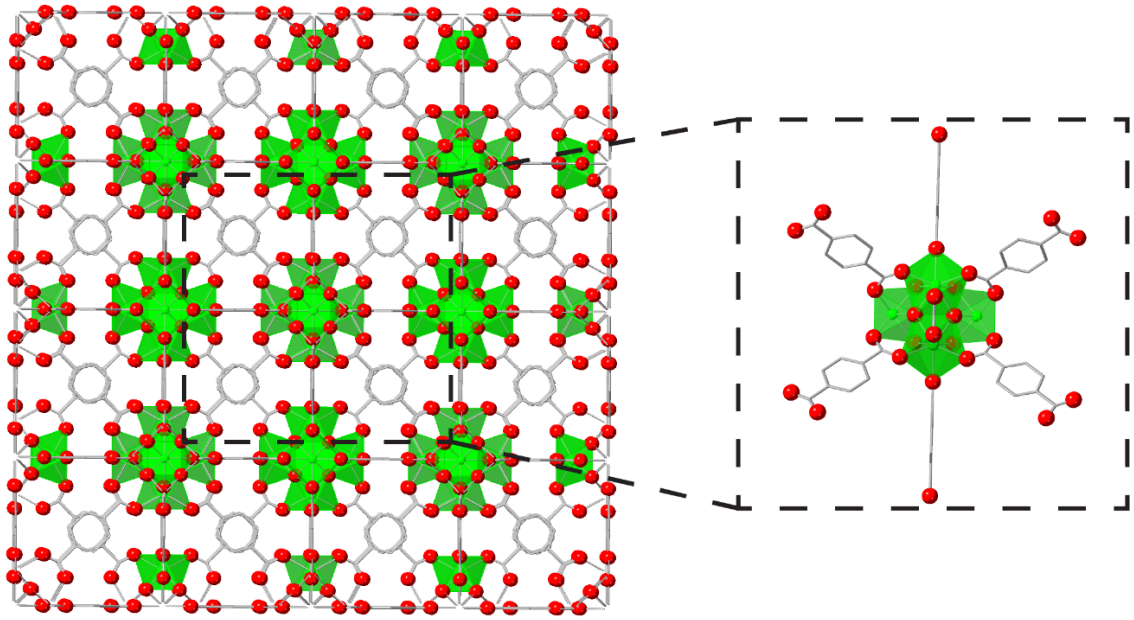

Figure 4.1 Cubic arrangement of UiO-66 with $[Zr_6O_4(OH)_4(BDC)_{12}]$ clusters.

* Norwegian: University of Oslo

4.1.1. Synthesis Methods

Originally, UiO-66 was synthesized by mixing $ZrCl_4$ with H_2BDC in DMF and heating at 120 °C in the oven for 24 hours. This resulted in low quality crystalline aggregates.[189] The issue of synthesizing reproducible high-quality crystals was solved by Behrens' group in 2011. They added carboxylate modulator (benzoic/acetic acid) to compete with BDC for binding sites. This approach slowed growth time allowing for the synthesis of larger more well-defined crystal. Furthermore, UiO-66 crystals were size tuneable from 122 to 458 nm by simply increasing the modulator ligand equivalents from 0 to 30.[191] Modulated solvothermal synthesis has become the standard protocol for UiO-66, though different research groups tend to use their own inhouse variants. However, this method is not without issues. The introduction of modulators introduces crystal defects into the material, leading to expansive research into methods to control their defectivity (4.1.1 Crystal Defects). The use of organic solvents like DMF is both environmentally hazardous and costly.[192, 193] High temperature syntheses limit the incorporation of thermally sensitive materials into the MOF.[14, 193] The long growth period ranging from 1 to 4 days is non-ideal. These factors along with the pursuit of precise size-controlled synthesis of nanoscale MOFs (4.1.3 Morphology) has driven further development into new UiO-66 synthesis methods including MW/US,[194-196] electrochemical[197] and mechanosynthesis.[198, 199] A full review of all UiO-66 synthetic methods would be well beyond the scope of this thesis.

Significant advances have been made towards environmentally friendly UiO-66 synthesis through the development of mechanosynthesis and ambient temperature hydrothermal synthesis. Mechanosynthesis involves the introduction of the metal and ligand by grinding mechanisms such as ball milling or liquid assisted grinding. However, such methods are often complex and result in poor quality crystals in low yields. An alternative approach has been to develop methods to synthesize UiO-66 in aqueous or ambient conditions. However, this has been an ongoing challenge for several reasons. Firstly, H_2BDC is insoluble in aqueous conditions. Secondly, the presence of water can induce defects in the final crystal (4.1.2 Crystal Defects). Finally, room temperature syntheses often result in materials with low porosity and pore crystallinity. A breakthrough in this regard was achieved by Farha's group in 2016, when they successfully synthesized UiO-66 at room temperature in DMF from the pre-synthesized metal clusters. They pre-synthesized the $Zr(O)_4(OH)_4(CH_3COO)_{12}$ cluster by reacting the zirconium salt with acetic acid (1:443 equivalents) at temperatures between 40 and 120 °C before substituting the acetic acid with BDC at room temperature.[14] Another major milestone

was achieved by Zhao's group in 2015 with the first aqueous synthesis of UiO-66. Furthermore, this required refluxing and unintentional defects were introduced into the crystal due to the heterogenous distribution of insoluble ligands in the solution hence H_2BDC was functionalized with hydrophilic amine, alcohol and carboxylic acid groups, to iron out defects.[192] These approaches were combined by Pakamore and colleagues in 2018 to allow for the first aqueous room temperature synthesis of a UiO-66 derivative. To achieve this, H_2BDC was substituted with amino groups which was then solubilized by deprotonation in dilute NaOH. Meanwhile $Zr(O)_4(OH)_4(CH_3COO)_{12}$ clusters were pre-synthesized from $ZrOCl_2.8H_2O$ using Farha's method but substituting DMF for water. The two solutions were then mixed over a 24-hour period. Whilst promising, this method is only applicable to UiO-66-NH_2 and not UiO-66 itself.[193] Attempts to replicate this synthesis using H_2BDC result in a non-crystalline material (Figure B.7). To date, a room temperature, aqueous synthesis of UiO-66 has still not been realized.

4.1.2. Crystal Defects

The high connectivity and stability of UiO-66 suggests that it is possible for it to maintain its overall structure even when one or two linkers from its unit cell are lost. Indeed, this was confirmed in 2011 by Valenzano and colleagues. They reported that analysis of the thermal decomposition of UiO-66 suggested that less BDC was present in the structure then the idealized formula predicts. This was termed a missing linker defect[200]. At missing linker sites, the metal cluster is capped with water, hydroxide or carboxylate modulators replacing the absent ligand. A 2014 study by Goodwin's group demonstrated that defects can also occur due to the loss of zirconium clusters and their surrounding ligands (missing cluster defects). Importantly, both missing linker and missing cluster defects result in a deficit of BDC.[201] As a result of these defects, the typical **fcu** topology is altered to either **bcu**, **scu**, or **reo** at the afflicted sites (Figure 4.2). As of 2019, Liu and colleagues have confirmed the presence of these topologies by direct imaging using high resolution TEM. Where **bcu** is the result of missing linker defects, **reo** and **scu** result from missing cluster defects. However, **reo** and **scu** differ in the connectivity of the remaining clusters. The **reo** clusters are 8 connected whereas **scu** clusters are 4 connected.[202]

Defectivity has a significant role in the material properties of UiO-66. The presence of defects reduces the thermal stability of the material. Furthermore, the BET surface area increases on the inclusion of defects. This was first observed in a 2013 study by Zhou and colleagues, who systematically increased the amount of missing linker defects causing a 32%

increase in the BET surface area.[203] This has allowed researchers to synthesize UiO-66 with surface areas of up to 1890 m^2g^{-1} despite the theoretical maximum surface area of ideal UiO-66 being significantly less than this.[204] Unsurprisingly, this significantly impacts the gas adsorption properties of guest molecules such as H_2O and CO_2 adsorption.[205, 206] This can also have significant impact on the drug loading. This was highlighted by Shan and colleagues when they loaded ferrocene into UiO-66. Analysis of the pore size distribution of the material demonstrated that ferrocene near exclusively occupied defect sites. This was attributed to greater accessibility due to the enhanced void space.[204]

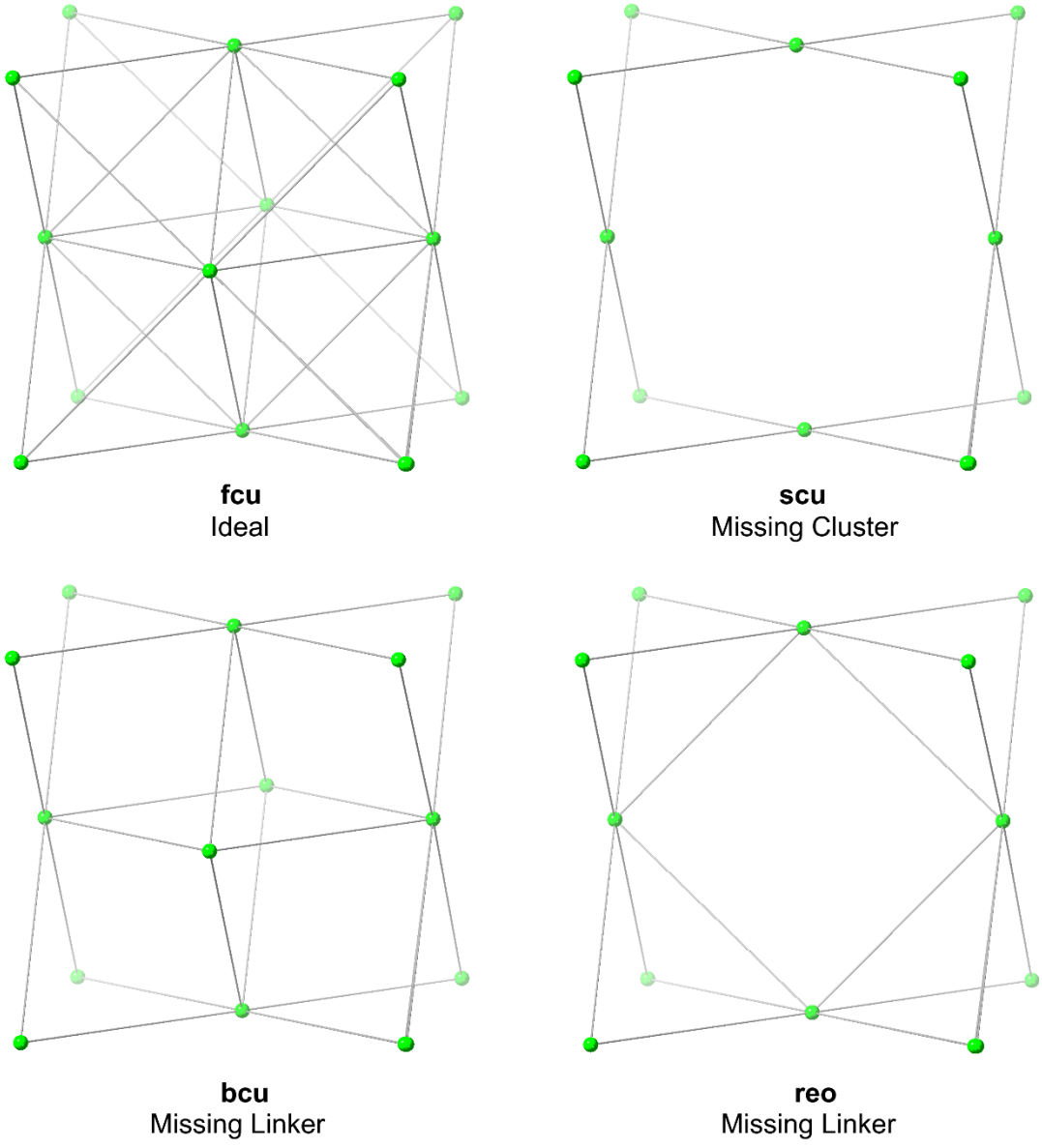

Figure 4.2 UiO-66 defects and corresponding topologies

Due to its impact on physical properties and applications, defect engineering has become a major field in UiO-66 research. One way this can be achieved is by altering the synthetic conditions. Whilst parameters such as reaction temperature, reaction time and the choice of metal salts have been shown to alter the defectivity, modulator-ligand competition has been highlighted as a primary contributor to crystal defects. Given that modulators bind the zirconium cluster in place of BDC, the presence of modulators result in missing linker defects. The greater the modulator to ligand ratio is the more competition exists for binding sites resulting in more defects. In addition, the acidity of the modulator plays a significant role as the zirconium clusters bind carboxylic acid groups in the deprotonated state. Modulators with lower pK_a values will more likely exist in the deprotonated state creating greater competition. For this reason, equivalent UiO-66 synthesized with acetic acid (pK_a = 4.76) will have fewer defects compared to a synthesis using equivalent amounts of trifluoracetic acid (pK_a = 0.23). As zirconium clusters are also modulated by binding water molecules and hydroxide ligands, using more water during the synthesis will increase the defectivity of the overall material.[207]

4.1.3. Morphology

UiO-66 growth is typically oriented along the [111] crystal faces resulting in an octahedral morphology. However, cubic or cuboctahedron morphologies have also been observed due to growth of the [100] facet or a combination of [100]/[111] growth (Figure 4.3). This was highlighted by Han and colleagues managed to isolate these morphologies by adding HF during synthesis. The addition of HF slows growth along the [111] face.[208] Furthermore, UiO-66 also forms amorphous aggregates, typically due to the presence of excess water during synthesis.[191]

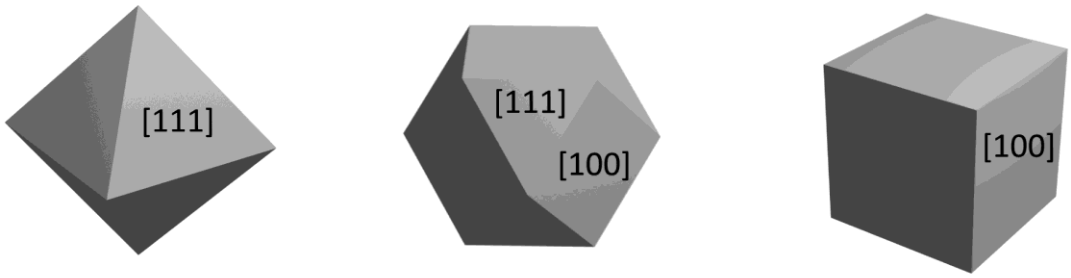

Figure 4.3 From left to right: octahedral, cuboctahedral, and cubic morphologies

The NP size of UiO-66 has significant variability within the literature, ranging from 14 nm to 300 μm.[191, 209] To date the smallest UiO-66 NPs (14 nm) were synthesized by Schaate and colleagues by adjusting the pKa and concentration of modulators during solvothermal

synthesis.[191] To date, researchers have adjusted the NP size of UiO-66 through a variety of mechanisms. For instance, Zhao and colleagues managed to tune UiO-66 dimensions from 2 μm to 500 nm by increasing the concentration of triethylamine used during solvothermal synthesis.[210] However, adjusting such parameters also impacts the defectivity of the material, decoupling of these two properties is a major challenge UiO-66 crystal design. In 2019, Decker and colleagues investigated the simultaneous use of three properties to tune the particle size and defectivity: the water equivalence, ligand to metal ratio and the reaction time. Whilst this approach allowed control of both NP size (20-120 nm) and defectivity (0-12%), it did not allow independent control. A reduction in NP size was generally correlated with decreased defectivity.[81] Hence, the rational design of UiO-66 NPs with a precise size and defectivity is still an ongoing challenge.

4.1.4. Research Outline

Like ZIF-8, the investigation of new methods to tune the morphology of UiO-66 is highly relevant because of UiO-66's prevalence and the potential scope of its applications. However, microemulsion synthesis of UiO-66 represents a far more significant target, given the difficulties in producing ambient temperature or aqueous synthetic methods. The microemulsion synthesis method described in the previous chapters is significantly less environmentally harmful than typical solvothermal methods. Furthermore, MOF defectivity when synthesized within microemulsions has yet to be studied and UiO-66 is an ideal MOF for defectivity analysis. The objective of this chapter was to synthesize UiO-66 using the microemulsion method developed in Chapter 2 - Zeolitic Imidazole Framework Synthesis in Microemulsions and characterize the morphology and defectivity of these materials when synthesized with various conditions. To achieve this goal UiO-66 was synthesized with variable ω_o and addition times. Characterization was performed as outlined in previous chapters. In addition, the surface area and pore size distribution were characterized using N_2 gas adsorption. Whereas the defectivity was determined using thermal gravimetric analysis (TGA).

4.2.Results

Microemulsion UiO-66 was synthesized using the method outlined in 4.4.1 Microemulsion UiO-66. The microemulsions were prepared with ω_o values of 27.8, 22.3, and 16.7. Further samples were prepared with 11.1, 10 and 5.6 ω_o. Though these latter three samples have not been fully characterized and this is an area of future research. These ω_o values correspond to 10, 8, 6, 4, 3.6, & 2 mL of water used during synthesis. For each ω_o value, UiO-66 was prepared

with a 120 or 30 min addition time. The samples are denoted UiO-66-volume-addtime e.g. UiO-66-10-120.

4.2.1. Topology

The PXRD patterns of all samples (Figure 4.4A & B) displayed peaks matching simulated UiO-66. Samples possessed peaks at 2θ values of 7.3, 8.7, 14.9, and 25.6°. These matched the simulated UiO-66 peaks for the [111], [002], [222] and [006] planes. In addition to simulated peaks, UiO-66 samples can also possess Bragg peaks at 4.45 and 6.0° from the [001] and [011] reflections.[202] These peaks occur due to correlated regions of **reo** defects that arise from missing linkers. Whilst no discrete peaks are identifiable, increased intensity is observed in all samples where these reflections would be expected. As all samples experience significant peak broadening, these peaks are not expected as they would be masked into a "broad peak" in this region.[207] Hence, the intensity at 4.44° as a percentage of the 7.3° peak was determined to investigate possible trends in defectivity (Figure 4.4C & Table C.5). It was found that the relative intensity increases as the aqueous volume decreased. Furthermore, an increase in the relative intensity was observed when the addition time was decreased. For the 120 min samples, the relative intensity decreases from 4.8% to 37.5% between the 10 mL and 2 mL samples. The same trend is observed for the 30 min samples, where the relative intensity increases from 6.5% to 44.6% for the 10 mL and 2 mL samples. Furthermore, for both addition times a dramatic increase in relative intensity was observed for between the 4 mL and 2 mL samples.

Another noticeable feature of the UiO-66 PXRD patterns is that they exhibit significant peak broadening (Figure 4.4D & Table C.6). Peak broadening occurs where there is a reduction in the number of units along a plane (loss of periodicity) or coherence in long-range ordering is lost due to crystal strain. In this case, loss of periodicity is more likely because the ambient synthesis conditions used are unlikely to cause significant crystal strain. The length of a periodic domain (grain size) can be determined using the Scherrer equation[211] (A.1.1. Powder X-ray Diffraction)[*]. This was performed measuring the peak broadening of the [111], [002] and [006] peaks. Grain size was averaged from all peaks assuming an isotropic crystallite. As a general trend the grain size decreased as the water volume decreased. For instance, UiO-66-10-120 exhibited a grain size of 16.3 nm which reduced to 10.4 for UiO-66-4-120. Furthermore, the 120 min addition time produced crystals with less peak broadening than the 30 min synthesis, in all cases. The calculated grain size of UiO-66-10-120 and UiO-66-4-120

[*] ZIF-8 samples reported a larger size and do not possess significant defectivity. Therefore, it possessed significantly less size induced broadening. Instrumental broadening from the diffractometer masks this effect; particularly with larger crystallites. For this reason, the Scherrer equation could not be reasonably applied to most ZIF-8 samples.

were 2.6 nm and 0.1 nm larger than their 30 min equivalents. Unfortunately, this method could not be performed for the 2 mL and 3.6 mL samples because the [111] and [002] peaks merged. Reduced grain size suggests a decreased NP size or increased defectivity.[212] Amongst all samples the greatest variance observed in the grain size between different PXRD peaks was 4.7 nm with most samples varying by 2-3 nm. This is relatively consistent.

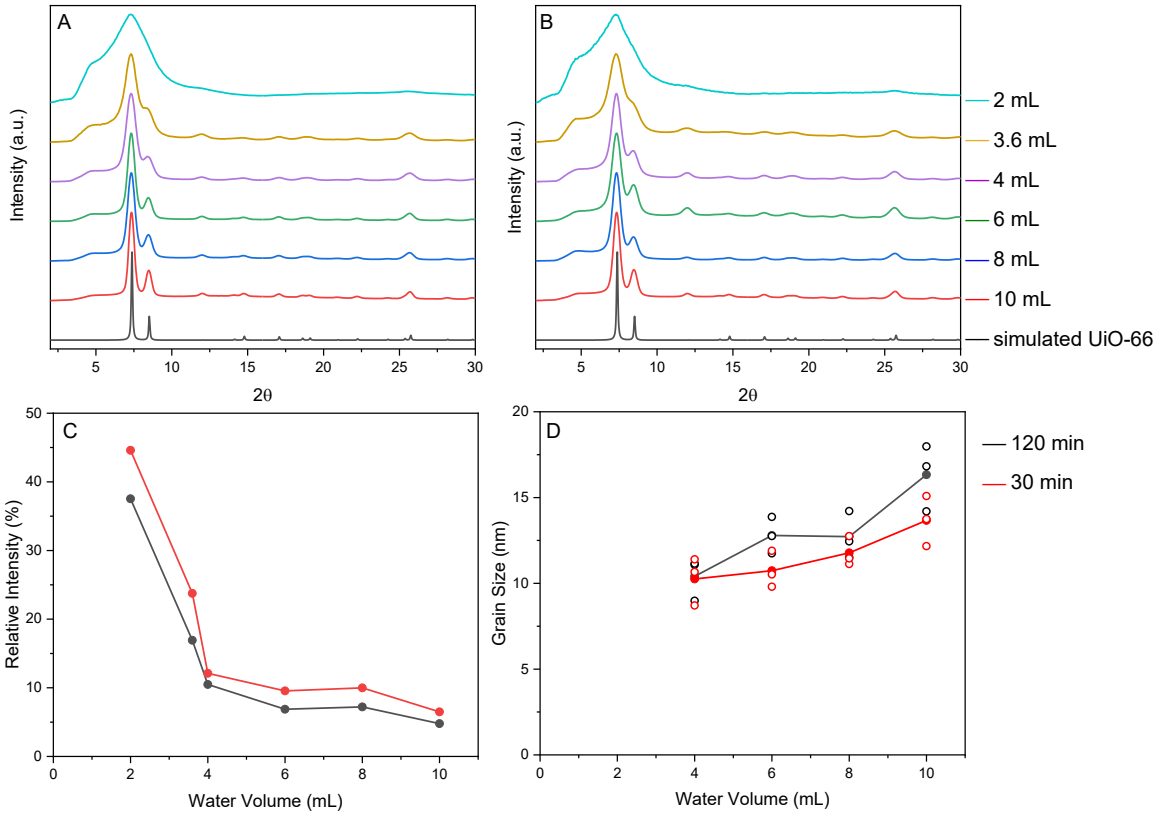

Figure 4.4 PXRD of UiO-66 synthesized in microemulsions with variable aqueous volumes. Samples were synthesized with a 120 (A) or 30 (B) minute addition time. (C) Relative intensity of the PXRD at 4.44° of the 7.30° peak. (D) Grain size. Filled dots are the averaged values. Open dots represent values obtained by individual PXRD peaks.

4.2.2. Morphology

Through TEM imaging (Figure 4.5), it was observed that UiO-66 samples generally consisted of discreet NPs with a consistent psuedospherical morphology. The NP size decreases between 10 mL and 6 mL water volumes for both addition times. However, for 4 mL samples the resolution of the TEM was insufficient at the enhanced magnification required to image the samples. Whilst UiO-66-4-120 could be imaged and was consistent with this trend, UiO-66-4-30 had poor image resolution and appeared to be amorphous. It should be noted that, cuboctahedron and spherical samples are difficult to distinguish through TEM of NPs as the

limited size of the crystallites makes edges difficult to define. Thus, the possibility of the crystallites being cuboctahedron is left open. However, cubic and octahedral morphologies are more easily identified and do not appear to be present in these samples. At water volumes less than 4 mL, sample amorphization becomes apparent. For both the 3.6 mL and 2 mL samples, large amorphous low crystalline materials without discernible NPs are present. Another interesting feature found through TEM imaging is that all NP samples have some degree of agglomeration where NPs are clustered together. This is likely the result of the small NP size (> 40 nm). As NP size decreases the outer surface area becomes a larger fraction of the total surface area. Hence, NPs have a larger exposed area to attract other NPs. It should be noted that agglomerations were excluded from size analysis using imaging software (A.1.2 Transmission Electron Microscopy).

Such agglomeration could rationalize the amorphization of the 2 and 3.6 mL samples. As the water volume decreases the NP size decreases until discreet NPs are no longer formed. As the NP size decreases the outer surface of the NP becomes a larger fraction of the total surface area. With a larger exposed surface area to agglomerate NP agglomeration is encouraged. For the below 4 mL samples discreet NPs do not form instead partially formed NPs agglomerate creating amorphous UiO-66 samples.

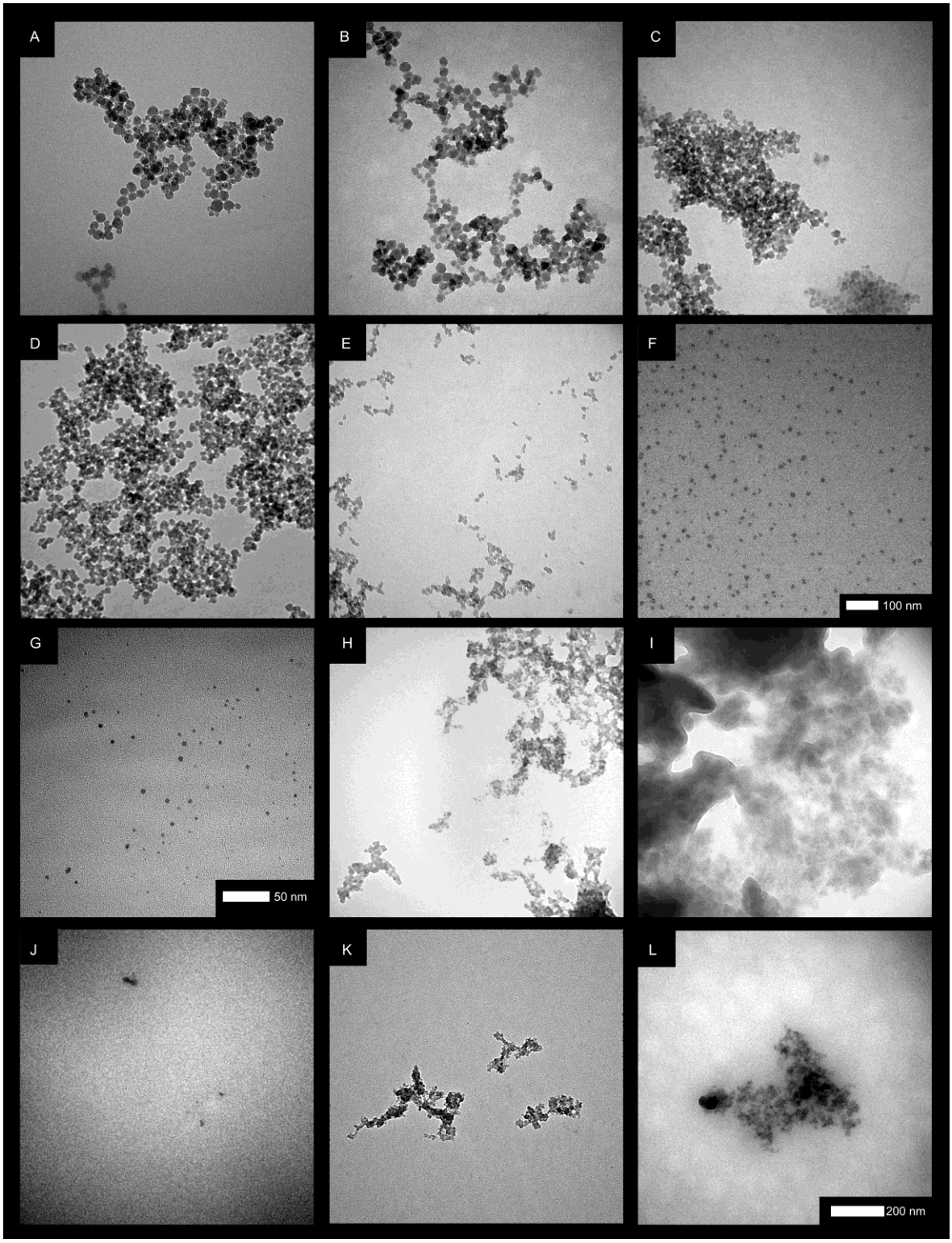

Figure 4.5 TEM images of (A) UiO-66-10-120, (B) UiO-66-8-120, (C) UiO-66-6-120, (D) UiO-66-10-30, (E) UiO-66-8-30, (F) UiO-66-6-30 with a 100 nm scale. (G) UiO-66-4-120 with a 50 nm scale. (H) UiO-66-3.6-120, (I) UiO-66-2-120, (J) UiO-66-4-30, (K) UiO-66-3.6-30, (L) UiO-66-2-30,

One of the major objectives of this research was to determine the effectiveness of microemulsion synthesis as a NP size control technique. As such, the particle size and distribution of the UiO-66 samples were determined from the TEM images (Figure 4.6 & Table B.5). A reduction in NP size was observed when reducing the addition time from 120 min to 30 min. This was consistent for all water volumes. However, the difference in average size between samples with equivalent conditions was minor. At maximum, the difference in average particle size was 5.0 nm observed between the 10 mL samples. The smallest difference observed was 2.1 nm between the 6 mL samples. This result is consistent with the results for ZIF-8 previously discussed (2.2.3 Addition Rate). The observed increase in NP size with an increased addition time was unsurprising since a reduction in the addition time would likely increase the nucleation rate.[133] Due to agglomeration and amorphization, discreet NPs could not be identified in the 2 mL and 3.6 mL samples for both addition times as well as the 30 min 4 mL sample.

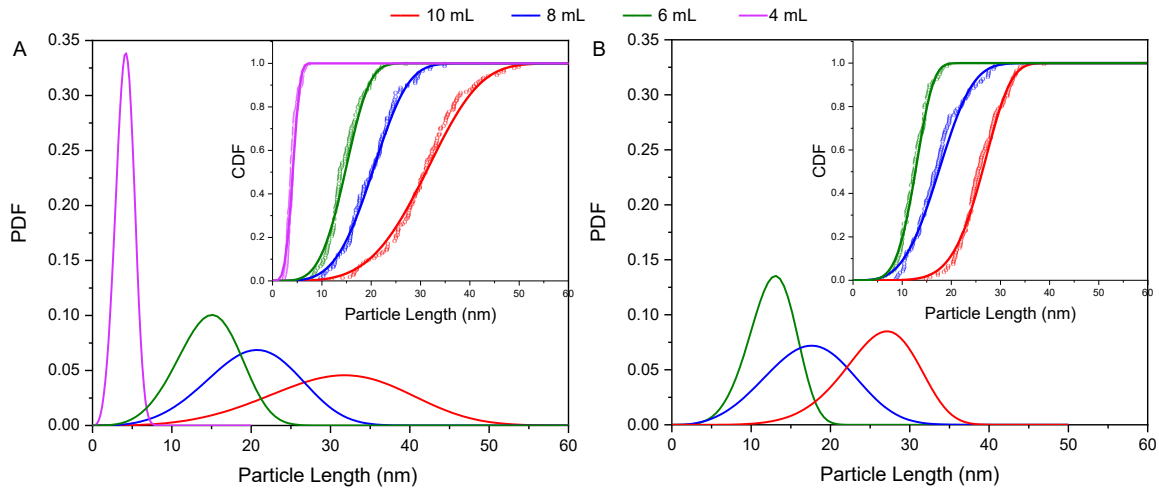

Figure 4.6 UiO-66 PSD from TEM images for the (A) 120 minute and (B) 30 minute microemulsion synthesized samples. Outset: Modelled Weibull distribution PDF of sample PSD. Inset: Modelled Weibull (line) and experimental raw data (dots) CDF.

Another noticeable trend was that the average NP size decreased as the water volume decreased. Unlike the subtle variation induced by adjusting the addition times, altering the water volume dramatically reduced the NP size. For the 120 min samples, the average NP size was tuned from 31.0 ± 8.0 (N = 141 nm) for UiO-66-10-120 to 4.09 ± 1.05 (N = 107) nm) for UiO-66-4-120. With a 4.09 nm average particle size, UiO-66-4-120 is the smallest ever recorded UiO-66 sample. It has a length of approximately two unit cells, based on a unit cell parameter of a = 20.7 Å. It should be noted that the literature record of 14 nm was recorded by

PXRD,[191] which generally underestimates the NP size with the presence of defects. Hence, the actual NP size is likely larger.

Another notable feature of the PSD was the SD. For the 30 min samples, the percentage SD ranged from 16.9% to 29.5% with no obvious trends. Whereas for the 120 min samples, the SD increased as the average NP size increased. However, the percentage SD remained relatively consistent for all samples (between 24.3% and 26.8%). For UiO-66-4-120, this manifested as a SD of 1.05 nm (25.7% SD). Nonetheless, using a 120 min addition time, all NP containing samples displayed a highly uniform morphology. Furthermore, by varying the aqueous volume the NP size is tuneable without significantly altering the dispersity. For this reason, microemulsion synthesis appears to be an excellent technique for obtaining UiO-66 NPs with desired sizes.

The two smallest samples synthesized with the 120 min addition time (UiO-66-4-120 & UiO-66-6-120) did not conform to a Gaussian distribution but did conform more closely to a Weibull distribution (Figure 4.7). This was previously observed with the smallest ZIF-8 samples (Chapter 2 - Zeolitic Imidazole Framework Synthesis in Microemulsions). This result was attributed to lower tail inaccuracy of the Gaussian distribution due to instability of NPs below a critical nuclei radius. The NP size of UiO-66-4-120 for a Weibull distribution was 4.08 ± 1.14 nm (N = 107, RSD = 27.9%). The NP size of UiO-66-6-120 for a Weibull distribution was 14.6 ± 3.9 nm (N = 101, RSD = 27.9%).

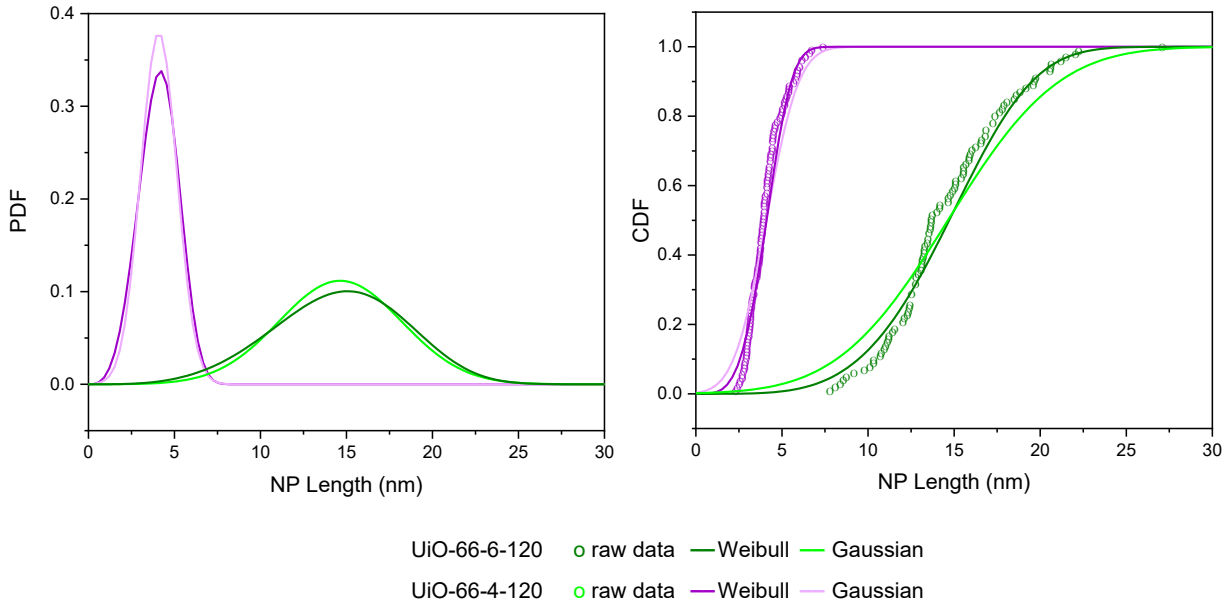

Figure 4.7 UiO-66 PSD from TEM images for the (A) 120 minute and (B) 30 minute microemulsion synthesized samples. Outset: Modelled Weibull distribution PDF of sample PSD. Inset: Modelled Weibull (line) and experimental raw data (dots) CDF.

4.2.3. Defectivity

The presence of defects and the thermal stability of the UiO-66 samples were determined by TGA analyses in air (Figure 4.8 & Table B.6). Decomposition of UiO-66 was observed in two temperature ranges (~200-300 & ~500ºC). These correspond to the two steps typically associated with UiO-66 decomposition. From the first derivative curves (Figure 4.7C& D), it was determined that the first decomposition step ends prior to 375 ºC and the second step has ended completely by 550 ºC. The residual material left in the TGA pan at 550 ºC was assumed to be ZrO_2. The percentage decomposition of BDC was ascertained from the weight loss between 375 ºC and 550 ºC. For the 120 min samples, the percentage of missing linkers decreased consistently from 17.5% for UiO-66-10-120 to 12.9% for UiO-66-8-120 and finally 11.2% for UiO-66-6-120 (A.3.1 Total Defects). The 30 min samples generally had more missing linkers than the equivalent 120 min sample. The percentage defects were 21.8, 28.5 and 22.5% for UiO-66-10-30, UiO-66-8-30, and UiO-66-6-30 respectively. Whilst, the 30 min samples possessed more defects, no obvious correlation between water volume and defectivity was observed. The range in defectivity across all samples is between 11.2 and 28.5%. This is an absence of 0.672 to 1.71 of the 6 ligands per unit cell that would be expected in non-

defective UiO-66.This is consistent with a typical defectivity range observed in the literature.[14, 193, 207]

Interestingly, the decomposition temperature varied slightly with the sample. The dehydroxylation of UiO-66 occurs for 120 min samples at ~300 ºC. Whereas for 30 min samples, this appears to be a convolution of two steps at ~230 and 280 ºC. It is unclear why this occurs, but it could be instrumental error. For the linker decomposition step there does not appear to be any correlation between particle size or defectivity with the decomposition temperature in the 120 min samples. For the 30 min samples, the decomposition temperature decreases from 501 to 490 ºC from UiO-66-10-30 to UiO-666-30. This broadly corresponds with the decrease in NP size. There does not appear to be any correlation between the NP size and defectivity with the change in the BDC decomposition temperature. This is likely because both factors contribute to the decomposition temperature and are difficult to deconvolute.

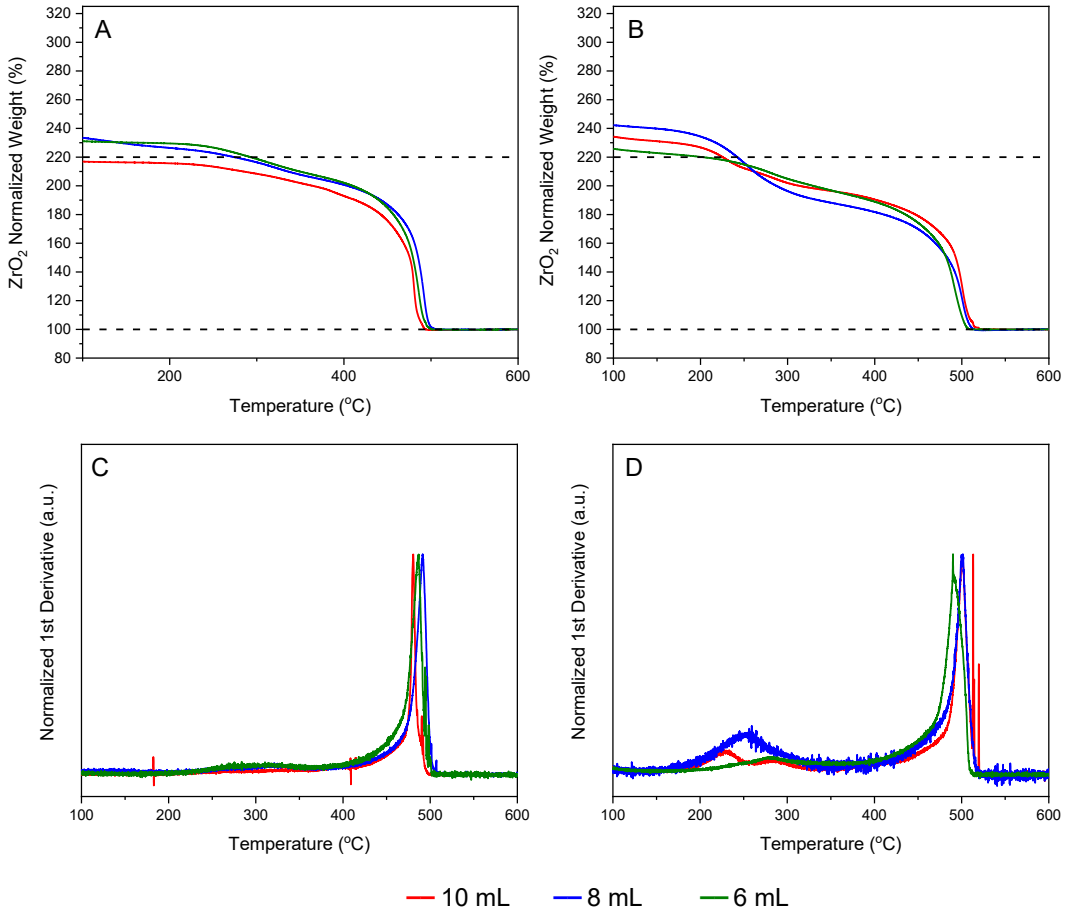

Figure 4.8 TGA normalized against the ZrO_2 plateau for 120 min (A) and 30 min (B) samples and their corresponding 1st derivative curve (C&D). Dotted lines show 100% and 220% normalized mass.

Notably, small NPs may not necessarily possess the ideal amount of BDC, even if the crystal possesses no internal defects. This is because they have a larger surface area to volume ratio. Hence, the absence of ligands on the surface due to network termination (a completely different phenomenon to the absence of ligands from the framework itself) contribute more significantly. The percentage of surface defects as a function of the NP size was modelled for UiO-66 (Figure 4.9). The model derivation can be found in the appendix (A.3.2 Surface Defects). The model assumes that the morphology is octahedral and that the entire outer surface is charge neutral. Both assumptions potentially overestimate the percentage surface defects. Despite this overestimation, all samples possessed significantly more defects than modelled.

Therefore, the defectivity present in each sample cannot solely be attributed to surface defects. Hence, analysed samples must possess missing linkers within their interior.

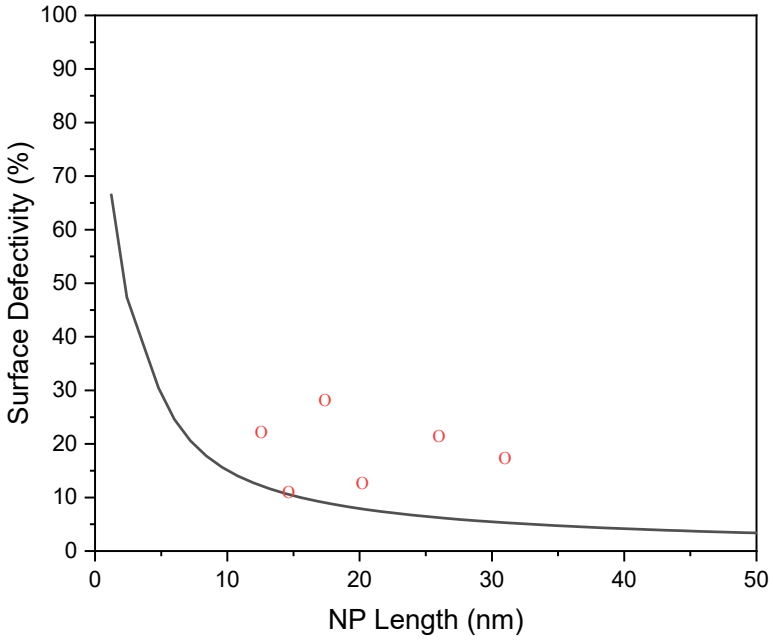

Figure 4.9 Modelled percentage of surface defects in UiO-66 as a function of NP size (black) along with experimental samples (red).

4.2.4. Gas Adsorption Properties

Gas adsorption of UiO-66 (Figure 4.10A&B) samples showed a decreasing surface area as the water volume and addition time decreased. For the 120 min samples, the BET surface area was 1818, 1262, and 1183 m^2g^{-1} for the 10, 8, and 6 mL samples, respectively. At 1818 m^2g^{-1}, UiO-66-10-120 has a surface area well beyond the theoretical maximum of 1644 m^2g^{-1} for an idealized UiO-66 crystal.[66] Similar surface areas have been achieved by researchers using UiO-66 samples with approximately the same degree of defectivity.[207] For the 30 min samples, the BET surface area decreased to 1186, 1079, and 926 m^2g^{-1} for the 10, 8, and 6 mL samples. This trend is also apparent in the total pore volume. For the 30 min samples, the total pore volume decreased from 1.19 to 0.97, and 0.87 cm^3g^{-1} for the 10, 8, and 6 mL samples. For the 120 min samples, the total pore volume was 1.77, 1.11, and 1.2 cm^3g^{-1} for the 10, 8, and 6 mL samples. This is consistent with previous literature, suggesting that the surface area and pore volume decreases as the NP size decreases. Curiously, the surface area and pore volumes were consistently larger for the 120 min samples compared to the more defective 30 min samples. This is in contrast with the literature which suggests an increased surface area would be expected due to enhanced defectivity. This implies the NP size has a more substantial influence than defectivity on the absorption properties of the material.

For both the 120 min and 30 min samples, a peak can be detected in the pore size distribution at 1.22 nm. This is consistent with the largest of the two micropores that exist in UiO-66. For each sample sets further peaks are visible for mesopores ranging from ~3.4 nm to 25 nm that would not be present in simulated UiO-66. Such mesopores can exist due to defects in the crystals or interstitial void. Interstitial voids occur due to agglomeration of multiple crystals leaving a void space between them.[66] UiO-66-10-120 and UiO-66-10-30 NPs are 31.0 and 26.0 nm respectively and are 17.5 and 21.8% defective. A NP of this size and defectivity could not possess a 15 nm average pore within the crystal. This leads to the conclusion that the mesopores are due to interstitial voids.

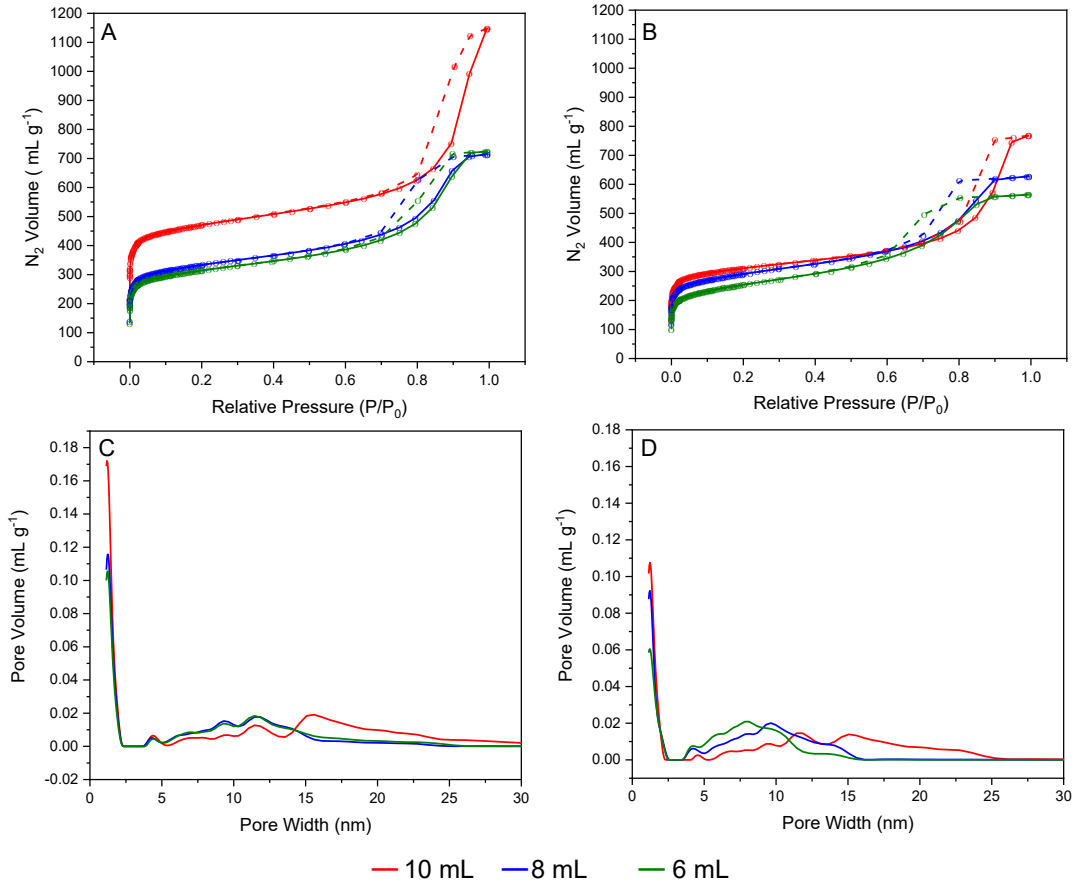

Figure 4.10 N_2 adsorption isotherm at 77 K measured for 120 min (A) and 30 min (B) samples. Isotherms display raw data points (dots) along with the adsorption (solid lines) and desorption (dashed) curves. Pore size distribution of 120 min (C) and 30 min (D) samples estimated from the adsorption isotherms.

4.3. Discussion & Future Work

A summary table of the characterization data is provided below (Table 4.1). It should be noted that both the TGA and PXRD show increased defectivity with a 30 min addition time. This is good agreement given both measurement measure different properties. The relative intensity of the **reo** region is proportional to the number of correlated **reo** defects. Whereas, TGA measures the amount of BDC lost regardless of its location within the sample.

Table 4.1 Summary Table of UiO-66 Characterizations

Sample	Size (nm)		Defects (%)		SA (m^2g^{-1})*	V (cm^3g^{-1})†
	PXRD	TEM	PXRD	TGA		
UiO-66-10-120	16.33	31.0	4.78	17.5	1818	1.77
UiO-66-8-120	12.72	20.2	7.22	12.9	1262	1.105
UiO-66-6-120	12.79	14.6	6.88	11.2	1183	1.20
UiO-66-4-120	10.40	4.09	10.49	--	--	--
UiO-66-3.6-120	--	--	16.92	--	--	--
UiO-66-2-120	--	--	37.53	--	--	--
UiO-66-10-30	13.67	26.0	6.50	21.8	1186	1.19
UiO-66-8-30	11.78	17.4	10.00	28.5	1079	0.97
UiO-66-6-30	10.74	12.6	9.55	22.5	926	0.87
UiO-66-4-30	10.26	--	12.14	--	--	--
UiO-66-3.6-30	--	--	23.76	--	--	--
UiO-66-2-30	--	--	44.59	--	--	--

For samples UiO-66-3.6-120, UiO-66-3.6-30, UiO-66-2-120 and UiO-66-2-30, there is broad agreement between the TEM and PXRD data. The PXRD of these samples illustrates

* Surface area
† Total pore volume

that they possess significantly higher defectivity compared to all samples. This is highlighted by both the high relative intensity of the **reo** peak and the significant peak broadening apparent through the PXRDs. This is consistent with the TEM images which show large amorphous material with no discreet NPs. Such a material could form by highly defective prenucleation clusters aggregating. Notably the characterization of these could not be fully completed. Whilst, it would be interesting to confirm this hypothesis by TGA defect analysis of the resulting samples, poorly crystalline samples are not of any particular research interest. Given the available information a complete characterization of the 4 mL samples would be of significant interest given the small dimensions of the UiO-66 NPs present.

This study demonstrated several features which are highly interesting in the field of UiO-66 morphological control. Though, this was achieved only with a narrow range of ω_o values. Firstly, NPs maintained a uniform pseudospherical morphology and a narrow size distribution. Second, the NP length could be rationally tuned between 31.0 to 4.1 nm by altering ω_o values. This is consistent with many prior microemulsion studies. The 4.1 nm sample is the smallest recorded UiO-66 sample to date. This is promising for later studies investigating how NP size affects physical properties. Finally, particle size and defectivity appear to be uncorrelated. Further research is required to investigate potential factors that may alter the defectivity. If both the defectivity and NP size can be tuned individually the applicability of this technique for UiO-66 morphological control would be greatly enhanced. For instance, the 30 min addition time samples possessed significantly more defects than the equivalent 120 min addition time. Later studies should investigate whether longer addition times reduce defectivity. Another factor worth investigate in future studies is the pre-treatment heating of the $ZnOCl_2$ solution. Before synthesis, the aqueous $ZnOCl_2$ stock used during synthesis was heated to 60ºC with acetic acid. DeStefano uses this same pre-treatment procedure to prenucleation clusters for UiO-66 synthesis. The treatment temperature was varied from 45 ºC to 130 ºC and the defectivity changed from 1.3 to 0.2 missing linkers per unit cell. The impact of treatment temperature on UiO-66 defectivity using the microemulsion synthesis protocol is worth investigating.

4.4. Conclusion

This study reports the use of microemulsion synthesis to produce UiO-66. This synthesis is achieved in room temperature conditions without the use of DMF. Hence, it shows great promise as an environmentally friendly synthetic protocol. Furthermore, between ω_o values of

27.8 and 11.1 (10 to 4 mL of water) discreet pseudospherical UiO-66 crystals were obtained. Though, significant amorphization occurred outside this range. Within this range, NP size could be turned from 31.0 to 4.1 nm (the smallest UiO-66 sample in the literature) and had a low dispersity which remained consistent regardless of aqueous volume. Furthermore, all samples possessed defectivity between 0.67 and 1.71 missing linkers per unit cell. Further work is required to investigate tuning the defectivity of these materials. However, such a study would greatly enhance the results achieved in this chapter.

4.5.Experimental Methods

4.5.1. Materials

As per section 2.4.1. Materials, all chemicals and reagents were sourced from commercial suppliers at a purity of 99.8% or greater and used without further purification.

4.5.2. Microemulsion UiO-66

For all UiO-66 samples prepared using microemulsion synthesis, two solutions were prepared by mixing TX-100 (12.48g, 18.2 mmol), 1-hexanol (4.8, 38.6 mmol) and cyclohexane (40 mL, 370 mmol). Two microemulsions were prepared (μEM, μEL) were prepared by adding a variable amount of an aqueous phase solution (Table 4.2). The aqueous phase volume of μEM was always equal to the aqueous volume of μEL. The aqueous phase of μEM was prepared by dissolving $ZrOCl_2.8H_2O$ (3.22g, 10 mmol) in water (85 mL) and acetic acid (15 mL). The resulting mixture was heated to 60ºC under reflux for 2 hours before cooling to room temperature. For μEL, the aqueous phase solution was prepared by adding H_2BDC (1.66 g, 10 mmol) to aqueous NaOH (100 mL, 0.2 M) and heating at 60ºC until the solid was fully dissolved. The mixture was cooled to room temperature before further use. Once prepared, μEL (40 mL) was added to μEM (40 mL) dropwise over a set addition time. The solution was then left stirring for 24 hours. The resulting mixture was ruptured with methanol/acetone (50% v/v, 40 mL). MOF crystals were extracted by centrifugation at 6000 rpm for 20 min. The extracted solid was washed with acetone, cyclohexane, and methanol (20 mL) before lyophilization overnight.

Table 4.2 Microemulsion UiO-66 Synthesis

Sample	Addition Time (min)	Aqueous Volume (mL)
UiO-66-10-120	120	10
UiO-66-8-120	120	8
UiO-66-6-120	120	6
UiO-66-4-120	120	4
UiO-66-3.6-120	120	3.6
UiO-66-2-120	120	2
UiO-66-10-30	30	10
UiO-66-8-30	30	8
UiO-66-6-30	30	6
UiO-66-4-30	30	4
UiO-66-3.6-30	30	3.6
UiO-66-2-30	30	2

4.5.3. Characterization Methods

Samples were characterized using the method outline in 2.4.1 Characterization Methods. In addition, activation of samples was performed at 120ºC for 20 hours under vacuum before gas adsorption analysis. TGA were used to further characterize the inactivated samples.

4.5.3.1. Gas Adsorption

Approximately 50 mg of each sample was activated by heating to 160 ºC for 18 hours in a vacuum to remove adsorbed guest molecules. N_2 was measured for the activated samples at 77 K using a Quantachrome Autosorb IQ. Sample data was analyzed using pyGaps 2.0.2.[213] Calculations of pore size and surface area are provided in the appendix (A.2 Porosity). BET values calculated between for $0.2<p/p_0<0.3$. Total pore volume was calculated for $p/p_0 = 0.98$.

4.5.3.2. Thermal Gravimetric Analysis

TGA data was collected by heating samples (~3-10 mg) to 900ºC at a rate of 5ºC min^{-1} under air using a TA Instruments Q500 TGA.

Chapter 5 - Summary & Perspective

5.1. Future Work & Perspective

In the previous chapters, future work was discussed when it related specifically to the chapter content. As a summary, in chapter two, two rare ZIF phases were found by mixing Zn and HIM using the microemulsion method. Whilst further exploration was outside the scope of this project due to time constraints, investigating whether microemulsion synthesis topologies could be used to tune the topology of Zn-IM MOFs represented an interesting field of further exploration. In chapter 3, further work was required to elucidate the impact of microemulsion synthesis on the activity of enzyme@ZIF-8 complexes. Finally, in chapter 4, it was noted that the UiO-66-4-120 sample still requires characterization by both TGA and gas adsorption. Furthermore, further work to investigate whether the levels of defects in the UiO-66 samples could be tuned would greatly enhance the UiO-66 work as a whole.

However, in this section, the focus of discussion is the general perspective on future work in the field of microemulsion synthesis obtained from this study. As such, it is noted that there were two main limitations in this study:

Firstly, development of microemulsion synthesis protocols was largely trial and error. Initially it was thought that pre-existing aqueous protocols could be utilized to develop microemulsion protocols based on the templating model. However, the microemulsion synthesized MOFs displayed morphological behaviour distinctly different from the equivalent aqueous protocol. Whilst ZIF-8 could be synthesized using both approaches, it displayed substantially different morphological trends. For UiO-66, microemulsion synthesis could be achieved. However, no aqueous room temperature synthesis methods are available. Therefore, there is a limitation in the current understanding of the mechanisms behind microemulsion synthesis. This limits the ability to rationally develop microemulsion methods for novel MOFs.

The second major limitation of this study was its limited investigation of reaction parameters. Addition rate and ω_o were extensively studied. However, the cosurfactant concentration, pH and solvent selection amongst others were not investigated. Given the scope of reaction parameters in these systems, their will likely be significant room for high throughput screening or extensive parameter analysis for a rather long time. However, such studies are tedious and may not necessarily provide significant insight. For instance, UiO-66 and ZIF-8 responded very differently to the change in ω_o. No clear trend was observed for ZIF-8 in response to ω_o. Whereas, UiO-66 reduced in NP size as ω_o decreased. Hence, even after extensive analysis observed trends may not be generalizable.

Herein, it is proposed that the mechanism of MOF formation within a microemulsion should be studied for either UiO-66, ZIF-8, or Zn-IM. This is because current research has a limited understanding of the mechanisms involved in microemulsion synthesis or MOF formation. Providing further insight into the mechanism of MOF formation within a microemulsion system may prove fruitful for developing generalized rules for microemulsion protocols. Techniques that may prove useful to achieve this goal are: cryo-TEM, dynamic light scattering (DLS), *in situ* PXRD, and small angle X-ray scattering (SAXS). However, for various reasons these techniques could not be applied in this study.

Cryo-TEM is a technique whereby samples are frozen and sliced into thin subsections before imaging. The technique has two advantages over standard TEM imaging. First, soft material (e.g. micelles) too delicate for conventional TEM are preserved by fast freezing before TEM analysis this allows characterization of micellular structures. Second, sample freezing stops the reaction process. Hence, samples can be taken from different stages in the reaction process allowing for time-resolved study.[214] The application of this technique during microemulsion synthesis would allow the resolution of MOF and micellular morphology at different intervals throughout the formation process providing insight into possible formation mechanisms.

DLS is a technique which measures the intensity and fluctuation of backscattered laser light transmitted through a sample. By correlating the intensity of backscattered light to the intensity after a time delay, the diffusion rate and hence the NP size and PSD can be calculated. Whilst commonly, utilized in NP analysis. The usefulness in this study was limited. Firstly, accurate DLS data could not be obtained for NP containing microemulsions. This could be because the refractive index of the samples were inaccurately determined since the refractive index of the structure would be the combined refractive index of the micelles and NPs. Furthermore, even measurement of MOF NP radius after extraction from the microemulsion proved difficult. Samples were freeze dried as part of the extraction procedure. Thus, agglomeration of MOF NPs was encouraged and homogenous resuspension of samples was difficult. Also, the porosity of MOFs produces extra drag during diffusion. Hence, MOF samples diffuses slower than a solid spherical NP of equivalent dimensions. Furthermore, DLS measures the hydrodynamic radius which includes the NP radius along with any molecules bound to its surface e.g. surfactants and water. These estimation errors tend to result in DLS overestimating the size of MOF NPs and not being directly comparable to the size determined by imaging.[71, 81] Furthermore, whilst DLS was available, booking requirements meant it was not available for

general screening. So, whilst significant attempt was made to utilize DLS its actual application was quite limited.

For real time SAXS and *in situ* PXRD a specialized setup is required where the sample flows through a capillary tube in front of the detector. Furthermore, both techniques are generally performed at a synchrotron or with a specialized detector. This obviously precludes these techniques from regular usage during screening in this study. However, further characterization using these techniques would be particularly advantageous. *In situ* PXRD allows the discovery of topological intermediates during synthesis by measuring the PXRD of the solution phase sample over time.[77] This would be particularly useful for topologically rich systems e.g. Zn-IM. SAXS is a technique whereby elastic scattering of X-rays from a sample are measured at small angles (0.1 – 10º). The technique allows for the determination of the size, shape, and distribution of nanoscale structures. In fact, it has been used previous for the determination of NP/ micelle shape and size in real time with non-MOF systems.[105, 215]

Another area of future work is investigating new methods to synthesize MOFs in microemulsions. Despite developing a new microemulsion synthesis protocol for $Zn(IM)_2$ **neb** and UiO-66 which have not previously been synthesized using this method, these syntheses are far from outliers in the existing literature. In both cases, the ligand used could be solubilized in the aqueous phase before incorporation in the microemulsion. In the case of UiO-66, BDC has readily been incorporated in many microemulsion MOFs. However, UiO-66 itself has not been synthesized. This is likely due to the challenges in synthesizing the zirconium SBU. For $Zn(IM)_2$ **neb**, the structure chemically varies from ZIF-8 only by a methyl group. ZIF-8 has been extensively synthesized using microemulsion synthesis. Many MOFs use large hydrophobic ligands which could not be solubilized in these emulsions e.g. NU-1000 or MUF-77. To diversify the MOFs that can be made using microemulsion synthesis a new strategy to solubilize the ligand is required. An interesting approach would be to move away from w/o microemulsions towards systems where this is more easily achieved. Whilst DMF in oil microemulsions would conceivably work, adding DMF is counterproductive towards the goal of green synthesis. Instead, future work should be focussed on ionic liquid in oil microemulsions. Ionic liquids are generally good solvents for organics with tuneable solubility parameters. These solvents are also typically regarded as more environmentally friendly than typical organic solvent.[216] This would allow the selection of an ionic liquid based on the desired MOF. Furthermore, ionic liquid microemulsions have precedent since both ionic liquid in oil and water in ionic liquid microemulsions have been prepared.[217] However, only ionic water in

ionic liquid microemulsions have been used in MOF synthesis making this proposal a substantially new area of research in the MOF field.[108, 109]

5.2. Conclusions

In chapter 1, a brief introduction was given of the history, properties, and applications of MOFs. Further discussion was given into how researchers have been investigating methods such as reaction tuning and microwave synthesis to try and control the physical properties of MOFs on the nanoscale. One such method was to synthesize these materials within a microemulsion. Whilst promising, researcher into this field has been incredibly limited. As such this work was intended as a broad investigation into the conditions that may affect the topology and morphology of nanoscale MOFs synthesize in a TX-100 non-ionic microemulsion system; particularly the ω_o and the addition time.

In chapter 2, this microemulsion system was applied to synthesize sod ZIF-8; one of the most common MOFs in the literature. Several conditions were varied including the ω_o value, ligand to metal equivalents, and the addition time. Results of other conditions were inconsistent. However, changing the addition time from 0 minutes to 2 hours was a reliable method to change the NP size and morphology while maintaining a uniform dispersity. Psuedospherical particles were obtained between 0 and 30 minutes. Increasing this time further resulted in the formation of more typical rhombic dodecahedral, truncated rhombic dodecahedral and cubic crystals. As the time increased there was also a noticeable increase in particle size from 27.3 ± 9.1 to 87.3 ± 22.4 nm. Further work with Zn-IM demonstrated that by changing ω_o two rare topologies were obtained (**neb** and unknown).

In chapter 3, it was demonstrated that microemulsion synthesis could be utilized to synthesize BSA@ZIF-8 NPs. The resulting materials had high LE values up to ~17%. Furthermore, the particle size could be finely tuned from 69.7 ± 15.1 to 87.6 ± 24.5 nm by adjusting the addition time. All samples had a relatively consistent RSD between 21.6 and 27.9%. Microemulsion synthesis was then applied to synthesize BHG@ZIF-8 crystals. BHG was successfully encapsulated despite the reports of significant difficulties in the literature. This marks the first facile and reproducible approach to synthesize this protein@MOF complex. Furthermore, like BSA@ZIF-8 and ZIF-8 the NP size could be tuned by modifying the addition time. Thus, marking this approach as a potentially generic method to produce tuneable sized protein@ZIF-8 NPs.

In chapter 4, microemulsion synthesis was utilized to synthesize UiO-66. It was found that, when synthesized with a 120 and 30 min addition time, psuedospherical nanoparticles were

obtained. Furthermore, the size of UiO-66 NPs could be adjusted from 31.0 ± 8.0 to 4.1 ± 1.1 nm by reducing the ω_o value. This change in NP size was independent of the sample's defectivity. Thus, microemulsion synthesis potentially offers a "defect independent" route to synthesizing size controlled UiO-66 NPs. Further work to investigate tuning the defectivity of UiO-66 within microemulsions by adjusting the addition time or pre-synthesis treatment temperature of the μEM aqueous phase would significantly compliment this work. Nevertheless, the method for synthesizing UiO-66 developed in this work offers a MOF NP product with sub-100 nm dimensions, precise tuneability, and low dispersity using temperature DMF free conditions.

Overall, this works highlights two potential methods to tune the particle morphology of MOF NPs in a TX-100/hexanol w/o microemulsion: addition time and ω_0 modification. As this field is still in its infancy, further work is still required to understand the mechanisms and interactions involved in microemulsion synthesis of MOFs before rational synthesis can be achieved. Nevertheless, the potential application for precise synthetic control and green synthesis demonstrated in this thesis suggests further work is well warranted.

References

1. Yuan, S.; Feng, L.; Wang, K.; Pang, J.; Bosch, M.; Lollar, C.; Sun, Y.; Qin, J.; Yang, X.; Zhang, P.; Wang, Q.; Zou, L.; Zhang, Y.; Zhang, L.; Fang, Y.; Li, J.; Zhou, H.-C., Stable Metal-Organic Frameworks: Design, Synthesis, and Applications. *Adv. Mater.* **2018,** *30* (37), 1704303.

2. Farha, O. K.; Eryazici, I.; Jeong, N. C.; Hauser, B. G.; Wilmer, C. E.; Sarjeant, A. A.; Snurr, R. Q.; Nguyen, S. T.; Yazaydın, A. Ö.; Hupp, J. T., Metal–Organic Framework Materials with Ultrahigh Surface Areas: Is the Sky the Limit? *J. Am. Chem. Soc.* **2012,** *134* (36), 15016-15021.

3. Furukawa, H.; Ko, N.; Go, Y. B.; Aratani, N.; Choi, S. B.; Choi, E.; Yazaydin, A. O.; Snurr, R. Q.; O'Keeffe, M.; Kim, J.; Yaghi, O. M., Ultrahigh Porosity in Metal-Organic Frameworks. *Science* **2010,** *329* (5990), 424-428.

4. Gómez-Gualdrón, D. A.; Moghadam, P. Z.; Hupp, J. T.; Farha, O. K.; Snurr, R. Q., Application of Consistency Criteria To Calculate BET Areas of Micro- And Mesoporous Metal–Organic Frameworks. *J. Am. Chem. Soc.* **2016,** *138* (1), 215-224.

5. Moghadam, P. Z.; Li, A.; Wiggin, S. B.; Tao, A.; Maloney, A. G. P.; Wood, P. A.; Ward, S. C.; Fairen-Jimenez, D., Development of a Cambridge Structural Database Subset: A Collection of Metal–Organic Frameworks for Past, Present, and Future. *Chem. Mater.* **2017,** *29* (7), 2618-2625.

6. Furukawa, H.; Cordova, K. E.; O'Keeffe, M.; Yaghi, O. M., The Chemistry and Applications of Metal-Organic Frameworks. *Science* **2013,** *341* (6149), 1230444-1230444.

7. Groom, C. R.; Bruno, I. J.; Lightfoot, M. P.; Ward, S. C., The Cambridge Structural Database. *Acta Crystallogr. Sect. B-Struct. Sci.Cryst. Eng. Mat.* **2016,** *72*, 171-179.

8. Lock, N.; Wu, Y.; Christensen, M.; Cameron, L. J.; Peterson, V. K.; Bridgeman, A. J.; Kepert, C. J.; Iversen, B. B., Elucidating Negative Thermal Expansion in MOF-5. *J. Phys. Chem. C* **2010,** *114* (39), 16181-16186.

9. Chui, S. S., A Chemically Functionalizable Nanoporous Material [Cu3(TMA)2(H2O)3]n. *Science* **1999,** *283* (5405), 1148-1150.

10. Mark; Mejia-Ariza, R.; Jeroen; Huskens, J., Hierarchical Pore Structures as Highways for Enzymes and Substrates. *Chem.* **2016,** *1* (1), 29-31.

11. Lee, S. J.; Doussot, C.; Baux, A.; Liu, L.; Jameson, G. B.; Richardson, C.; Pak, J. J.; Trousselet, F.; Coudert, F.-X.; Telfer, S. G., Multicomponent Metal–Organic Frameworks as Defect-Tolerant Materials. *Chem. Mater.* **2016,** *28* (1), 368-375.

12. Park, K. S.; Ni, Z.; Cote, A. P.; Choi, J. Y.; Huang, R.; Uribe-Romo, F. J.; Chae, H. K.; O'Keeffe, M.; Yaghi, O. M., Exceptional chemical and thermal stability of zeolitic imidazolate frameworks. *P. Natl. Acad. Sci.* **2006,** *103* (27), 10186-10191.

13. Eddaoudi, M. Y., O. M., Systematic Design of Pore Size and Functionality in Isoreticular MOFs and Their Application in Methane Storage. *Science* **2002,** *295* (5554), 469-472.
14. Destefano, M. R.; Islamoglu, T.; Garibay, S. J.; Hupp, J. T.; Farha, O. K., Room-Temperature Synthesis of UiO-66 and Thermal Modulation of Densities of Defect Sites. *Chem. Mater.* **2017,** *29* (3), 1357-1361.
15. Shi, Q.; Kang, X. Z.; Shi, F. N.; Dong, J. X., Zn-10(Im)(20)center dot 4DBF: an unprecedented 10-nodal zeolitic topology with a 10-MR channel and 10 crystallographically independent Zn atoms. *Chem. Commun.* **2015,** *51* (6), 1131-1134.
16. Noh, K.; Lee, J.; Kim, J., Compositions and Structures of Zeolitic Imidazolate Frameworks. *Isr. J. Chem.* **2018,** *58* (9-10), 1075-1088.
17. Hoskins, B. F.; Robson, R., Design and construction of a new class of scaffolding-like materials comprising infinite polymeric frameworks of 3D-linked molecular rods. A reappraisal of the zinc cyanide and cadmium cyanide structures and the synthesis and structure of the diamond-related frameworks $[N(CH_3)_4][Cu^{I}Zn^{II}(CN)_4]$ and CuI[4,4',4",4"'-tetracyanotetraphenylmethane]$BF_4.xC_6H_5NO_2$. *J. Am. Chem. Soc.* **1990,** *112* (4), 1546-1554.
18. https://apps.webofknowledge.com/Search.do?product=WOS&SID=C6vs6Lw5Ynk6yoRj8ke&search_mode=GeneralSearch&prID=ce63975c-630b-45d6-bab0-bd1bb6923a67 (accessed 22nd February).
19. Metzger, E. D.; Comito, R. J.; Wu, Z. W.; Zhang, G. H.; Dubey, R. C.; Xu, W.; Miller, J. T.; Dinca, M., Highly Selective Heterogeneous Ethylene Dimerization with a Scalable and Chemically Robust MOF Catalyst. *ACS Sustain. Chem. Eng.* **2019,** *7* (7), 6654-6661.
20. Zhang, X.; Huang, Z.; Ferrandon, M.; Yang, D.; Robison, L.; Li, P.; Wang, T. C.; Delferro, M.; Farha, O. K., Catalytic chemoselective functionalization of methane in a metal−organic framework. *Nat. Catal.* **2018,** *1* (5), 356-362.
21. Cornelio, J.; Zhou, T. Y.; Alkas, A.; Telfer, S. G., Systematic Tuning of the Luminescence Output of Multicomponent Metal-Organic Frameworks. *J. Am. Chem. Soc.* **2018,** *140* (45), 15470-15476.
22. Kalinke, L. H. G.; Cangussu, D.; Mon, M.; Bruno, R.; Tiburcio, E.; Lloret, F.; Armentano, D.; Pardo, E.; Ferrando-Soria, J., Metal-Organic Frameworks as Playgrounds for Reticulate Single-Molecule Magnets. *Inorg. Chem.* **2019,** *58* (21), 14498-14506.
23. Yang, C. Q.; Dong, R. H.; Wang, M.; St Petkow, P.; Zhang, Z. T.; Wang, M. C.; Han, P.; Ballabio, M.; Brauninger, S. A.; Liao, Z. Q.; Zhang, J. C.; Schwotzer, F.; Zschech, E.; Klauss, H. H.; Canovas, E.; Kaskel, S.; Bonn, M.; Zhou, S. Q.; Heine, T.; Feng, X. L., A semiconducting layered metal-organic framework magnet. *Nat. Comm.* **2019,** *10*, 9.

24. Chen, Z. J.; Li, P. H.; Anderson, R.; Wang, X. J.; Zhang, X.; Robison, L.; Redfern, L. R.; Moribe, S.; Islamoglu, T.; Gomez-Gualdron, D. A.; Yildirim, T.; Stoddart, J. F.; Farha, O. K., Balancing volumetric and gravimetric uptake in highly porous materials for clean energy. *Science* **2020,** *368* (6488), 297-+.
25. Kim, H.; Rao, S. R.; Kapustin, E. A.; Zhao, L.; Yang, S.; Yaghi, O. M.; Wang, E. N., Adsorption-based atmospheric water harvesting device for arid climates. *Nat. Comm.* **2018,** *9* (1).
26. O'Sullivan, K. Limerick researchers develop material that 'produces water from air'. https://www.irishtimes.com/news/science/limerick-researchers-develop-material-that-produces-water-from-air-1.4065959 (accessed 20 February).
27. Technology. https://molecule.us/the-technology/ (accessed 22 May 2020).
28. Wang, H.; Yao, K. X.; Zhang, Z. J.; Jagiello, J.; Gong, Q. H.; Han, Y.; Li, J., The first example of commensurate adsorption of atomic gas in a MOF and effective separation of xenon from other noble gases. *Chem. Sci.* **2014,** *5* (2), 620-624.
29. McDonald, T. M.; Mason, J. A.; Kong, X.; Bloch, E. D.; Gygi, D.; Dani, A.; Crocellà, V.; Giordanino, F.; Odoh, S. O.; Drisdell, W. S.; Vlaisavljevich, B.; Dzubak, A. L.; Poloni, R.; Schnell, S. K.; Planas, N.; Lee, K.; Pascal, T.; Wan, L. F.; Prendergast, D.; Neaton, J. B.; Smit, B.; Kortright, J. B.; Gagliardi, L.; Bordiga, S.; Reimer, J. A.; Long, J. R., Cooperative insertion of CO2 in diamine-appended metal-organic frameworks. *Nature 519* (7543), 303-308.
30. Li, J. R.; Kuppler, R. J.; Zhou, H. C., Selective gas adsorption and separation in metal-organic frameworks. *Chem. Soc. Rev.* **2009,** *38* (5), 1477-1504.
31. Sholl, D. S.; Lively, R. P., Seven chemical separations to change the world. *Nature* **2016,** *532* (7600), 435-437.
32. Qazvini, O. T.; Babarao, R.; Shi, Z. L.; Zhang, Y. B.; Telfer, S. G., A Robust Ethane-Trapping Metal-Organic Framework with a High Capacity for Ethylene Purification. *J. Am. Chem. Soc.* **2019,** *141* (12), 5014-5020.
33. Carrillo-Carrion, C., Nanoscale metal-organic frameworks as key players in the context of drug delivery: evolution toward theranostic platforms. *Anal. Bioanal. Chem.* **2020,** *412* (1), 37-54.
34. Wang, L.; Zheng, M.; Xie, Z. G., Nanoscale metal-organic frameworks for drug delivery: a conventional platform with new promise. *J. Mat. Chem. B* **2018,** *6* (5), 707-717.
35. Teplerisky, M. H.; Fantham, M.; Li, P.; Wang, T. C.; Mehta, J. P.; Young, L. J.; Moghadam, P. Z.; Hupp, J. T.; Farha, O. K.; Kaminski, C. F.; Fairen-Jimenez, D., Temperature Treatment of Highly Porous Zirconium-Containing Metal-Organic Frameworks Extends Drug Delivery Release. *J. Am. Chem. Soc.* **2017,** *139* (22), 7522-7532.

36. Tan, L. L.; Li, H. W.; Zhou, Y.; Zhang, Y. Y.; Feng, X.; Wang, B.; Yang, Y. W., Zn2+-Triggered Drug Release from Biocompatible Zirconium MOFs Equipped with Supramolecular Gates. *Small* **2015,** *11* (31), 3807-3813.
37. Rieter, W. J.; Pott, K. M.; Taylor, K. M. L.; Lin, W. B., Nanoscale coordination polymers for platinum-based anticancer drug delivery. *J. Am. Chem. Soc.* **2008,** *130* (35), 11584-11585.
38. Cai, W.; Wang, J.; Chu, C.; Chen, W.; Wu, C.; Liu, G., Metal–Organic Framework-Based Stimuli-Responsive Systems for Drug Delivery. *Int. J. Adv. Sci. Technol.* **2019,** *6* (1), 1801526.
39. Sun, C. Y.; Qin, C.; Wang, X. L.; Yang, G. S.; Shao, K. Z.; Lan, Y. Q.; Su, Z. M.; Huang, P.; Wang, C. G.; Wang, E. B., Zeolitic imidazolate framework-8 as efficient pH-sensitive drug delivery vehicle. *Dalton Trans.* **2012,** *41* (23), 6906-6909.
40. Tiwari, A.; Singh, A.; Garg, N.; Randhawa, J. K., Curcumin encapsulated zeolitic imidazolate frameworks as stimuli responsive drug delivery system and their interaction with biomimetic environment. *Sci Rep* **2017,** *7*, 12598.
41. Kaur, H.; Mohanta, G. C.; Gupta, V.; Kukkar, D.; Tyagi, S., Synthesis and characterization of ZIF-8 nanoparticles for controlled release of 6-mercaptopurine drug. *J. Drug Deliv. Sci. Technol.* **2017,** *41*, 106-112.
42. Zheng, C. C.; Wang, Y.; Phua, S. Z. F.; Lim, W. Q.; Zhao, Y. L., ZnO-DOX@ZIF-8 Core-Shell Nanoparticles for pH-Responsive Drug Delivery. *ACS Biomater. Sci. Eng.* **2017,** *3* (10), 2223-2229.
43. Giménez-Marqués, M.; Hidalgo, T.; Serre, C.; Horcajada, P., Nanostructured metal–organic frameworks and their bio-related applications. *Coord Chem Rev* **2016,** *307*, 342-360.
44. Chen, T.-T.; Yi, J.-T.; Zhao, Y.-Y.; Chu, X., Biomineralized Metal–Organic Framework Nanoparticles Enable Intracellular Delivery and Endo-Lysosomal Release of Native Active Proteins. *J. Am. Chem. Soc.* **2018,** *140* (31), 9912-9920.
45. Wang, Z.; Wu, Z. M.; Liu, J. P.; Zhang, W. L., Particle morphology: an important factor affecting drug delivery by nanocarriers into solid tumors. *Expert Opin. Drug Deliv.* **2018,** *15* (4), 379-395.
46. Hoop, M.; Walde, C. F.; Ricco, R.; Mushtaq, F.; Terzopoulou, A.; Chen, X. Z.; deMello, A. J.; Doonan, C. J.; Falcaro, P.; Nelson, B. J.; Puigmarti-Luis, J.; Pane, S., Biocompatibility characteristics of the metal organic framework ZIF-8 for therapeutical applications. *Appl. Mater. Today* **2018,** *11*, 13-21.
47. Baati, T.; Njim, L.; Neffati, F.; Kerkeni, A.; Bouttemi, M.; Gref, R.; Najjar, M. F.; Zakhama, A.; Couvreur, P.; Serre, C.; Horcajada, P., In depth analysis of the in vivo toxicity of nanoparticles of porous iron(III) metal-organic frameworks. *Chem. Sci.* **2013,** *4* (4), 1597-1607.

48. Luzuriaga, M. A.; Welch, R. P.; Dharmarwardana, M.; Benjamin, C. E.; Li, S. B.; Shahrivarkevishahi, A.; Popal, S.; Tuong, L. H.; Creswell, C. T.; Gassensmith, J. J., Enhanced Stability and Controlled Delivery of MOF-Encapsulated Vaccines and Their Immunogenic Response In Vivo. *ACS Appl. Mater. Interfaces* **2019,** *11* (10), 9740-9746.
49. Pan, Y. B.; Wang, S. Q.; He, X. C.; Tang, W. W.; Wang, J. H.; Shao, A. W.; Zhang, J. M., A combination of glioma in vivo imaging and in vivo drug delivery by metal-organic framework based composite nanoparticles. *J. Mat. Chem. B* **2019,** *7* (48), 7683-7689.
50. Lu, K. D.; He, C. B.; Guo, N. N.; Chan, C.; Ni, K. Y.; Lan, G. X.; Tang, H. D.; Pelizzari, C.; Fu, Y. X.; Spiotto, M. T.; Weichselbaum, R. R.; Lin, W. B., Low-dose X-ray radiotherapy-radiodynamic therapy via nanoscale metal-organic frameworks enhances checkpoint blockade immunotherapy. *Nat. Biomed. Eng* **2018,** *2* (8), 600–610.
51. Institute, N. C., Phase I Study of RiMO-301 With Radiation in Advanced Tumors. National Institute of Heath: 2020.
52. Yang, D.; Gates, B. C., Catalysis by Metal Organic Frameworks: Perspective and Suggestions for Future Research. *ACS Catal.* **2019,** *9* (3), 1779-1798.
53. Lee, J.; Farha, O. K.; Roberts, J.; Scheidt, K. A.; Nguyen, S. T.; Hupp, J. T., Metal–organic framework materials as catalysts. *Chem. Soc. Rev.* **2009,** *38* (5), 1450-1459.
54. Fu, Y.; Sun, D.; Chen, Y.; Huang, R.; Ding, Z.; Fu, X.; Li, Z., An Amine-Functionalized Titanium Metal-Organic Framework Photocatalyst with Visible-Light-Induced Activity for CO2 Reduction. *Angew. Chem. Int. Edit.* **2012,** *51* (14), 3364-3367.
55. Zhao, J.; Lee, D. T.; Yaga, R. W.; Hall, M. G.; Barton, H. F.; Woodward, I. R.; Oldham, C. J.; Walls, H. J.; Peterson, G. W.; Parsons, G. N., Ultra-Fast Degradation of Chemical Warfare Agents Using MOF-Nanofiber Kebabs. *Angew. Chem. Int. Edit.* **2016,** *55* (42), 13224-13228.
56. Palomba, J. M.; Credille, C. V.; Kalaj, M.; DeCoste, J. B.; Peterson, G. W.; Tovar, T. M.; Cohen, S. M., High-throughput screening of solid-state catalysts for nerve agent degradation. *Chem. Commun.* **2018,** *54* (45), 5768-5771.
57. Huang, Y. B.; Liang, J.; Wang, X. S.; Cao, R., Multifunctional metal-organic framework catalysts: synergistic catalysis and tandem reactions. *Chem. Soc. Rev.* **2017,** *46* (1), 126-157.
58. Cho, S.-H.; Ma, B.; Nguyen, S. T.; Hupp, J. T.; Albrecht-Schmitt, T. E., A metal–organic framework material that functions as an enantioselective catalyst for olefin epoxidation. *Chem. Commun.* **2006,** (24), 2563-2565.
59. Horike, S.; Dinca, M.; Tamaki, K.; Long, J. R., Size-selective lewis acid catalysis in a microporous metal-organic framework with exposed Mn2+ coordination sites. *J. Am. Chem. Soc.* **2008,** *130* (18), 5854-5855.
60. Öhrström, L., Let's Talk about MOFs-Topology and Terminology of Metal-Organic Frameworks and Why We Need Them. *Crystals 5* (1), 154-162.

61. Delgado-Friedrichs, O.; O'Keeffe, M., Crystal nets as graphs: Terminology and definitions. *J. Solid State Chem.* **2005,** *178* (8), 2480-2485.
62. O'Keeffe, M.; Peskov, M. A.; Ramsden, S. J.; Yaghi, O. M., The Reticular Chemistry Structure Resource (RCSR) Database of, and Symbols for, Crystal Nets. *Accounts Chem. Res.* **2008,** *41* (12), 1782-1789.
63. Liu, Y. Z.; O'Keeffe, M., Regular Figures, Minimal Transitivity, and Reticular Chemistry. *Isr. J. Chem.* **2018,** *58* (9-10), 962-970.
64. Xing, J. F.; Schweighauser, L.; Okada, S.; Harano, K.; Nakamura, E., Atomistic structures and dynamics of prenucleation clusters in MOF-2 and MOF-5 syntheses. *Nat. Comm.* **2019,** *10*, 2345.
65. Lyu, J.; Zhang, X.; Otake, K.-I.; Wang, X.; Li, P.; Li, Z.; Chen, Z.; Zhang, Y.; Wasson, M. C.; Yang, Y.; Bai, P.; Guo, X.; Islamoglu, T.; Farha, O. K., Topology and porosity control of metal–organic frameworks through linker functionalization. *Chem. Sci.* **2019,** *10* (4), 1186-1192.
66. Connolly, B. M.; Aragones-Anglada, M.; Gandara-Loe, J.; Danaf, N. A.; Lamb, D. C.; Mehta, J. P.; Vulpe, D.; Wuttke, S.; Silvestre-Albero, J.; Moghadam, P. Z.; Wheatley, A. E. H.; Fairen-Jimenez, D., Tuning porosity in macroscopic monolithic metal-organic frameworks for exceptional natural gas storage. *Nat. Comm.* **2019,** *10*, 11.
67. Mao, Y. Y.; Cao, W.; Li, J. W.; Liu, Y.; Ying, Y. L.; Sun, L. W.; Peng, X. S., Enhanced gas separation through well-intergrown MOF membranes: seed morphology and crystal growth effects. *J. Mater. Chem. A* **2013,** *1* (38), 11711-11716.
68. Wang, B.; Liu, W.; Zhang, W.; Liu, J., Nanoparticles@nanoscale metal-organic framework composites as highly efficient heterogeneous catalysts for size- and shape-selective reactions. *Nano Res.* **2017,** *10* (11), 3826-3835.
69. Chulkaivalsucharit, P.; Wu, X.; Ge, J., Synthesis of enzyme-embedded metal–organic framework nanocrystals in reverse micelles. *RSC Advances* **2015,** *5* (123), 101293-101296.
70. Avci, C.; Imaz, I.; Carne-Sanchez, A.; Pariente, J. A.; Tasios, N.; Perez-Carvajal, J.; Alonso, M. I.; Blanco, A.; Dijkstra, M.; Lopez, C.; Maspoch, D., Self-assembly of polyhedral metal-organic framework particles into three-dimensional ordered superstructures. *Nature Chem.* **2018,** *10* (1), 78-84.
71. Marshall, C. R.; Staudhammer, S. A.; Brozek, C. K., Size control over metal-organic framework porous nanocrystals. *Chem. Sci.* **2019,** *10* (41), 9396-9408.
72. Danaei, M.; Dehghankhold, M.; Ataei, S.; Davarani, F. H.; Javanmard, R.; Dokhani, A.; Khorasani, S.; Mozafari, M. R., Impact of Particle Size and Polydispersity Index on the Clinical Applications of Lipidic Nanocarrier Systems. *Pharmaceutics* **2018,** *10* (2), 51.
73. Polte, J., Fundamental growth principles of colloidal metal nanoparticles - a new perspective. *Crystengcomm* **2015,** *17* (36), 6809-6830.

74. Fitzner, M.; Sosso, G. C.; Cox, S. J.; Michaelides, A., The Many Faces of Heterogeneous Ice Nucleation: Interplay Between Surface Morphology and Hydrophobicity. *J. Am. Chem. Soc.* **2015,** *137* (42), 13658-13669.
75. Zobrist, B.; Marcolli, C.; Peter, T.; Koop, T., Heterogeneous ice nucleation in aqueous solutions: the role of water activity. *J. Phys. Chem. A* **2008,** *112* (17), 3965-3975.
76. Van Vleet, M. J.; Weng, T. T.; Li, X. Y.; Schmidt, J. R., In Situ, Time-Resolved, and Mechanistic Studies of Metal-Organic Framework Nucleation and Growth. *Chem. Rev.* **2018,** *118* (7), 3681-3721.
77. Yeung, H. H. M.; Sapnik, A. F.; Massingberd-Mundy, F.; Gaultois, M. W.; Wu, Y.; Fraser, D. A. X.; Henke, S.; Pallach, R.; Heidenreich, N.; Magdysyuk, O. V.; Vo, N. T.; Goodwin, A. L., Control of Metal-Organic Framework Crystallization by Metastable Intermediate Pre-equilibrium Species. *Angew. Chem. Int. Edit.* **2019,** *58* (2), 566-571.
78. Barmparis, G. D.; Lodziana, Z.; Lopez, N.; Remediakis, I. N., Nanoparticle shapes by using Wulff constructions and first-principles calculations. *Beilstein J. Nanotechnol.* **2015,** *6*, 361-368.
79. Umemura, A.; Diring, S.; Furukawa, S.; Uehara, H.; Tsuruoka, T.; Kitagawa, S., Morphology Design of Porous Coordination Polymer Crystals by Coordination Modulation. *J. Am. Chem. Soc.* **2011,** *133* (39), 15506-15513.
80. Schejn, A.; Balan, L.; Falk, V.; Aranda, L.; Medjahdi, G.; Schneider, R., Controlling ZIF-8 nano- and microcrystal formation and reactivity through zinc salt variations. *CrystEngComm* **2014,** *16* (21), 4493-4500.
81. Decker, G. E.; Stillman, Z.; Attia, L.; Fromen, C. A.; Bloch, E. D., Controlling Size, Defectiveness, and Fluorescence in Nanoparticle UiO-66 through Water and Ligand Modulation. *Chem. Mater.* **2019,** *31* (13), 4831–4839.
82. Kida, K.; Okita, M.; Fujita, K.; Tanaka, S.; Miyake, Y., Formation of high crystalline ZIF-8 in an aqueous solution. *CrystEngComm* **2013,** *15* (9), 1794-1801.
83. Schafer, P.; Kapteijn, F.; van der Veen, M. A.; Domke, K. F., Understanding the Inhibiting Effect of BTC on CuBTC Growth through Experiment and Modeling. *Cryst. Growth Des.* **2017,** *17* (11), 5603-5607.
84. Biemmi, E.; Christian, S.; Stock, N.; Bein, T., High-throughput screening of synthesis parameters in the formation of the metal-organic frameworks MOF-5 and HKUST-1. *Microporous Mesoporous Mat.* **2009,** *117* (1-2), 111-117.
85. Khan, N. A.; Jhung, S. H., Synthesis of metal-organic frameworks (MOFs) with microwave or ultrasound: Rapid reaction, phase-selectivity, and size reduction. *Coord Chem Rev* **2015,** *285*, 11-23.
86. Haque, E.; Khan, N. A.; Park, J. H.; Jhung, S. H., Synthesis of a Metal-Organic Framework Material, Iron Terephthalate, by Ultrasound, Microwave, and Conventional Electric Heating: A Kinetic Study. *Chem. Eur. J.* **2010,** *16* (3), 1046-1052.

87. Jhung, S. H.; Lee, J. H.; Chang, J. S., Microwave synthesis of a nanoporous hybrid material, chromium trimesate. *Bull Korean Chem Soc* **2005,** *26* (6), 880-881.
88. Laybourn, A.; Katrib, J.; Ferrari-John, R. S.; Morris, C. G.; Yang, S. H.; Udoudo, O.; Easun, T. L.; Dodds, C.; Champness, N. R.; Kingman, S. W.; Schroder, M., Metal-organic frameworks in seconds via selective microwave heating. *J. Mater. Chem. A* **2017,** *5* (16), 7333-7338.
89. Katsenis, A. D.; Puškarić, A.; Štrukil, V.; Mottillo, C.; Julien, P. A.; Užarević, K.; Pham, M.-H.; Do, T.-O.; Kimber, S. A. J.; Lazić, P.; Magdysyuk, O.; Dinnebier, R. E.; Halasz, I.; Friščić, T., In situ X-ray diffraction monitoring of a mechanochemical reaction reveals a unique topology metal-organic framework. *Nat. Comm.* **2015,** *6* (1), 6662.
90. Ma, M.; Zacher, D.; Zhang, X. N.; Fischer, R. A.; Metzler-Nolte, N., A Method for the Preparation of Highly Porous, Nanosized Crystals of Isoreticular Metal-Organic Frameworks. *Cryst. Growth Des.* **2011,** *11* (1), 185-189.
91. Pan, Y.; Heryadi, D.; Zhou, F.; Zhao, L.; Lestari, G.; Su, H.; Lai, Z., Tuning the crystal morphology and size of zeolitic imidazolate framework-8 in aqueous solution by surfactants. *CrystEngComm* **2011,** *13* (23), 6937-6940.
92. Hoar, T. P.; Schulman, J. H., Transparent water-in-oil dispersions the oleopathic hydro-micelle. *Nature* **1943,** *152*, 102-103.
93. Cosgrove, T., Microemulsions. In *Colloid Science: Principles, Methods and Applications*, 2 ed.; John Wiley & Sons, I., Ed. 2010.
94. Fanun, M., *Microemulsions : properties and applications*. CRC Press: Boca Raton, FL, 2009.
95. Zemb, T. N.; Klossek, M.; Lopian, T.; Marcus, J.; Schoettl, S.; Horinek, D.; Prevost, S. F.; Touraud, D.; Diat, O.; Marcelja, S.; Kunz, W., How to explain microemulsions formed by solvent mixtures without conventional surfactants. *P. Natl. Acad. Sci.* **2016,** *113* (16), 4260-4265.
96. Domschke, M.; Kraska, M.; Feile, R.; Stuhn, B., AOT microemulsions: droplet size and clustering in the temperature range between the supercooled state and the upper phase boundary. *Soft Matter* **2013,** *9* (48), 11503-11512.
97. Kopanichuk, I. V.; Vedenchuk, E. A.; Koneva, A. S.; Vanin, A. A., Structural Properties of Span 80/Tween 80 Reverse Micelles by Molecular Dynamics Simulations. *Journal of Physical Chemistry B* **2018,** *122* (33), 8047-8055.
98. Lawrence, M. J.; Rees, G. D., Microemulsion-based media as novel drug delivery systems. *Adv. Drug Deliv. Rev.* **2012,** *64*, 175-193.
99. Khalil, R. A.; Zarari, A. H. A., Theoretical estimation of the critical packing parameter of amphiphilic self-assembled aggregates. *Appl. Surf. Sci.* **2014,** *318*, 85-89.
100. Boutonnet, M.; Kizling, J.; Stenius, P.; Maire, G., The preparation of monodisperse colloidal metal particles from microemulsions. *Colloids Surf.* **1982,** *5* (3), 209-225.

101. Eastoe, J.; Hollamby, M. J.; Hudson, L., Recent advances in nanoparticle synthesis with reversed micelles. *Adv. Colloid Interface Sci.* **2006,** *128*, 5-15.
102. Malik, M. A.; Wani, M. Y.; Hashim, M. A., Microemulsion method: A novel route to synthesize organic and inorganic nanomaterials. *Arab. J. Chem.* **2012,** *5* (4), 397-417.
103. Li, L.; Qing-Sheng, W.; Ya-Ping, D.; Pei-Ming, W., Control synthesis of semiconductor ZnSe quasi-nanospheres by reverse micelles soft template. **2005,** *59* (13), 1623-1626.
104. Calandra, P.; Longo, A.; Marcianò, V.; Turco Liveri, V., Physicochemical Investigation of Lightfast AgCl and AgBr Nanoparticles Synthesized by a Novel Solid−Solid Reaction. **2003,** *107* (28), 6724-6729.
105. Sunaina; Sethi, V.; Mehta, S. K.; Ganguli, A. K.; Vaidya, S., Understanding the role of co-surfactants in microemulsions on the growth of copper oxalate using SAXS. *Phys. Chem.* **2019,** *21* (1), 336-348.
106. Rieter, W. J.; Taylor, K. M. L.; An, H.; Lin, W.; Lin, W., Nanoscale Metal−Organic Frameworks as Potential Multimodal Contrast Enhancing Agents. *J. Am. Chem. Soc.* **2006,** *128* (28), 9024-9025.
107. Sargazi, G.; Afzali, D.; Mostafavi, A., A novel synthesis of a new thorium (IV) metal organic framework nanostructure with well controllable procedure through ultrasound assisted reverse micelle method. *Ultrason. Sonochem.* **2018,** *41*, 234-251.
108. Zheng, W.; Hao, X.; Zhao, L.; Sun, W., Controllable Preparation of Nanoscale Metal–Organic Frameworks by Ionic Liquid Microemulsions. *Ind. Eng. Chem. Res.* **2017,** *56* (20), 5899-5905.
109. Shang, W.; Kang, X.; Ning, H.; Zhang, J.; Zhang, X.; Wu, Z.; Mo, G.; Xing, X.; Han, B., Shape and Size Controlled Synthesis of MOF Nanocrystals with the Assistance of Ionic Liquid Mircoemulsions. *Langmuir* **2013,** *29* (43), 13168-13174.
110. Rieter, W. J.; Taylor, K. M. L.; An, H. Y.; Lin, W. L.; Lin, W. B., Nanoscale metal-organic frameworks as potential multimodal contrast enhancing agents. *J. Am. Chem. Soc.* **2006,** *128* (28), 9024-9025.
111. Xu, H.; Liu, F.; Cui, Y.; Chen, B.; Qian, G., A luminescent nanoscale metal–organic framework for sensing of nitroaromatic explosives. *Chem. Commun.* **2011,** *47* (11), 3153.
112. Sun, W.; Zhai, X.; Zhao, L., Synthesis of ZIF-8 and ZIF-67 nanocrystals with well-controllable size distribution through reverse microemulsions. *Chem. Eng. J.* **2016,** *289*, 59-64.
113. Taylor, K. M. L.; Rieter, W. J.; Lin, W. B., Manganese-Based Nanoscale Metal-Organic Frameworks for Magnetic Resonance Imaging. *J. Am. Chem. Soc.* **2008,** *130* (44), 14358–14359.
114. Xia, T.; Zhu, F.; Jiang, K.; Cui, Y.; Yu, Y.; Qian, G., A Luminescent Ratiometric pH Sensor Based on Nanoscale and Biocompatible Eu/Tb-mixed MOF. *Dalton Trans.* **2017**.

115. Rodpun, K.; Lucas, N. T.; Tan, E. W.; Meledandri, C. J., Development of Solvent-Dispersible Coordination Polymer Nanocrystals and Application as Efficient Heterogeneous Catalysts. *Cryst. Growth Des.* **2016,** *16* (7), 3940-3946.
116. Liu, Y.; Zhang, L.; Willis, B. G.; Mustain, W. E., Importance of Particle Size and Distribution in Achieving High-Activity, High-Stability Oxygen Reduction Catalysts. *ACS Catal.* **2015,** *5* (3), 1560-1567.
117. Fang, Z. G.; Patterson, B. R.; Turner, M. E., Modeling particle size distributions by the Weibull distribution function. *Mater. Charact.* **1993,** *31* (3), 177-182.
118. Tian, Y.-Q.; Yao, S.-Y.; Gu, D.; Cui, K.-H.; Guo, D.-W.; Zhang, G.; Chen, Z.-X.; Zhao, D.-Y., Cadmium Imidazolate Frameworks with Polymorphism, High Thermal Stability, and a Large Surface Area. *Chem. Eur. J.* **2010,** *16* (4), 1137-1141.
119. Karagiaridi, O.; Bury, W.; Sarjeant, A. A.; Stern, C. L.; Farha, O. K.; Hupp, J. T., Synthesis and characterization of isostructural cadmium zeolitic imidazolate frameworks via solvent-assisted linker exchange. *Chem. Sci.* **2012,** *3* (11), 3256-3260.
120. Battisti, A.; Taioli, S.; Garberoglio, G., Zeolitic imidazolate frameworks for separation of binary mixtures of CO2, CH4, N-2 and H-2: A computer simulation investigation. *Microporous Mesoporous Mat.* **2011,** *143* (1), 46-53.
121. Huang, X. C.; Lin, Y. Y.; Zhang, J. P.; Chen, X. M., Ligand-directed strategy for zeolite-type metal-organic frameworks: Zinc(II) imidazolates with unusual zeolitic topologies. *Angew. Chem. Int. Edit.* **2006,** *45* (10), 1557-1559.
122. Van Cleuvenbergen, S.; Smith, Z. J.; Deschaume, O.; Bartic, C.; Wachsmann-Hogiu, S.; Verbiest, T.; van der Veen, M. A., Morphology and structure of ZIF-8 during crystallisation measured by dynamic angle-resolved second harmonic scattering. *Nat. Comm.* **2018,** *9*, 3418.
123. Polyzoidis, A.; Altenburg, T.; Schwarzer, M.; Loebbecke, S.; Kaskel, S., Continuous microreactor synthesis of ZIF-8 with high space-time-yield and tunable particle size. *Chem. Eng. J.* **2016,** *283*, 971-977.
124. Wei, T.-H.; Wu, S.-H.; Huang, Y.-D.; Lo, W.-S.; Williams, B. P.; Chen, S.-Y.; Yang, H.-C.; Hsu, Y.-S.; Lin, Z.-Y.; Chen, X.-H.; Kuo, P.-E.; Chou, L.-Y.; Tsung, C.-K.; Shieh, F.-K., Rapid mechanochemical encapsulation of biocatalysts into robust metal–organic frameworks. *Nat. Comm.* **2019,** *10* (1), 5002.
125. Cravillon, J.; MüNzer, S.; Lohmeier, S.-J.; Feldhoff, A.; Huber, K.; Wiebcke, M., Rapid Room-Temperature Synthesis and Characterization of Nanocrystals of a Prototypical Zeolitic Imidazolate Framework. *Chem. Mater.* **2009,** *21* (8), 1410-1412.
126. Pan, Y. C.; Liu, Y. Y.; Zeng, G. F.; Zhao, L.; Lai, Z. P., Rapid synthesis of zeolitic imidazolate framework-8 (ZIF-8) nanocrystals in an aqueous system. *Chem. Commun.* **2011,** *47* (7), 2071-2073.

127. Cravillon, J.; Schroder, C. A.; Bux, H.; Rothkirch, A.; Caro, J.; Wiebcke, M., Formate modulated solvothermal synthesis of ZIF-8 investigated using time-resolved in situ X-ray diffraction and scanning electron microscopy. *Crystengcomm* **2012,** *14* (2), 492-498.
128. Zheng, G.; Chen, Z.; Sentosun, K.; Perez-Juste, I.; Bals, S.; Liz-Marzan, L. M.; Pastoriza-Santos, I.; Perez-Juste, J.; Hong, M., Shape control in ZIF-8 nanocrystals and metal nanoparticles@ZIF-8 heterostructures. *Nanoscale* **2017,** *9* (43), 16645-16651.
129. Cravillon, J.; Nayuk, R.; Springer, S.; Feldhoff, A.; Huber, K.; Wiebcke, M., Controlling Zeolitic Imidazolate Framework Nano- and Microcrystal Formation: Insight into Crystal Growth by Time-Resolved In Situ Static Light Scattering. *Chem. Mater.* **2011,** *23* (8), 2130-2141.
130. Qin, J. N.; Wang, S. B.; Wang, X. C., Visible-light reduction CO2 with dodecahedral zeolitic imidazolate framework ZIF-67 as an efficient co-catalyst. *Appl. Catal. B-Environ.* **2017,** *209*, 476-482.
131. Bennett, T. D.; Goodwin, A. L.; Dove, M. T.; Keen, D. A.; Tucker, M. G.; Barney, E. R.; Soper, A. K.; Bithell, E. G.; Tan, J. C.; Cheetham, A. K., Structure and Properties of an Amorphous Metal-Organic Framework. *Phys. Rev. Lett.* **2010,** *104* (11), 115503.
132. Wang, Y. H.; Fin, H.; Ma, Q.; Mo, K.; Mao, H. Z.; Feldhoff, A.; Cao, X. Z.; Li, Y. S.; Pan, F. S.; Jiang, Z. Y., A MOF Glass Membrane for Gas Separation. *Angew. Chem. Int. Edit.* **2020,** *59* (11), 4365-4369.
133. Lan, X. C.; Huang, N.; Wang, J. F.; Wang, T. F., A general and facile strategy for precisely controlling the crystal size of monodispersed metal-organic frameworks via separating the nucleation and growth. *Chem. Commun.* **2018,** *54* (6), 584-587.
134. Vaidya, S.; Rastogi, P.; Agarwal, S.; Gupta, S. K.; Ahmad, T.; Antonelli, A. M.; Ramanujachary, K. V.; Lofland, S. E.; Ganguli, A. K., Nanospheres, nanocubes, and nanorods of nickel oxalate: Control of shape and size by surfactant and solvent. *J. Phys. Chem. C* **2008,** *112* (33), 12610-12615.
135. Xu, X. X., Controllable synthesis of ultra-small metal-organic framework nanocrystals composed of copper(II) carboxylates. *Nanoscale* **2016,** *8* (37), 16725-16732.
136. Chen, R. Z.; Yao, J. F.; Gu, Q. F.; Smeets, S.; Baerlocher, C.; Gu, H. X.; Zhu, D. R.; Morris, W.; Yaghi, O. M.; Wang, H. T., A two-dimensional zeolitic imidazolate framework with a cushion-shaped cavity for CO2 adsorption. *Chem. Commun.* **2013,** *49* (82), 9500-9502.
137. Saliba, D.; Ammar, M.; Rammal, M.; Al-Ghoul, M.; Hmadeh, M., Crystal Growth of ZIF-8, ZIF-67, and Their Mixed-Metal Derivatives. *J. Am. Chem. Soc.* **2018,** *140* (5), 1812-1823.
138. Wang, X. G.; Cheng, Q.; Yu, Y.; Zhang, X. Z., Controlled Nucleation and Controlled Growth for Size Predicable Synthesis of Nanoscale Metal-Organic Frameworks (MOFs): A General and Scalable Approach. *Angew. Chem. Int. Edit.* **2018,** *57* (26), 7836-7840.

139. Schroder, C. A.; Saha, S.; Huber, K.; Leoni, S.; Wiebcke, M., Metastable metal imidazolates: development of targeted syntheses by combining experimental and theoretical investigations of the formation mechanisms. *Z. Krist.-Cryst. Mater.* **2014,** *229* (12), 807-822.
140. Tian, Y. Q.; Cai, C. X.; Ren, X. M.; Duan, C. Y.; Xu, Y.; Gao, S.; You, X. Z., The silica-like extended polymorphism of cobalt(II) imidazolate three-dimensional frameworks: X-ray single-crystal structures and magnetic properties. *Chem. Eur. J.* **2003,** *9* (22), 5673-5685.
141. Nadar, S. S.; Rathod, V. K., Facile synthesis of glucoamylase embedded metal-organic frameworks (glucoamylase-MOF) with enhanced stability. *Int. J. Biol. Macromol.* **2017,** *95*, 511-519.
142. Wang, H.; Zhao, Z.; Liu, Y.; Shao, C.; Bian, F.; Zhao, Y., Biomimetic enzyme cascade reaction system in microfluidic electrospray microcapsules. *Sci. Adv.* **2018,** *4* (6), eaat2816.
143. Beloqui, A.; Kobitski, A. Y.; Nienhaus, G. U.; Delaittre, G., A simple route to highly active single-enzyme nanogels. *Chem. Sci.* **2018,** *9* (4), 1006-1013.
144. Yan, B.; Boyer, J.-C.; Habault, D.; Branda, N. R.; Zhao, Y., Near Infrared Light Triggered Release of Biomacromolecules from Hydrogels Loaded with Upconversion Nanoparticles. *J. Am. Chem. Soc.* **2012,** *134* (40), 16558-16561.
145. Xu, H.; Dai, H.; Chen, G., Direct electrochemistry and electrocatalysis of hemoglobin protein entrapped in graphene and chitosan composite film. *Talanta* **2010,** *81* (1-2), 334-338.
146. Lian, X. Z.; Fang, Y.; Joseph, E.; Wang, Q.; Li, J. L.; Banerjee, S.; Lollar, C.; Wang, X.; Zhou, H. C., Enzyme-MOF (metal-organic framework) composites. *Chem. Soc. Rev.* **2017,** *46* (11), 3386-3401.
147. Matsuura, Y.; Takehira, M.; Joti, Y.; Ogasahara, K.; Tanaka, T.; Ono, N.; Kunishima, N.; Yutani, K., Thermodynamics of protein denaturation at temperatures over 100 degrees C: CutA1 mutant proteins substituted with hydrophobic and charged residues. *Sci Rep* **2015,** *5*.
148. England, J. L.; Haran, G., Role of Solvation Effects in Protein Denaturation: From Thermodynamics to Single Molecules and Back. In *Annu. Rev. Phys. Chem.*, Leone, S. R.; Cremer, P. S.; Groves, J. T.; Johnson, M. A., Eds. 2011; Vol. 62, pp 257-277.
149. Liang, K.; Ricco, R.; Doherty, C. M.; Styles, M. J.; Bell, S.; Kirby, N.; Mudie, S.; Haylock, D.; Hill, A. J.; Doonan, C. J.; Falcaro, P., Biomimetic mineralization of metal-organic frameworks as protective coatings for biomacromolecules. *Nat. Comm.* **2015,** *6* (1), 7240.
150. Gascón, V.; Castro-Miguel, E.; Díaz-García, M.; Blanco, R. M.; Sanchez-Sanchez, M., In situ and post-synthesis immobilization of enzymes on nanocrystalline MOF platforms to yield active biocatalysts. *J. Chem. Technol. Biotechnol.* **2017,** *92* (10), 2583-2593.
151. Liao, F. S.; Lo, W. S.; Hsu, Y. S.; Wu, C. C.; Wang, S. C.; Shieh, F. K.; Morabito, J. V.; Chou, L. Y.; Wu, K. C. W.; Tsung, C. K., Shielding against Unfolding by Embedding

Enzymes in Metal-Organic Frameworks via a de Novo Approach. *J. Am. Chem. Soc.* **2017,** *139* (19), 6530-6533.
152. Lykourinou, V.; Chen, Y.; Wang, X.-S.; Meng, L.; Hoang, T.; Ming, L.-J.; Musselman, R. L.; Ma, S., Immobilization of MP-11 into a Mesoporous Metal–Organic Framework, MP-11@mesoMOF: A New Platform for Enzymatic Catalysis. *J. Am. Chem. Soc.* **2011,** *133* (27), 10382-10385.
153. Chen, Y.; Han, S.; Li, X.; Zhang, Z.; Ma, S., Why Does Enzyme Not Leach from Metal–Organic Frameworks (MOFs)? Unveiling the Interactions between an Enzyme Molecule and a MOF. *Inorg. Chem.* **2014,** *53* (19), 10006-10008.
154. Knedel, T. O.; Ricklefs, E.; Schlüsener, C.; Urlacher, V. B.; Janiak, C., Laccase Encapsulation in ZIF-8 Metal-Organic Framework Shows Stability Enhancement and Substrate Selectivity. *ChemistryOpen* **2019,** *8* (11), 1337-1344.
155. Li, Z. X.; Xia, H.; Li, S. M.; Pang, J. F.; Zhu, W.; Jiang, Y. B., In situ hybridization of enzymes and their metal-organic framework analogues with enhanced activity and stability by biomimetic mineralisation. *Nanoscale* **2017,** *9* (40), 15298-15302.
156. Raja, D. S.; Liu, W. L.; Huang, H. Y.; Lin, C. H., Immobilization of Protein on Nanoporous Metal-Organic Framework Materials. *Comments Inorg. Chem.* **2015,** *35* (6), 332-350.
157. Cui, J. D.; Ren, S. Z.; Sun, B. T.; Jia, S. R., Optimization protocols and improved strategies for metal-organic frameworks for immobilizing enzymes: Current development and future challenges. *Coord Chem Rev* **2018,** *370*, 22-41.
158. Chen, Y.; Lykourinou, V.; Vetromile, C.; Hoang, T.; Ming, L.-J.; Larsen, R. W.; Ma, S., How Can Proteins Enter the Interior of a MOF? Investigation of Cytochrome c Translocation into a MOF Consisting of Mesoporous Cages with Microporous Windows. *J. Am. Chem. Soc.* **2012,** *134* (32), 13188-13191.
159. Li, P.; Justin; Ashlee; Ernesto; Peyman; Randall; Mrksich, M.; Joseph; Omar, Toward Design Rules for Enzyme Immobilization in Hierarchical Mesoporous Metal-Organic Frameworks. *Chem* **2016,** *1* (1), 154-169.
160. Lian, X.; Chen, Y.-P.; Liu, T.-F.; Zhou, H.-C., Coupling two enzymes into a tandem nanoreactor utilizing a hierarchically structured MOF. *Chem. Sci.* **2016,** *7* (12), 6969-6973.
161. Chen, Y. J.; Li, P.; Modica, J. A.; Drout, R. J.; Farha, O. K., Acid-Resistant Mesoporous Metal-Organic Framework toward Oral Insulin Delivery: Protein Encapsulation, Protection, and Release. *J. Am. Chem. Soc.* **2018,** *140* (17), 5678-5681.
162. Li, P.; Chen, Q.; Wang, T. C.; Vermeulen, N. A.; Mehdi, B. L.; Dohnalkoya, A.; Browning, N. D.; Shen, D.; Anderson, R.; Gomez-Gualdron, D. A.; Cetin, F. M.; Jagiello, J.; Asiri, A. M.; Stoddart, J. F.; Farhal, O. K., Hierarchically Engineered Mesoporous Metal-Organic Frameworks toward Cell-free Immobilized Enzyme Systems. *Chem* **2018,** *4* (5), 1022-1034.

163. Feng, L.; Wang, K.-Y.; Lv, X.-L.; Yan, T.-H.; Zhou, H.-C., Hierarchically porous metal–organic frameworks: synthetic strategies and applications. *Natl. Sci. Rev.* **2019**, nwz170.
164. Lyu, F.; Zhang, Y.; Zare, R. N.; Ge, J.; Liu, Z., One-Pot Synthesis of Protein-Embedded Metal–Organic Frameworks with Enhanced Biological Activities. *Nano Lett.* **2014,** *14* (10), 5761-5765.
165. Liang, K.; Coghlan, C. J.; Bell, S. G.; Doonan, C.; Falcaro, P., Enzyme encapsulation in zeolitic imidazolate frameworks: a comparison between controlled co-precipitation and biomimetic mineralisation. *Chem. Commun.* **2016,** *52* (3), 473-476.
166. Liang, K.; Riccò, R.; Doherty, C.; Styles, M. J.; Falcaro, P., Amino acids as biomimetic crystallization agents for the synthesis of ZIF-8 particles. *CrystEngComm* **2016,** *18* (23), 4264-4267
167. Loera-Serna, S.; Zarate-Rubio, J.; Medina-Velazquez, D. Y.; Zhang, L.; Ortiz, E., Encapsulation of urea and caffeine in $Cu_3(BTC)_2$ metal-organic framework. *Surf. Innov.* **2016,** *4* (2), 76-87.
168. Liang, K.; Richardson, J. J.; Cui, J. W.; Caruso, F.; Doonan, C. J.; Falcaro, P., Metal-Organic Framework Coatings as Cytoprotective Exoskeletons for Living Cells. *Adv. Mater.* **2016,** *28* (36), 7910-7914.
169. Alsaiari, S. K.; Patil, S.; Alyami, M.; Alamoudi, K. O.; Aleisa, F. A.; Merzaban, J. S.; Li, M.; Khashab, N. M., Endosomal Escape and Delivery of CRISPR/Cas9 Genome Editing Machinery Enabled by Nanoscale Zeolitic Imidazolate Framework. *J. Am. Chem. Soc.* **2018,** *140* (1), 143-146.
170. Li, S. B.; Dharmarwardana, M.; Welch, R. P.; Benjamin, C. E.; Shamir, A. M.; Nielsen, S. O.; Gassensmith, J. J., Investigation of Controlled Growth of Metal-Organic Frameworks on Anisotropic Virus Particles. *ACS Appl. Mater. Interfaces* **2018,** *10* (21), 18161-18169.
171. Shieh, F. K.; Wang, S. C.; Yen, C. I.; Wu, C. C.; Dutta, S.; Chou, L. Y.; Morabito, J. V.; Hu, P.; Hsu, M. H.; Wu, K. C. W.; Tsung, C. K., Imparting Functionality to Biocatalysts via Embedding Enzymes into Nanoporous Materials by a de Novo Approach: Size-Selective Sheltering of Catalase in Metal-Organic Framework Microcrystals. *J. Am. Chem. Soc.* **2015,** *137* (13), 4276-4279.
172. Gascon, V.; Carucci, C.; Jimenez, M. B.; Blanco, R. M.; Sanchez-Sanchez, M.; Magner, E., Rapid InSitu Immobilization of Enzymes in Metal-Organic Framework Supports under Mild Conditions. *Chemcatchem* **2017,** *9* (7), 1182-1186.
173. Pu, S. J.; Zhang, X.; Yang, C. L.; Naseer, S.; Zhang, X. T.; Ouyang, J.; Li, D. L.; Yang, J. F., The effects of NaCl on enzyme encapsulation by zeolitic imidazolate frameworks-8. *Enzyme Microb. Technol.* **2019,** *122*, 1-6.
174. Liang, W.; Xu, H.; Carraro, F.; Maddigan, N. K.; Li, Q.; Bell, S. G.; Huang, D. M.; Tarzia, A.; Solomon, M. B.; Amenitsch, H.; Vaccari, L.; Sumby, C. J.; Falcaro, P.; Doonan,

C. J., Enhanced Activity of Enzymes Encapsulated in Hydrophilic Metal–Organic Frameworks. *J. Am. Chem. Soc.* **2019,** *141* (6), 2348-2355.
175. Hu, C.; Bai, Y. X.; Hou, M.; Wang, Y. S.; Wang, L. C.; Cao, X.; Chan, C.; Sun, H.; Li, W. B.; Ge, J.; Ren, K. N., Defect-induced activity enhancement of enzyme-encapsulated metal-organic frameworks revealed in microfluidic gradient mixing synthesis. *Sci. Adv.* **2020,** *6* (5).
176. Cui, J. D.; Feng, Y. X.; Lin, T.; Tan, Z. L.; Zhong, C.; Jia, S. R., Mesoporous Metal-Organic Framework with Well-Defined Cruciate Flower-Like Morphology for Enzyme Immobilization. *ACS Appl. Mater. Interfaces* **2017,** *9* (12), 10587-10594.
177. Wu, X. L.; Yue, H.; Zhang, Y. Y.; Gao, X. Y.; Li, X. Y.; Wang, L. C.; Cao, Y. F.; Hou, M.; An, H. X.; Zhang, L.; Li, S.; Ma, J. Y.; Lin, H.; Fu, Y. A.; Gu, H. K.; Lou, W. Y.; Wei, W.; Zare, R. N.; Ge, J., Packaging and delivering enzymes by amorphous metal-organic frameworks. *Nat. Comm.* **2019,** *10*, 5165
178. Maddigan, N. K.; Tarzia, A.; Huang, D. M.; Sumby, C. J.; Bell, S. G.; Falcaro, P.; Doonan, C. J., Protein surface functionalisation as a general strategy for facilitating biomimetic mineralisation of ZIF-8. *Chem. Sci.* **2018,** *9* (18), 4217-4223.
179. Liang, W.; Ricco, R.; Maddigan, N. K.; Dickinson, R. P.; Xu, H.; Li, Q.; Sumby, C. J.; Bell, S. G.; Falcaro, P.; Doonan, C. J., Control of Structure Topology and Spatial Distribution of Biomacromolecules in Protein@ZIF-8 Biocomposites. *Chem. Mater.* **2018,** *30* (3), 1069-1077.
180. Duan, Y.; Ye, F. G.; Huang, Y. L.; Qin, Y. M.; He, C. M.; Zhao, S. L., One-pot synthesis of a metal-organic framework-based drug carrier for intelligent glucose-responsive insulin delivery. *Chem. Commun.* **2018,** *54* (42), 5377-5380.
181. Liang, Z. Z.; Yang, Z. Y.; Yuan, H. T.; Wang, C.; Qi, J.; Liu, K. Q.; Cao, R.; Zheng, H. Q., A protein@metal-organic framework nanocomposite for pH-triggered anticancer drug delivery. *Dalton Trans.* **2018,** *47* (30), 10223-10228.
182. Carraro, F.; Williams, J. D.; Linares-Moreau, M.; Parise, C.; Liang, W. B.; Amenitsch, H.; Doonan, C.; Kappe, C. O.; Falcaro, P., Continuous-Flow Synthesis of ZIF-8 Biocomposites with Tunable Particle Size. *Angew. Chem. Int. Edit.* **2020,** *59* (21), 8123-8127.
183. McClements, D. J., Encapsulation, protection, and delivery of bioactive proteins and peptides using nanoparticle and microparticle systems: A review. *Adv. Colloid Interface Sci.* **2018,** *253*, 1-22.
184. Momoh, M. A.; Franklin, K. C.; Agbo, C. P.; Ugwu, C. E.; Adedokun, M. O.; Anthony, O. C.; Chidozie, O. E.; Okorie, A. N., Microemulsion-based approach for oral delivery of insulin: formulation design and characterization. *Heliyon* **2020,** *6* (3), e03650.
185. Perinelli, D. R.; Cespi, M.; Pucciarelli, S.; Vincenzetti, S.; Casettari, L.; Lam, J. K. W.; Logrippo, S.; Canala, E.; Soliman, M. E.; Bonacucina, G.; Palmieri, G. F., Water-in-Oil

Microemulsions for Protein Delivery: Loading Optimization and Stability. *Curr. Pharm. Biotechnol.* **2017,** *18* (5), 410-421.
186. Hu, Y.; Kazemian, H.; Rohani, S.; Huang, Y. N.; Song, Y., In situ high pressure study of ZIF-8 by FTIR spectroscopy. *Chem. Commun.* **2011,** *47* (47), 12694-12696.
187. Barth, A., Infrared spectroscopy of proteins. *Biochim. Biophys. Acta. Bioenerg.* **2007,** *1767* (9), 1073-1101.
188. Bradford, M. M., A rapid and sensitive method for the quantitation of microgram quantities of protein utilizing the principle of protein-dye binding. *Anal. Biochem.* **1976,** *72* (1-2), 248-254.
189. Cavka, J. H.; Jakobsen, S.; Olsbye, U.; Guillou, N.; Lamberti, C.; Bordiga, S.; Lillerud, K. P., A New Zirconium Inorganic Building Brick Forming Metal Organic Frameworks with Exceptional Stability. *J. Am. Chem. Soc.* **2008,** *130* (42), 13850-13851.
190. Winarta, J.; Shan, B. H.; McIntyre, S. M.; Ye, L.; Wang, C.; Liu, J. C.; Mu, B., A Decade of UiO-66 Research: A Historic Review of Dynamic Structure, Synthesis Mechanisms, and Characterization Techniques of an Archetypal Metal-Organic Framework. *Cryst. Growth Des.* **2020,** *20* (2), 1347-1362.
191. Schaate, A.; Roy, P.; Godt, A.; Lippke, J.; Waltz, F.; Wiebcke, M.; Behrens, P., Modulated Synthesis of Zr-Based Metal-Organic Frameworks: From Nano to Single Crystals. *Chem. Eur. J.* **2011,** *17* (24), 6643-6651.
192. Hu, Z. G.; Peng, Y. W.; Kang, Z. X.; Qian, Y. H.; Zhao, D., A Modulated Hydrothermal (MHT) Approach for the Facile Synthesis of UiO66-Type MOFs. *Inorg. Chem.* **2015,** *54* (10), 4862-4868.
193. Pakamorė, I.; Rousseau, J.; Rousseau, C.; Monflier, E.; Szilágyi, P. Á., An ambient-temperature aqueous synthesis of zirconium-based metal–organic frameworks. *Green Chem.* **2018,** *20* (23), 5292-5298.
194. Homaee, M.; Hamadi, H.; Nobakht, V.; Javaherian, M.; Salahshournia, B., Ultrasound-assisted synthesis of UiO-66-NHSO3H via post-synthetic modification as a heterogeneous Bronsted acid catalyst. *Polyhedron* **2019,** *165*, 152-161.
195. Li, Y. F.; Liu, Y.; Gao, W. Y.; Zhang, L. M.; Liu, W.; Lu, J. J.; Wang, Z.; Deng, Y. J., Microwave-assisted synthesis of UIO-66 and its adsorption performance towards dyes. *Crystengcomm* **2014,** *16* (30), 7037-7042.
196. Taddei, M.; Dau, P. V.; Cohen, S. M.; Ranocchiari, M.; van Bokhoven, J. A.; Costantino, F.; Sabatini, S.; Vivani, R., Efficient microwave assisted synthesis of metal-organic framework UiO-66: optimization and scale up. *Dalton Trans.* **2015,** *44* (31), 14019-14026.
197. Wei, J. Z.; Gong, F. X.; Sun, X. J.; Li, Y.; Zhang, T.; Zhao, X. J.; Zhang, F. M., Rapid and Low-Cost Electrochemical Synthesis of UiO-66-NH2 with Enhanced Fluorescence Detection Performance. *Inorg. Chem.* **2019,** *58* (10), 6742-6747.

198. Karadeniz, B.; Howarth, A. J.; Stolar, T.; Islamoglu, T.; Dejanovic, I.; Tireli, M.; Wasson, M. C.; Moon, S. Y.; Farha, O. K.; Friscic, T.; Uzarevic, K., Benign by Design: Green and Scalable Synthesis of Zirconium UiO-Metal-Organic Frameworks by Water-Assisted Mechanochemistry. *ACS Sustain. Chem. Eng.* **2018,** *6* (11), 15841-15849.
199. Uzarevic, K.; Wang, T. C.; Moon, S. Y.; Fidelli, A. M.; Hupp, J. T.; Farha, O. K.; Friscic, T., Mechanochemical and solvent-free assembly of zirconium-based metal-organic frameworks. *Chem. Commun.* **2016,** *52* (10), 2133-2136.
200. Valenzano, L.; Civalleri, B.; Chavan, S.; Bordiga, S.; Nilsen, M. H.; Jakobsen, S.; Lillerud, K. P.; Lamberti, C., Disclosing the Complex Structure of UiO-66 Metal Organic Framework: A Synergic Combination of Experiment and Theory. *Chem. Mater.* **2011,** *23* (7), 1700-1718.
201. Cliffe, M. J.; Wan, W.; Zou, X. D.; Chater, P. A.; Kleppe, A. K.; Tucker, M. G.; Wilhelm, H.; Funnell, N. P.; Coudert, F. X.; Goodwin, A. L., Correlated defect nanoregions in a metal-organic framework. *Nat. Comm.* **2014,** *5*, 4176.
202. Liu, L.; Chen, Z.; Wang, J.; Zhang, D.; Zhu, Y.; Ling, S.; Huang, K.-W.; Belmabkhout, Y.; Adil, K.; Zhang, Y.; Slater, B.; Eddaoudi, M.; Han, Y., Imaging defects and their evolution in a metal–organic framework at sub-unit-cell resolution. *Nature Chem.* **2019,** *11* (7), 622-628.
203. Wu, H.; Chua, Y. S.; Krungleviciute, V.; Tyagi, M.; Chen, P.; Yildirim, T.; Zhou, W., Unusual and Highly Tunable Missing-Linker Defects in Zirconium Metal–Organic Framework UiO-66 and Their Important Effects on Gas Adsorption. *J. Am. Chem. Soc.* **2013,** *135* (28), 10525-10532.
204. Shan, B. H.; McIntyre, S. M.; Armstrong, M. R.; Shen, Y. X.; Mu, B., Investigation of Missing-Cluster Defects in UiO-66 and Ferrocene Deposition into Defect-Induced Cavities. *Ind. Eng. Chem. Res.* **2018,** *57* (42), 14233-14241.
205. Ghosh, P.; Colon, Y. J.; Snurr, R. Q., Water adsorption in UiO-66: the importance of defects. *Chem. Commun.* **2014,** *50* (77), 11329-11331.
206. Koutsianos, A.; Kazimierska, E.; Barron, A. R.; Taddei, M.; Andreoli, E., A new approach to enhancing the CO2 capture performance of defective UiO-66 via post-synthetic defect exchange. *Dalton Trans.* **2019,** *48* (10), 3349-3359.
207. Shearer, G. C.; Chavan, S.; Bordiga, S.; Svelle, S.; Olsbye, U.; Lillerud, K. P., Defect Engineering: Tuning the Porosity and Composition of the Metal–Organic Framework UiO-66 via Modulated Synthesis. *Chem. Mater.* **2016,** *28* (11), 3749-3761.
208. Han, Y. T.; Liu, M.; Li, K. Y.; Zuo, Y.; Wei, Y. X.; Xu, S. T.; Zhang, G. L.; Song, C. S.; Zhang, Z. C.; Guo, X. W., Facile synthesis of morphology and size-controlled zirconium metal-organic framework UiO-66: the role of hydrofluoric acid in crystallization. *Crystengcomm* **2015,** *17* (33), 6434-6440.

209. Trickett, C. A.; Gagnon, K. J.; Lee, S.; Gandara, F.; Burgi, H. B.; Yaghi, O. M., Definitive Molecular Level Characterization of Defects in UiO-66 Crystals. *Angew. Chem. Int. Edit.* **2015,** *54* (38), 11162-11167.
210. Zhao, Y. J.; Zhang, Q.; Li, Y. L.; Zhang, R.; Lu, G., Large-Scale Synthesis of Monodisperse UiO-66 Crystals with Tunable Sizes and Missing Linker Defects via Acid/Base Co-Modulation. *ACS Appl. Mater. Interfaces* **2017,** *9* (17), 15079-15085.
211. Scherrer, P. G., N. G. W. , Nachrichten von der Gesellschaft der Wissenschaften zu Göttingen, Mathematisch-Physikalische Klasse. *Math. Phys.* **1918,** *2*, 98-100.
212. Borchert, H.; Shevehenko, E. V.; Robert, A.; Mekis, I.; Kornowski, A.; Grubel, G.; Weller, H., Determination of nanocrystal sizes: A comparison of TEM, SAXS, and XRD studies of highly monodisperse COPt3 particles. *Langmuir* **2005,** *21* (5), 1931-1936.
213. Iacomi, P.; Llewellyn, P. L., pyGAPS: a Python-based framework for adsorption isotherm processing and material characterisation. *Adsorption* **2019,** *25* (8), 1533-1542.
214. De Yoreo, J. J.; Sommerdijk, N., Investigating materials formation with liquid-phase and cryogenic TEM. *Nat. Rev. Mater.* **2016,** *1* (8).
215. Buckley, P.; Hargreaves, N.; Cooper, S., Nucleation of quartz under ambient conditions. *Commun. Chem.* **2018,** *1*, 49.
216. Wang, L. S.; Wang, X. X.; Li, Y.; Jiang, K.; Shao, X. Z.; Du, C. J., Ionic liquids: Solubility parameters and selectivities for organic solutes. *AIChE J.* **2013,** *59* (8), 3034-3041.
217. Hejazifar, M.; Lanaridi, O.; Bica-Schroder, K., Ionic liquid based microemulsions: A review. *J. Mol. Liq.* **2020,** *303*, 112264.

Appendix A - Calculations

A.1. Particle Size & Distribution

A.1.1. Powder X-ray Diffraction

From selected powder patterns, the length of the coherent scattering domain perpendicular to the plane (ϕ) could be determined from the PXRD peak associated with that plane using the Scherrer equation (eq. A.1), lambda is the source wavelength (0.15418 nm), B(2θ) is the peak broadening, and theta is the Bragg's diffraction angle.[1]

A.1
$$\boldsymbol{\phi = \frac{0.9\lambda}{B(2\theta)\cos\theta}}$$

For the selected peaks, the peak was modelled with a Gaussian fit using Origin 2018 SR1 b9.5.1.195 to deconvolute merged peaks. From these peaks, the peak broadening was defined as the full width half maximum (FWHM) in radians.[2] Typically, instrumental broadening would be corrected by collecting a pattern for a bulk crystallite with negligible size induced broadening such as LaB_6. The peak broadening would then be plotted against 2θ and then fit with a polynomial.[3] An LaB_6 standard was available and a PXRD was collected. However, the smallest angle peak of LaB_6 is at $2\theta = 21^{o}$.[4, 5] This is substantially larger than the smallest angle peaks measured in the samples (7.3°). Using this standard for MOFs would require significant extrapolation of the instrumental peak broadening for the peaks observed. Therefore, instrumental correction was not performed, and a better correction standard should be selected in future. However, it should be noted that instrumental correction is not strictly necessary in the context of this thesis because all samples would have been corrected by the same amount. Thus, general trends in the crystallite size of each sample still hold.

A.1.2. Transmission Electron Microscopy

The particle size was determined from TEM images using ImageJ 1.52a (Figure A.1).[6] The scale was set by using the set scale tool to set the scale to be equal to the scale bar in the image. Once this was set, the image was masked with a black and white threshold. The threshold was set manually to include the most individual particles. In the Analyse Particles, menu the circularity and size filters were manually set to exclude the largest aggregates and partial crystals but maintain the largest number of particles possible. Finally, amorphous, or aggregate particles were manually excluded from the selection. The longest distance between two points in the particle was automatically calculated for every selected particle. In the case of pseudospherical particles this is approximately equal to the diameter.

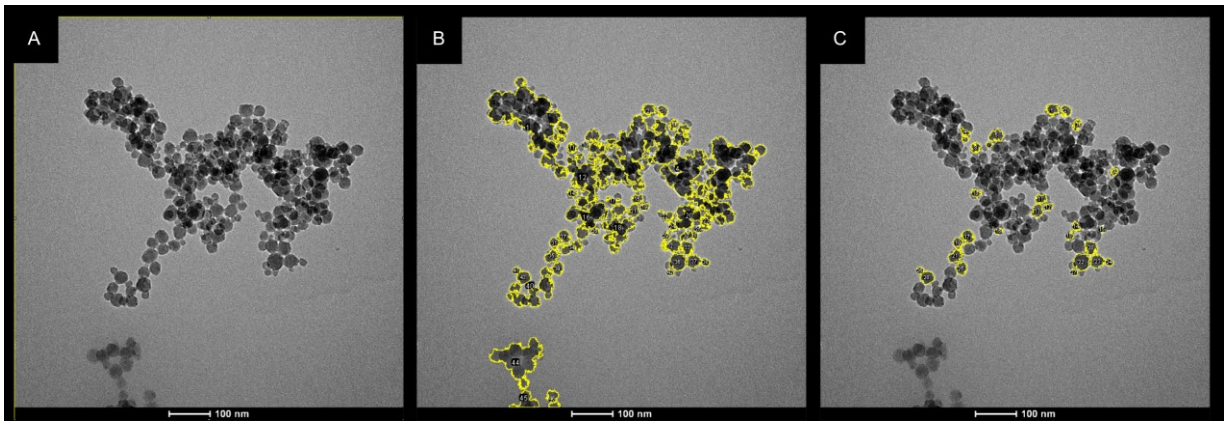

Figure A.1 Filtering aggregates from size analysis of TEM images. The (A) raw image is first (B) masked automatically to isolate all particles including aggregates. Aggregate particles are removed by (C) manual exclusion.

A.1.3. Particle Size Distribution Modelling

The empirical probability distribution function (PDF) was determined by plotting the PSD as a histogram with bins between 1 nm and 20 nm depending on the sample. Empirical PDFs for all samples were plotted and can be found within Appendix B. Empirical CDFs (ECDFs) were calculated from the raw particle size by dividing the sum of all particles less than or equal to a specific size (t) by the number of particles in the sample (N) (eq. A.2). The specified size (t) is the next largest uncounted particle in the series. E.g. For the dataset x = 1.0, 1.3, 1.6, 1.8, 1.8, 2.2, 2.7, 2.9, 3.0, 3.1 the ECDF is represented by (x,y) = (1.0, 0.1), (1.3, 0.2), (1.6, 0.3), (1.8, 0.5), (2.2, 0.6), (2.7, 0.7), (2.9, 0.8), (3.0, 0.9), (3.1, 1.0).

A.2 $$\boldsymbol{ECDF(x) = \frac{1}{N}\sum_{i=0}^{N} x_i \leq t}$$

For each sample where the PSD was measured, the ECDF was fitted automatically with the Weibull and Gaussian distribution using the implementation of least squared fitting in Origin 2018 SR1 b9.5.1.195.

A.1.4. Kolmogorov Smirnov Tests

The Kolmogorov Smirnov Test is a test to determine whether two distribution are the same. Within this study, the Kolmogorov Smirnov Test is used to determine whether a model for the PSD is a good fit for the experimental data. (Figure A.2). The test compares the cumulative distribution of the model and sample. The maximum vertical distance (D) between the two samples is found (eq. A.3).

A.3 $$\boldsymbol{D = \sup|F_1(x) - F_2(x)|}$$

The null hypothesis is that the two datasets come from the same distribution. The null hypothesis is rejected if D is greater than the critical value (Z) which is determined from a table internally in Origin 2018 SR1 b9.5.1.195 with a 95% confidence interval.[7]

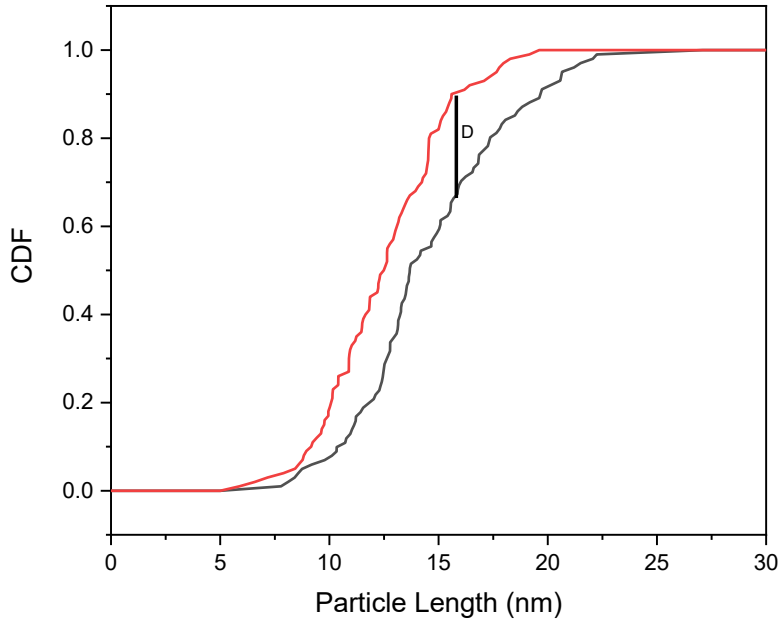

Figure A.2 Kolmogorov Smirnov Test applied to comparing two datasets (red & black) The Kolmogorov statistic (D) is determined as the maximum vertical distance between the two datasets

The Kolmogorov Smirnoff Test was selected because non-parametric CDF test. This means it makes no assumptions of the distribution during the test. Furthermore, it uses the CDF instead of the PDF for determining goodness of fit (unlike the Chi-Squared test).[8] Given the experimental PDF is subject to artefacts due to the arbitrary selection of bins for histogram plotting, a CDF test is more appropriate for this application.

A.1.5. Particle Size Corrections using the Weibull Model

For some samples, the Gaussian distribution did not fit the experimental data. In these cases, the Weibull model (eq. A.4) still maintained a good fit for the experimental PSD. To compare the modelled size with the experimental data, the average NP size (ϕ)(eq. A.5) and SD (eq. A.6) were calculated from the Weibull distribution with the shape (β) and scale (α) parameters where Γ(z) represents the gamma function (eq. A.7).[9]

A.4 $$PDF(x) = \frac{\beta}{\alpha}\left(\frac{x}{\alpha}\right)^{\beta-1} e^{-\left(\frac{x}{\alpha}\right)^{\beta}}$$

A.5 $$\phi = \alpha\Gamma\left(\frac{1}{\beta}+1\right)$$

A.6 $$SD = \alpha\sqrt{\Gamma\left(\frac{2}{\beta}+1\right)+\Gamma\left(\frac{1}{\beta}+1\right)^{2}}$$

A.7 $$\Gamma(z) = \int_{o}^{\infty} y^{z-1}e^{-y}.dy$$

A.2. Porosity & Surface Area

A.2.1. BET Surface Area

The surface area of UiO-66 was determined by measuring the volume of nitrogen gas absorbed by the material as a function of pressure. The surface area was determined from the volume of absorbed gas using Brunauer Emmett Teller (BET) theory. [10]It assumes that gas molecules are physical absorbed onto a material surface in layers and that each gas molecule interacts only with the adjacent layer. It further assumes the enthalpy of absorption is highest for the first layer (E_1) and all subsequent layers have an enthalpy of absorption equal to the enthalpy of liquification (E_L). Given these assumptions eq. A.8 and A.9 were derived with the equilibrium pressure (p), the saturation pressure (p_o), the volume of a monolayer (v_m) and the total volume of adsorbed gas (v).

A.8 $$\frac{1}{v\left[\left(\frac{p_0}{p}\right)-1\right]} = \frac{c-1}{v_m c}\left(\frac{p}{p_0}\right) + \frac{1}{v_m c}$$

A.9 $$c = e^{\frac{E_1 - E_L}{RT}}$$

From eq. A.8. there is a linear relation between $\frac{1}{v\left[\left(\frac{p_0}{p}\right)-1\right]}$ and $\frac{p}{p_0}$. This is a linear relationship for $0.2 < \frac{p}{p_0} < 0.3$. From this linear relationship eq. A.10 and A.11 are derived using the gradient (g) and intercept (i).

A.10 $$v_m = \frac{1}{g+i}$$

A.11 $$c = 1 + \frac{g}{i}$$

The BET surface area is determined from eq. A.12. using Avogadro's number (N_A), the cross-sectional area of the absorbent (s), the molar volume of N_2 (V) and the mass of UiO-66 used.

A.12 $$S_{BET} = \frac{v_m N_A s}{VM}$$

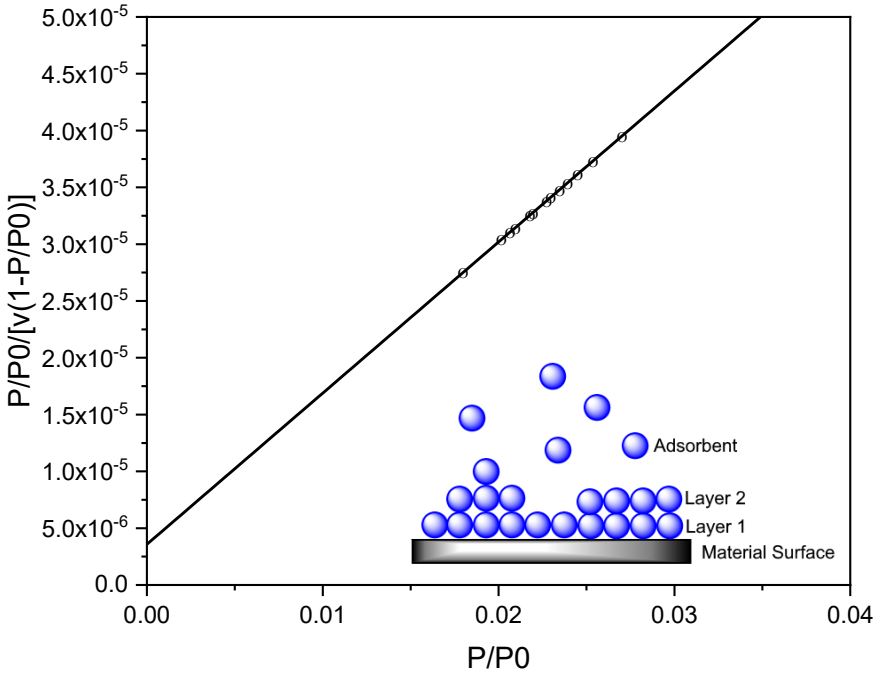

Figure A.3 (Inset) adsorption of gas molecules into monolayers according to BET theory. (outset) linear fit of BET eq. A.7.

A.2.2. Total Pore Volume

When calculating the total pore volume, it is assumed that all pores are fully occupied with condensed phase gas where p/p_0 is greater than 0.95. Therefore, the total pore volume can be determined from the amount of N_2 absorbed* where p/p_0 equals 0.99 (V_{N2}). The adsorbed gas condenses when adsorbed into the pores. Therefore, the uncondensed N_2 must be converted to a condensed volume. For N_2 at 77 K, the uncondensed to condensed volume ratio is 647. As the total pore volume (V_{pore}) is assumed to be equal to the condensed phase volume, the total pore volume was determined using eq. A.13.

A.13 $$V_{pore} = \frac{V_{N2}}{647}$$

* mL g^{-1}: volume absorbed N_2 per gram of sample

A.3. Defectivity

A.3.1. Total Defects

The prevalence of defects was determined using the method derived by the Lillerud group[11]. Decomposition of dehydroxylated UiO-66 ($Zr_6O_6(BDC)_6$) was measured during TGA under air at ~500°C. During this step, it is assumed that dehydroxylated UiO-66 decomposes to ZrO_2 (eq. A.14) and that no other decomposition steps occur at this temperature.

A.14 $$\boldsymbol{Zr_6O_6(BDC)_6 + 3O_2 \rightarrow 6ZrO_2 + 6BDC}$$

From this assumption, the mass of 6 ZrO_2 molecules is normalized at 100% mass. E.g. complete decomposition mass. Ideal UiO-66 has a formula mass of 220% the mass of 6 ZrO_6. Hence, any decomposition less than that implies the loss of BDC. From this assumption Lillerud derived the equation for the number of missing linkers per unit cell (x) (eq. A.15).

A.15 $$\boldsymbol{x = 6 - \frac{NL-100}{20.03}}$$

The percentage of defects is the number of defects per unit cell divided by the number of BDC linkers in an idealized unit cell (6) multiplied by 100 (eq. A.16)

A.16 $$\boldsymbol{\%\, Defects = \frac{x}{6} * 100}$$

The number of defects per unit cell was determined by multiplying the defect percentage by the number of BDC molecules in a non-defective crystal (6) (eq. A.17).

A.17 $$\boldsymbol{N_{defects} = 6 * \frac{\%\, Defects}{100}}$$

A.3.2. Surface Defects

On the outer surface of any extended network, local sites may not adhere to the unit cell formula due to termination of the network. For large networks, this effect is negligible. However, as the crystal dimensions shrink, the outer surface becomes a larger proportion of the overall surface area. Hence, if a crystal is small enough, it will appear defective regardless of the presence of internal defects. To model this effect on UiO-66 two assumption were made:

1. UiO-66 growth is along the [111] face and the overall morphology is octahedral.
2. The crystal has a net neutral surface charge.

The assumption of an octahedral morphology is generally reasonable for UiO-66. Furthermore, octahedral growth is easier to model. However, the samples in this study do not follow this morphology and instead have a pseudospherical morphology. Given, that the surface area for an octahedral is smaller than a sphere of the same length. This model would underestimate the contribution of surface defects to the overall defectivity. This is reasonable in the context it is applied. The second is assumption that the crystal surface is net neutral would imply the surface is populated by hydroxide or acetic acid capped zirconium clusters. This assumption is used often in the literature.

A fully occupied UiO-66 cluster has 12 coordination sites with 4 sites above, below and in-plane. Hence, each cluster coordinates four clusters above or below it towards the centre. Therefore, the primitive (smallest possible) octahedron (n=1) was thought of as three planes with 1,4 and 1 clusters in each plane. The second smallest octahedron (n=2) would consist of 1,4,9,4,1 clusters. The value n was determined to be the particle length (Φ) divided by the UiO-66 octahedron length (L_o) rounded to the nearest integer (eq. A.18).

A.18
$$\boldsymbol{n = \left\lfloor \frac{\Phi}{1.22\ nm} + \frac{1}{2} \right\rfloor}$$

There are four possible arrangements of a cluster within an octahedral. It can be on the edge, face, vertex, or buried within the octahedral. The number of each is a function of the octahedral length (eq. A.19).

A.19

$$N_{vertex\ cluster} = 6$$

$$N_{edge\ cluster} = 12(n-1)$$

$$N_{face\ cluster} = \sum_{i=1}^{n-2} 8i$$

$$N_{buried\ cluster} = n^2 + \sum_{i=1}^{n-1} 2i^2$$

$$N_{clusters} = (n-1)^2 + 12(n-1) + 6 + \sum_{i=1}^{n-2} 2i^2 + \sum_{i=1}^{n-2} 8i$$

By bisecting the outer surface clusters with the surfaces they contact the number of BDC substituted at the surface was determined. For a buried cluster, all ligands would be present. At a vertex there are four ligands and eight modulators bound. At an edge there are seven ligands and five modulators bound. At a face there are 9 ligands and 3 modulators bound. The number of ligands in the cluster is half the number of ligand binding sites available to each cluster because each ligand has a connectivity of two (eq. A.20).

A.20 $N_{ligands} = 6n^2 + \sum_{i=1}^{n-1} 12i^2 + 42(n-1) + 24 + \sum_{i=1}^{n-2} 36i$

The defect percentage was determined by finding the ratio of ligands clusters and dividing as a percentage of the idealized UiO-66 formula. Ideal UiO-66 has 6 BDC linkers per cluster (eq. A.21)

A.21 $\%Defects = 100\left(\frac{N_{ligands}}{N_{clusters}}\right)\left(\frac{1}{6}\right)$

A.4. Protein Properties

A.4.1. Isoelectric Point

For each protein, the isoelectric point was estimated from the amino acid sequence by summing the charges of all amino acid residues using the Henderson-Hasselbalch equation (eq. A.22).

A.22 $$q = \sum_{i=1}^{n} \frac{10^{\pm pK_{ai} \pm pH}}{10^{\pm pK_{ai} \pm pH} + 1}$$

The pI was determined as the pH where the net charge on the protein was 0 ± 0.0001. The average residue pK_a values and the final pI where determined using Expasy[12].

A.4.2. Loading Efficiency

The loading efficiency (LE) was defined as the percentage mass of protein encapsulated out of the total mass of the protein@MOF complex (eq. A.23).

A.23 $$LE = 100 \frac{m_{protein}}{m_{complex}}$$

The LE was determined using a Bradford Assay. During a Bradford assay, Coomassie Blue G-250 is added to a protein@ZIF-8 complex. In acidic conditions (pH > 5), ZIF-8 degrades releasing the protein. Coomassie Blue G-250 binds to the amino and aromatic groups of the protein. This causes a shift in the dye's UV-vis absorption peak from 465 to 595 nm.[13] A calibration curve was obtained for the increased absorbance at 595 nm (Abs_{595}) as a function of protein quantity (m). For BSA (Figure A.4), the absorbance is represented by eq. A.24.

A.24 $$Abs_{595} = 0.00119\, m_{BSA}$$

The LE was determined by dividing the amount of BSA determined from UV-vis by the amount of BSA@ZIF-8 digested (A.25).

A.25 $$LE = 100 * \frac{Abs_{595}}{0.00119} * \frac{1}{m_{BSA@ZIF-8}}$$

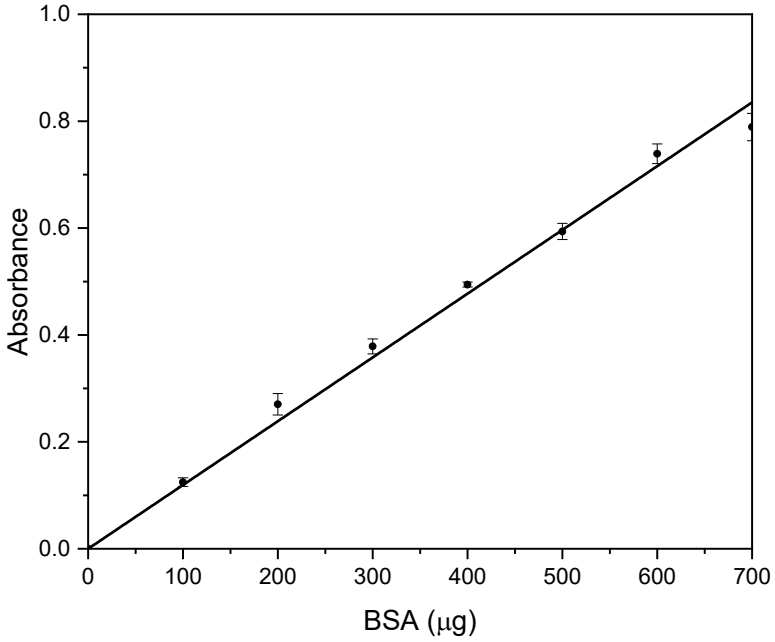

Figure A.4 Bradford assay calibration curve measuring absorbance at 595 nm. Abs = 0.00119*BSA

A.4.3. Encapsulation Efficiency

The encapsulation efficiency or the percentage protein encapsulated of the total protein added (eq. A.26) is calculated by multiplying the fraction of protein in the protein MOF complex by the total yield of complex (mg). This is then divided by the total amount of protein added to μEL. This is expressed as the protein concentration (mg mL^{-1}) multiplied by the volume of aqueous phase in μEL (1.8 mL)(eq. A.27).

A.26 $$\boldsymbol{EE = 100 * \frac{m_{protein\ encapsulated}}{m_{protein\ total}}}$$

A.27 $$\boldsymbol{EE = 100 * \frac{0.01 * m_{protein@MOF} * LE}{1.8[protein]}}$$

Appendix B - Experimental Data

Table B.1 ZIF PSD modelling Parameters

		Weibull		Gaussian		Test
Sample	Model	α	β	ϕ	SD	
ZIF-8a-1x	Weibull	77.30	2.34	--	--	Reject
	Gaussian	--	--	68.66	31.27	Reject
ZIF-8b-0	Weibull	30.48	3.07	--	--	Pass
	Gaussian	--	--	27.33	9.13	Reject
ZIF-8b-15	Weibull	58.04	4.01	--	--	Pass
	Gaussian	--	--	52.71	14.40	Pass
ZIF-8b-60	Weibull	84.42	4.39	--	--	Pass
	Gaussian	--	--	77.04	18.93	Pass
ZIF-8b-90	Weibull	87.27	3.22	--	--	Pass
	Gaussian	--	--	78.24	25.68	Pass
ZIF-8c-4	Weibull	67.35	2.98	--	--	Pass
	Gaussian	--	--	59.98	22.00	Reject
ZIF-8c-3	Weibull	44.87	2.66	--	--	Pass
	Gaussian	--	--	39.86	15.69	Reject
ZIF-8c-2	Weibull	64.69	2.99	--	--	Pass
	Gaussian	--	--	57.80	20.42	Pass
ZIF-8c-1	Weibull	79.68	3.01	--	--	Pass
	Gaussian	--	--	71.07	25.53	Pass
ZIF-8d-120	Weibull	95.96	4.19	--	--	Pass
	Gaussian	--	--	87.33	22.40	Pass
ZIF-8d-30	Weibull	81.58	4.35	--	--	Pass
	Gaussian	--	--	74.59	17.95	Pass
ZIF-67	Weibull	129.97	5.58	--	--	Pass
	Gaussian	--	--	120.67	22.00	Pass

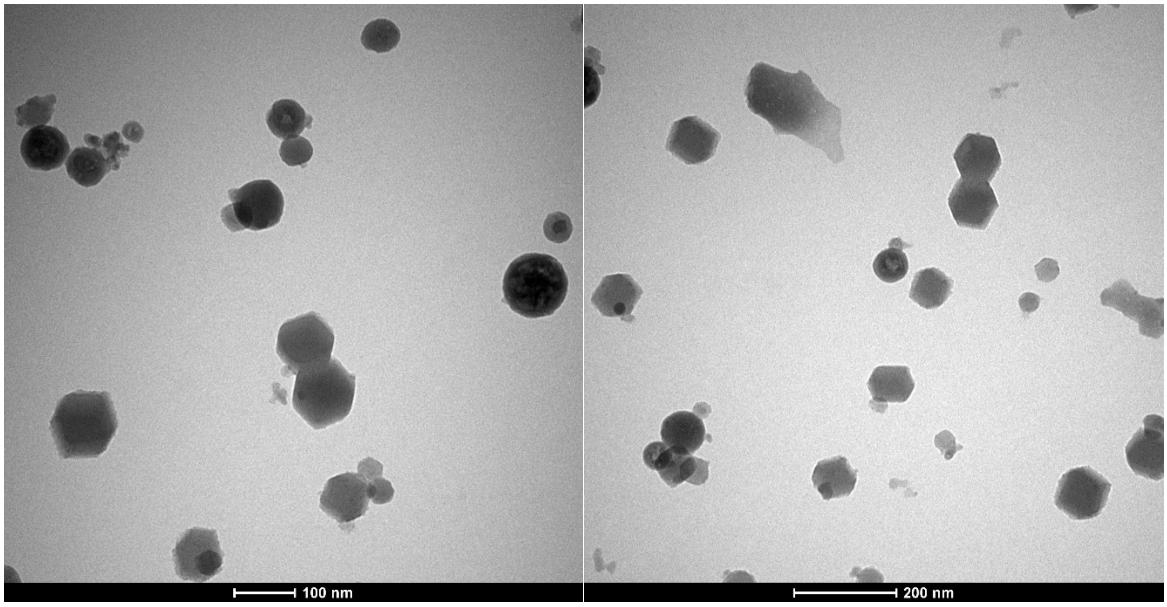

Figure B.1 Additional TEM images of ZIF-8a-1x.

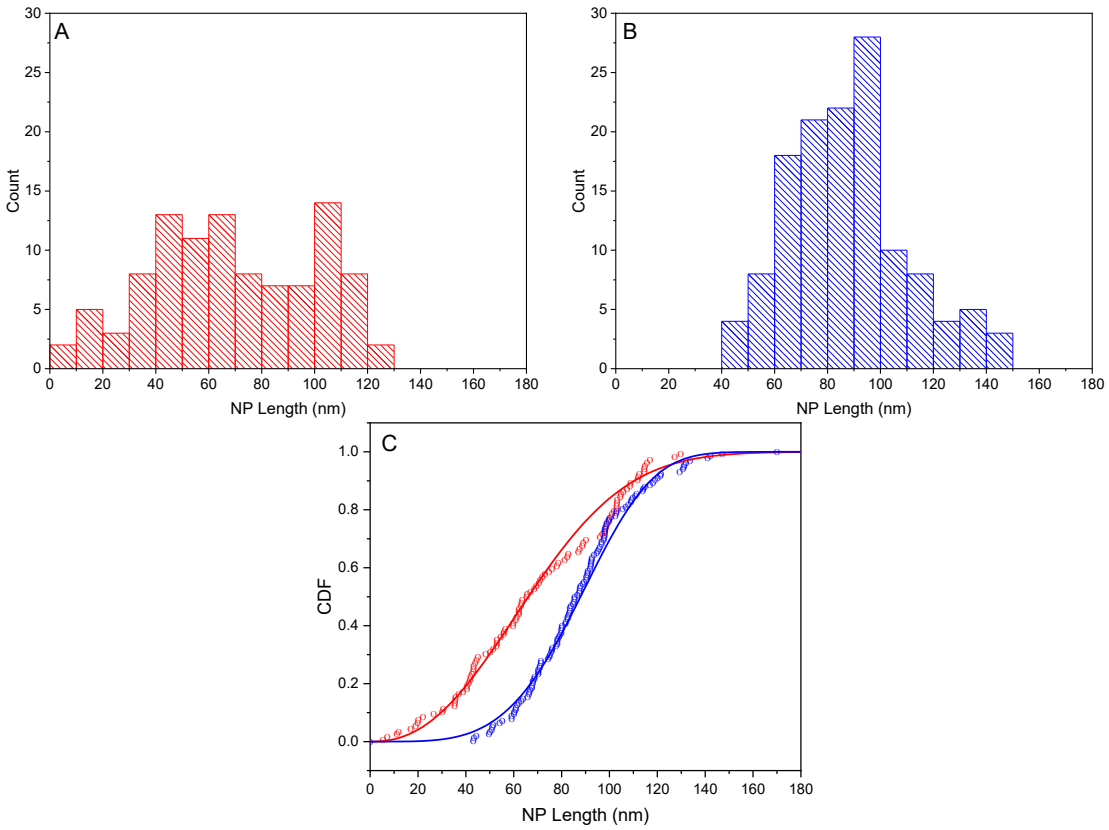

Figure B.2 PSD of (A) ZIF-8a-1x and (B) ZIF-8d-120. (C) Cumulant distribution of sample PSDs with a Weibull fit.

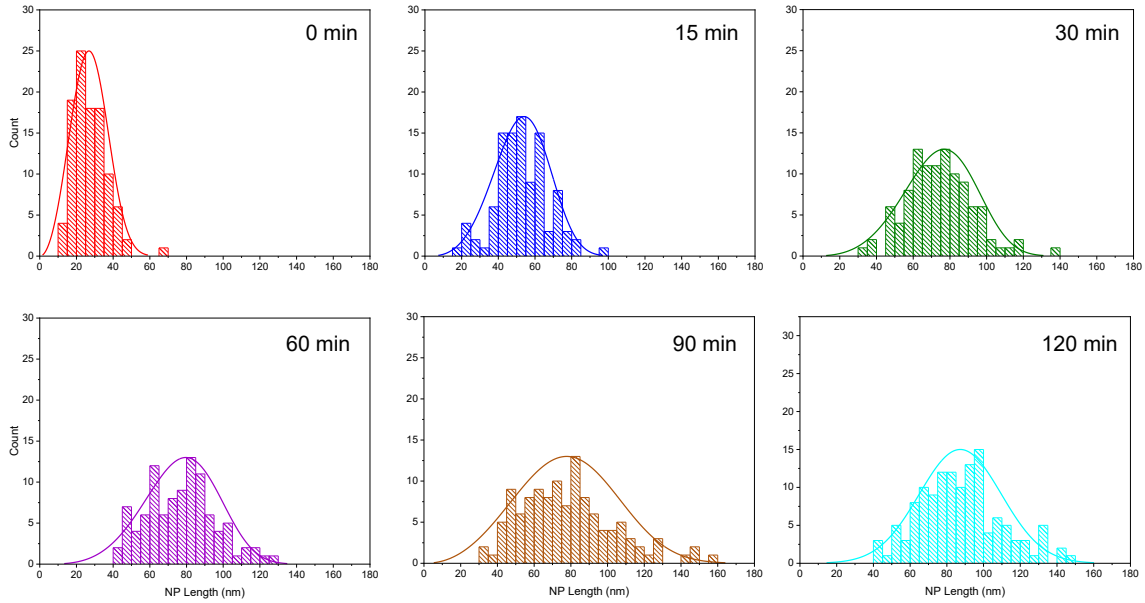

Figure B.3 PSD of ZIF-8 synthesized using variable addition times.

Table B.2 TEM determined ZIF-8 samples synthesized with variable addition times

Sample	Φ (nm)	N	SD (nm)	RSD (%)
ZIF-8b-0	27.3	103	9.13	33.4
ZIF-8b-15	52.7	102	14.4	27.3
ZIF-8b-30	74.6	107	18.0	24.1
ZIF-8b-60	77.0	100	18.9	24.7
ZIF-8b-90	78.2	118	25.7	32.8
ZIF-8b-120	87.3	131	22.4	25.6

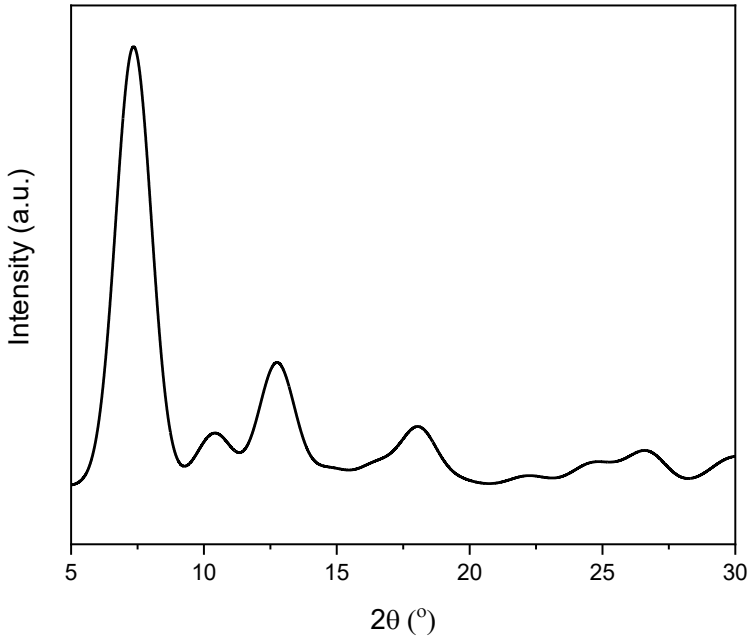

Figure B.4 Simulated PXRD of 5 nm ZIF-8 crystallite. Simulated using CystalMaker 10.4.2.

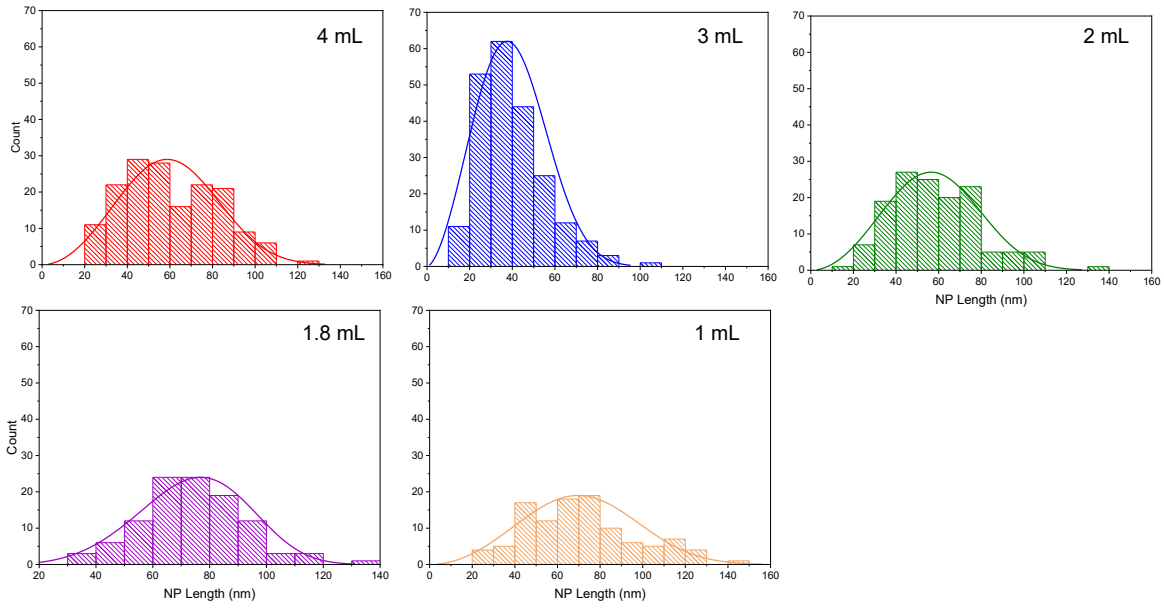

Figure B.5 PSD of ZIF-8 synthesized with various aqueous volumes

Table B.3 TEM determined ZIF-8 samples synthesized with variable addition times

Sample	Φ (nm)	N	SD (nm)	RSD (%)
ZIF-8c-4	60.0	165	22.0	36.7
ZIF-8c-3	39.9	218	15.9	39.3
ZIF-8c-2	57.8	138	20.4	35.3
ZIF-8c-1.8	74.6	107	18.0	24.0
ZIF-8c-1	71.1	108	25.5	35.9

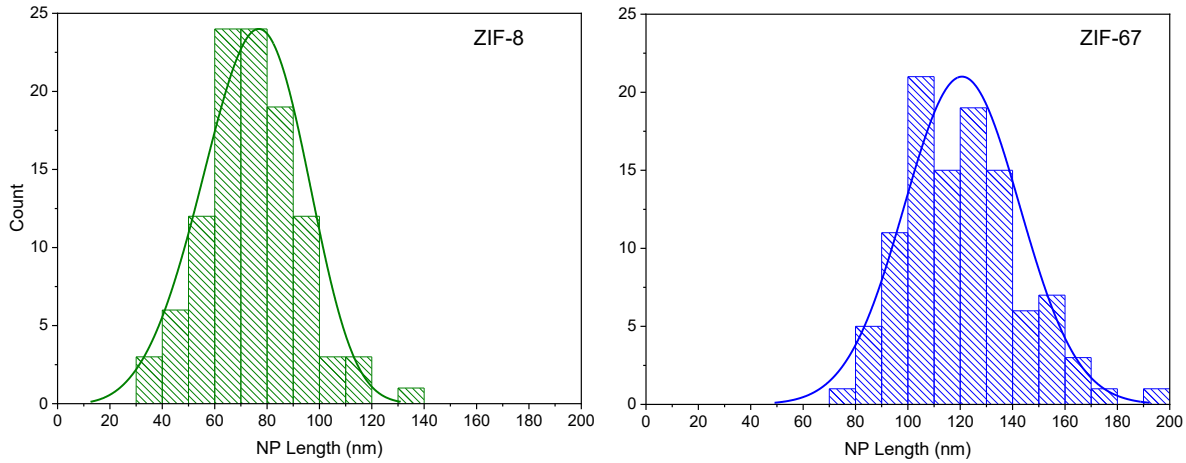

Figure B.6 ZIF-8 and ZIF-67 PSD synthesized using microemulsion synthesis.

Table B.4 Protein@ZIF-8 PSD modelling Parameters

Sample	Φ	SD	Test
BSA@ZIF-8a-2.5	57.99	15.73	Pass
BSA@ZIF-8a-5	82.35	21.68	Pass
BSA@ZIF-8c	72.22	16.98	Pass
BSA@ZIF-8b-15	69.72	15.09	Pass
BSA@ZIF-8b-120	87.59	24.48	Pass
BHG@ZIF-8-15	55.92	22.40	Pass
BHG@ZIF-8-30	62.58	21.73	Pass
BHG@ZIF-8-120	75.27	29.91	Pass

Table B.5 Summary of Protein@ZIF-8 NP size determined by TEM

Sample	Protein		Addition Time (min)	TEM data			
	Type	Quantity (mg mL^{-1})*		Φ (nm)	N	SD (nm)	RSD (%)
ZIF-8b-15	--	--	15	52.7	102	14.4	27.3
ZIF-8d-30	--	--	30	74.6	107	18.0	24.1
ZIF-8d-120	--	--	120	87.3	131	22.4	25.6
BSA@ZIF-8a-2.5	BSA	2.5	30	58.0	132	15.7	27.1
BSA@ZIF-8a-5	BSA	5	30	82.3	113	21.7	26.3
BSA@ZIF-8c	BSA	10	30	72.2	119	17.0	23.5
BSA@ZIF-8b-15	BSA	10	15	69.7	103	15.1	21.6
BSA@ZIF-8b-120	BSA	10	120	87.6	108	24.5	27.9
BHG@ZIF-8-15	BHG	10	15	55.9	105	22.4	40.1
BHG@ZIF-8-30	BHG	10	30	62.6	107	21.7	35.3
BHG@ZIF-8-120	BHG	10	120	75.3	103	29.9	39.7

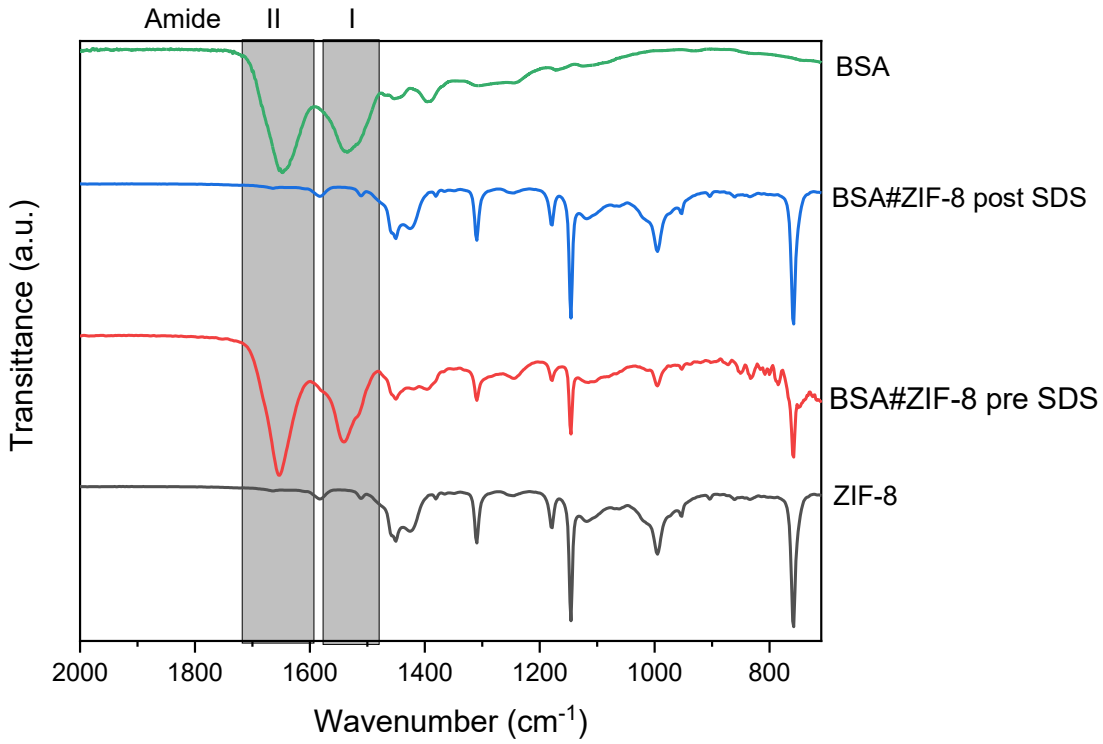

Figure B.7 SDS treatment of ZIF-8 surface coated with BSA.

* This is the amount of protein per mL of aqueous 2-methylimidazole.

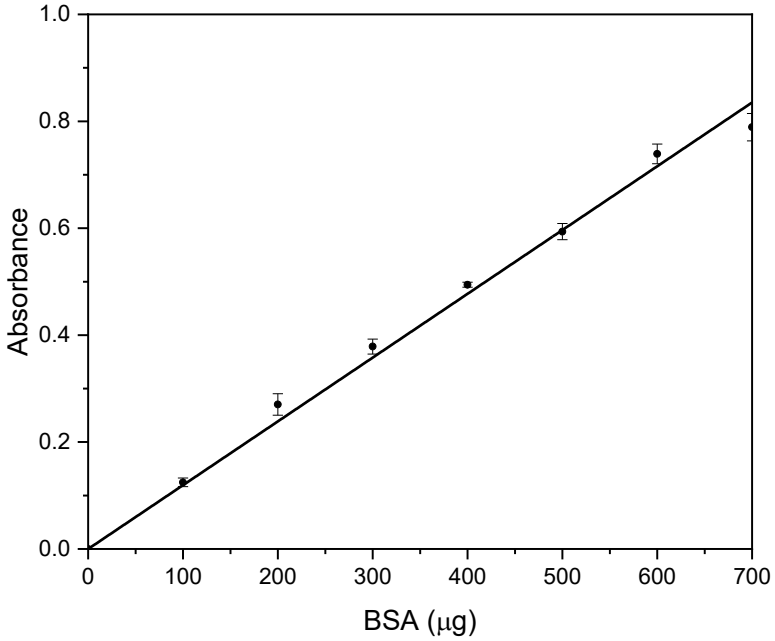

Figure B.8 Bradford assay calibration curve measuring absorbance at 595 nm. Abs = 0.00119*BSA

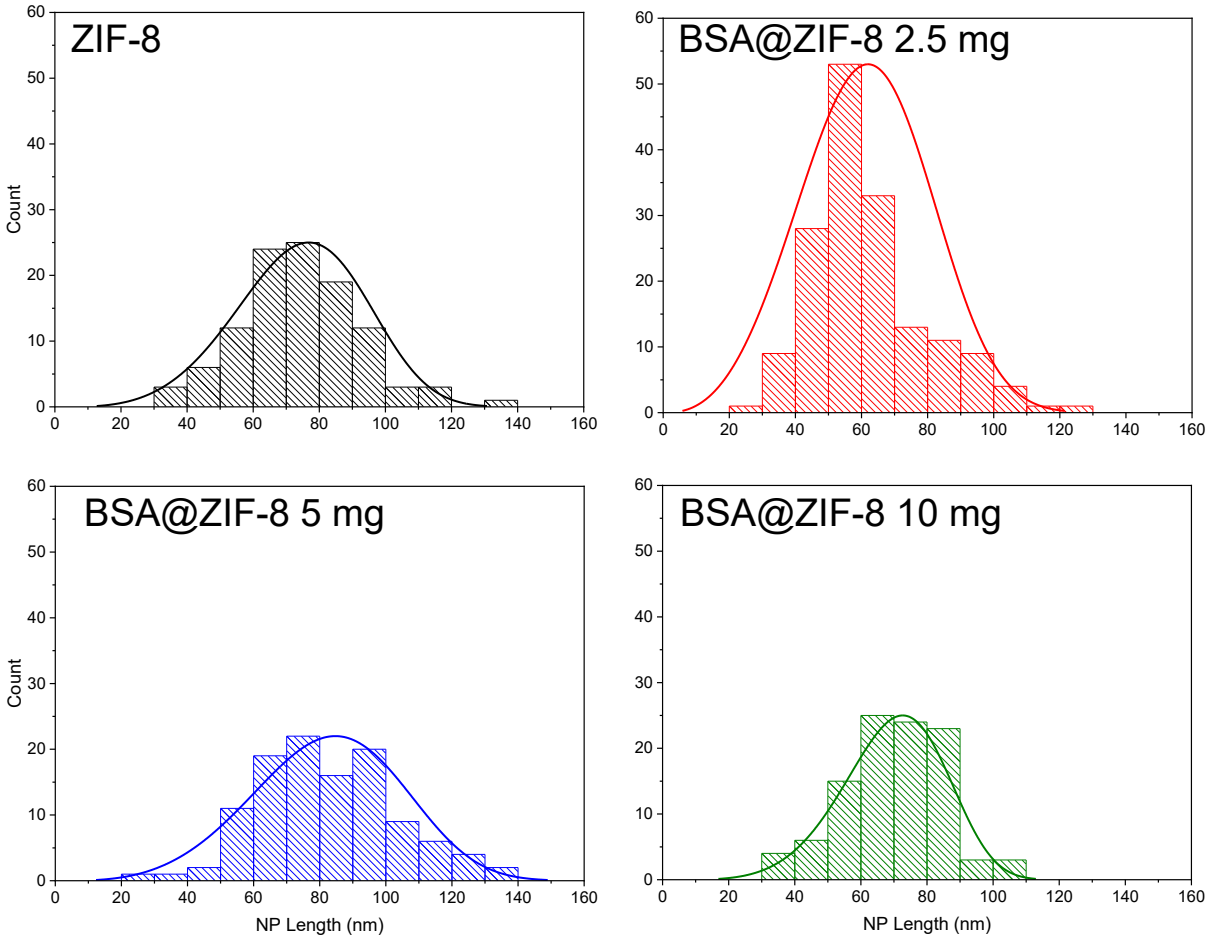

Figure B.9 PSD of BSA@ZIF-8 samples synthesized with variable quantities of BSA

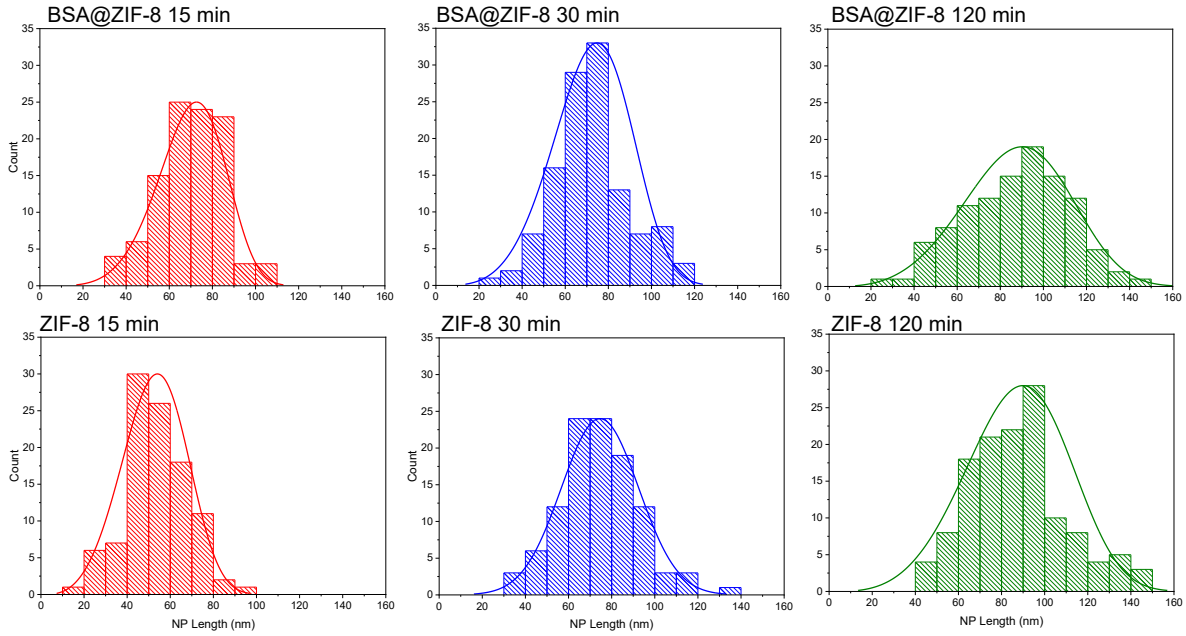

Figure B.10 PSD of BSA@ZIF-8 samples synthesized with avariable addition times.

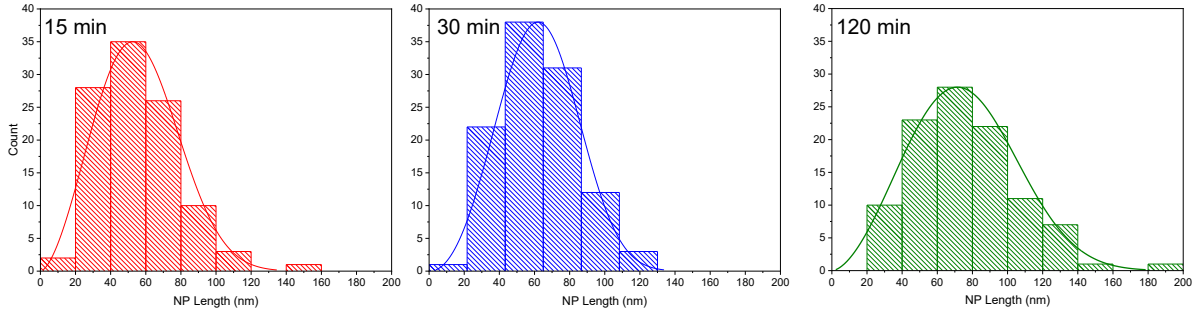

Figure B.11 PSD of BHG@ZIF-8 samples synthesized with a variable addition times.

Table B.6 PSD modelling parameters of UiO-66 samples

		Weibull		Gaussian		Test
Sample	Model	α	β	ϕ	SD	
UiO-66-10-120	Weibull	34.03	4.09	--	--	Pass
	Gaussian	--	--	30.99	8.02	Pass
UiO-66-8-120	Weibull	22.26	4.02	--	--	Pass
	Gaussian	--	--	20.20	5.43	Pass
UiO-66-6-120	Weibull	16.04	4.25	--	--	Pass
	Gaussian	--	--	14.64	3.57	Reject
UiO-66-4-120	Weibull	4.50	4.00	--	--	Pass
	Gaussian	--	--	4.09	1.05	Reject
UiO-66-10-120	Weibull	27.86	6.36	--	--	Pass
	Gaussian	--	--	26.00	4.42	Pass
UiO-66-8-120	Weibull	19.27	3.61	--	--	Pass
	Gaussian	--	--	17.37	5.15	Pass
UiO-66-6-120	Weibull	13.67	4.92	--	--	Pass
	Gaussian	--	--	12.56	2.77	Pass

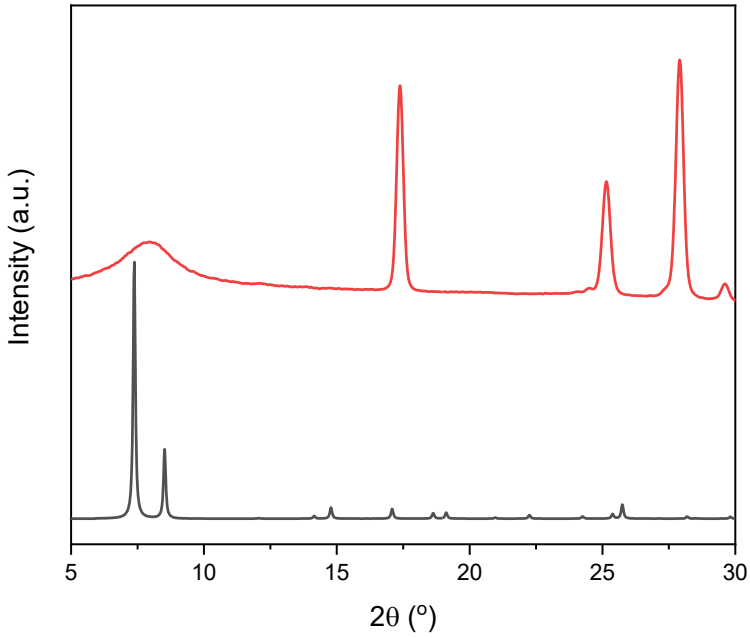

Figure B.12 PXRD of simulated UiO-66 (black) and UiO-66 synthesized using Pakamore's method (red).[14]

Table B.7 Extracted data from microemulsion UiO-66 PXRD patterns

Sample	$\frac{I_{[001]}}{I_{[111]}}$ (%)*	Φ_{ave} (nm)†	$\Phi_{[111]}$ (nm)	$\Phi_{[002]}$ (nm)	$\Phi_{[006]}$(nm)
UiO-66-10-120	4.78	16.33	16.82	14.19	17.98
UiO-66-8-120	7.22	12.72	12.44	11.51	14.21
UiO-66-6-120	6.88	12.79	12.76	11.75	13.87
UiO-66-4-120	10.49	10.40	8.98	11.08	11.15
UiO-66-3.6-120	16.92	--	--	--	--
UiO-66-2-120	37.53	--	--	--	--
UiO-66-10-30	6.50	13.67	13.75	12.17	15.09
UiO-66-8-30	10.00	11.78	11.12	11.45	12.75
UiO-66-6-30	9.55	10.74	9.80	10.52	11.90
UiO-66-4-30	12.14	10.26	10.66	8.71	11.40
UiO-66-3.6-30	23.76	--	--	--	--
UiO-66-2-30	44.59	--	--	--	--

* Relative intensity of the [001] to [111] peaks
† Average grain size across three peaks using the Scherrer equation

Table B.8 Summary of UiO-66 particle sizes determined by TEM

Sample	Φ (nm)	N	SD (nm)	SD (%)
UiO-66-10-120	31.0	141	7.99	25.8
UiO-66-8-120	20.2	125	5.41	26.8
UiO-66-6-120	14.6	101	3.56	24.3
UiO-66-4-120	4.09	107	1.05	25.7
UiO-66-3.6-120	--	--	--	--
UiO-66-2-120	--	--	--	--
UiO-66-10-30	26.0	119	4.40	16.9
UiO-66-8-30	17.4	115	5.13	29.5
UiO-66-6-30	12.6	100	2.76	22.0
UiO-66-4-30	--	--	--	--
UiO-66-3.6-30	--	--	--	--
UiO-66-2-30	--	--	--	--

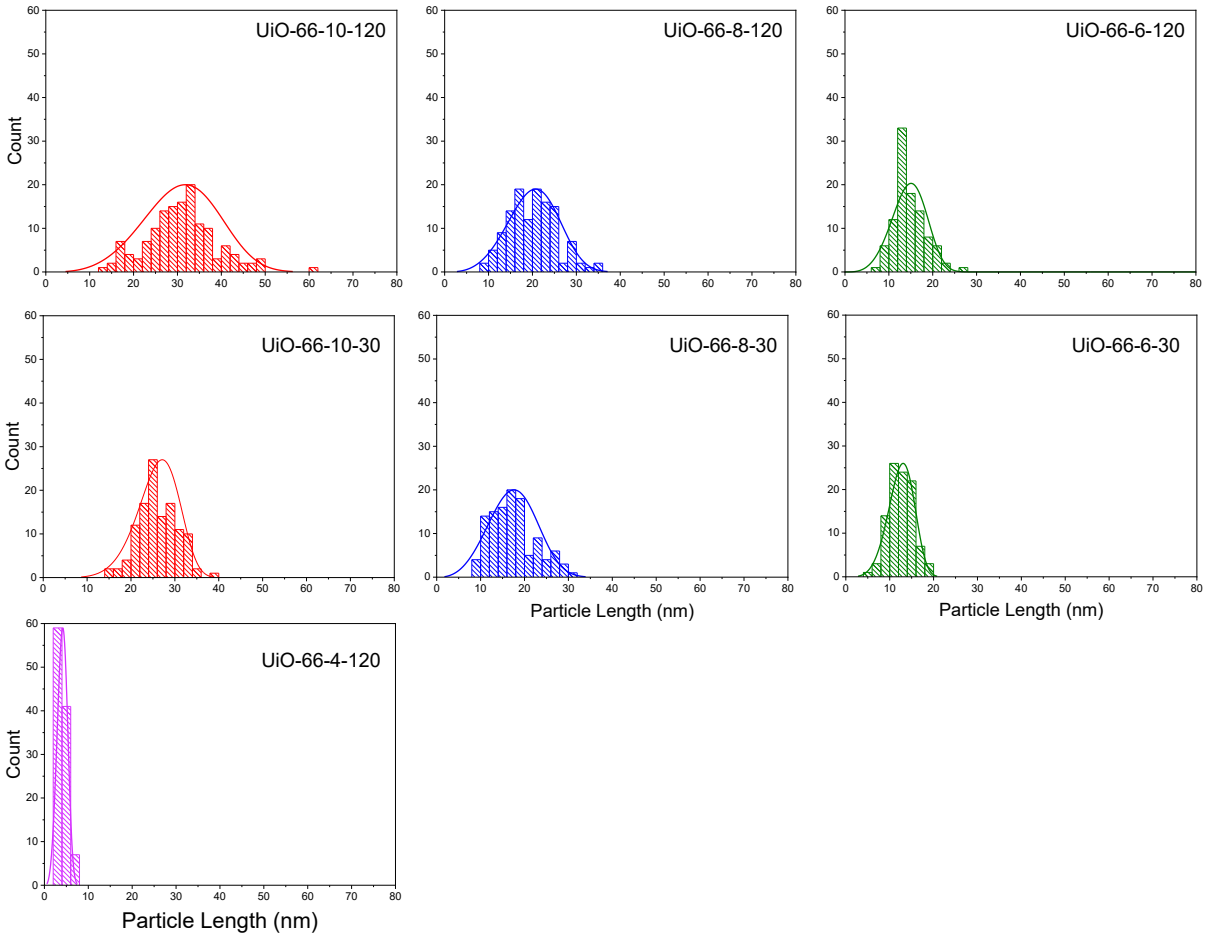

Figure B.13 Experimental PSD of microemulsion synthesized UiO-66 samples with a Weibull fit.

Table B.9 TGA Decomposition Temperatures and Defectivity of UiO-66 samples

Sample	Decomposition Step 1 (°C)	Decompositon Step 2 (°C)	Step 2 W (%)	% Defects
UiO-66-10-120	256	479	199	17.5
UiO-66-8-120	310	492	205	12.9
UiO-66-6-120	301	487	206	11.2
UiO-66-10-30	222 & 289	501	194	21.8
UiO-66-8-30	246	499	186	28.5
UiO-66-6-30	280	490	193	22.5

Appendix C - Structures

Table C.1 Protein Structures Obtained from the Protein Data Bank (PDB)

Protein	*Bovine Serum Albumin*	*Haemoglobin*
PDB ID	4F5S[15]	1HDA[16]
Organism	*Bos taurus*	*Bos taurus*
Mass (KDa)	66.6	64.6
Residue Number	1160	572
pI (Calculated)[*]	5.60	8.19
Length (nm)[†]	14.9	6.62
Width (nm)	8.14	5.76
Depth (nm)	6.14	5.37

Table C.2 CCDC[18] Accessed Structures

MOF	Metal Cluster	Ligand	Topology	CCDC Ref.[‡]	Reference
MOF-5	Zn_4O	BDC	**pcu**	MIBQAR	[19]
HKUST-1	$Cu_2(CO_2)_4$	BTC	**tbo**	BODPAN	[20]
NU-1000	$Zr_6O_4(OH)_4$	TABPy[§]	**csq**	FIFFUX	[21]
NU-901	$Zr_6O_4(OH)_4$	TABPy	**scu**	--[**]	[22]
ZIF-8	Zn^{2+}	mIM	**sod**	FAWCEN	[23]
ZIF-L	Zn^{2+}	mIM	**2D-Sheets**	IWOZOL	[24]
ZIF-67	Co^{2+}	mIM	**sod**	GITTOT02	[25]
$Zn(IM)_2$ neb	Zn^{2+}	IM	**neb**	KEVLEE	[26]
UiO-66	$Zr_6O_4(OH)_4$	BDC	**fcu**	RUBTAK	[27]

[*] The pI was calculated using the Henderson-Hasselbalch equation (A.4.1 Isoelectric Point)
[†] Protein dimensions were calculated from the PDB structures using the Draw_Protein_Dimensions.py script from the Pymol script repository[17]
[‡] Cambridge Crystallographic Data Centre entry reference
[§] 1,3,6,8-tetrakis(p-benzoic acid)pyrene
[**] Structure was not obtained from the CCDC.

Appendix References

1. Holzwarth, U.; Gibson, N., The Scherrer equation versus the 'Debye-Scherrer equation'. *Nat. Nanotechnol.* **2011,** *6* (9), 534-534.

2. Jensen, H.; Pedersen, J. H.; Jorgensen, J. E.; Pedersen, J. S.; Joensen, K. D.; Iversen, S. B.; Sogaard, E. G., Determination of size distributions in nanosized powders by TEM, XRD, and SAXS. *J. Exp. Nanosci.* **2006,** *1* (3), 355-373.

3. Rehani, B. R.; Joshi, P. B.; Lad, K. N.; Pratap, A., Crystallite size estimation of elemental and composite silver nano-powders using XRD principles. *Indian J. Pure Appl. Phys.* **2006,** *44* (2), 157-161.

4. Guangrong, N.; Flemming, R. L., Rietveld refinement of La B6: data from micro-XRD. *J. Appl. Crystallogr.* **2005,** *38*, 757-759.

5. Jain, A.; Ong, S. P.; Hautier, G.; Chen, W.; Richards, W. D.; Dacek, S.; Cholia, S.; Gunter, D.; Skinner, D.; Ceder, G.; Persson, K. a., The Materials Project: A materials genome approach to accelerating materials innovation. *APL Materials* **2013,** *1* (1), 011002.

6. Schneider, C. A.; Rasband, W. S.; Eliceiri, K. W., NIH Image to ImageJ: 25 years of image analysis. *Nat. Methods* **2012,** *9* (7), 671-675.

7. D'Agostino, R., *Goodness-of-Fit-Techniques*. First edition ed.; Taylor and Francis: 2017.

8. Slakter, M. J., A Comparison of the Pearson Chi-Square and Kolmogorov Goodness-of-Fit Tests with Respect to Validity. *J. Am. Stat. Assoc.* **1965,** *60* (311), 854-858.

9. Deng, B.; Jiang, D. Y., Determination of the Weibull parameters from the mean value and the coefficient of variation of the measured strength for brittle ceramics. *Journal of Advanced Ceramics* **2017,** *6* (2), 149-156.

10. Brunauer, S.; Emmett, P. H.; Teller, E., Adsorption of gases in multimolecular layers. *J. Am. Chem. Soc.* **1938,** *60*, 309-319.

11. Shearer, G. C.; Chavan, S.; Bordiga, S.; Svelle, S.; Olsbye, U.; Lillerud, K. P., Defect Engineering: Tuning the Porosity and Composition of the Metal–Organic Framework UiO-66 via Modulated Synthesis. *Chem. Mater.* **2016,** *28* (11), 3749-3761.

12. Bjellqvist, B.; Hughes, G. J.; Pasquali, C.; Paquet, N.; Ravier, F.; Sanchez, J. C.; Frutiger, S.; Hochstrasser, D., The focus positions of polypeptides in immobilized pH gradients can be predicted from their amino acid sequences. *Electrophoresis* **1993,** *14* (10), 1023-1031.

13. Bradford, M. M., A rapid and sensitive method for the quantitation of microgram quantities of protein utilizing the principle of protein-dye binding. *Anal. Biochem.* **1976,** *72* (1-2), 248-254.

14. Pakamorė, I.; Rousseau, J.; Rousseau, C.; Monflier, E.; Szilágyi, P. Á., An ambient-temperature aqueous synthesis of zirconium-based metal–organic frameworks. *Green Chem.* **2018,** *20* (23), 5292-5298.

15. Bujacz, A., Structures of bovine, equine and leporine serum albumin. *Acta Crystallogr. Sect. D-Biol. Crystallogr.* **2012,** *68*, 1278-1289.
16. Perutz, M. F.; Fermi, G.; Poyart, C.; Pagnier, J.; Kister, J., A novel allosteric mechanism in haemoglobin. Structure of bovine deoxyhaemoglobin, absence of specific chloride-binding sites and origin of the chloride-linked Bohr effect in bovine and human haemoglobin. *J. Mol. Biol.* **1993,** *233* (3), 536-545.
17. Schrodinger, LLC, The PyMOL Molecular Graphics System, Version 1.8. 2015.
18. Groom, C. R.; Bruno, I. J.; Lightfoot, M. P.; Ward, S. C., The Cambridge Structural Database. *Acta Crystallogr. Sect. B-Struct. Sci.Cryst. Eng. Mat.* **2016,** *72*, 171-179.
19. Lock, N.; Wu, Y.; Christensen, M.; Cameron, L. J.; Peterson, V. K.; Bridgeman, A. J.; Kepert, C. J.; Iversen, B. B., Elucidating Negative Thermal Expansion in MOF-5. *J. Phys. Chem. C* **2010,** *114* (39), 16181-16186.
20. Ahmed, A.; Hodgson, N.; Barrow, M.; Clowes, R.; Robertson, C. M.; Steiner, A.; McKeown, P.; Bradshaw, D.; Myers, P.; Zhang, H. F., Macroporous metal-organic framework microparticles with improved liquid phase separation. *J. Mater. Chem. A* **2014,** *2* (24), 9085-9090.
21. Mondloch, J. E.; Bury, W.; Fairen-Jimenez, D.; Kwon, S.; DeMarco, E. J.; Weston, M. H.; Sarjeant, A. A.; Nguyen, S. T.; Stair, P. C.; Snurr, R. Q.; Farha, O. K.; Hupp, J. T., Vapor-Phase Metalation by Atomic Layer Deposition in a Metal-Organic Framework. *J. Am. Chem. Soc.* **2013,** *135* (28), 10294-10297.
22. Lyu, J.; Zhang, X.; Otake, K.-I.; Wang, X.; Li, P.; Li, Z.; Chen, Z.; Zhang, Y.; Wasson, M. C.; Yang, Y.; Bai, P.; Guo, X.; Islamoglu, T.; Farha, O. K., Topology and porosity control of metal–organic frameworks through linker functionalization. *Chem. Sci.* **2019,** *10* (4), 1186-1192.
23. Morris, W.; Stevens, C. J.; Taylor, R. E.; Dybowski, C.; Yaghi, O. M.; Garcia-Garibay, M. A., NMR and X-ray Study Revealing the Rigidity of Zeolitic Imidazolate Frameworks. *J. Phys. Chem. C* **2012,** *116* (24), 13307-13312.
24. Chen, R. Z.; Yao, J. F.; Gu, Q. F.; Smeets, S.; Baerlocher, C.; Gu, H. X.; Zhu, D. R.; Morris, W.; Yaghi, O. M.; Wang, H. T., A two-dimensional zeolitic imidazolate framework with a cushion-shaped cavity for CO2 adsorption. *Chem. Commun.* **2013,** *49* (82), 9500-9502.
25. Kwon, H. T.; Jeong, H. K.; Lee, A. S.; An, H. S.; Lee, J. S., Heteroepitaxially Grown Zeolitic Imidazolate Framework Membranes with Unprecedented Propylene/Propane Separation Performances. *J. Am. Chem. Soc.* **2015,** *137* (38), 12304-12311.
26. Schroder, C. A.; Saha, S.; Huber, K.; Leoni, S.; Wiebcke, M., Metastable metal imidazolates: development of targeted syntheses by combining experimental and theoretical investigations of the formation mechanisms. *Z. Krist.-Cryst. Mater.* **2014,** *229* (12), 807-822.

27. Cavka, J. H.; Jakobsen, S.; Olsbye, U.; Guillou, N.; Lamberti, C.; Bordiga, S.; Lillerud, K. P., A New Zirconium Inorganic Building Brick Forming Metal Organic Frameworks with Exceptional Stability. *J. Am. Chem. Soc.* **2008,** *130* (42), 13850-13851.